Dissertation

submitted to the

Combined Faculties of the Natural Sciences and Mathematics

of the Ruperto-Carola-University of Heidelberg, Germany

for the degree of

Doctor of Natural Sciences

Put forward by

Chintan Shah

born in: Dabhoi, Vadodara (India)

Oral examination: 8$^{\text{th}}$ December 2015

Measuring and modeling of anisotropic and polarized x-ray emission following resonant recombination into highly charged ions

Referees: Priv.-Doz. Dr. Stanislav Tashenov

Priv.-Doz. Dr. Zoltán Harman

Abstract

The angular distribution and polarization of x rays emitted due to resonant recombination into highly charged ions were studied experimentally using an electron beam ion trap. In the first experiment, the linear polarization of x rays produced by dielectronic recombination into highly charged krypton ions was measured using the Compton polarimetry technique. In the second experiment, the electron-ion collision energy was scanned over the K-shell dielectronic, trielectronic and quadruelectronic recombination resonances in highly charged iron and krypton ions. The angular distribution of x rays following resonant recombination was measured by observing x rays in the direction along and perpendicular to the electron beam propagation direction. Both the x-ray angular distribution and polarization reveal the alignment of the populated excited states.

The experiments revealed a high sensitivity of the x-ray angular distribution and polarization to the relativistic effects such as the Breit interaction. Measurements show that most of the transitions lead to polarization, including hitherto neglected trielectronic and quadruelectronic recombination channels. Moreover, these channels dominate the ionization balance and the polarization of the prominent $K\alpha$ x rays emitted by hot anisotropic plasmas. The experimental results benchmark relativistic atomic calculations and are expected to play an important role in accurate diagnostics of hot astrophysical plasmas of solar flares and active galactic nuclei, and laboratory fusion plasmas of tokamaks.

Zusammenfassung

Die Winkelverteilung und Polarisation von Röntgenquanten, die in resonanter Rekombination in hochgeladene Ionen erzeugt werden, wurden mithilfe einer Elektronenstrahl-Ionenfalle experimentell untersucht. Im ersten Experiment wurde die lineare Polarisation von Röntgenquanten, die durch dielektronische Rekombination in hochgeladene Ionen erzeugt wurden, durch Compton Polarimetrie gemessen. Im zweiten Experiment wurde die Elektronen-Ionen Kollisionsenergie über die K-Schalen dielektronische, trielektronische und quatroelektronische Rekombination Resonanzen in hochgeladene Eisen und Krypton Ionen gescannt. Die Winkelverteilung der Röntgenquanten, die auf die resonante Rekombination folgen, wurde gemessen, indem die Röntgenstrahlung in der Richtung entlang und im rechten Winkel zur Elektronenstrahlrichtung gemessen wurde. Die Winkelverteilung und die Polarisation der Röntgenquanten geben jeweils Auskunft über das Alignment der bevölkerten angeregten Zustände.

Die Experimente zeigen eine hohe Empfindlichkeit der Winkelverteilung und Polarisation der Röntgenquanten auf relativistische Effekte wie die Breit-Wechselwirkung. Die Messungen zeigen, dass die meisten Übergänge zu Polarisation führen, auch bei den bisher nicht beachteten trielektronischen und quatroelektronischen Rekombinationskanälen. Des weiteren dominieren diese Kanäle das Ionisationsgleichgewicht und die Polarisation von wichtigen $K\alpha$ Röntgenquanten, die in heißen Plasmen emittiert werden. Die experimentellen Befunde überprüfen relativistische atomare Rechnungen und man erwartet, dass sie eine wichtige Rolle in der genauen Diagnostik von heißen astrophysische Plasmen von Sonneneruptionen und aktiven galaktischen Kernen und laboratorische Fusionsplasmen von Tokamaks spielen.

को अद्धा वेद क इह प्र वोचत्कुत आजाता कुत इयं विसृष्टिः ।
अर्वाग्देवा अस्य विसर्जनेनाथा को वेद यत आबभूव ॥

इयं विसृष्टिर्यत आबभूव यदि वा दधे यदि वा न ।
यो अस्याध्यक्षः परमे व्योमन्त्सो अङ्ग वेद यदि वा न वेद ॥

Who really knows? Who will here proclaim it?
Whence was it produced? Whence is this creation?
The gods came afterwards, with the creation of this universe.
Who then knows whence it has arisen?

Whence this creation has arisen
- perhaps it formed itself, or perhaps it did not -
the One who looks down on it,
in the highest heaven, only He knows
or perhaps even He does not know.

<div style="text-align: right">

The Creation Hymn of Rig Veda, 10:129 (1700–1100 BC)
–Translation by Wendy Doniger O'Flaherty

</div>

to my mother

Contents

Chapter 1

Introduction

1.1 Polarimetry in x-ray astronomy

A significant fraction of the matter in the Universe is in a highly ionized state emanating a broad range of electromagnetic spectra, including x rays [1, 2]. Astronomers could not have envisioned the Universe as such a violent place without the rapid developments of x-ray observations. Since the Earth's atmosphere is optically thick to the x rays, observations became only possible with the development of space technology. In fact, shortly after the Sun was observed to be a powerful source of x rays [3], it was predicted that the detection of x-ray sources outside the solar system would be nearly impossible, as the Sun appears to be x-ray bright solely due to its proximity to the Earth. However, it turned out that there exist much more powerful x-ray sources in the Universe. Beside the Sun, Scorpius X-1 became the first x-ray source discovered outside the solar system, with a remarkable launch of sounding rocket carrying a highly sensitive x-ray detector in 1962 [4].

Since 1962, x-ray observations have been used to increase our knowledge of many cosmic phenomena, including black holes, supernovas, and neutron stars. The imaging and spectroscopic information from missions such as the *Einstein* observatory in the late 1970s and the ongoing missions of the *Chandra* and *XMM-Newton* x-ray observatories have unraveled detailed physical conditions of the most violent environments in the Universe. They have shown us the flow of gases, when galaxies collide, given us the estimates of the size of neutron stars and revealing conditions at the center of our galaxy [5]. When combined with measurements from other parts of the spectrum, x-
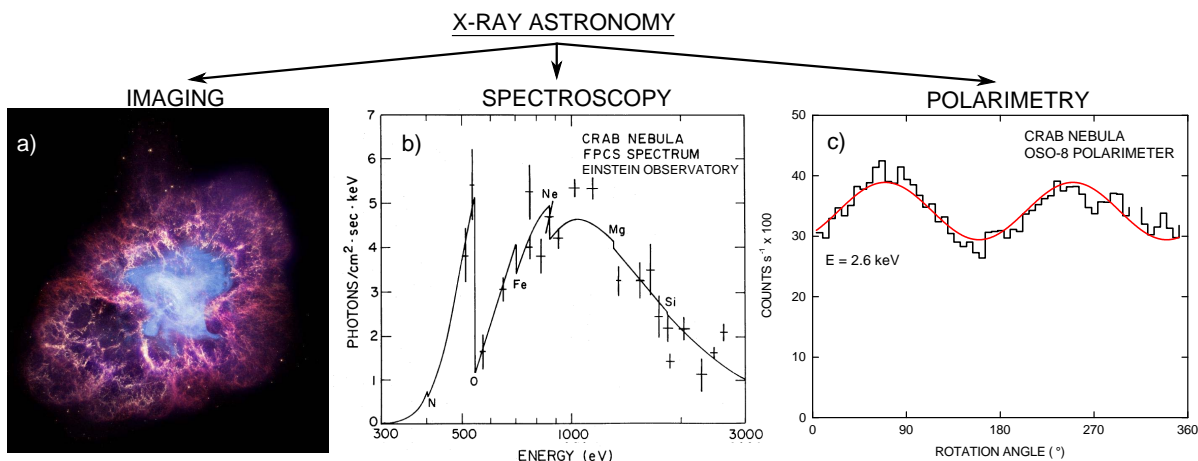
Figure 1.1: X-ray imaging, spectroscopy and polarimetry: (a) Multi-wavelength view of the Crab nebula: The optical image in red and yellow (by *Hubble* Space Telescope), the x-ray image in blue (by *Chandra* observatory), and the infrared image in purple (by *Spitzer* Space Telescope). Image courtesy: ESA. (b) Measurements of the Crab Nebula x-ray flux spectrum (crosshairs) are shown, along with a model that incorporates interstellar medium absorption by several elements (reproduced from [6]). (c) Modulation curve obtained at 2.6 keV during observation of the Crab nebula with the *OSO-8* polarimeter (modified from [7]).

ray observation can also help to determine the underlying physical phenomena. For example, the *Chandra* x-ray image of the Crab Nebula shows the synchrotron radiation emitted by highly energetic electrons, which are concentrated close to the central pulsar, a powerhouse of the entire nebula. The size of the x-ray image is smaller than the optical image because the high energy electrons radiate away their energy more quickly in the region close to the neutron star where magnetic fields are stronger, see Fig. 1.1 (a). X-ray spectroscopic measurements are used to determine the temperatures, densities, ionization states, and elemental compositions of hot cosmic plasmas[1]. As an example, the spectroscopic observations of Crab Nebula by the *Einstein* satellite have shown the elemental composition, including N, O, Fe, Ne, Mg and Si (see Fig. 1.1 (b)).

In addition to imaging and spectroscopy, polarimetry is the third pillar of the x-ray astronomy. Polarimetry adds two more observables to the conventional astronomical parameter space (energy and time): the degree and angle of polarization [8]. They give direct insight to the geometry and orientation of the x-ray source with respect to the observer. Polarization radiation from cosmic sources carries information over the dynamical processes that generated it in the first place: the presence of directed

---

[1]The plasma often called the fourth state of matter – an ionized gas consisting of electrons, atoms, positive and negative ions and molecules. It is believed to be the most abundant and common form of matter in the universe.

relativistic jets, of magnetic fields in the solar flare, or the signature of synchrotron radiation in hot halos are the prime examples. Distance degrades this information less than that of the imaging data. Thus, x-ray polarimetry is a powerful tool to investigate the geometries of cosmic sources and is opening a view to the inner workings of these cosmic sites.

The importance of x-ray polarization observations has been expressed in a number of theoretical studies on various types of cosmic sources such as accreting pulsars or supernova remnants [9–14]. In spite of such significance, to this date, x-ray polarization measurements of only one cosmic object, the Crab nebula, has been taken at a significant level [7, 15]. The degree of polarization (∼19%) was measured at 2.6 keV and 5.2 keV by the polarimeter on board the *OSO-8* satellite, see Fig. 1.1 (c). The results had proved the synchrotron origin of the Crab nebula's x-ray emission. After this initial effort, no experiments have been carried out in order to measure x-ray polarization from the cosmic x-ray sources. Few attempts were made to design and build x-ray polarimeters for space mission *XPE* [16] and *PLEXAS* [17], but, unfortunately, these missions were not materialized. The need for developing reliable methods for x-ray polarimetry can be understood from the fact that, in the absence of dedicated x-ray polarimeters, there were many efforts to recover polarimetry information from the existing spectroscopic instruments on board of *INTEGRAL-IBIS/SPI* missions [18–21]. However, since the detectors have not been designed or optimized for polarization observation, such data remain inconclusive.

The scientific harvest of space and balloon-borne x-ray polarimetry missions has been outlined by Krawczynski (see [22] and references therein), and by Soffitta in relation to the *XIPE (X-ray Imaging Polarimetry Explorer)* mission [23]. Recently, *XIPE* has been announced as one of three candidates selected for the next medium-sized space mission led by the European Space Agency (ESA) [24]. *XIPE* aims to study anisotropies of astrophysical plasmas which are found in the most extreme yet inadequately understood sites of the Universe. For instance, unknown mechanisms generating relativistic plasma jets from active galactic nuclei can be at the focus of this mission or tests of fundamental physics related to General Relativity, measurements of black hole spin or the detection of vacuum polarization in extreme magnetic fields [23]. Besides *XIPE*, the Cadmium Zinc Telluride Imager (CZTI) detector on board the *ASTROSAT*, the Indian multi-wavelength space observatory, would be able to do sensitive polarization measurements for bright cosmic x-ray sources [25].

19

1.2 Atomic processes in x-ray spectroscopy

Sufficient understanding of the atomic physics underlying x-ray emission is essential for any reliable spectroscopic interpretation. Emergent spectra can be modeled by detailed calculations of level populations, accounting for all relevant atomic processes. Similarly, the interpretation of x-ray polarimetry data requires comprehensive knowledge about the polarization mechanisms in atomic collision processes. In this section, we briefly introduce the atomic processes that control level population in the plasmas. They consist of ionization, recombination, collisional excitation and deexcitation. These processes usually lead to the emission of polarized radiation.

• The dominant process leading to continuum x-ray emission in the plasmas is bremsstrahlung. It is caused by deceleration of an electron in the Coulomb field of an ion:

$$X^{q+} + e^-(E_0) \; \rightarrow \; X^{q+} + e^-(E_1) + \hbar\omega,$$
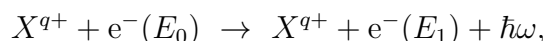
where q refers to the charge state of the ion X, and $E_{0,1}$ denote the kinetic energies of the electron before and after the collision. The x-ray polarization of the continuum due to bremsstrahlung is reasonably well understood [26].

• Electron-impact ionization and its time–reverse process three-body recombination:

$$X^{q+} + e^- \; \rightleftharpoons \; X^{(q+1)+} + e^- + e^-.$$
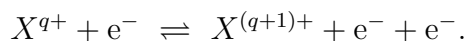
• Photoemission and its time–reverse process photoexcitation:

$$[X^{q+}]^* \; \rightleftharpoons \; X^{q+} + \hbar\omega.$$
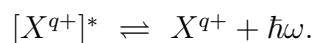
• Photoionization: an inner-shell electron is ejected leaving the ion in the excited state, and it time–reverse process radiative recombination: emission of a photon under recombination of an electron into an ion

$$X^{q+} + \hbar\omega \; \rightleftharpoons \; [X^{(q+1)+}]^* + e^-,$$
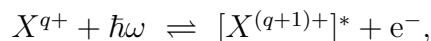
where the asterisk refers the excited ionic state.

• Dielectronic recombination is a resonant two-step process involving the capture of a free electron into an ion with simultaneous excitation of a bound electron forming excited ion core. This is the first step (dielectronic capture) and, in the second step (radiative stabilization), the excited state radiatively decays to the ground state:

$$X^{q+} + e^- \; \rightleftharpoons \; [X^{(q-1)+}]^{**} \; \rightarrow [X^{(q-1)+}] + \hbar\omega.$$
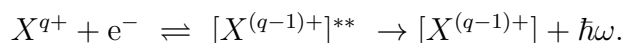
The time–reverse to the first step of the dielectronic recombination is autoionization. Here, it leads to the emission of an electron instead of a photon.

The probability of these level populating processes is measured by the cross sections σ. It is defined as the ratio of the event rate per target particle to the incident projectile flux. For plasma diagnostics, it is convenient to describe cross sections with rate coefficients, expressed as,

$$\alpha = \int \mathrm{v}\sigma(E)f(E)dE, \tag{1.1}$$

where v is the collision velocity and $f(E)$ is the electron energy distribution. Usually for the plasmas, the latter is taken to be Maxwellian.

The x-ray polarization due to radiative recombination has been studied and it is well understood [27, 28]. In contrast to that, polarization is not well understood for bound–bound processes: the emission of characteristic x rays following dielectronic recombination. This thesis focuses on these two processes. They are described in details in the following Chapter 2.

Mechanisms yielding polarized x rays in the plasmas:

A polarization occurs when the radiation component polarized with the electric field vector parallel and perpendicular to the electron beam direction has different intensities, $I_\parallel$ and $I_\perp$, respectively. The degree of linear polarization $P(\theta)$ for the radiation emitted at an angle θ to the beam direction is given by

$$P(\theta) = \frac{I_\parallel(\theta) - I_\perp(\theta)}{I_\parallel(\theta) + I_\perp(\theta)}. \tag{1.2}$$

The degree, direction, and energy dependence of the polarization provide an insight to the properties of the non-thermal electron velocity distribution, and possible magnetic field configurations [29]. Since electrons follow the magnetic field lines, polarization could thus reveal the presence and orientation of currents and magnetic fields in the plasmas. The following are examples of processes yielding polarized x rays in the cosmic sources;

- Synchrotron radiation, where relativistic charged particles are accelerated in a magnetic field.
- Thermal emission from a hot dense gas in a strong magnetic field.
- Bremsstrahlung, which occurs whenever electrons collide with ions.

Similar processes have been found in solar flares [30–33], in cosmic x-ray sources such as active galactic nuclei (AGN) [34–36], clusters of galaxies [37–39], gamma-ray bursts [18–20], pulsars, and neutron stars [12, 40]. Source mechanism generating polarized x rays in these cosmic objects are reviewed by Kallman [41].

The above situation is not only relevant in astrophysical objects, it can also appear in laboratory plasmas. Plasma, produced within high current discharges in Z-pinches, plasma focus or tokamak machines, compressed by its own magnetic field is essentially anisotropic and emit polarized x rays. In such machines, this phenomenon is apparently connected with the direction of the current flow. Likewise, hot atomic plasmas produced in the electron beam ion traps and storage rings usually emit polarized x rays, because of the direction of electrons or ions involved in the collision processes [42–47]. Anisotropic plasmas emitting polarized x rays can appear in magnetic cusps [48], Z-pinches [49, 50], fusion devices such as tokamaks [51, 52] and stellarators, and laser-produced plasmas [53–55]. Polarization can diagnose the presence and orientation of currents and magnetic fields, yielding information on the plasma heating and confinement mechanisms [56]. Therefore, a study of anisotropy in laboratory plasmas could also pave the way to understand future celestial plasma observations.

1.3   Need of laboratory atomic data

X-ray line and continuum observations can determine the electron temperature, estimate the radiation field or electron density and reveal charge state balance of the plasmas. Polarimetric observation can determine the presence and direction of the electron beams and the magnetic field in the plasmas. However, such interpretations require adequate understanding of all electron-ion collision processes mentioned in the previous section 1.2. Their accurate atomic data including the transition energies, cross sections, oscillator strengths, rate coefficients and polarization are required. For example, the recombination and scattering of electrons from ions are important in low-temperature photoionized plasmas[2] such as those appearing in the vicinity and the jets of active galactic nuclei and x-ray binaries [57, 58]. In high-temperature collisionally ionized plasmas, the ions are mostly ionized by electron impact, while recombination is dominated by resonant and radiative recombination. Experimental data of such atomic processes are rarely available, thus complex plasma models are largely derived from theoretical calculations. To achieve a reliable scientific interpretation of the spectroscopic or polarimetric observations, theoretical calculations must be verified by the results obtained from spectroscopic measurements in the laboratory. The need of laboratory data has been reviewed by many authors in the past years [59–62]. This section focuses on some recent observations which clearly indicate the need of laboratory data for electron-ion recombination processes and

---

[2]The electron temperature $k_{\mathrm{B}}T_e$ is much smaller than the typical ionization energy I_p of ions in photoionized plasmas, while $k_{\mathrm{B}}T_e$ is of the same scale as I_p in case of collisionally ionized plasmas.
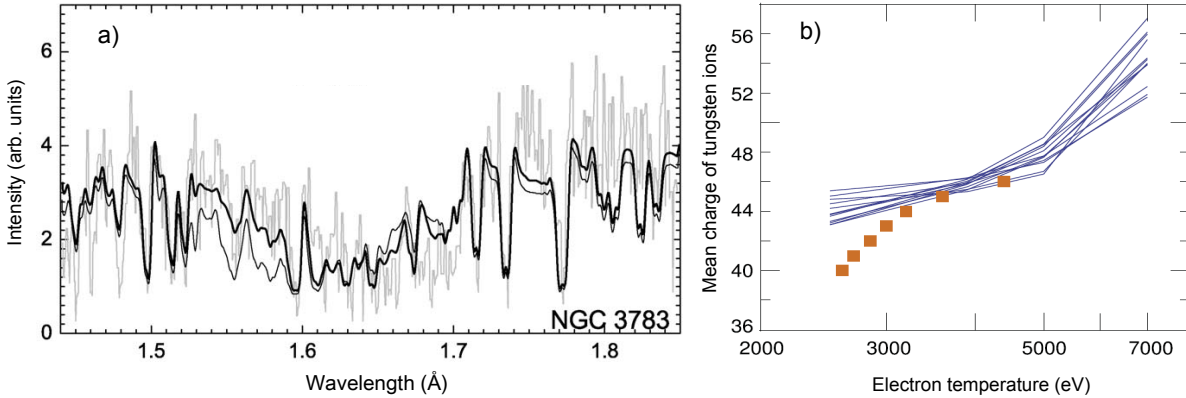
Figure 1.2: (a) Chandra x-ray spectrum of the active galaxy *NGC 3783* together with theoretical calculations. The data were published by Netzer *et al.* [63]. The measured absorption spectrum (light gray) is well described by the calculations (solid thick line) with enhanced recombination rates of $Fe^{8+..14+}$ ions. The thin solid line refers to the calculations based on the available limited atomic data sets (modified from [61]). (b) The mean charge state of the tungsten ions observed as a function of electron temperature from *ASDEX* tokamak (orange squares) [64]. The solid blue lines refer to the different ionization balance calculations presented in NLTE-7 workshop [65] (modified from [66]).

their polarization.

The ionization and recombination rates determine the charge state balance of the plasmas. They are necessary to understand observations and modeling of astrophysical plasmas. For example, Fig. 1.2 (a) shows the *Chandra* x-ray spectrum of the active galaxy *NGC 3783*. The spectrum agrees well with the ad-hoc calculation which assumes recombination rates for iron ions are greater than the predicted theoretical rates [61, 63]. The agreement between the model and the observations is greatly improved by this enhancement in the recombination rates of iron, that clearly indicate that the theoretical recombination cross sections used in the original model might be too small. Clearly, this indicates that further developments of the theory and experiment are necessary.

It was recently observed that the newly found additional ionization and recombination channels can remarkably modify the ionization balance (or charge state balance) of the plasmas. Hahn *et al.* [67] observed that the process of electron-impact multiple ionization can affect the charge balance of the collisionally ionized plasmas [67, 68]. Similarly, newly found recombination channels such as trielectronic and quadruelectronic recombination processes can affect the charge balance of the plasmas. These processes involve two and three bound electrons that are excited to a higher shell while capturing a free electron (explained later in Sec. 2.1.3). The correlated excitation of two or more bound electrons appears to be unlikely, therefore, it was neglected in the earlier plasma models. However, direct evidence of dominant *intra-shell* trielectronic recombination

was obtained in several experiments [69–72]. The *inter-shell* trielectronic recombination was also experimentally observed for ions relevant to astrophysics [73–76]. In those experiments, the trielectronic recombination rates are found comparable to or higher than that of dielectronic recombination.

The *intra/inter-shell* higher-order resonant recombination processes provide new electron–recombining–channels in the plasmas. Since their rate coefficients are comparable to the dielectronic recombination, they cannot be neglected and must be included in the ionization balance calculations. Unfortunately, so far, none of the plasma models calculating the ionization balance have included these processes. Omitting such recombination channels means that the mean ion charge will be predicted higher than it actually is. For example, Putterich *et al.* [64] had measured the ionization balance of tungsten in plasmas produced in the *ASDEX* Upgrade tokamak and compared with dozens of ionization balance calculations performed by different teams and codes. All calculations predict the mean charge of the tungsten below 4 keV temperature to be consistently higher than the measurements performed (see Fig. 1.2 (b)). This systematic discrepancy between the calculations and measurement is striking. Beiersdorfer *et al.* [66] recently suggested that this discrepancy is due to the large contribution of higher-order resonant recombination. The contribution can be large and increases as the mean ion charge tends towards ions with open-shell electronic configurations. The inclusion of these processes may further modify the opacity of plasmas and by this the transport of energy through them [77]. We will discuss the importance of higher-order resonant processes in particular to plasma diagnostics in Chapter 6.

Need of atomic polarization data:

The x-ray polarization as a new observable has a high discovery potential in astrophysics. It can address fundamental questions concerning high density, high temperature, non-thermal electron distribution, strong electric and magnetic fields and strong gravity effects in the plasmas. The physics behind the magnetars, pulsars, neutron stars and spin of the black hole can be discovered with it [23, 40]. Despite of this promising potential, the required level of understanding of polarization properties of many elementary atomic processes is missing. This would compromise the interpretation of the astrophysical observations. Moreover, the intended use of gas polarimeter [78] for an upcoming x-ray polarimetry mission *XIPE* [23] suffers from low energy resolution. Hence, the observed polarization from such polarimeter will contain contributions from many x-ray lines as well as from continuum radiation. Interpretation of their data requires a systematic understanding of the polarization mechanisms of both of x-ray discrete

transitions and the continuum. A similar situation will likely arise in the polarization diagnostics of magnetically confined fusion plasmas [52, 56].

The laboratory experiments measuring recombination cross sections or rate coefficients require the knowledge of polarization to interpret their measurements. This requirement arises from the fact that polarized radiation also exhibits strong emission anisotropy. In experiments, the radiation is nearly always observed at an angle. Nearly all of those experiments rely on the theoretical calculations of x-ray polarization and anisotropy [79–81]. The theory based on photon-polarization density-matrix formalism for the polarization of photons emitted by ions is well established since last four decades [82, 83]. However, most predictions based on this theory have not been experimentally verified. To date, x-ray polarization and angular distributions have been measured for only few selected transitions in a few elements using electron beam ion traps [47, 84–93] and a heavy ion storage ring [45, 94, 95]. Some of those experiments also showed the discrepancy with the theoretical calculations [90, 92].

Disagreements of theories with laboratory data have shown that the models and the calculations are incomplete, i. e., it is likely that the theoretical predictions are missing crucial physics as a part of their approximations. Laboratory data are required to benchmark the calculations and plasma diagnostics codes. They can provide a standard to check the accuracy of these codes. A better approach, therefore, is to use the atomic data validated by the experiments in the plasma models, not to rely on most recent calculations which are often equated with the best.

1.4 Current experimental knowledge of resonant recombination processes

Resonant recombination processes can occur in both collisional and photoionized plasmas. This makes them the necessary focus of experimental studies. In this section, we give a brief review about the current experimental knowledge of resonant recombination processes. These experiments have measured the cross sections, rates of resonant recombination, and angular distribution and polarization of x rays emitted in this process.

Resonant recombination processes are often divided into two classes. The first class is where the excited ion core does not change the principal quantum number n of the active electron ($\Delta n = 0$). Such recombination channels usually occur at low temperatures and dominate radiative rates for many low- and high-Z highly charged ions in photoionized plasmas. In the second class, the excited ion core changes the principle quantum number

of the active electron ($\Delta n \geq 1$). Such recombination channels usually occur at high temperatures and dominate the recombination rates in collisionally ionized plasmas.

Cross sections and recombination rate coefficients:

Burgess (1964) was the first to realize the importance of dielectronic recombination (DR) [96] in highly charged ions of the hot solar corona plasma and derived the generalized formula for evaluating the DR rate coefficients [97]. Since then there have been many detailed investigation of DR rate coefficients for the K-shell and L-shell ions. Low-energy DR rate coefficients ($\Delta n = 0$) for the photoionized plasmas were measured at the ion storage ring for ions relevant in astrophysics (see [61] and references therein). The high-energy DR rate coefficients ($\Delta n \geq 1$) were measured for a number of ions at the electron beam ion traps [79, 80, 98–101]. The accurate DR resonance energies and resonance strengths were also measured [80, 100, 102–112]. Accurate values of such quantities are crucial for modeling high-temperature plasmas.

The role of DR extends beyond the processes governing the ionization balance inside the plasmas [113]. DR also provides resolved spectral lines that are used for temperature diagnostics [98, 114]. Studies of impurities in tokamaks have greatly contributed to understanding K-shell DR spectra [115–118] and the density dependence of L-shell emission lines [119, 120].

In addition to DR and radiative recombination (RR), trielectronic recombination was recently emphasized to be very important. In low-temperature photoionized plasmas, the recombination rates were shown to be dominated by intra-shell trielectronic recombination [69, 70, 72, 121]. Whereas in high-temperature collisionally ionized plasmas, inter-shell trielectronic recombination plays very important role in plasma cooling since this additional recombination channel produces high energy photons.

Recently, trielectronic recombination process was measured to have sizable and even major strengths, compared to first-order dielectronic recombination for low-Z elements such as silicon [76], argon and iron [74, 75].

Apart from application relevance of DR in plasmas diagnostics, the interest in DR also arises from the point of view of understanding electron–electron interaction in the strong Coulomb field of highly charged ions. Quantum interference effects between
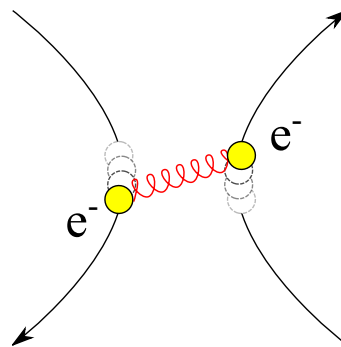
Figure 1.3: The Breit interaction: Exchange of a virtual photon between the free and bound electron of an ion.
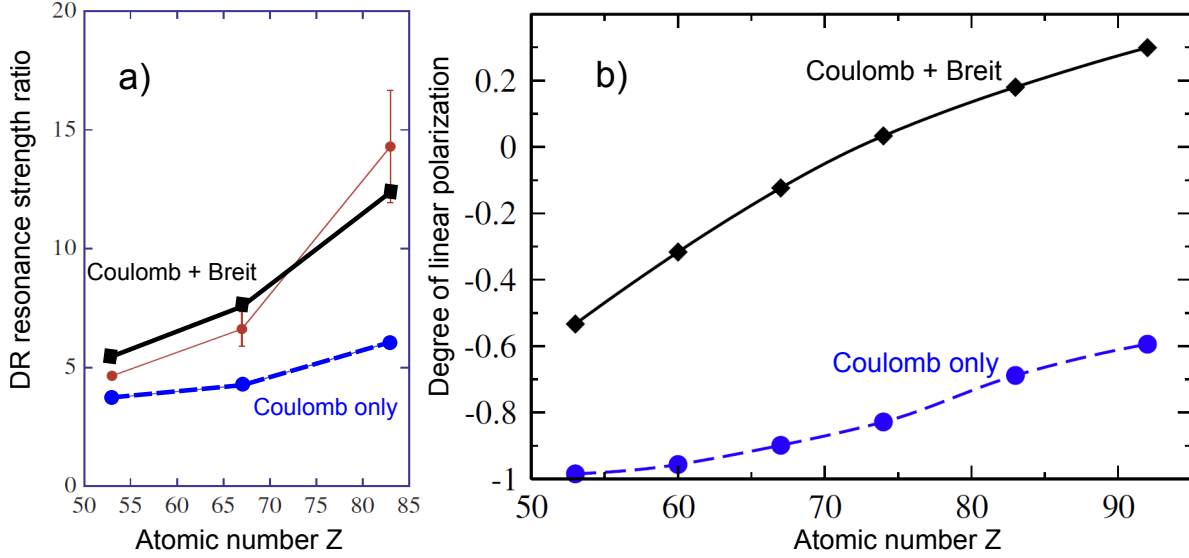
Figure 1.4: (a) Strength ratio of DR resonances $[1s2s^22p_{1/2}]_1$ and $[1s2s2p_{1/2}^2]_1$ (modified from [134]). (b) Degree of linear polarization of x rays followed by DR resonance $[1s2s^22p_{1/2}]_1$ (modified from [136]). In both figures, the blue dashed lines represent the calculations with only the Coulomb repulsion, while black solid lines represent the full Coulomb+Breit interaction calculations.

RR and DR was studied [122–125]. DR also gives an insight of multichannel effects [126, 127]. Furthermore, it is also a suitable tool to probe isotope shifts and hyperfine effects [128–130]. Earlier, it was predicted that the relativistic effects may modify the DR cross sections [131] and the rates [132, 133]. Recently, the influence of generalized Breit interaction on the DR resonance strength was measured for heavy ions at an electron beam ion trap as well as at the storage ring [134, 135], giving access to the lowest order QED effect. The retardation in the exchange of a single virtual photon between the free and bound electron of an ion and magnetic corrections to the electron–electron Coulomb repulsion are known as the generalized Breit interaction [134], see Fig. 1.3 (a). The first experimental evidence of the generalized Breit interaction effect on DR resonance strengths is shown in Fig. 1.4 (a) for heavy Li-like holmium and bismuth ions.

Angular distribution and polarization of x rays:

Many DR experiments measured energies, cross sections and rates, yet, less attention has been paid to the angular distribution and polarization of the emitted x rays. An additional qualitative information about the plasma state can be inferred from the linear polarization of the DR satellites, which is highly sensitive to the directionality of the recombining electrons [137, 138]. In fact, the directionality of anisotropic plasma electrons

not only results in polarized DR lines but also in anisotropic x-ray emission [139]. Thus, the polarization of x rays can strongly influence the temperature diagnostics based on DR satellite lines since the observed intensities of lines are affected [98]. Due to this fact, polarization measurements of the DR satellites lines are in fact necessary for the diagnostics of anisotropies and temperatures of hot plasmas. Earlier, Shlyptseva and coworkers have studied polarization properties of dielectronic satellite lines of astrophysical relevant Li-, Be- and B-like iron ions, both theoretically and experimentally [87, 88, 140]. Unfortunately, no information on degree or angle of polarization of DR transition has been extracted from those experiments. Moreover, a number of experiments that measured DR cross sections or resonance strengths using electron beam ion traps had observed x rays emitted perpendicular to the electron beam axis. As discussed earlier, the interpretation of those experiments requires accurate knowledge of the x-ray angular distribution and polarization [80, 100, 110–112]. Recently, the angular distribution of DR x rays was measured for just one electronic transition in Li-like heavy praseodymium, holmium and gold ions [93, 141].

The influence of generalized Breit interaction on DR resonance strengths was already experimentally shown by the Tokyo-EBIT group [134]. Recently, Fritzsche *et al.* [136] predicted that the angular distribution and polarization of x rays produced in DR process are strongly modified by Breit interaction (see Ref. [142] and Fig. 1.4 (b)), which was later confirmed experimentally for heavy ions [93, 141]. This makes measurements of linear polarization of DR x rays, one of the most sensitive probes of the electron–electron interaction in strong Coulomb fields. Furthermore, measurements of the x-ray emission anisotropy and polarization can complement each other to access effects beyond the electric-dipole approximation [46, 94].

1.5 Motivation and organization of the thesis

As mentioned in previous sections, having fundamental and plasma diagnostic importance, a number of experiments have been performed to measure the DR cross sections and rate coefficients. However, just a few experiments have measured the angular distribution or polarization of DR x rays. The effect of relativity and multipole radiation have been shown to be contributed for only high-Z ions. These effects are still unexplored in low- and medium-Z ions related to the astrophysical and laboratory plasmas. Moreover, neither angular distribution nor polarization of x rays emitted in higher-order resonant recombination processes were measured so far. These facts made resonant recombination the focus of our experimental studies.

In this work, we address the present lack of data by measuring the strongest $K\alpha$ x-ray lines of resonant recombination into highly charged ions of iron and krypton. Iron and krypton ions are chosen since they are crucial in the complex intermediate coupling regime with a strong role in astrophysical and tokamak plasmas [143–147]. We investigate angular distribution and polarization of x rays following resonant recombination into highly charged iron and krypton ions using novel experimental techniques. The systematic study was performed measuring the polarization of more than a hundred x-ray transitions. In addition to that, the contributions of Breit interaction and higher-order resonant recombination on the angular distribution and polarization of x rays were also investigated.

This thesis is organized as follows:

- Chapter 2 introduces the theoretical background of resonant recombination processes and describes theoretical formalism to treat the linear polarization and angular distribution of x rays emitted in these processes.

- Chapter 3 introduces the experimental facility used in this work, the electron beam ion trap (EBIT). The main components, operational principle, and electron beam dynamics are briefly reviewed.

- Chapter 4 describes the first measurement of the linear polarization of x rays emitted due to dielectronic recombination into highly charged krypton ions by means of the Compton polarimetry technique. A brief description of the newly built Compton polarimeter used in the measurement is given. The influence of Breit interaction on the degree of linear polarization is investigated for five dielectronic recombination resonances.

- Chapter 5 introduces a new fast method (in comparison to the direct polarization measurement) to determine the degree of linear polarization. The polarization is accessed by measuring the angular distribution of x rays. More than one hundred transitions involving dielectronic, trielectronic and quadruelectronic recombination resonances in highly charged iron and krypton ions were studied. The experimental results comprehensively benchmark relativistic atomic calculations by the FAC and RATIP computer codes.

- Chapter 6 describes the importance of resonant recombination processes in the plasma modeling and diagnostics. The collisional-radiative model is applied in order to determine the recombination rates and ionization balance inside optically thin plasmas. Theoretical data on polarization and angular distribution of x rays are further implemented in our model to determine the total polarization of $K\alpha$ lines. The influence of higher-order resonant recombination processes on plasma conditions are thoroughly investigated. Further, the potential of polarization measurements is demonstrated to

investigate directionality of electron beams inside the hot anisotropic plasmas.

- Chapter 7 summarizes the work presented in the thesis and gives an outlook of the present investigations.

In Appendices A, B and C, theoretical data are presented. The FAC calculations are presented including resonance energies and strengths, and the degree of polarization of K-shell x rays emitted by resonant recombination into highly charged iron and krypton ions. Moreover, the theoretical RR cross sections and polarization of x rays emitted by RR into highly charged krypton ions is presented.

Chapter 2

Theoretical description

2.1 Electron-ion-recombination

Electron-ion recombination is one of the most fundamental processes largely determining the state of the matter, both in astrophysical and laboratory plasmas. The most common processes are radiative recombination (RR) – time reverse to the photoionization process - and dielectronic recombination (DR) – time reverse to the Auger process. The top path of the Fig. 2.1 shows a scheme of the direct process RR and the bottom path shows the resonant process DR. Both processes start with the same initial state and end with the same final state of the recombined ion, except DR reaches the final state via intermediate excited states. As described in Sec. 1.4, both processes have been thoroughly investigated up to the heaviest highly charged ions [61, 71, 99, 148]. Beyond the well-known DR, the higher-order resonant recombination channels, involving excitation of more than one electron under the capture of a free electron, also play an important role [69, 70, 73]. The present section deals with the basic theory of non-resonant RR process and resonant DR and higher-order recombination processes. Subsequently, in the section 2.2, the theoretical framework is outlined to calculate the angular distribution and polarization of x rays emitted due to resonant recombination processes.
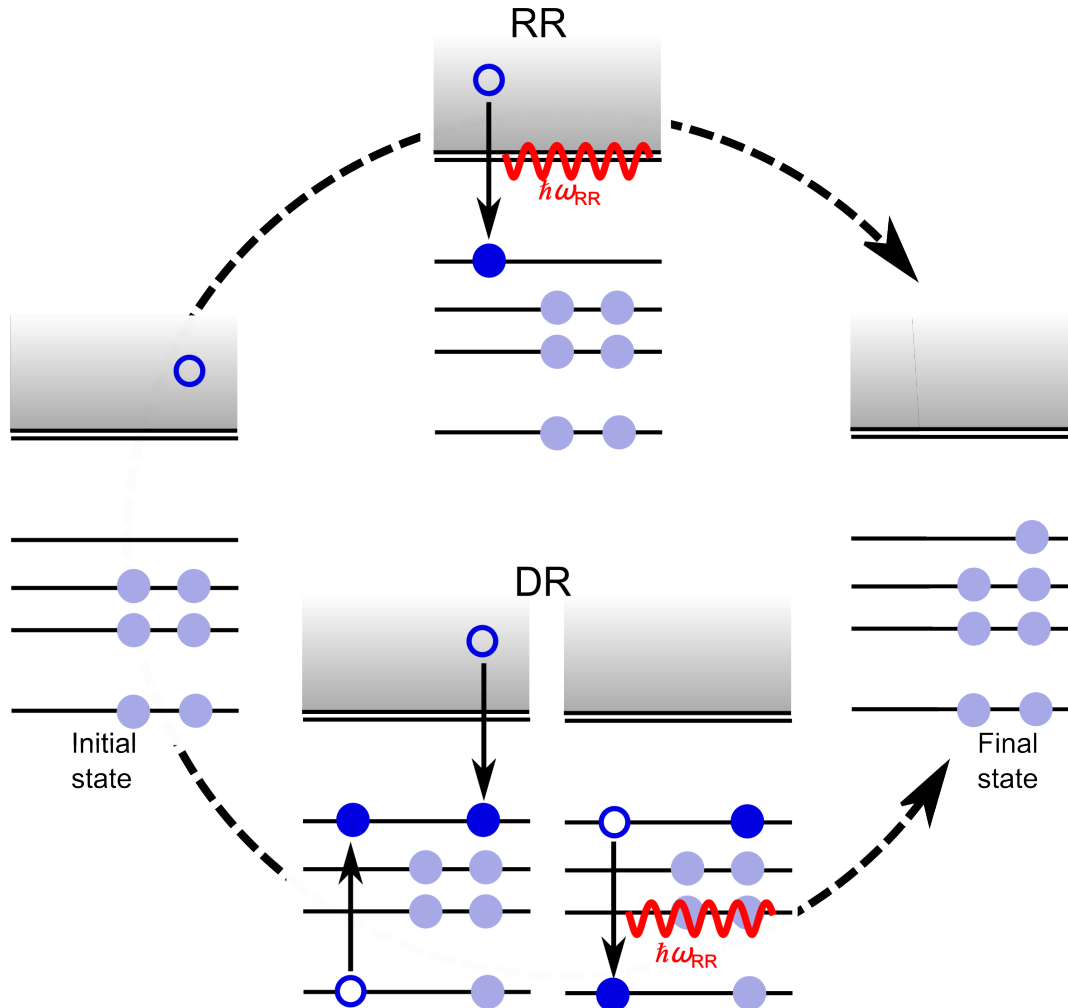
Figure 2.1: Scheme of radiative recombination (RR) and dielectronic recombination (DR) into carbon-like initial ions: RR and DR both start on the left side with the same initial state. RR finishes in a single step to reach final state while the DR reach to the same final state via an intermediate excited state. Thus, DR is a two step process. Both processes reduce the charge state of an ion by a unit.

2.1.1 Radiative recombination and its cross sections

Radiative recombination is a non-resonant one-step process, which can be symbolically written as:

$$X^{q+} + e^- \rightarrow [X^{(q-1)+}] + \hbar\omega_{RR}. \tag{2.1}$$
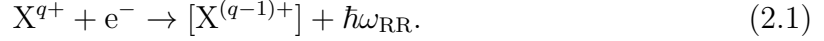
Here, an electron is captured into a bound state of an ion, emitting a photon with an energy equal to the sum of the electron's kinetic energy E_e and the binding energy E_b of the bound level into which an electron is captured: $E_e + E_b = \hbar\omega_{RR}$.

RR is the time–reverse process of photoionization (PI), and the relevant cross sections and rates are usually obtained from photoionization calculations through the principle of detailed balance. The RR cross sections are related to the PI cross sections through the well–known Milne's formula:

$$\sigma_{RR}(E_e)g_{q+1} = \frac{(\hbar\omega)^2}{2m_e c^2 E_p} \; g_q \sigma_{PI}, \tag{2.2}$$

where m_e denotes the electron mass, E_p is the energy of ejected photo-electron and g_q and g_{q+1} are the statistical weights of the initial and final states, respectively. For a recombination into certain n level, a semi–classical description of the process was applied in 1923 by Kramers [149]. The $\sigma_{RR}(E_e)$ cross section of RR can be parameterized in terms of n, z and E_H as:

$$\sigma_{RR}(E_e) = 2.10 \times 10^{-22} \, [\text{cm}^2] \; \frac{z^4 E_H^2}{n E_e (z^2 E_H + n^2 E_e)}, \tag{2.3}$$

where z is the residual charge of the ion, E_H is the Rydberg energy and n is the principal quantum number of the recombined electron. The total RR cross section is given by the sum over all possible n states. This formula gives accurate cross sections for recombination into high n states ($n > 10$) [150, 151]. For the recombination into low n states, equation (2.3) needs to be corrected by the Gaunt factor g_n [152]. In plasma modeling, a simple analytical fit formula is used to calculate the Maxwellian-averaged RR rate coefficients.

2.1.2 Dielectronic recombination

The DR is a resonant two–step process, in which a free electron is captured into an ionic state X^{q+}, while a bound electron is simultaneously excited. Thereby, an intermediate excited state $[X^{(q-1)+}]^*$, or resonance, is formed. In the second step, DR process is completed by radiative emission. The DR process is schematically illustrated in the

Fig. 2.1 following the bottom path. The radiative transition probabilities are very high in highly charged ions, and the competition of radiative emission and Auger decay of the intermediate state is biased towards the first step. DR can be schematically represented as

$$X^{q+} + e^- \rightarrow [X^{(q-1)+}]^* \rightarrow [X^{(q-1)+}] + \hbar\omega_{\mathrm{DR}}. \tag{2.4}$$
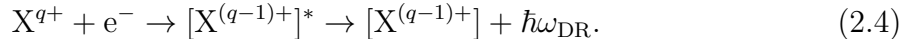
Since it is a resonant process, it can only happen when the sum of the kinetic energy of the electron E_e and the binding energy E_b of the recombined state is equal to the energy difference ΔE_{core} between the core electron state and the state in which the second electron is excited. This condition can be written as: $E_e + E_b = \Delta E_{core}$.

Dielectronic recombination is the time–reversed Auger process, thus the corresponding DR pathways are labeled according to standard Auger notations. For example, as shown in Fig. 2.1, in a *KLL* DR resonance for a carbon-like initial state, the free electron is captured into the *L*-shell of the ion, while a bound electron is promoted from the *K*-shell to the *L*-shell to form an intermediate excited state. Whereas in the case of the *KLM* resonance, a free electron is captured into the *M*-shell, while the *K*-shell electron is promoted to the *L*-shell. Since the electrons are indistinguishable, this process is equivalent to capture into the *L*-shell and excitation into the *M*-shell.

DR is of a paramount importance for the physics of outer planetary atmospheres [96] and interstellar clouds. It is an important mechanism of radiative cooling in hot astrophysical and laboratory plasmas. Hence, the precise knowledge of the DR process, its cross sections and rates is very important for plasma modeling (see Sec. 1.3 and 1.4). From a more fundamental point of view, the selectivity of DR allows stringent testing of sophisticated atomic structure and dynamics calculations, in particular relativistic and quantum electrodynamics (QED) effects in heavy highly charged ions [123, 141]. It should be noted that the RR occurs at any electron energy, thus also at the DR resonance energy (E_{res}), therefore, the two processes may interfere quantum mechanically [124].

DR cross sections and resonance strengths

In the isolated resonance approximation, the DR cross sections can be expressed as [153]

$$\sigma^{\mathrm{DR}}_{i\rightarrow d\rightarrow f}(E_e) = \frac{2\pi^2\hbar^3}{p_e^2} \ W_a(i \rightarrow d) \ L_d(E_e) \ \omega_d, \tag{2.5}$$

where p_e denotes the electron momentum, which can be nonrelativistically approximated as $p_e^2/2m_e = E_e$. The quantity $W_a(i \rightarrow d)$ represents the total probability per second for the dielectronic capture, and $L_d(E_e)$ is the Lorentzian profile of the resonance. ω_d denotes the fluorescence yield of the intermediate excited state, defined as the radiative

decay width of the state divided by the total decay width that contains both radiative and Auger decays.

The dielectronic capture rate $W_a(i \to d)$ is related to the rate of its time–reversed (Auger) process by principle of detailed balance. According to Fermi's golden rule, it can be expressed as [75]

$$
\begin{aligned}
W_a(d \to i) &= \frac{g_d}{2g_i} A_a(d \to i) \\
&= \frac{2\pi}{2g_i} \sum_{M_d} \sum_{M_i m_s} \int \sin\theta d\theta d\phi |\langle \Psi_d; J_d M_d \| V \| \Psi_i E_e; J_i M_i, \vec{p}_e m_s \rangle|^2 \\
&= 2\pi \sum_\kappa |\langle \Psi_d; J_d \| V \| \Psi_i E_e; J_i j, J_d \rangle|^2.
\end{aligned}
\tag{2.6}
$$

where J_i and J_d are the total angular momentum numbers of the initial and intermediate states, respectively. g_i and g_d are statistical weights of states $|i\rangle$ and $|d\rangle$, given by $(2J_i + 1)$ and $(2J_d + 1)$, respectively. The factor 2 reflects the two possible spin states of an electron in the continuum state. The last line of equation (2.6) is the partial wave expansion of the reduced matrix elements, obtained by averaging over the initial magnetic quantum number M_i, m_s and the direction (θ, ϕ) of the incoming continuum electron and then performing summation over the magnetic quantum number M_d of the autoionizing state. κ is the relativistic angular quantum number in the partial wave expansion of the continuum electron. The operator V is the frequency-dependent two–electron interaction operator, which is taken to be the sum of the Coulomb and Breit interaction operator ($\mathbf{R} = |r_i - r_j|$ with r_i being the position of the ith electron) [131]:

$$
\begin{aligned}
V &= V^C + V^B \\
&= \sum_{i<j} \left[\frac{1}{\mathbf{R}} + \left(-(\alpha_i \cdot \alpha_j)\frac{\cos(\omega\mathbf{R})}{\mathbf{R}} + (\alpha_i \cdot \bigtriangledown_i)(\alpha_j \cdot \bigtriangledown_j)\frac{\cos(\omega\mathbf{R}) - 1}{\omega^2\mathbf{R}} \right) \right],
\end{aligned}
\tag{2.7}
$$

where ω denotes the frequency of the exchanged virtual photon and α_i is the vector of Dirac matrices associated with the ith particle. The last two terms in Eq. (2.7), commonly referred to Breit interaction [142], account for the magnetic interaction and the retardation between the two electrons.

The function $L_d(E_e)$ is defined as

$$
L_d(E_e) = \frac{\Gamma_d/2\pi}{(E_e - E_{res})^2 + \Gamma_d^2/4},
\tag{2.8}
$$

with the normalization $\int L_d(E_e)\, dE_e = 1$. E_{res} is the resonance energy: $E_{res} = E_d - E_i$.

The fluorescence yield can be given by

$$\omega_d = \frac{\Gamma_r}{\Gamma_a + \Gamma_r} = \frac{\Gamma_r}{\Gamma_d}, \tag{2.9}$$

where Γ_r and Γ_a are the radiative and Auger widths, respectively and Γ_d is the total natural width of the intermediate state $|d\rangle$, given as the sum of the radiative and autoionization widths: $\Gamma_d = \Gamma_r + \Gamma_a$. Note that the rates and the associated line widths are related by: $\Gamma_a = \hbar A_a(d \to i)$.

Using equations (2.5), (2.6), (2.8) and (2.9), we obtain the following expression for the DR cross section:

$$\sigma_{i \to d \to f}^{\mathrm{DR}}(E_e) = \frac{\pi \hbar^2}{p_e^2} \frac{g_d}{2g_i} \frac{\Gamma_a(d \to i)\Gamma_r(d \to f)}{(E_e - E_{res})^2 + \Gamma_d^2/4}. \tag{2.10}$$

The natural width Γ_d is usually much smaller than the experimental line widths. In such cases, the theoretical line profile can be approximated by a delta function, resulting into the following cross section:

$$\sigma_{i \to d \to f}^{\mathrm{DR}}(E_e) = \frac{2\pi^2 \hbar^2}{p_e^2} \frac{g_d}{2g_i} \frac{\Gamma_a(d \to i)\Gamma_r(d \to f)}{\Gamma_d} \delta(E_e - E_{res}). \tag{2.11}$$

This suggests that the resonance strength can be calculated from the cross section $\sigma^{DR}(E)$ integrated over the kinetic energy of the electron E_e,

$$S_{i \to d \to f}^{\mathrm{DR}} = \int \sigma_{i \to d \to f}^{\mathrm{DR}}(E_e) dE_e = \frac{2\pi^2 \hbar^2}{p_e^2} \frac{2J_d + 1}{2(2J_i + 1)} \frac{\Gamma_a \Gamma_r}{\Gamma_d}. \tag{2.12}$$

For plasma diagnostics, the DR rate coefficient is a more convenient quantity. It can be obtained by integrating over the Maxwellian velocity distribution of the electrons:

$$\alpha^{\mathrm{DR}}(T_e) = \left(\frac{2\pi \hbar^2}{m_e k_B T_e}\right)^{3/2} \frac{2J_d + 1}{2(2J_i + 1)} \frac{\Gamma_a \Gamma_r}{\Gamma_d} \exp\left(\frac{-E_{res}}{k_B T_e}\right), \tag{2.13}$$

where k_B is the Boltzmann constant and T_e is the electron temperature.

2.1.3 Higher-order resonant recombination processes

Beyond the DR process, higher-order (HO) resonant recombination can also be relevant. As shown in Fig. 2.2, under the HO resonant capture of a free electron, two or even three bound electrons can be simultaneously excited, leading to trielectronic recombination (TR) or quadruelectronic recombination (QR), respectively. In Fig. 2.2, we employed
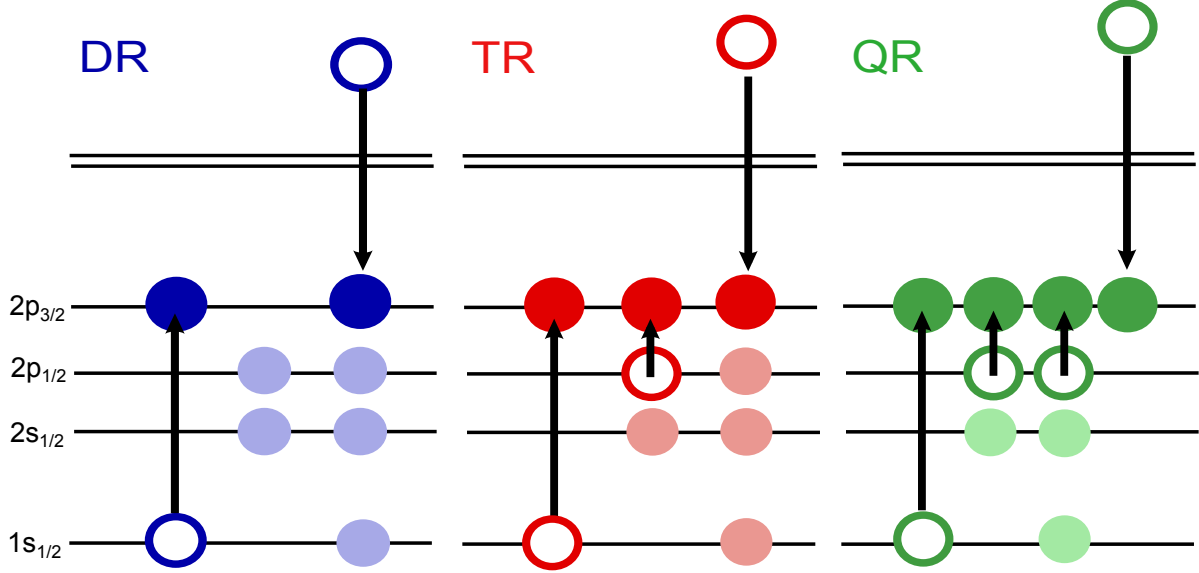
Figure 2.2: Scheme of resonant recombination processes: In DR (blue diagram) one bound electron is excited by the captured electron; In TR (red diagram) and QR (green diagram) two and three electrons are excited by the captured electron. DR, TR, and QR can be represented as *K-LL*, *KL-LLL*, and *KLL-LLLL*, respectively, where the final and initial shells of the bound and active electrons are specified.

standard Auger notations and the natural extension to HO processes.

In general, these resonant recombination processes can be summarized by the equation,

$$\mathrm{X}^{q+} + \mathrm{e}^- \rightarrow [\mathrm{X}^{(q-1)+}]^{(n+1)*} \rightarrow [\mathrm{X}^{(q-1)+}] + \sum_i \hbar\omega_i, \qquad (2.14)$$

where n is the order of the recombination process nR with $n = 1$, 2 and 3 for DR, TR and QR, respectively. In calculating these interactions usually independent-particle models are used where normally only the most relevant two electrons interact and the rest of electrons in atomic system are considered as pure spectators. Therefore, these HO processes, nR with $n > 1$ can only occur through configuration mixing of the bound electrons [75], i. e., via correlation between electrons in the intermediate excited state, $|nR\rangle = \sum_k C_k |\alpha_k JP\rangle$, where C_k is the mixing coefficient for the configuration state function $|\alpha_k JP\rangle$ and α_k contains all quantum numbers to define the configuration state function. Therefore, the higher-order recombination processes appear only if electron correlation effects are taken into account and their measurement can benchmark more thoroughly their theoretical description both in terms of structure and dynamics. Moreover, as described in Sec. 1.3, TR and QR offer new recombination channels in hot plasmas. Therefore, their contribution to the radiative cooling and opacities of plasmas has to be considered in the corresponding simulations codes. Exact quantitative descrip-

tion of such correlation-induced processes and their scaling with the number of involved electrons can be very useful for the plasma modeling.

2.2   Angular distribution and polarization of x rays

In the plasma, when the electron distribution is anisotropic, the radiation emitted following electron collisional excitation, ionization, or resonant dielectronic capture can be anisotropic and polarized [139]. This occurs in some hot astrophysical plasmas, e. g., solar flare [30, 31, 143] as well as in laboratory plasmas where the ions are excited by a directed electron beam [47, 154]. Under this circumstance, the magnetic sublevels of the excited states may have uneven populations. The degree of polarization depends on the extent of deviation from the statistical population of the excited magnetic sublevels of the ions. Relativistic effects have been found to have a strong influence on the polarization of radiation emitted from the ions excited by the directed electron beam [136, 139]. In this section, we first derive theoretical expressions to describe the alignment of an ion in the resonant capture process and, second, the angular distribution and polarization of x rays following resonant capture process.

2.2.1   Alignment of the excited state following resonant capture

Here, DR is treated as a two-step process: dielectronic capture followed by radiative stabilization (see Sec. 2.1.2). The effect of overlapping resonances and the interference between the non-resonant RR and resonant DR are neglected. In DR, the resonant capture of an electron by an ion usually leads to the non-statistical population of magnetic sublevels. Thus, the x rays following resonant capture process are anisotropic and polarized. To describe this process quantum mechanically, we follow the density matrix theory described in Refs. [83, 155]. The distribution of nonstatistical magnetic sublevel population of an intermediate excited state is described most naturally in terms of alignment parameter $\mathcal{A}_\lambda$. For the resonant capture of an unpolarized electron, the alignment parameter can be expressed in the form of [131]:

$$\mathcal{A}_\lambda = \frac{P_{J_i J_d}^{(\lambda)}}{P_{J_i J_d}^{(0)}}, \tag{2.15}$$

where

$$
\begin{aligned}
P^{(\lambda)}_{J_i J_d} = & \frac{(-1)^{J_i+\lambda+J_d-1/2}}{2(2J_i+1)} \sum_{ljl'j'} \mathrm{i}^{l-l'} \left[j,j',l,l',\lambda \right]^{1/2} \begin{pmatrix} l & l' & \lambda \\ 0 & 0 & 0 \end{pmatrix} \\
& \times \begin{Bmatrix} j' & j & \lambda \\ l & l' & 1/2 \end{Bmatrix} \begin{Bmatrix} J_d & J_d & \lambda \\ j & j' & J_i \end{Bmatrix} \langle \Psi_{J_d} \| V \| \Psi_{J_i}, \phi_{lj} \rangle \langle \Psi_{J_d} \| V \| \Psi_{J_i}, \phi_{l'j'} \rangle^*.
\end{aligned}
\tag{2.16}
$$

Here, $[a,b,...] = (2a+1)(2b+1)...$, the quantity in large parentheses is a Wigner 3-j symbol and, the quantities in large curly braces denote the Wigner 6-j symbol. The reduced matrix element $\langle \Psi_{J_d} \| V \| \Psi_{J_i}, \phi_{lj} \rangle$ refers to the electron–electron interaction that leads to the formation of the intermediate excited state in the course of the collision, starting with an ion in the initial state and a free continuum electron with orbital and total angular momentum, l and j, respectively. The operator V is the frequent-dependent electron–electron interaction operator, containing both the Coulomb and Breit interaction terms (see Eq. (2.7)).

The alignment parameter $\mathcal{A}_\lambda$ can also be represented in terms of the partial cross sections σ_{M_d} for the population of the magnetic substates with the different magnetic quantum number M_d:

$$
\mathcal{A}_\lambda = (-1)^{J_d+M_d} \sum_{M_d} \sqrt{(2J_d+1)(2\lambda+1)} \begin{pmatrix} J_d & J_d & \lambda \\ -M_d & M_d & 0 \end{pmatrix} \frac{\sigma_{M_d}}{\sum_{M'_d} \sigma_{M'_d}}.
\tag{2.17}
$$

Here, J_d and M_d are the total angular and magnetic quantum numbers of the excited intermediate state $|d\rangle$ of DR process, and σ_{M_d} are the partial magnetic sublevel cross sections. The magnetic quantum number of M_d can have values from $-J_d$ to J_d. λ is a multipole order of emitted radiation: $\lambda = 2^L$, where $L=1$ for the electric dipole $E1$ and magnetic dipole $M1$ transitions, and $L=2$ for the electric quadrupole $E2$ and magnetic quadrupole $M2$ transitions and so on.

If the incident electron beam is unidirectional and unpolarized, the excited ions appeared to be aligned which means that their sublevels with the same modulus of the magnetic quantum number are equally populated, i. e., $\sigma_{M_d} = \sigma_{-M_d}$. It should be noted from the Eq. (2.17) and from the properties of Clebsch–Gordan coefficients, the alignment parameter $\mathcal{A}_\lambda$ do not vanish only if λ is even and if $\lambda \le 2J_d$. This restriction implies that the intermediate excited states with $J_d = 0$ or $J_d = 1/2$ cannot be aligned.

For example, there is only one non-vanishing parameter $\mathcal{A}_2$ for the recombination of a free electron into the intermediate excited state with $J_d = 1$ or $3/2$. There are two non-vanishing parameters $\mathcal{A}_2$, $\mathcal{A}_4$ for $J_d = 2$ or $5/2$; and three non-vanishing parameters

$\mathcal{A}_2$, $\mathcal{A}_4$, and $\mathcal{A}_6$ for $J_d = 3$:

For $J_d = 1$:

$$\mathcal{A}_2^{J_d=1} = \frac{\sqrt{2}\,(\sigma_1 - \sigma_0)}{\sigma_0 + 2\sigma_1}. \tag{2.18}$$

For $J_d = 3/2$:

$$\mathcal{A}_2^{J_d=3/2} = \frac{\sigma_{\frac{3}{2}} - \sigma_{\frac{1}{2}}}{\sigma_{\frac{1}{2}} + \sigma_{\frac{3}{2}}}. \tag{2.19}$$

For $J_d = 2$:

$$\mathcal{A}_2^{J_d=2} = -\frac{\sqrt{\frac{10}{7}}\,(\sigma_0 + \sigma_1 - 2\sigma_2)}{\sigma_0 + 2\,(\sigma_1 + \sigma_2)},$$

$$\mathcal{A}_4^{J_d=2} = \frac{\sqrt{\frac{2}{7}}\,(3\sigma_0 - 4\sigma_1 + \sigma_2)}{\sigma_0 + 2\,(\sigma_1 + \sigma_2)}. \tag{2.20}$$

For $J_d = 5/2$:

$$\mathcal{A}_2^{J_d=5/2} = -\frac{4\sigma_{\frac{1}{2}} + \sigma_{\frac{3}{2}} - 5\sigma_{\frac{5}{2}}}{\sqrt{14}\left(\sigma_{\frac{1}{2}} + \sigma_{\frac{3}{2}} + \sigma_{\frac{5}{2}}\right)},$$

$$\mathcal{A}_4^{J_d=5/2} = \frac{\sqrt{\frac{3}{14}}\left(2\sigma_{\frac{1}{2}} - 3\sigma_{\frac{3}{2}} + \sigma_{\frac{5}{2}}\right)}{\sigma_{\frac{1}{2}} + \sigma_{\frac{3}{2}} + \sigma_{\frac{5}{2}}}. \tag{2.21}$$

For $J_d = 3$:

$$\mathcal{A}_2^{J_d=3} = \frac{-2\sigma_0 - 3\sigma_1 + 5\sigma_3}{\sqrt{3}\,(\sigma_0 + 2\,(\sigma_1 + \sigma_2 + \sigma_3))},$$

$$\mathcal{A}_4^{J_d=3} = \frac{\sqrt{\frac{2}{11}}\,(3\sigma_0 + \sigma_1 - 7\sigma_2 + 3\sigma_3)}{\sigma_0 + 2\,(\sigma_1 + \sigma_2 + \sigma_3)},$$

$$\mathcal{A}_6^{J_d=3} = \frac{-10\sigma_0 + 15\sigma_1 - 6\sigma_2 + \sigma_3}{\sqrt{33}\,(\sigma_0 + 2\,(\sigma_1 + \sigma_2 + \sigma_3))}. \tag{2.22}$$

2.2.2 Angular distribution and polarization of the subsequent radiative decay

Equations (2.15), (2.16) and (2.17) collectively describe the alignment of the exited ion following the resonant capture of an electron. The subsequent decay of these ions then leads to the emission of one or several x rays, until their ground state is reached. Knowing the alignment of intermediate excited state of an ion, the linear polarization $P(\theta)$ and angular distribution coefficient $W(\theta)$ of the subsequent x rays are given by:

$$P(\theta) = \Lambda(\pi) \frac{\sum\limits_{\lambda=\text{even}} f_\lambda \alpha_\lambda^{df} \mathcal{A}_\lambda P_\lambda^{(2)}(\cos\theta)}{\sum\limits_{\lambda=\text{even}} \alpha_\lambda^{df} \mathcal{A}_\lambda P_\lambda(\cos\theta)}, \tag{2.23}$$

$$W(\theta) = \frac{d\Omega}{4\pi} \sum\limits_{\lambda=\text{even}} \alpha_\lambda^{df} \mathcal{A}_\lambda P_\lambda(\cos\theta), \tag{2.24}$$

where θ is the angle between x-ray emission direction and the electron beam propagation direction. α_λ^{df} is the intrinsic anisotropy parameter. The function $\Lambda(\pi)$ determines the sign, $\Lambda(E) = 1$ for electric multipole transitions and $\Lambda(M) = -1$ for magnetic multipole transitions. $P_\lambda(\cos\theta)$ and $P_\lambda^{(2)}(\cos\theta)$ represent the Legendre and associated Legendre polynomials, respectively[1].

The coefficient f_λ is given by

$$f_\lambda = -\left[\frac{(\lambda-2)!}{(\lambda+2)!}\right]^{1/2} \frac{\begin{pmatrix} L & L & \lambda \\ 1 & 1 & -2 \end{pmatrix}}{\begin{pmatrix} L & L & \lambda \\ 1 & -1 & 0 \end{pmatrix}}, \tag{2.25}$$

where L called by Stefan and Alder is the order of pure 2^L decay[2] [83].

If the emitted x rays are described by a single multipole operator, the intrinsic anisotropy parameter α_λ^{df} for transition from a doubly excited state to the final state is

---

[1] $P_0(\cos\theta) = 1$ and $P_0^{(2)}(\cos\theta) = 0$;
$P_2(\cos\theta) = \frac{1}{2}(3\cos^2\theta - 1)$ and $P_2^{(2)}(\cos\theta) = -3(\cos^2\theta - 1)$;
$P_4(\cos\theta) = \frac{1}{8}(35\cos^4\theta - 30\cos^2\theta + 3)$ and $P_4^{(2)}(\cos\theta) = -\frac{15}{2}(\cos^2\theta - 1)(7\cos^2\theta - 1)$.

[2] $f_0(1) = 0$; $f_0(2) = 0$
$f_2(1) = -\frac{1}{2}$; $f_2(2) = \frac{1}{2}$; $f_4(2) = -(\frac{1}{12})^{1/2}$.

J_d	J_f	α_1^{df}	α_2^{df}	J_d	J_f	α_1^{df}	α_2^{df}
0	1	0	0	1/2	1/2	$1/\sqrt{3}$	0
1	0	$1/\sqrt{2}$	$1/\sqrt{2}$	1/2	3/2	$-1/2\sqrt{3}$	0
1	1	$1/2\sqrt{2}$	$-1/2\sqrt{2}$	3/2	1/2	$\sqrt{5}/2\sqrt{3}$	1/2
1	2	$-1/2\sqrt{2}$	$1/10\sqrt{2}$	3/2	3/2	$1/\sqrt{15}$	$-2/5$
2	1	$\sqrt{3}/2\sqrt{2}$	$\sqrt{7}/2\sqrt{10}$	3/2	5/2	$-\sqrt{3}/2\sqrt{5}$	1/10
2	2	$1/2\sqrt{6}$	$-\sqrt{7}/2\sqrt{10}$	5/2	3/2	$\sqrt{7}/2\sqrt{5}$	$\sqrt{7}/5\sqrt{2}$
2	3	$-1/\sqrt{6}$	$1/\sqrt{70}$	5/2	5/2	$1/\sqrt{35}$	$-4\sqrt{2}/5\sqrt{7}$
3	2	$1/\sqrt{3}$	$\sqrt{3}/5$	5/2	7/2	$-\sqrt{5}/2\sqrt{7}$	$1/2\sqrt{14}$
3	3	$1/4\sqrt{3}$	$-\sqrt{3}/4$	7/2	5/2	$3/2\sqrt{7}$	$\sqrt{3}/2\sqrt{7}$
3	4	$-\sqrt{3}/4$	$1/4\sqrt{3}$	7/2	7/2	$1/3\sqrt{7}$	$-2/\sqrt{21}$
4	3	$\sqrt{5}/4$	$\sqrt{11}/4\sqrt{7}$	7/2	9/2	$-\sqrt{7}/6$	$\sqrt{7}/10\sqrt{3}$
4	4	$1/4\sqrt{5}$	$-\sqrt{77}/20$	9/2	7/2	$\sqrt{11}/6$	$\sqrt{11}/2\sqrt{30}$
4	5	$-1/\sqrt{5}$	$\sqrt{7}/5\sqrt{11}$	9/2	9/2	$1/3\sqrt{11}$	$-4\sqrt{2}/\sqrt{165}$

Figure 2.3: The intrinsic anisotropy parameter α_λ^{df} ($\lambda = 1, 2$) for transition from a doubly excited state to the final state, see Eq. (2.26) (modified from Ref. [155]).

given by

$$
\begin{aligned}
\alpha_\lambda^{df}(J_d, J_f) = (-1)^{J_f + J_d - 1} [(2J_d + 1)(2\lambda + 1)]^{1/2} \\
\times (2L+1) \begin{pmatrix} L & L & \lambda \\ 1 & -1 & 0 \end{pmatrix} \begin{Bmatrix} L & L & \lambda \\ J_d & J_d & J_f \end{Bmatrix},
\end{aligned}
\tag{2.26}
$$

where the quantity in large parentheses denotes the Wigner 6-j symbol. The figure 2.3 represents the calculated values of $\alpha_{\lambda=1,2}^{df}$ for different transitions $J_d \to J_f$.

Electric dipole ($E1$) approximation

Equations (2.23) and (2.24) represent the most general form of the angular distribution and polarization of the characteristic radiation following resonant capture of an electron into excited ionic state. They include the summation over all different multipoles of radiation owing to the allowed parity and angular momentum selection rules. Often, there is

only one allowed multipole term which dominates the radiative decay for a given pair of intermediate excited and final states. For low- and mid-Z few–electron ions, the electric dipole $E1$ channel usually dominates the radiative decay. In such case, the contributions from non-dipole component of the radiation are negligible compared to $E1$ component. Therefore, in dipole approximation ($L = 1$ & $\lambda = 2$), the equations (2.17), (2.25), and (2.26) are simplified to:

$$A_2 = \sum_{M_d} (-1)^{J_d + M_d} \, [5(2J_d + 1)]^{1/2} \begin{pmatrix} J_d & J_d & 2 \\ -M_d & M_d & 0 \end{pmatrix} \frac{\sigma_{M_d}}{\sum_{M_d'} \sigma_{M_d'}}, \tag{2.27}$$

$$f_2(L = 1) = -\frac{1}{2}, \tag{2.28}$$

and

$$\alpha_2^{df}(J_d, J_f) = (-1)^{J_d + J_f - 1} \left[\frac{3(2J_d + 1)}{2} \right]^{1/2} \begin{Bmatrix} 1 & 1 & 2 \\ J_d & J_d & J_f \end{Bmatrix}. \tag{2.29}$$

Using the above equations, the degree of linear polarization and angular distribution coefficient can be expressed as:

$$P^{E1}(\theta) = -\frac{3 A_2 \alpha_2^{df} \sin^2 \theta}{2 - A_2 \alpha_2^{df} (1 - 3 \cos^2 \theta)}, \tag{2.30}$$

and

$$W^{E1}(\theta) \propto 1 + \frac{1}{2} A_2 \alpha_2^{df} (3 \cos^2 \theta - 1). \tag{2.31}$$

Equations (2.30) and (2.31) describe the linear polarization and angular distribution of $E1$ photons emitted if the ions undergo a transition between two levels with well-defined total angular momenta and parity. However, in resonant recombination, an excited intermediate resonance state $|d\rangle$ usually decays into several close–lying different final states $|f\rangle$ with different values of degree of linear polarization (see Fig. 2.4). Since the energy resolution of a silicon- or germanium-based x-ray detector is insufficient to resolve the energy splitting between these final states (few electron volts), only the superposition of individual $|d\rangle \to |f\rangle$ transitions can be observed. Therefore, the linear polarization of DR x rays detected perpendicular to the incident electron beam direction ($\theta = 90°$) is given by:

$$P_{\text{DR}}^{E1} = -\frac{3 A_2 \bar{\alpha}_2^{df}}{2 - A_2 \bar{\alpha}_2^{df}}, \tag{2.32}$$
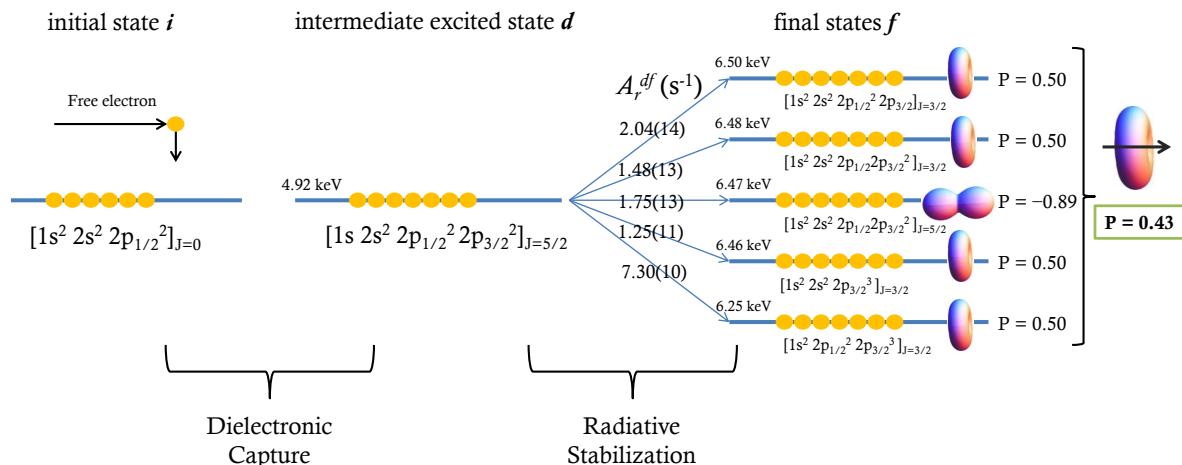
Figure 2.4: Radiative decay scheme of an intermediate excited state $|d\rangle$ to several close–lying different final states $|f\rangle$ with different values of degree of linear polarization. The "effective" observed degree of linear polarization can be calculated according to Eq. (2.32). The x-ray transition energy, the radiative rates (A_r^{df}) and degree of linear polarization (P) of the corresponding x-ray transition are shown. Values in the round bracket represent powers of 10.

where $\bar{\alpha}_2^{df} = \sum_f \alpha_2^{df} A_r^{df} / \sum_f A_r^{df}$ is the new "effective" anisotropy parameter, obtained upon summation over the unresolved final states, and A_r^{df} is the rate of the corresponding transition. For example, Fig. 2.4 shows the calculated "effective" degree of linear polarization of $E1$ x rays following the resonant recombination of a free electron into carbon-like iron ions.

It should also be noted that, for high-Z ions, a significant change in x-ray polarization and angular distribution may arise due to the contribution of higher-order multipoles and may lead to sizable deviation when compared to the electric

Figure 2.5: Measured polarization of the Ly-α_1 transition following the radiative electron capture into U^{92+} ions is compared to the theory with (solid line) and without (dashed line) taking $E1 - M2$ interference into account. The figure is taken from Ref. [94].

dipole approximation [156]. For example, for U^{91+} ions, it has been shown that the multipole mixing between the leading electric dipole $E1$ and weaker magnetic quadrupole $M2$ amplitudes modifies the degree of linear polarization of Lyman α_1 ($2p_{3/2} \rightarrow 1s_{1/2}$) transition significantly [46, 94] (see Fig. 2.5). Moreover, as shown in Fig. 1.4 (b), the angular distribution and polarization of x rays produced in DR process are strongly

affected by relativistic effects, e. g., by the Breit interaction [136].

2.3   Computation

The atomic data including the energy levels, radiative transition rates, autoionization rates and resonant capture rates are needed to be computed in order to describe the resonant recombination processes. The Flexible Atomic Code (FAC v1.1.1) developed by M. F. Gu (2004) [157, 158] is used to generate the required atomic data. FAC is a free-to-use software package[3]. It is distributed with a manual and several unpublished papers to describe the theoretical background and numerical techniques and to compare a few example calculations with other codes.

The atomic structure calculation in FAC is based on the relativistic configuration interaction method with independent-particle basis wave-functions. These basis wave-functions are derived from a local central potential, which is self-consistently determined to represent electronic screening of the nuclear potential. Relativistic effects are taken into account using the Dirac Coulomb Hamiltonian. Relativistic corrections to the electron–electron interaction are included with the Breit interaction in the zero energy limit for the exchanged photon ($\omega \to 0$ in equation (2.7)). QED corrections are treated as hydrogenic approximations for self-energy and vacuum polarization effects. Autoionization processes are treated in first-order perturbation theory using a distorted-wave approximation for the continuum electron. Such a treatment ignores the coupling between the resonances and continuum background and assumes no overlap between different resonances. The radiative transition amplitudes are calculated in the single multipole approximation. This means that the interference between the different multipoles is not taken into account, although rates corresponding to arbitrary multipoles can be calculated.

Testing of the FAC code was done by its author M. F. Gu who carried out calculations with his code and other available codes each with the same set of configurations. The comparisons of results with the few experimental results and with different codes led him to conclude that, the ions other than H-like, the computed energy levels are accurate up to a few eV or $10 - 30$ mÅ at ~ 10 Å. Radiative transitions rates and cross sections are accurate to $\sim 10 - 20\%$. Near-neutral ions or atoms may have even larger errors (cf. FAC manual and Ref. [158]).

The resonance energies and resonance strengths of *KLL* DR resonances in He- through O-like Fe and Kr ions are calculated with the help of FAC code. For *KLL* DR calculation,

---

[3]http://sprg.ssl.berkeley.edu/~mfgu/fac/
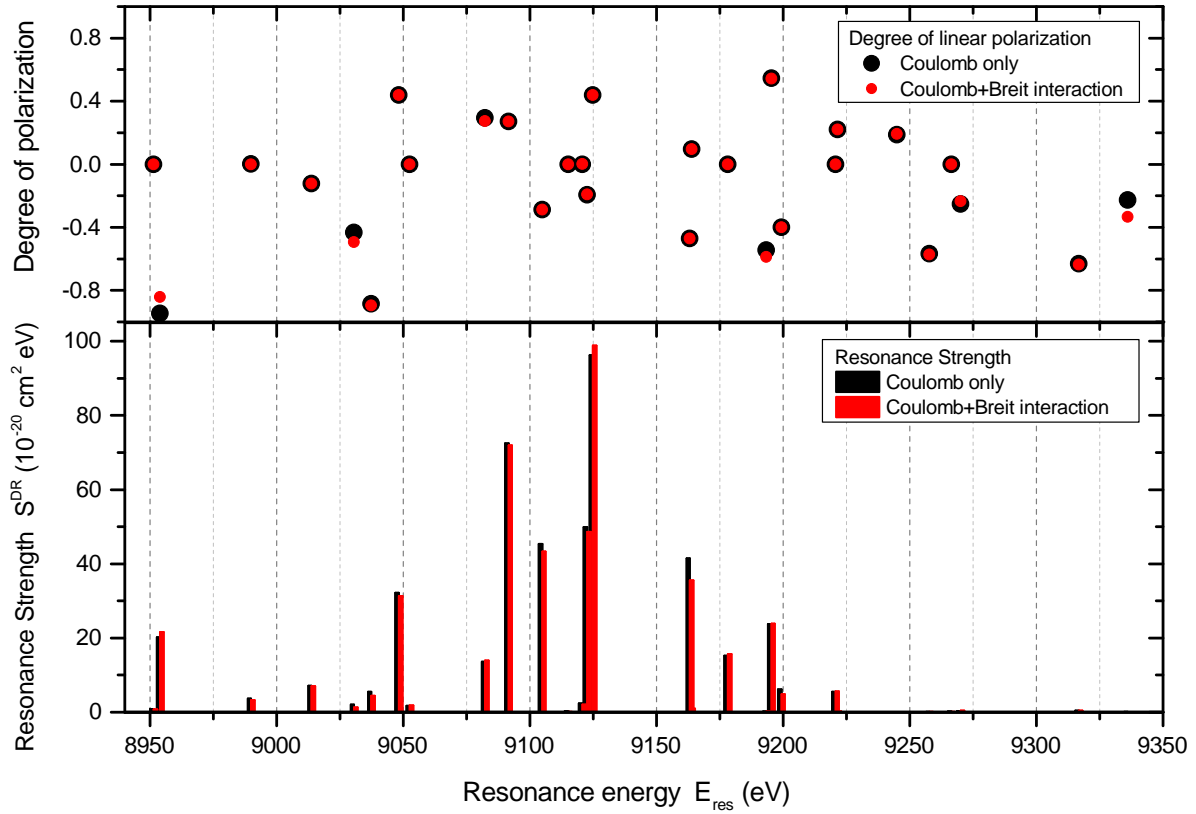
Figure 2.6: The *KLL* DR resonance strength (bottom panel) and the degree of linear polarization (top panel) of dominant $E1$ x rays emitted due to DR are calculated according to Eqs. (2.12) and (2.30) for lithium-like krypton ions using FAC code.

$1s^2(2l)^e$ configurations were included in the initial states, and $1s(2l)^{e+2}$ configurations were included in the intermediate states. $1s^2(2l)^{e+1}$ configurations were included in the final states. Here, e is the number of electrons in the L-shell, from zero to six, for He-like to O-like charge states, respectively.

In the calculations, beyond DR, HO resonant processes like trielectronic recombination (TR) and quadruelectronic recombination (QR) are also taken into account. However, as more than two electrons are actively involved in HO, independent-particle models such as the (Dirac-) Hartree-Fock method cannot adequately describe it. These processes can only be mediated by configuration mixing [75]. Therefore, to treat HO recombination processes, extended sets of configurations [159] with full–order relativistic configuration interaction and configuration mixing between the states are taken into account in FAC calculations. The FAC code gives the approximate atomic state function by mixing the basis states $|\Phi_k\rangle$ with same symmetries

$$\Psi = \sum_k C_k |\Phi_k\rangle , \qquad (2.33)$$

where C_k are the mixing coefficients obtained from diagonalizing the total Hamiltonian [158].

The cross section of magnetic sublevels excited by a unidirectional electron beam can also be calculated to determine the degree of linear polarization and angular distribution of the emitted photons (Sec. 3.4. of Ref. [158]). The Breit interaction can be switched on and off anytime in the code in order to evaluate the influence of the Breit interaction on the resonance strengths and polarization of the x rays. For example, the FAC computed quantities like DR resonance energies, its resonance strengths and the polarization of emitted x rays are shown with and without consideration of the Breit interaction effect in the Fig. 2.6. These computed values are also compared with the calculations done with MCDF [125] and RATIP [160] computer codes. A good agreement is observed between these different computer codes.

Within the theoretical framework outlined in the present chapter, the full set of calculated data for resonant recombination processes are presented. It includes the resonance energy, resonance strength, alignment parameter, intrinsic anisotropy parameter and degree of linear polarization of x rays emitted due to resonant recombination into highly charged iron and krypton ions. They are presented in appendix A and B. Moreover, the total cross sections and the degree of linear polarization of x rays emitted due to radiative recombination into highly charged krypton are presented in appendix C.

Chapter 3

Experimental setup

The experimental study of resonant recombination into highly charged ions requires sources of ions and electrons. An electron beam ion trap is a device that produces and traps very highly charged ions at rest. It also allows observing the photons emitted by the trapped ions. A monoenergetic electron beam focused with a strong magnetic field is utilized for the production of ions via electron impact ionization and at the same time for scanning the recombination resonances. Electron-ion recombination processes are observed by detecting the emitted x rays. This chapter introduces the experimental facility used in this work, the electron beam ion trap (EBIT). The main components of the EBIT, its operational principle and electron beam dynamics, and x-ray spectroscopy setup are briefly reviewed in the present chapter.

3.1   The electron beam ion trap (EBIT)

A schematic of the working principle of the EBIT is shown in figure 3.1. The device consists of three main assemblies: the electron gun assembly, the drift tube assembly, and the collector assembly. Electrons emitted from a thermionic cathode are accelerated towards the trap region, which is biased positively with respect to the laboratory ground. As the electron beam is accelerated towards the trap area, it is simultaneously compressed by a high axial magnetic field generated by two superconducting Helmholtz coils. After passing through the trap region, the electrons are decelerated as they approach the collector region, which is biased positively with respect to the cathode. At the collector, the magnetic field reduces, resulting in re-expansion of the electron beam and dump inside the collector.
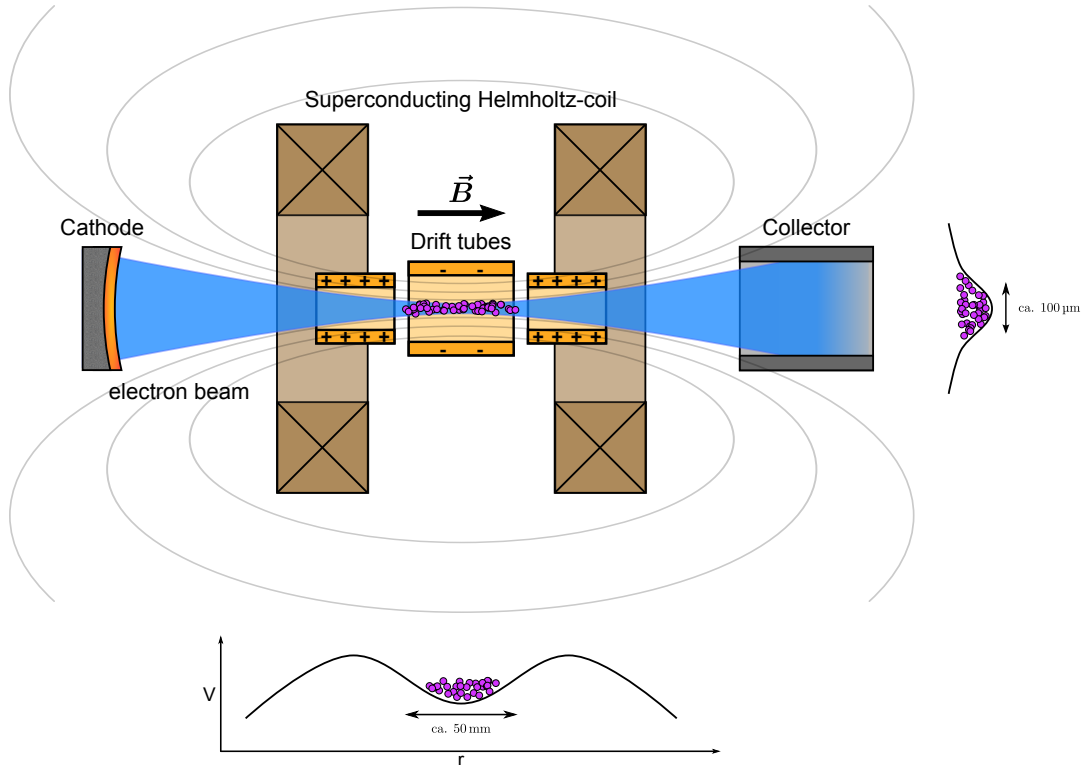
Figure 3.1: The principle of an electron beam ion trap. The electron beam is accelerated towards the trap center, passes the drift tube assembly (three out of nine drift tubes are shown here) almost at a constant velocity, and is then decelerated as it approaches the collector. The highly charged ions are trapped radially by the electron beam's space charge potential and axially by electrostatic potential given to the set of drift tubes (modified from [161]).

The highly charged ions are produced by successive electron impact ionization from neutral or lowly charged ions introduced into the trap region. The combination of the high axial magnetic field and the space charge potential of the electron beam results in the trapping of highly charged ions in the radial direction, while axial trapping results from the appropriate voltages given to the set of cylindrically shaped electrodes called drift tubes. The central drift tube is usually biased negatively with respect to the two neighboring drift tubes. Figure 3.1 shows the trapping potential in the radial and axial (longitudinal) direction.

3.1.1 History

The use of an electron beam to ionize and trap ions was first employed in the electron beam ion source (EBIS), invented by Donets and coworkers in 1965 in Dubna, Russia. They exhibited the production of bare nitrogen and Au^{19+} [162]. Further changes were

made to include a superconducting solenoid and drift tubes at cryogenic temperatures. KRYON-II became the first EBIS to produce bare Ne, Ar, Kr, and Xe ions [163]. From that point forward the EBIS development continued around the world, to provide a source of ions and as an injector into heavy-ion accelerators and colliders.

In the meantime, atomic physics experiments began constructing and using EBIS devices in laboratories around the world. Litwin (1982) [164] concluded based on his extensive experience with the EBIS that the typical long electron beam path tends to generate plasma instabilities heating up the trapped ions and reduce the interaction time between electrons and ions, therefore, shorter electron beam would be ideal. Moreover, the EBIS design did not offer observation ports for spectroscopic measurements. A few years later, both problems were overcome with the invention of the EBIT by Morton Levine and Ross Marrs [165] at Lawrence Livermore National Laboratory (LLNL) in 1988. Their changes in electron beam design and reduction in total length of the device led to a more stable electron beam. Moreover, superconducting coils in Helmholtz configuration were introduced in order to compress the electron beam and allowed optical access to the center of the trap. After the construction of the first EBIT at Livermore, a second advance was made – a high energy version of the first machine –known as Super EBIT– was built in order to reach electron beam currents up to 200 mA and electron beam energies up to 200 keV [166]. The Super EBIT even demonstrated production of fully stripped (bare) uranium (U^{92+}) in 1994 [167]. Soon after the demonstration of EBITs effectiveness, other EBITs were also constructed at Oxford [168] and NIST [169] laboratories using the Livermore low energy EBIT design. This design was further modified to make the Berlin EBIT [81].

Later on, the EBIT in Tokyo (1997) [170], in Heidelberg [171] (originally built at Freiburg (1998)) and in Shanghai (2004) [172, 173] were built based on the same principle as Super-EBIT. The EBIT in Heidelberg has a worldwide unique design which provides a horizontal electron beam, in contrast to the vertical design of all other EBITs around the world. In addition to this, two more specific EBITs were built in Heidelberg: A high current (5 A) EBIT (TITAN-EBIT) for the charge breeding facility at TRIUMF, Canada [174] and another EBIT (FLASH-EBIT) for experiments at the VUV free electron laser (FEL) at Hamburg [175]. A similar EBIT with horizontal configuration was developed at Stockholm university in 2007 for spectroscopic and precision mass measurement studies [176]. Recently small EBITs are also being built, e. g., the commercially available Dresden EBIT [177], the Tokyo CoBIT [178] and various Mini-EBITs in Heidelberg [179].
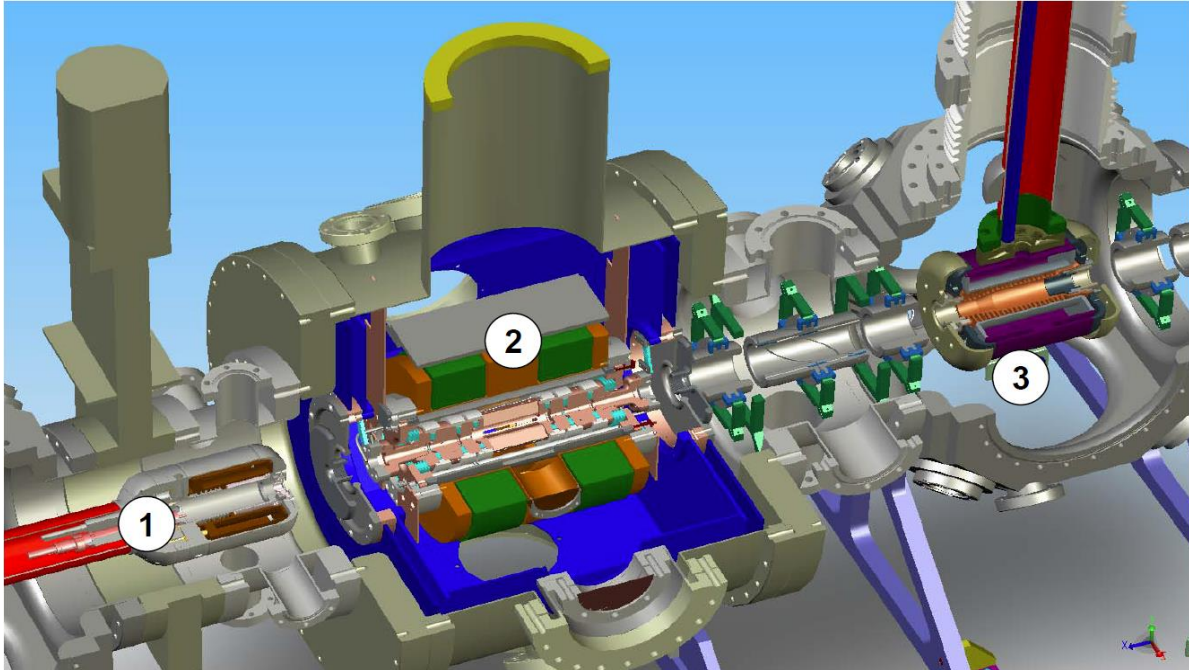
Figure 3.2: Cross-sectional view of the FLASH-EBIT: (1) electron gun, (2) the trap with nine drift tubes and superconducting Helmholtz coils and, (3) collector (modified from [180]).

3.1.2 FLASH-EBIT design

The FLASH-EBIT built at the Max-Planck-Institute for Nuclear Physics, Heidelberg, was designed for photonic studies of highly charged ions and has been used in several experiments at brilliant x-ray sources like synchrotrons and x-ray free electron lasers [175, 181, 182]. The entire apparatus was designed to be as compact as possible without compromising the performance and was built to exploit radiation facilities worldwide. It fits with its periphery, additional equipment and electronics in a modified shipping container.

At its most basic, FLASH-EBIT is essentially composed of an electron gun, a set of drift tubes, superconducting magnetic coils and an electron collector as illustrated in Fig. 3.2. It uses a focused electron beam of several hundred milliamperes to ionize and trap the highly charged ions. The electron beam is compressed to a diameter below 50 μm by 6 T magnetic fields at the trap center. To avoid unwanted charge exchange with residual gas atoms inside the chamber, the whole EBIT setup is kept under an ultra-high vacuum condition. A typical pressure at the center of the trap is of the order of 10^{-11} mbar. The main components of the FLASH-EBIT are described in detail in the following subsections.
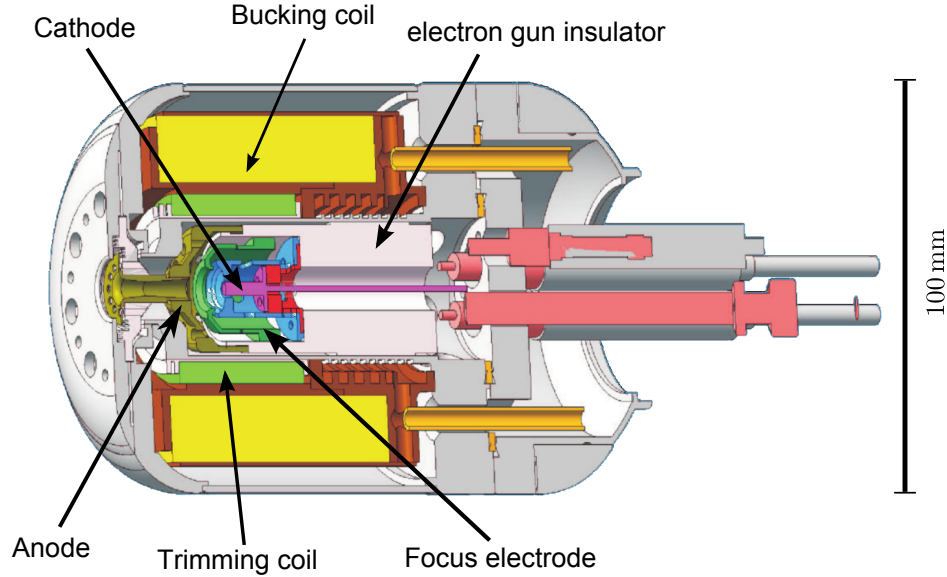
Figure 3.3: A cross-sectional view of the electron gun assembly in the FLASH-EBIT. The cathode (in purple) emits the electrons, which are then pulled by the focus electrode (in green) and accelerated towards the anode (in dark green). The large blue piece surrounding the cathode is the holder, and the large yellow area surrounding the electron gun electrodes are the bucking coils (modified from [161]).

Electron gun

The electron gun is located at the forefront of the EBIT. The essential part of the electron gun is a cathode, which is surrounded by electric field shaping electrodes to guide the electrons towards the trap. A cathode used in FLASH-EBIT consist of a tungsten heating filament coated with barium oxide. The surface emitting layer comprised of a mixed matrix of these elements, yielding work function of $\Phi_{W,BaO}$=2 eV. This low work function leads to lower operating temperatures ($\approx$ 1300-1500 K) necessary to produce electrons, which is also good for a longer lifetime of the cathode.

As illustrated in figure 3.3, the cathode is enclosed by a focus electrode, which assists in pulling electrons away from the cathode surface. The cathode voltage is typically around -2 kV and the beam energy is determined by the potential difference between cathode and central drift tubes. The electron beam current can be adjusted by changing the voltage of the focus electrode. An anode provides the extraction field for the electrons. The potential difference between the cathode and anode provides an acceleration of roughly 2 kV, at this point the electron beam is further accelerated towards the positively biased trap electrodes (see Fig. 3.4).

Two magnetic coils, the trimming and bucking coils, are in place around the cathode and shaping electrodes. They serve to compensate the residual magnetic field resulting
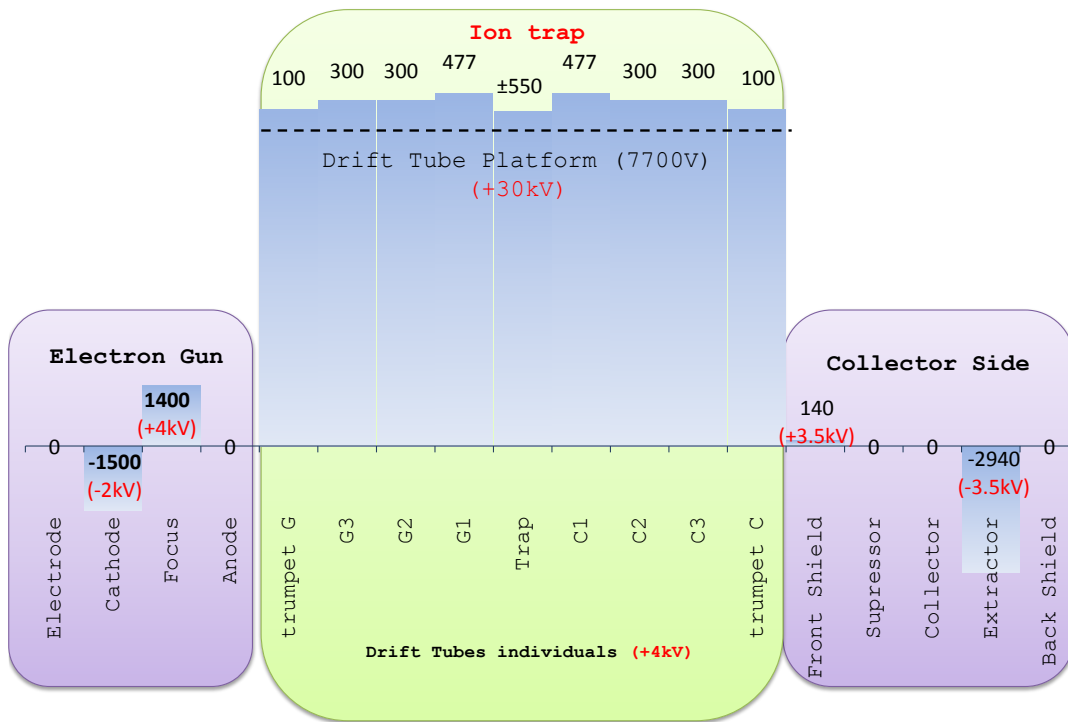
Figure 3.4: Typical power supply scheme of the FLASH-EBIT to perform DR experiments. The series of power supplies and its maximum voltage capacities (in red) are shown.

from the trap region, which would otherwise hinder the emission of the electron beam. It is crucially important to compensate and set the rest magnetic field at the cathode surface roughly to zero, as it can increase the electron beam radius in the trap (explained in 3.2.1). A larger beam radius in the trap can lead to lower ionization rate, which is undesirable to create enough ion density inside the trap. Excess heat from both the coils and the cathode are dissipated by a water cooling system.

Ion trap

As illustrated in figure 3.5, there are nine electrodes (drift tubes) made of highly pure copper in the FLASH-EBIT. These electrodes have a cylindrical shape, with a central bore whose radius diminishes towards the trap. The first four drift tubes are on the side of the electron gun, hence the labeling G1-G4. The last four (C1-C4) are on the collector side. This series of drift tube allows adjusting the trap length. The drift tubes form an axial potential, trapping the highly charged ions in the central drift tube. The central drift tube is particular important because it has eight slits, which enables the observation of the trap region for various spectroscopic techniques.

The voltage offset of all nine drift tubes can reach up to 30 kV with respect to the ground. This is known as drift tube platform voltage. It facilitates a systematic and stable offset in electron beam energy when performing measurements in the steps of energy. Moreover, the potential of each individual drift tube can also be varied up to 4 kV individually (see Fig. 3.4). The trapping potential can thereby be adjusted depending on the peculiarity of the measurement. Ion dumping can also be implemented by raising the central drift tube to a high relative voltage. The ions are thereby dumped from the trap, and one can avoid unwanted heavy ionic species inside the trap, e. g., barium and tungsten from the cathode.

Two superconducting magnet coils in Helmholtz configuration are located around the drift tubes as shown by Fig. 3.2. It squeezes the electron beam to a radius below $50\,\mu$m at the trap center. The coils are cryogenic and composed of Niobium-tin (Nb_3Sn), which is superconducting below 18 K temperature. A very high current of 114 A running through the coils produces a constant magnetic field of 6 T in the trap. In FLASH-EBIT, the magnet coils are cooled to 4 K by a helium compressor running in a closed cycle in contrast to other EBITs which use a helium cryostat. This setup rewards longer experimental stability, low maintenance and reduce the cost of running. Furthermore, this setup also helps to decrease the pressure in the EBIT even further by freezing any remaining oxygen or nitrogen in the trap.
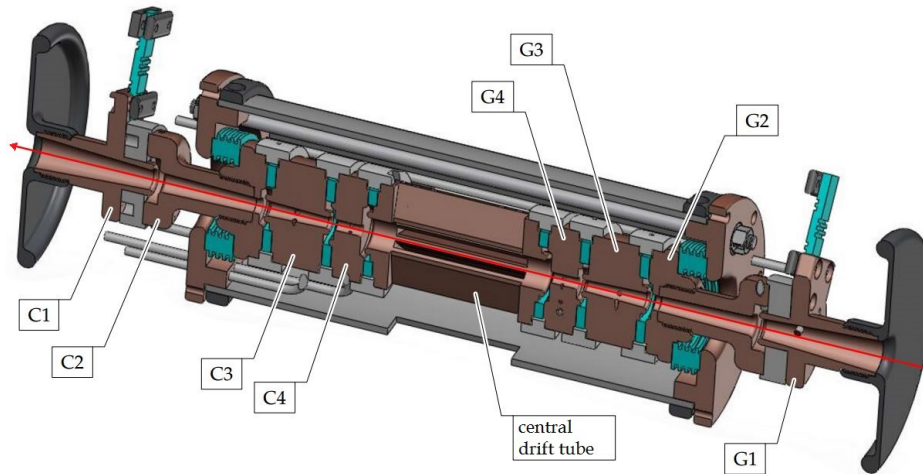
Figure 3.5: A cross-sectional view of the drift tubes in the FLASH-EBIT. The direction of the electron beam is indicated by the red arrow. Drift tubes G1-G4 and C1-C4 are the drift tubes on the gun and collector sides respectively (modified from [183]).

Electron collector

Once the electron beam passed through the trap region, it is transported to the collector assembly. The collector magnetic coil compensates the magnetic field from the trap region and the beam widens before entering the collector, as can be seen from Fig. 3.6. Inside the collector assembly, the electron beam begins to expand as the strength of magnetic field decreases and the electrons repel each other. The electron beam is deposited on the inner wall of the collector, where the associated heat is transported away by a water cooling system.

During the electron beam dumping process, ions are sputtered off the collector electrode surface, and secondary electrons are produced. The suppressor electrode at the entrance of the collector, biased negatively with respect to the collector, prevents the escape of the secondary electrons from the collector. The collector current and suppressor current are regularly monitored to check the beam condition. The extractor electrode is located at the exit of the collector, operated at a high negative voltage compared to the cathode, to ensure that no electrons can pass the collector. In addition, the extractor electrode is also used to separate the incoming ions from the trap along the electron beam axis, hence its name.
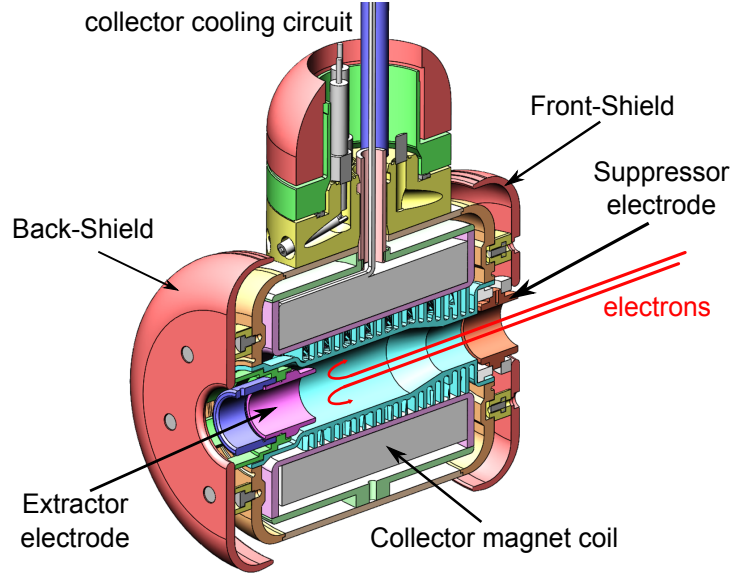
Figure 3.6: A cross-sectional view of the electron collector (modified from [161]).

Injection system

The injection system is connected to the side of the EBIT overlooking the trap region. FLASH-EBIT has a gas injector system which delivers a collimated atomic beam to the trap region through two-step differential pumping stages (see in figure 3.7). Elements or molecules which can be brought into the gas phase can be injected by this system, e. g., Ne, Ar, Kr, Xe, $Fe(CO)_5$, $W(CO)_5$ and more. A needle valve is installed at the end of the source, to adjust the size of the opening to the injection system, and hence the density of source gas in the setup. Two slits of 5 mm in width enable differential pumping between the injection system and the trap region. The pressure in the first stage of the injection system is usually of the order of 10^{-6}–10^{-7} mbar, whereas the overall pressure in the EBIT is 10^{-10} mbar. Figure 3.7 shows the atomic or molecular beam formed by slits at various differential pumping stages, that finally overlap with the electron beam at the trap center. The final density of the atomic beam in the ionization region is assumed to be reduced through collimation and cryogenic pumping by a few orders of magnitude ($\approx 10^{-13}$ mbar). The density of neutral atoms injected into the trap is proportional to the pressure measured in the second stage of the injector.

3.2   Electron beam dynamics

The electron beam is of the center of the EBIT as it performs several functions simultaneously such as ionization, excitation, and radial trapping. The electron beam
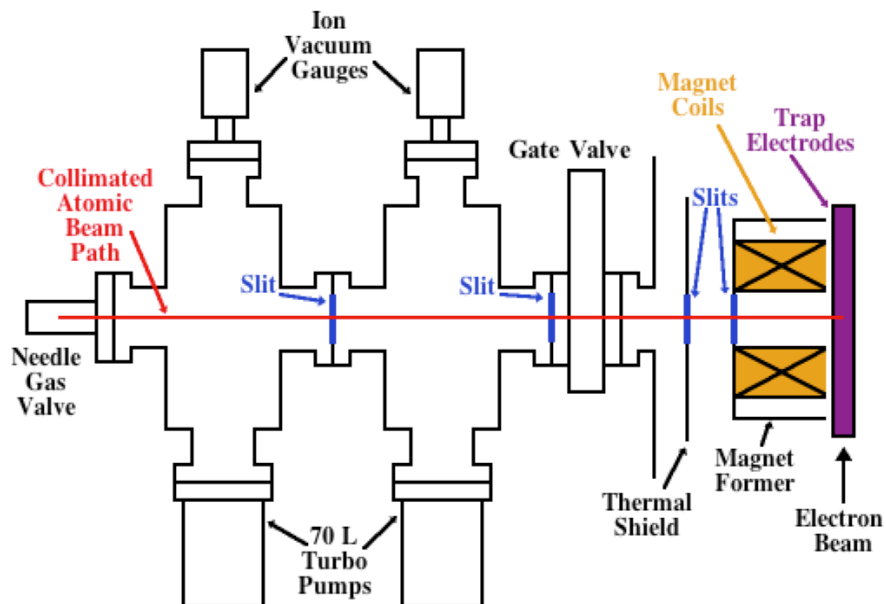
Figure 3.7: The two-stage differentially pumped gas injection system. This system is used to inject a collimated beam of neutral gas to the trapping region (located on the right in purple color), which then becomes ionized and trapped (modified from [184]).

properties directly play an important role in the production and trapping of ions. Studies of electron beam dynamics help to determine precise electron-ion interaction energies in the DR experiment and to estimate the radial energy component of the electron beam. There are three parameters charactering the beam condition: current, energy and radial distribution in the trap region.

The current output of the electron gun is expressed as

$$I_e = p \, V_{cathode}^{3/2}, \tag{3.1}$$

where p is the perveance (characteristic parameter for the electron gun) and $V_{cathode}$ is the voltage applied between cathode and anode. The electron gun used in the FLASH-EBIT has a perveance of 0.6 μperv.

3.2.1 Electron beam Radius and current density

The first model to determine electron beam radii was given by Brillion [185]. It describes a uniformly distributed electron beam propagating under the presence of a uniform axial magnetic field B. This theory is based on the assumption of laminar flow, which means that electron trajectories do not cross each other and the electrons are launched from

a region of zero magnetic field. It also neglects the temperature of the electrons at the cathode. The radius of the electron beam at the trap region according to this model is given as

$$r_B[\mu m] = \frac{150}{B[T]}\sqrt{\frac{I_e[A]}{E_e[keV]}}, \tag{3.2}$$

where I_e is the electron current in the beam, B the magnetic field at the trap, and E_e is the beam energy at the trap.

However, the flow of the electrons in an actual beam is quite non-laminar [186] and it has a finite temperature at the cathode. Herrmann [187] presented the more realistic theory based on a non-laminar optical model which treats thermal velocities as an integral part of the motion of the electrons. In this theory, the beam profile has a Gaussian distribution in radial direction and 80% of the electrons are enclosed within a cylinder of radius

$$r_H = r_B\sqrt{\frac{1}{2} + \frac{1}{2}\sqrt{1 + 4\left(\frac{8m_e k_B T_c r_c^2}{e^2 B^2 r_B^4} + \frac{B_c^2 r_c^4}{B^2 r_B^4}\right)}}, \tag{3.3}$$

where m_e is the electron mass, B_c is the rest magnetic field at the cathode, r_c is the cathode radius, and $k_B T_c$ is the characteristic electron temperature at the cathode.

As shown in Figure 3.8, the electron beam radius is smallest when the residual field at the cathode surface (B_c) is close to zero. This is ideal, as the smaller the radius, the higher the electron current density and thereby the ionization rate. This term is typically minimized in the experiments through bucking coil tuning. Assuming that the second term in Eq. (3.3) is minimized during the beam tuning, the Herrmann radius reduces to,

$$r_H \approx r_B\sqrt{\frac{1}{2} + \frac{1}{2}\sqrt{1 + \frac{32 m_e k_B T_c r_c^2}{e^2 B^2 r_B^4}}}. \tag{3.4}$$

The current density j of the electron beam is also an important parameter. For an electron beam with a current of I_e and radius r_H, the current density j in the trapping region can be given by

$$j = \frac{I_e}{\pi \, r_H^2}. \tag{3.5}$$

The dependence of the Herrmann radius on other experimental parameters is shown in Fig. 3.9. The subsets (a) & (b) show calculated Herrmann radii and resulting current densities in the trap as a function of the electron beam current and energy. It shows a smooth decrease of beam radius with decreasing electron beam current and increasing
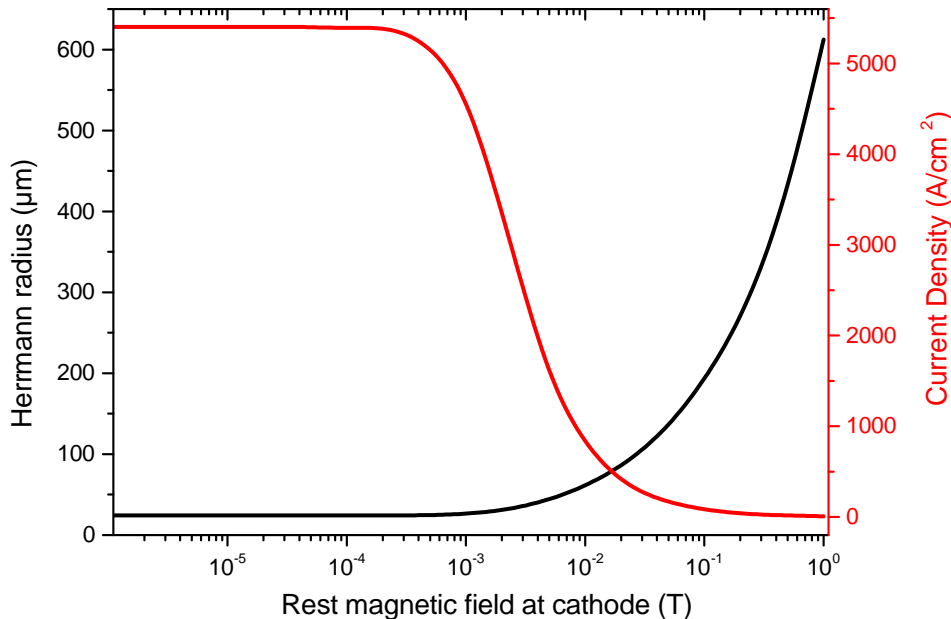
Figure 3.8: Calculated Herrmann radius (in black) and current density (in red) is plotted against the residual magnetic field B_c at the cathode. The following beam conditions were used for this calculation: $E_e = 10$ keV, B = 6 T, $T_c = 1400$ K, $I_e = 100$ mA. This graph demonstrates that optimum beam compression occurs when rest magnetic field at cathode B_c is minimized.

energy. The current density which determines the rate of ionization also increases rapidly with the beam current. It also demonstrates that, even using the modest electron beam energy of 10 keV, FLASH-EBIT can reach the current density of about 25,000 A/cm², as it is capable of reaching a maximum beam current of 550 mA. The subset (c) demonstrates the advantage of using larger magnetic fields for optimal beam compression and the subset (d) shows that electrons created with less thermal energy result in a more confined beam. It should be noted here that the calculated current density at the trap is for an effective electron beam radius which contains only about 80% of the electrons.

3.2.2 Electron beam energy

The electrons passing through the trap region experience a voltage difference

$$E_{beam} \approx |V_{cathode}| + |V_{platform}| + |V_{trap}| - |V_{space}|, \tag{3.6}$$

where $V_{cathode}$ is the bias voltage given to the cathode, V_{trap} is the voltage given to the central drift tube, $V_{platform}$ is the additional bias added to the drift tubes, and V_{space} is the potential generated by the space charge due to the beam electrons, scattered
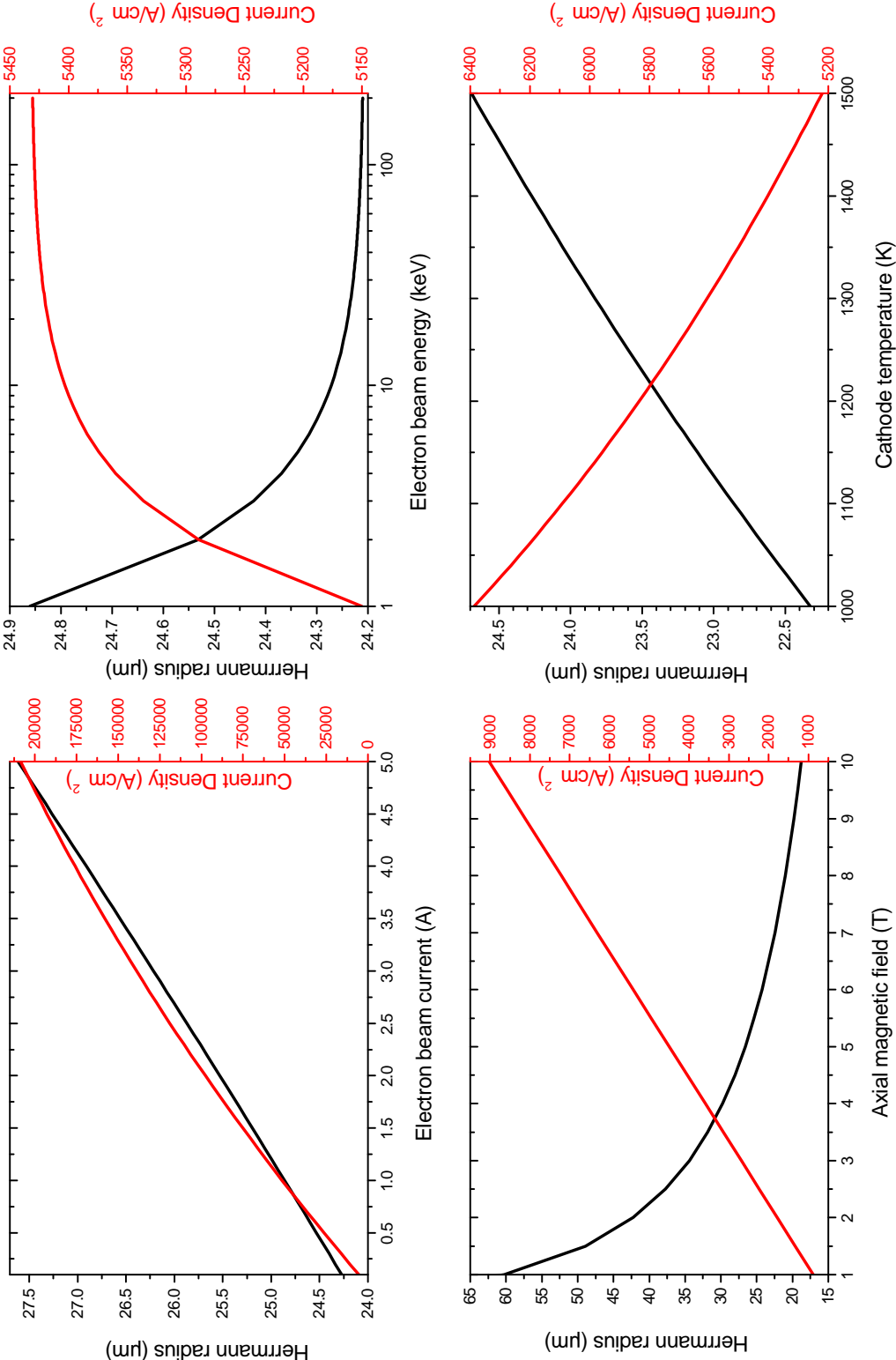
Figure 3.9: Calculated Herrmann radius (in black) and current density (in red) as a function of (a) electron beam current I_e, (b) electron beam energy E_e, (c) axial magnet field B and, (d) cathode temperature T_c. Unless varied, the following electron beam conditions were used: $E_e = 10$ keV, $I_e = 100$ mA, $B = 6$ T, $T_c = 1400$ K, $r_c = 1.5$ mm and $B_c = 0$.

electrons, and trapped electrons and ions. The space charge potential effectively reduces the interaction energy when compared to the applied acceleration potential between the cathode and trap electrodes. Space charge potential provides the radial trapping for the ions. Electrons at different radii see slightly different values of V_{space}. For a typical beam radius of 35 μm, the variation in V_{space} across the beam is $\sim 20 - 50$ volts.

3.2.3 Transversal energy component and pitch angle of electron beam energy

As discussed in Sec. 3.2.1, the electron beam in an EBIT is produced at the cathode with a finite non-vanishing thermal component. This component causes electrons to gyrate perpendicular to the magnetic field direction. Thus, electrons follow helical path instead of following magnetic field lines along the beam direction. This situation is not only relevant in laboratory environments, but it may also exist in astrophysical plasma, e. g., solar flares where electrons are spiraling around the strongly directed magnetic field lines with a certain pitch angle [30, 31, 143]. Therefore, it is important to estimate the amount of energy perpendicular to the beam direction since it has a systematic effect on the ion alignment and polarization measurements [188].

The properties of the electron beam in an EBIT can be described using the optical model developed by Herrmann (1958) [187]. According to this model, the motion of a given electron has a finite velocity component perpendicular to the z -axis, which is related to the electron's radial position and velocity at birth on the cathode of the electron gun. Herrmann showed that the magnitude of the transverse velocity is inversely proportional to the radii of the cathode images formed at various locations along the electron beam propagation direction. It means that the product of beam area and transverse electron energy $E_\perp$ are constant along the electron beam propagation direction, i. e., $E_\perp \cdot 2\pi r^2 = $ constant [84, 189]. Therefore, the transversal energy component of the electron beam $E_\perp$ can be estimated from the temperature of the cathode of the electron gun and the areal compression ratio of the beam from a radius at the cathode to a radius at the trap. It can be expressed as

$$\frac{E_\perp^{(t)}}{E_\perp^{(c)}} = \left(\frac{r_c}{r_t}\right)^2. \tag{3.7}$$

Because of the existence of the transverse component of the electron velocity, the velocity vector of a given electron is no longer aligned with the magnetic field or z-axis of the EBIT. It deviates from the z-axis by an angle γ (shown in Figure below),

$$\tan \gamma = \frac{\nu_\perp}{\nu_\parallel},$$

$$\cos \gamma = \frac{\nu_\parallel}{\sqrt{\nu_\parallel{}^2 + \nu_\perp{}^2}},$$

$$\sin^2\gamma = \frac{E_\perp}{E_e}, \;\; E_e = \frac{1}{2}m\nu_e^2, \qquad (3.8)$$
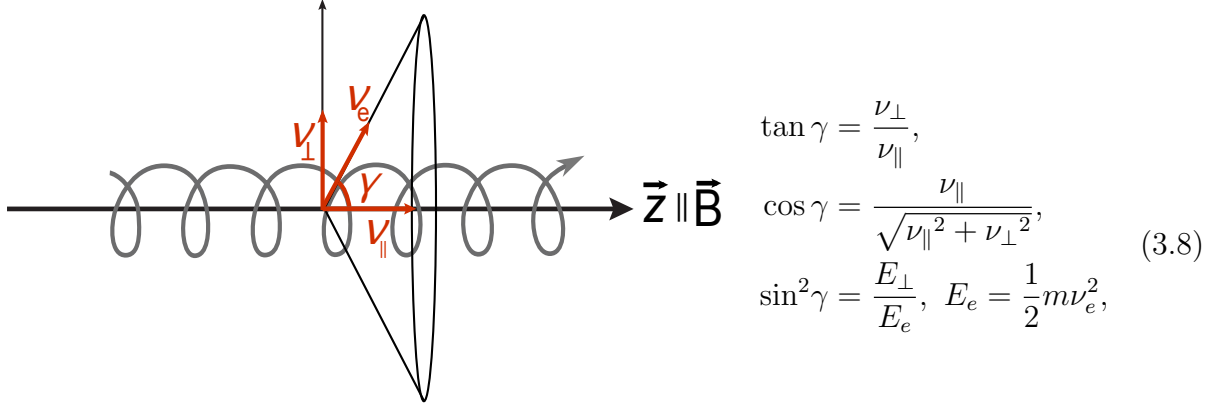
where E_e is the electron beam energy and $E_\perp$ is the transversal component of the electron beam energy.

According to the Eq. (3.7), we can estimate $E_\perp$ of the FLASH-EBIT for certain operating conditions. For example, for given FLASH-EBIT parameters:

$E_\perp^{(c)} \approx 0.121$ eV (from cathode temperature $T_c = 1400$ K),

$r_c = 1.5$ mm,

$r_t \approx 24.35$ μm (Herrmann radius for following beam conditions: $B_c = 0$ T, $B = 6$ T, E_e = 8954 eV),

Therefore, using equations (3.7) & (3.8), we can estimate,

$E_\perp^{(t)} \approx 457.856$ eV and $\gamma = 12.965°$.

However, the above values are only an estimate; they are not well known. Moreover, these estimated values are not experimentally measured for the FLASH-EBIT. Beiersdorfer *et al.*(2001) [189] inferred the transversal energy component in the Livermore EBIT-II electron beam ion trap from linear polarization measurement of K-shell x-ray lines produced by Mg^{10+} ions. The measured value was found to be 190 ± 30 eV of total electron beam energy, which was in good agreement with the theoretical prediction of the optical theory of Herrmann (≈ 194 eV). We also estimate our value of $E_\perp^{(t)}$ by using the same optical model. However, the design of the FLASH-EBIT is quite different from the Livermore EBIT [165, 175]. In FLASH-EBIT, the temperature of the filament may vary between 1000 to 1600 K, depending on the given filament heating current. Similarly, the radius of the electron beam may vary between 20 to 35 μm, depending on the various operating parameters of FLASH-EBIT such as beam current and bucking coil setting. As a result of this, the value of $E_\perp^{(t)}$ may vary between 200 to 600 eV for various operating parameters. Figure 3.10 shows the variation in the value of $E_\perp^{(t)}$ as a function of the Herrmann radius and the cathode temperature.

In the second approach, we can consider the principle of adiabatic invariant for a charged particle traveling through a fixed magnetic field, i. e., $\nu_\perp^2/B \approx$ `constant`.
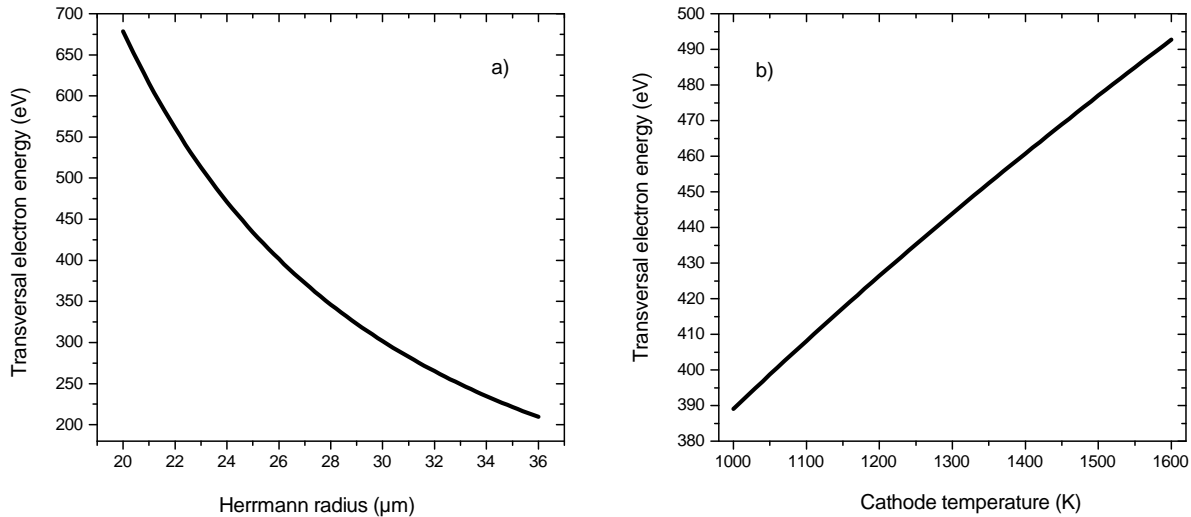
Figure 3.10: Calculated transversal electron energy plotted against (a) the Herrmann radius and (b) the cathode temperature. Unless varied, the following electron beam conditions were used: $r_c = 1.5$ mm, $T_c = 1400$ K (0.121 eV), $B = 6$ T, $I_e = 100$ mA, $E_e = 10$ keV.

Thus, we can make a second estimate as follows. We consider $\nu_\perp^2$ at the cathode is of order $2kT_c/m_e$, where $T_c = 1400$ K. The cathode magnetic field B_c is not well known, but it's believed to be of order a few hundred microteslas, depending on the bucking coil setting. From this approach we estimate the value of $E_\perp^{(t)}$ is about 1578 eV (for E_e = 8954 eV, $B_c = 300$ μm), which is quite higher than the prediction of optical theory of Herrmann. In reality, the fast moving electrons travel across the strong magnetic field gradient, from approximately a few microteslas field at the gun to the 6 Tesla at the trap, which invalidates the applicability of the principle of adiabatic magnetic flux invariance [189].

The large deviation in the estimation of the transversal energy component of the electron beam clearly makes the measurement highly desirable in order to discriminate amongst the models. We shall discuss experimental determination of transversal energy later in Sec. 6.2.1

3.3   X-ray spectroscopy

The energies and intensities of the photons emitted from the trap as well as the electron beam energy have to be measured in the present experiment. The semiconductor detectors are used which provides the large solid angle and covers a broad spectral range. Given that good energy resolution for x rays can be provided by detectors with
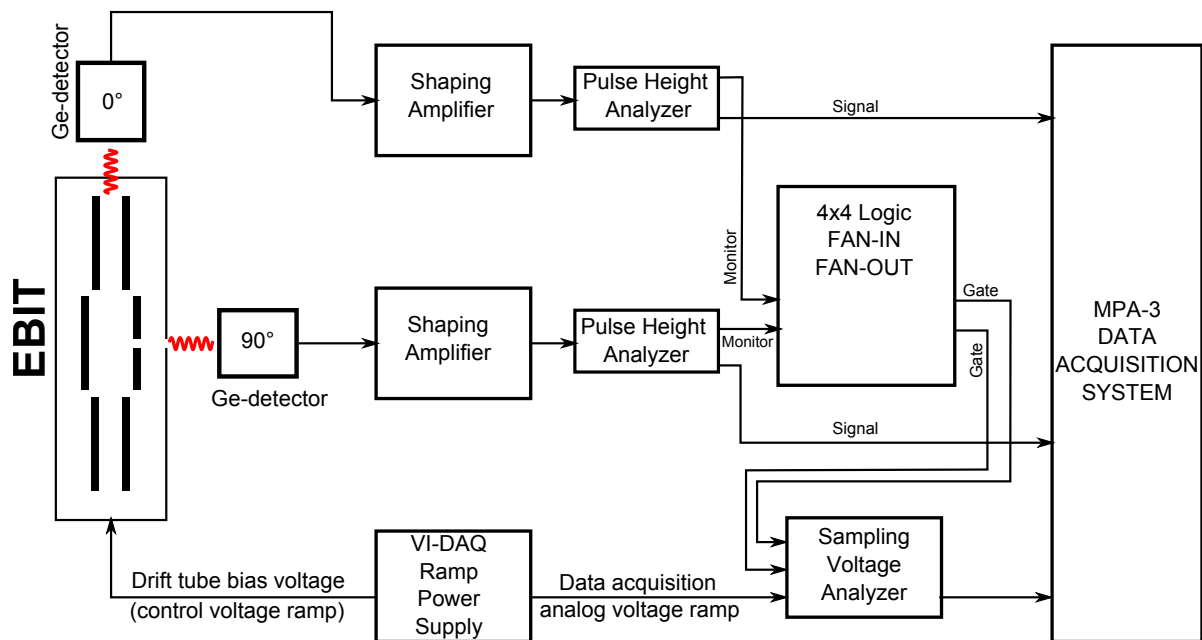
Figure 3.11: Scheme of x-ray spectroscopy and data acquisition system.

germanium or silicon crystals, an ORTEC high-purity Ge detector (see Table 3.1 for specifications) was selected.

Semiconductor detectors work as solid state ionization chambers. The passage of ionizing radiation creates electron-hole pairs which are then collected by an electric field. The advantage of using semiconductor detectors is that the average energy required to create an electron-hole pair (2.96 eV at 77 K for germanium) is 10 times smaller than in traditional gas chamber detectors [190]. Therefore, the amount of ionization produced for a given energy is an order of magnitude greater resulting in better resolution. Moreover, they are compact and can have a very fast response time. An electric field applied to the crystal results in the collection of the electrons, and hence a signal. The integrated charge of this signal corresponds to the number of electrons collected, and therefore, to the energy of the x rays deposited. This charge is then converted into a voltage by a preamplifier, before being shaped and amplified by a spectroscopy amplifier, see Fig. 3.11. The amplified detector pulse was feed to Pulse Height Analyzer (PHA) card and then to analog to digital converter (ADC) of MPA-3 data acquisition system to record the spectra.

The recorded pulse height spectra were then calibrated with known sources (^{241}Am) to translate the axis to energy units. The dominant x-ray lines of ^{241}Am are listed in Table 3.2. The known peak energies and their corresponding channel numbers were then plotted, and a linear fit was performed yielding the energy axis transformation.

Table 3.1: Some properties of the solid-state high purity germanium detector (Model: GLP-36360/13) used at the FLASH-EBIT.

Geometry	Coaxial
Energy range	3 to $\approx$ 300 keV
Active diameter	36 mm
Crystal dimension	Area: 1000 mm^2, Depth: 13 mm
Maximum Bias voltage	-2 kV
Be-window thickness	0.25 mm
Transmission	$\sim$ 82% at 6.5 keV
Resolution	700 eV FWHM at 13 keV

Table 3.2: Calibration Lines

Source	Dominant x-ray line energies (keV)			
^{241}Am	13.946	17.751	26.345	59.541
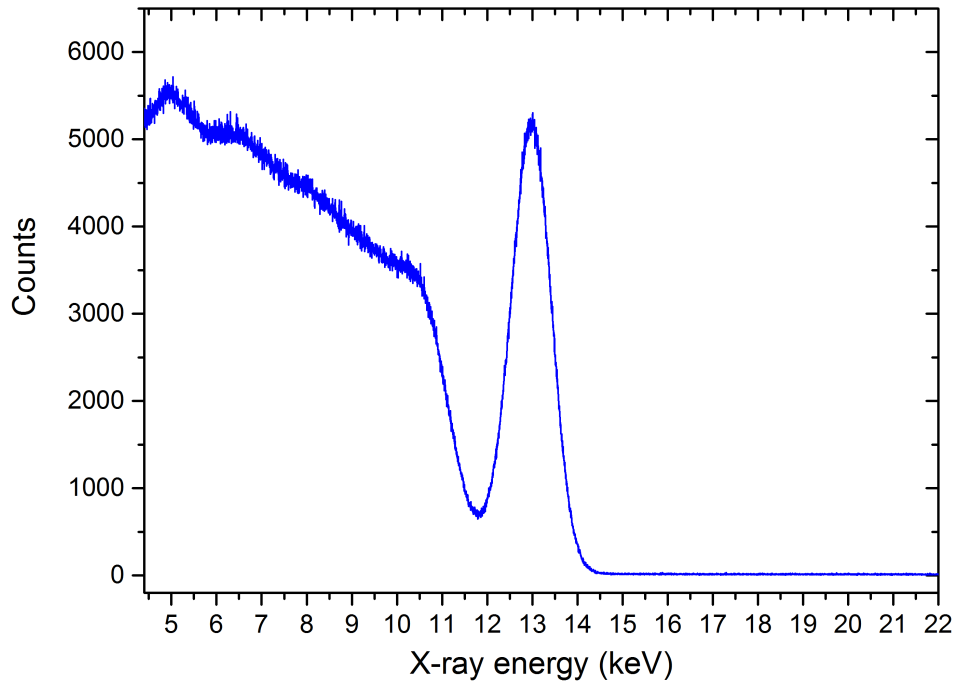
Figure 3.12: A typical x-ray spectrum detected by an high-purity germanium detector (ORTEC GLP36360/13). Krypton was injected during the measurement.

The produced spectra were then compared with the preliminary measurement of the *KLL* DR of carbon-like krypton and other ion species believed to be present in the trap, and matched with their respective characteristic x-ray emission lines. These lines are from the processes such as direct excitation, radiative recombination, and dielectronic recombination. Background ions such as barium and tungsten are also found in the EBIT trap, as these ionic species evaporate off the cathode and become ionized, thereby providing characteristic emission lines at charge states governed by the electron beam energy. Figure 3.12 shows a typical x-ray energy spectrum obtained from one of the germanium detectors. The lower energy x-ray spectrum is dominated by bremsstrahlung as well as distinct emission lines of background ions. On the higher energy side, an intense peak of $K\alpha$ emission of krypton ions at 13 keV can be seen, which is emitted due to resonant recombination processes.

Chapter 4

Polarization measurement of dielectronic recombination transitions

This chapter describes the first results of an experiment dedicated to measurements of linear polarization of x rays produced by dielectronic recombination (DR) into highly charged ions. As discussed in the section 1.4, to this date, little attention has been paid to the polarization measurements in the resonant recombination processes. Previously, Shlyptseva and coworkers had measured polarization properties of x rays in dielectronic satellite transitions using Bragg crystal spectrometer at Livermore EBIT [87, 88, 140]. Although Bragg crystal spectrometers have excellent energy resolutions, their efficiencies are typically small and also they have limited x-ray energy bandwidth. Moreover, the analysis of polarization-dependent spectra is difficult since they have to be corrected for the crystal's reflectivity and its polarization sensitivity. Therefore, no information on degree or angle of polarization was extracted in those experiments. These shortcomings of previously performed measurements calls for a new technique and a dedicated polarimeter which can be applicable to a wide range of x-ray energies.

For the present experiment, we have developed a dedicated polarimeter to measure the degree and angle of linear polarization of x rays following dielectronic recombination into highly charged krypton ions. This polarimeter applies the principle of Compton scattering. The Compton polarimeter consists of a scattering target and an array of silicon p-doped–intrinsic–n-doped (SiPIN) semiconductor junction diodes to sample the azimuthal distribution of the Compton scattered x rays. The x-ray polarization mea-

surements are carried out for five DR resonances and radiative recombination (RR) of electrons into the $n = 2$ shell of highly charged krypton ions. The degree of linear polarization of K-shell x rays is extracted and then compared with the theoretical calculations carried out using the relativistic configuration interaction based Flexible Atomic Code (FAC) [158]. Furthermore, the effects of Breit interaction on the polarization is also investigated in the present measurements.

In the Sec. 4.1, we describe our experimental setup and present the Compton polarimeter. The data analysis method used to extract the degree of linear polarization is described in Sec. 4.2. In Sec. 4.3, we compared experimental results with the theoretical predictions and discuss the final results. Finally, a summary is given in Sec. 4.4.

4.1 Experiment

4.1.1 DR measurement setup

The experimental setup used in the present measurement is shown in Fig. 4.1. The FLASH-EBIT [175, 181] developed at Max-Planck-Institute for Nuclear Physics was used. The details about the FLASH-EBIT device are discussed in chapter 3. Here, an electron beam of 100 mA of current emitted from a cathode is guided by a 6 T magnetic field through a set of drift tubes. The magnetic field of 6 T is achieved by superconducting Helmholtz coils with the current of 114 A. The beam is compressed by a strong magnetic field, and is reduced to a diameter below ~ 50 μm at the center of the trap. The beam diameter is calculated according to the operational parameter of the EBIT using Herrmann's optical theory of electron beam (see Sec. 3.2.1). The space charge potential of the highly compressed electron beam radially traps the ions. An electrostatic trap in the axial direction is created by biasing the middle drift tube to a lower potential, as compared to the neighboring drift tubes. The axial trap depth was set to roughly 100 V with the space charge potential correction (see Sec. 3.2.2).

In the present experiment, krypton gas was continuously injected into the trap by means of an atomic beam. Such a beam was created using a two-stage collimation and a differential pumping system. The details of differential pumping system are described in Sec. 3.1.2. The pressure at the injection and the trap was 4.16×10^{-7} mbar and 5×10^{-10} mbar, respectively. Highly charged krypton ions in the charge state from Kr^{18+} to Kr^{34+} were produced through successive electron impact ionization. The trapped ions are dumped every 300 sec from the trap with a period of 3 sec. This prevented accumulation of unwanted heavy ionic species emitted from the electron gun, such as
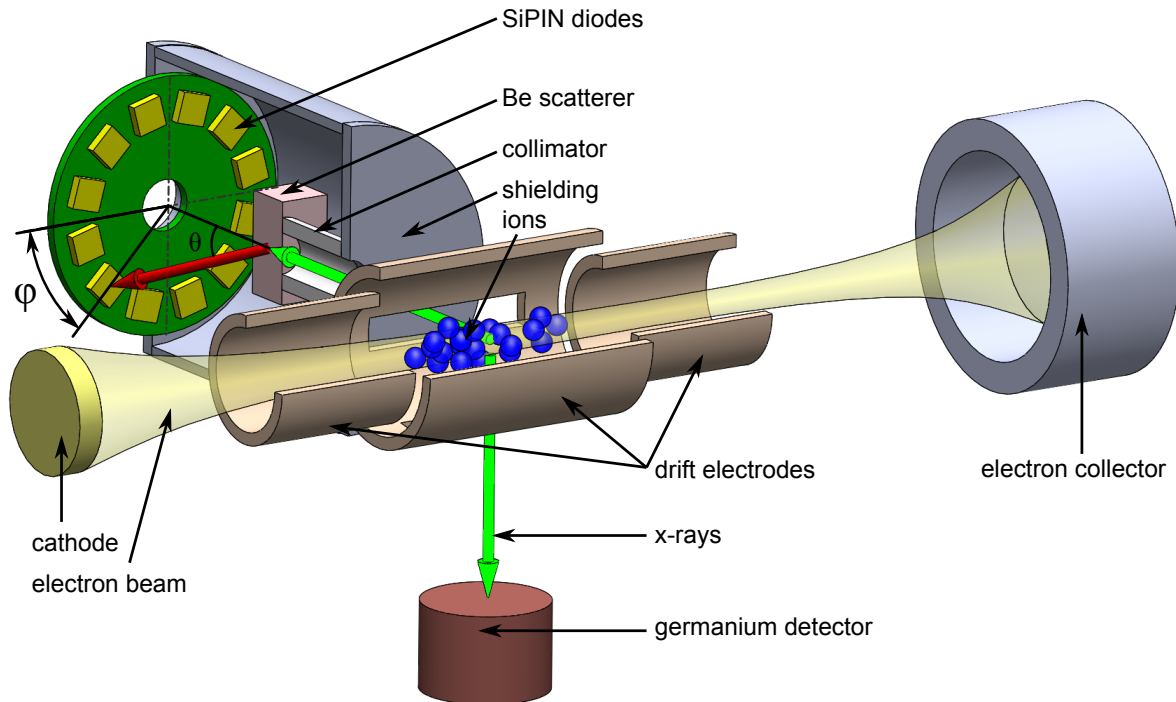
Figure 4.1: Schematic diagram of the EBIT and the layout of the Compton polarimeter. The electrons are emitted from the cathode and accelerated towards the trap center where they collide with trapped highly charged krypton ions. The x rays, emitted in the collision processes, are collimated and Compton-scattered in a block of beryllium and their azimuthal scattering distribution is recorded by 12 SiPIN diodes. Unscattered x rays are recorded by an additional germanium detector.

Table 4.1: Operational parameters of the FLASH-EBIT in the present experiment.

Parameter	Value
Electron beam current	100 mA
Magnetic field	6 T (Current: 114 A)
Trap voltage offset	100 V
Scan energy	8.6 – 9.7 keV
Sweep rate	1.8 eV/s
Beam radius	$\approx 24.42~\mu$m
Dump cycle	300 sec
Dump time	3 sec
Pressure of gas injector	4.16×10^{-7} mbar

barium and tungsten. The ions are dumped by lowering the first collector side (C1) drift tube potential to zero (relative to the central drift tube potential). The consecutive collector side drift tubes C2, C3 and Trumpet C was also set to zero potential relative to central drift tube potential.

The electron beam energy was swept across the range of *KLL* DR resonances, where a free electron is captured into the *L*-shell while exciting a bound electron from the *K*- to the *L*-shell of the ion. For this, the drift tube platform voltages are varied from 6.6 to 7.7 kV with a slow slew rate of 1.8 V/s with a triangular wave function. In addition to that, cathode was set at 2 kV. The slow variation of electron beam energy is necessary to ensure an equilibrium charge state distribution [99, 191] of krypton ions inside the trap. The experimental parameters were optimized to obtain a high x-ray count rate while allowing for the electron beam energy resolution sufficient to resolve the DR resonances. For a moderate beam current of 100 mA and the trap depth of 100 V, we achieved a collision energy resolution of 21 eV full width at half maximum (FWHM) at 9 keV. The details of operational parameter of FLASH-EBIT for the present experiment are given in the Table 4.1.

X rays emitted by the ions in the trap as the signature of RR and DR were detected with a high-purity germanium detector having the energy resolution of about 750 eV FWHM at 13 keV. The detector observed x rays emitted in a direction perpendicular to the electron beam propagation direction. The solid angle covered by this detector was 0.0087 sr. The characteristics of germanium detector used in the present experiment are discussed in the previous section 3.3. Fig. 4.2 (a) shows a typical x-ray energy spectrum observed by the germanium detector. At lower energies, the spectrum is dominated by bremsstrahlung and x-ray lines produced by the trapped impurity ion species. The faint feature at 10 keV is produced by RR into the $n = 3$ shell of highly charged krypton.

The x rays at 13 keV are produced by RR into the $n = 2$ shell and by the *KLL* DR processes. The intensity of the x rays as a function of the electron beam and x-ray energies is shown in Fig. 4.4 (a), where the diagonal window outlines the region of RR into the $n = 2$ shell and *KLL* DR resonances. The visible bright spots at well-defined electron and x-ray energies in Fig. 4.4 (a) correspond to the x-ray intensity enhancement due to DR resonances in different ionic charge states of krypton.

4.1.2 Polarization measurement setup

The linear polarization of 13 keV x rays emitted in RR and DR processes is measured perpendicular to the electron beam axis by the Compton polarimeter, see Fig. 4.1 and Fig. 4.3. The polarimeter was developed by our research group for x-ray energy regime from 10–30 keV to study various radiative atomic processes in low- and mid-Z ions. The detailed design and the operation principles of this polarimeter are discussed in Ref. [192].

In brief, polarized x rays from the EBIT is collimated by a round aperture with a diameter of 15 mm. Collimated x rays are scattered in 10 mm thick beryllium target with dimensions of $50 \times 50 \times 10$ mm. Beryllium was chosen for its low photo-absorption cross section. The energy-dependent x-ray transmission of the beryllium scatterer is shown in Fig. 4.2 (a). Collimated x rays are scattered at a polar angle of $\theta \approx 50°$. The scattered x rays are recorded by 12 SiPIN diodes, giving the azimuthal scattering intensity distribution. SiPIN diodes with the dimensions of $7 \times 7 \times 0.38$ mm are glued on small printed circuit board (PCB). The latter are arranged equidistantly on flat surface of PCB with their centroids forming a circle with a diameter of 49 mm (see Fig. 4.3 (a)). These diodes were operated at room temperature.

The signals from the SiPIN diodes are amplified with charge sensitive preamplifier, which were placed on the opposite side of the PCB (see Fig. 4.3 (b)). This minimize the path connecting the diodes and the preamplifiers. The preamplified signals from the SiPIN diodes were processed using 100 MHz sampling 14-bit analog-to-digital converters. The x-ray energies are extracted with the help of moving window deconvolution algorithm [193] implemented in a firmware of digitizer cards. This setup provided the x-ray energy resolution of 3.2 keV FWHM at 13 keV.

Fig. 4.2 (b) shows a typical x-ray spectrum observed by a SiPIN diode when the electron beam energy is tuned to the DR resonance. The peak at 13 keV corresponds to the x rays produced by RR into the $n = 2$ shell and *KLL* DR processes. Since SiPIN diodes have poor energy resolution compared to germanium detectors, the x
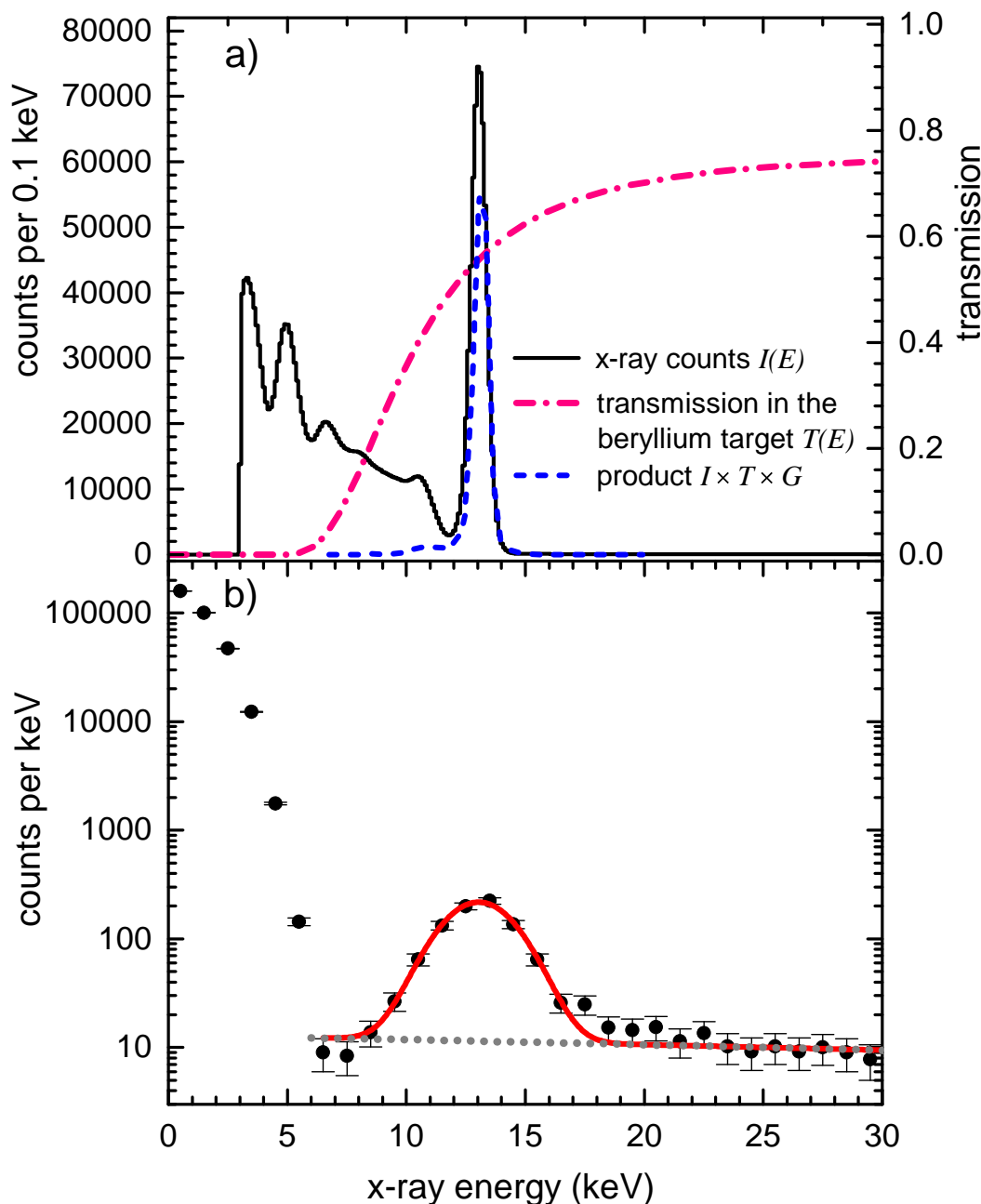
Figure 4.2: (a) An x-ray spectrum $I(E)$ recorded with the germanium detector (solid line). The dash-dotted line is the energy dependent x-ray transmission probability $T(E)$ through the 10 mm thick beryllium scattering target. The dashed line is the product of the both previous functions and the response function $G(E)$ of the SiPIN diode to 13 keV x rays: $G(E) = \exp\left(-4\ln 2\left(\frac{E-13\ \text{keV}}{3.2\ \text{keV}}\right)^2\right)$. (b) A typical x-ray energy spectrum observed by a SiPIN diode when the electron beam energy is tuned to a DR resonance. The solid curve represents the fitted DR peak having the profile of $G(E)$ and the background is shown as the dashed line.
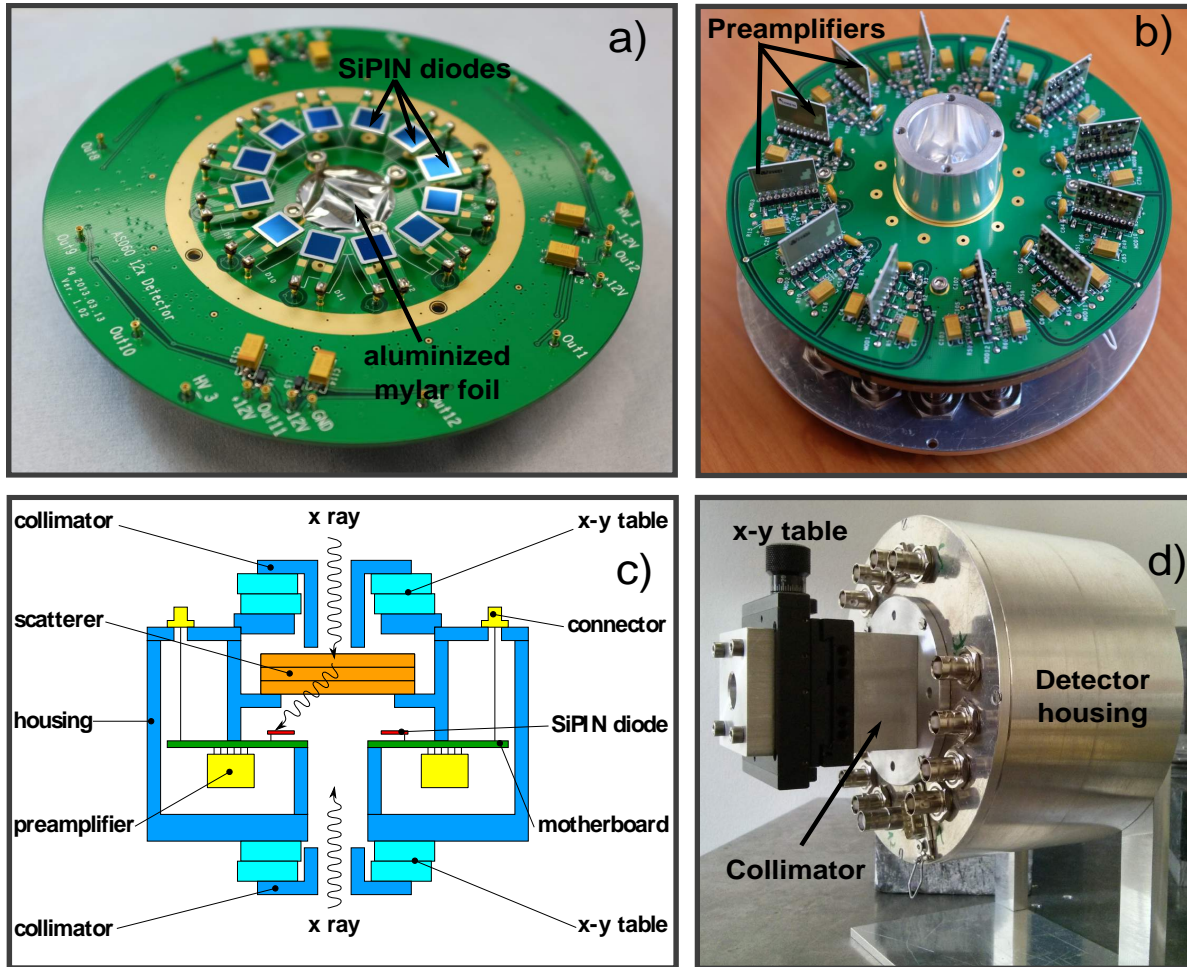
Figure 4.3: (a) Top side: SiPIN diodes mounted on printed circuit board (PCB). Thin aluminized Mylar foil is used to protect SiPIN diodes from the stray radiation. (b) Bottom side: Mounted preamplifiers on the back side of the PCB. (c) Cross-section of the polarimeter (from [192]). (d) Assembled polarimeter with mounted x-y table and the collimator. The x-y table helps to align the collimator in the center of the scattering target.

rays due to RR into the $n = 3$ shell and bremsstrahlung x rays also contribute to the observed intensity. Very high count rate feature below 6 keV is due to electronic noise. Furthermore, the detector housing protect SiPIN diodes from the unwanted ambient x rays. In addition, the diodes are also protected from stray light by thin aluminized Mylar foils.

4.2   Data analysis

The total number of x rays detected within the outlined window in the upper panel (a) of Fig. 4.4 is shown in the lower panel (b) of the same figure as a function of the electron beam energy. Since the energy spread of the electrons follow normal distribution and natural width of excited state is much smaller than the energy spread, each DR resonance can be described by a Gaussian centered around the resonant energy [99, 194]. Thus, all observed *KLL* DR resonances are fitted with a set of Gaussian functions. In the fitting procedure, the centroids and the amplitudes of the resonances are treated as free parameters while their widths are fixed to the experimental electron beam energy resolution of 21 eV.

The observed resonances were identified with the help of theoretical calculations performed with FAC code [158]. The details of calculations are described in Sec. 2.3. The resonances are labeled according to the initial charge state of the ion (before the capture of the electron) followed by a number. Similar nomenclature was used in earlier studies [110, 124, 141, 195]. The configurations of initial states responsible in formation of intermediate excited state (DR resonances) and radiative decay of these excited states to the many final states are given in standard atomic notations, see Table 4.2. The electron beam energy was calibrated using He1 and C1 resonances, having theoretical resonance energies of 8820.6 eV and 9430.5 eV, respectively. An overall very good quantitative agreement between the resonance energies obtained with FAC and the measured spectrum allows for identification of other DR resonances. We measured the linear polarization of x rays produced by the well-resolved He2, Li1, Be2, Be3, and B1 – DR resonances as well as by the RR process. It is known from the theory that the x rays produced by the He2 resonance are unpolarized; we used this resonance to control possible systematic effects in our experiment.

In the Compton polarimetry technique, the linear polarization of the x rays is determined by the angular distribution of the Compton-scattered x rays. This distribution
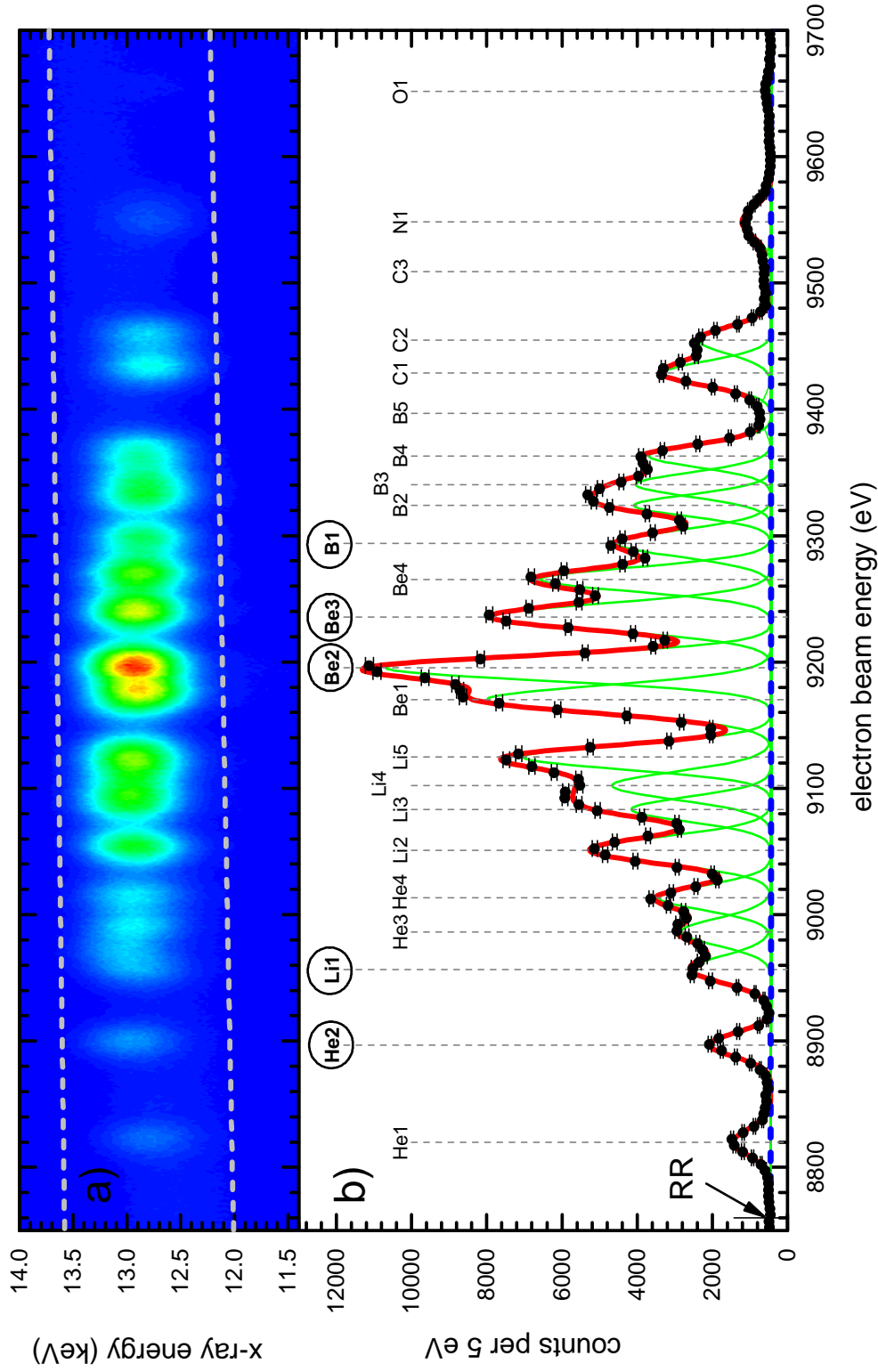
Figure 4.4: (a) Intensity of x rays recorded by the germanium detector as a function of the x-ray and the electron beam energies. The dashed lines represent a region of RR (n=2) and the *KLL* DR resonances. (b) Intensity of the x rays within the outlined energy window as a function of the electron beam energy. The blue dashed line represents the RR background, the thin green solid lines correspond to the fits of the individual *KLL* DR resonances, and the thick red solid line represents the cumulative fit of the spectrum. The resonances are labeled by their initial charge state followed by a number. The x-ray polarization was measured for the resonances marked by circles. The configuration states of these resonances are given in Table 4.2.
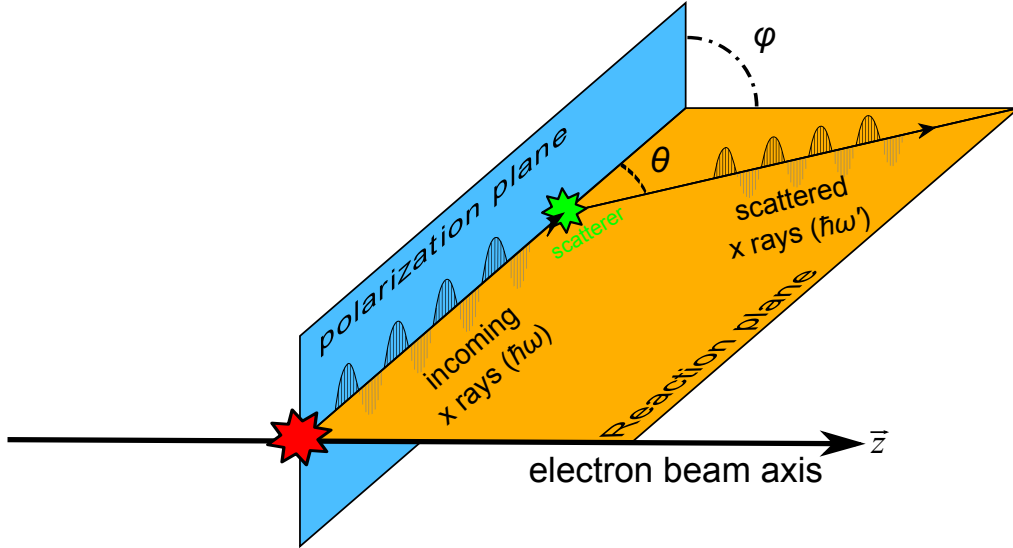
Figure 4.5: Geometry of Compton scattering. The scattered x-ray direction is defined by the polar angle θ and the azimuthal scattering angle φ. The polarization plane contain incident electric field vector of the polarized x-ray. The reaction plane is defined by the electron beam and the x-ray propagation direction.

can be described by the well known Klein-Nishina formula [45]:

$$\frac{d\sigma}{d\Omega} \propto \frac{\hbar\omega}{\hbar\omega'} + \frac{\hbar\omega'}{\hbar\omega} - \sin^2\theta - P\sin^2\theta\,\cos 2(\varphi - \varphi_0), \tag{4.1}$$

where $\hbar\omega$ and $\hbar\omega'$ are the energies of the incoming and the scattered x rays, respectively, and θ and φ are the polar and the azimuthal scattering angles, respectively (see Fig. 4.5). Both the degree of linear polarization P and the angle of linear polarization φ_0 can be determined from this angular distribution.

Here, φ and φ_0 are measured relative to the reaction plane defined by the electron beam and the x-ray propagation directions, see Fig. 4.5. The angle of linear polarization φ_0 vanishes, since the geometry of the radiative collision process is symmetric with respect to the reaction plane. In such case, the degree of linear polarization P is identical to the first Stokes parameter $P = (I_\parallel - I_\perp)/(I_\parallel + I_\perp)$, where $I_\parallel$ and $I_\perp$ are the intensities of x rays polarized within the reaction plane and perpendicular to it.

The intensities of the scattered DR x rays recorded by different SiPIN diodes are extracted by fitting the corresponding x-ray spectra with Gaussian functions together with the background approximated by a linear function, see Fig. 4.2 (b). In the fitting procedure, all parameters including the line intensity, width and centroid as well as the offset and the slope of the background are set as free. The intensities of the scattered DR x rays are extracted from the fits. Fig. 4.6 shows intensities of the scattered DR x rays

as a function of the azimuthal scattering angle φ. The intensity modulation is clearly observable, which indicates the linear polarization of the incoming x rays. According to Eq. (4.1), the intensity modulation was fitted with the function:

$$I(\varphi) \propto 1 - P\,M\cos 2(\varphi - \varphi_0). \tag{4.2}$$

Due to symmetry arguments, the angle φ_0 should vanish. However, we use it in the fitting procedure to account for a possible misalignment of the EBIT and polarimeter axes. The factor M represents the intensity modulation produced by a beam of 100 % polarized x rays. It was obtained by Monte-Carlo simulations using the GEANT4 toolkit [196, 197] together with the Livermore low-energy electromagnetic model for the scattering processes [198]. The GEANT4 simulations take Compton scattering, Rayleigh scattering, photoelectric effect, electron scattering, and bremsstrahlung into account. The dimensions of the collimator, the scatterer and the SiPIN diodes are also taken into account. The simulation results confirm the azimuthal scattering distribution of 13 keV x rays with a form of Eq. (4.2). The modulation factor found to be $M = 0.374$. The GEANT4 simulations are discussed in details, follow Ref. [192].

As previously discussed, SiPIN diode has a low energy resolution compared to germanium detector. Therefore, the contribution of bremsstrahlung and RR into $n = 2, 3$ shells cannot be separated from the x-ray line intensity observed by SiPIN diodes. Consequently, bremsstrahlung contributes to the extracted degree of linear polarization. In order to quantify these contributions, first we have estimated the contributions of bremsstrahlung and RR into $n = 3$ shells to the intensity of the x-ray line observed by the SiPIN diodes. For this, we have used the x-ray spectrum $I(E)$ recorded by the germanium detector where these contributions are clearly separated from the main x-ray line. The germanium x-ray spectrum is multiplied to the beryllium scatterer transmission probability $T(E)$ in order to obtain the spectrum of the x rays impinging on the SiPIN diodes. This $I(E) \times T(E)$ x-ray spectrum is further multiplied by the response function $G(E)$ of the SiPIN diode, which takes the energy resolution of the diode into account. The final $I(E) \times T(E) \times G(E)$ spectrum is shown in Fig. 4.2 (a) by the dashed line. The contributions of bremsstrahlung and RR into $n = 3$ shells to the main x-ray line are visible as a faint feature at energies lower than 11 keV. Both processes together contribute to the x-ray intensity by 1–5 % and hence they were neglected in the analysis.

Since the x rays produced by RR into $n = 2$ shell and by DR process has identical energies, the contribution of RR into $n = 2$ shell to the x-ray line intensity measured by the SiPIN diodes cannot be separated from that of DR. However, the contributions
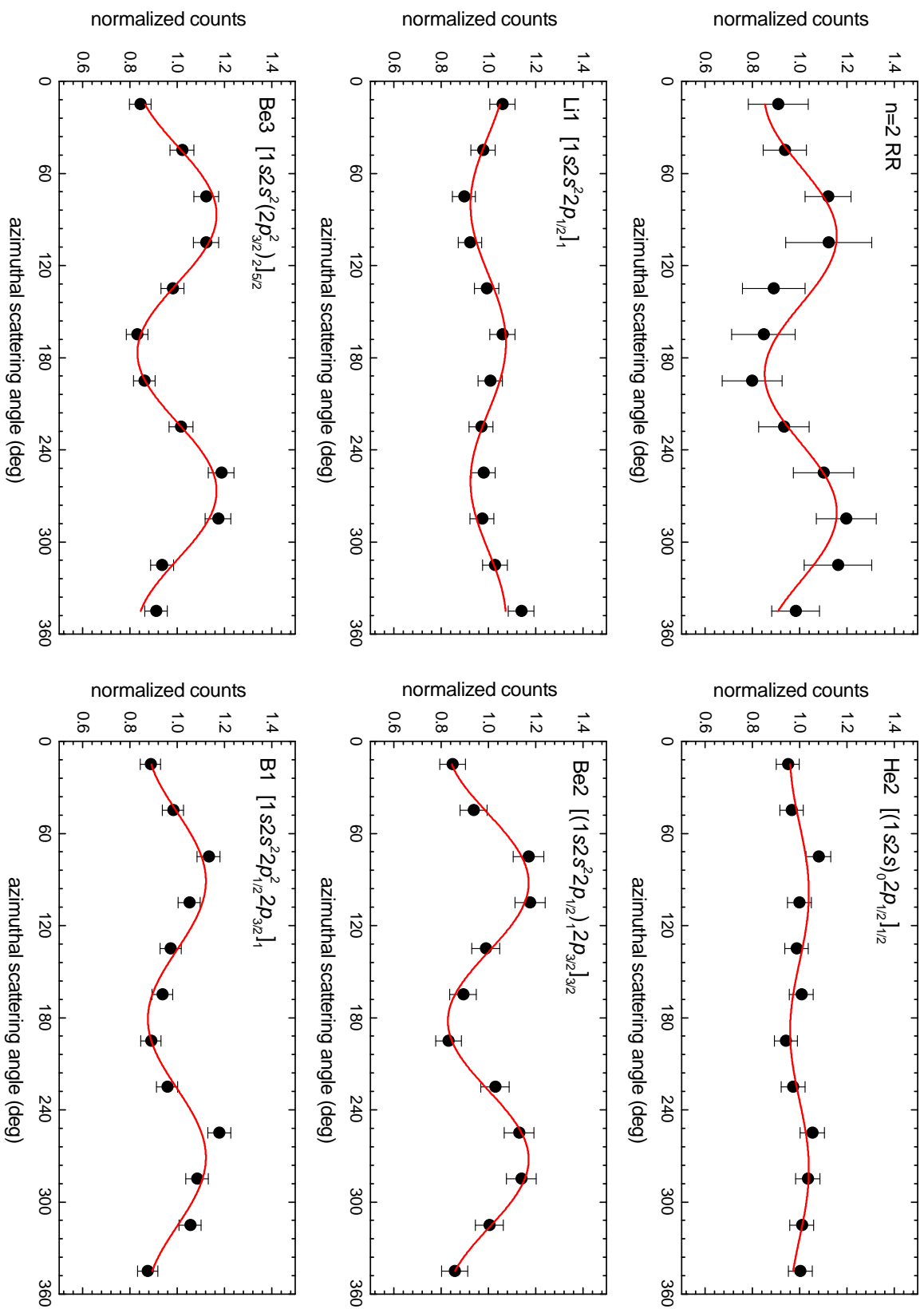
Figure 4.6: Measured azimuthal distributions of the Compton-scattered x rays produced by RR of free electrons into the $n = 2$ shell and due to the KLL DR resonances in krypton ions. The solid lines represent the fits of Eq. (4.2) to these distributions.

can be determined by fitting the observed x-ray intensity as a function of the electron beam energy using Gaussian functions for the DR transitions and a linear baseline for RR, see Fig. 4.4. The x-ray energy produced by RR is equal to the sum of the electron beam energy and binding energy of the recombined state, thus, it can be approximated by a linear function. The contributions of RR (f_{RR}) to the DR resonances He2, Li1, Be2, Be3, and B1 were found to be 22 %, 18 %, 4 %, 6 % and 10 %, respectively. Their values and respective statistical errors corresponding to 1σ are given in Table 4.3.

It follows from Eq. (4.1) and (4.2) the measured degree of polarization P is formed by the polarization of the RR x rays (P_{RR}) and DR x rays (P_{DR}):

$$P = P_{RR}\, f_{RR} + P_{DR}\,(1 - f_{RR}). \tag{4.3}$$

In order to determine the degree of linear polarization of RR x rays, we measured the RR polarization at a fixed electron beam energy of 8760 eV. The degree of linear polarization of RR x rays is extracted from the intensity modulation observed by the SiPIN diodes, and it is found to be $P_{RR} = 0.41 \pm 0.1$. This experimental value was compared with the results of the relativistic distorted–wave calculations performed with FAC for the electrons recombining into $2s_{1/2}$, $2p_{1/2}$, and $2p_{3/2}$ subshells of initially He-like through N-like krypton ions. The calculated RR cross sections and the polarization is presented in appendix C. The theoretical result $P_{RR} \approx 0.59$ does not agree with the experimental value. Since statistics for RR in the present experiment is very low, we have not concluded on any specific reason for such a discrepancy. This discrepancy will be addressed in future experiments.

Using the He2 resonance having the total angular momentum $J_d = 1/2$ and producing unpolarized x rays, we have verified that our experimental setup does not have instrumental asymmetries affecting the polarization measurement. The modulation of the azimuthal angular distribution of the scattered x rays following He2 resonance seen in Fig. 4.6 is due to the admixture of the polarized RR x rays.

Following the data analysis method, the degree of polarization of DR x rays P_{DR} is extracted by deconvoluting the polarization of RR x rays P_{RR} according to Eq. (4.3). The experimental findings are summarized in Table 4.3. The uncertainties in the degrees of KLL DR polarization P_{DR} are caused by the fits of Eq. (4.2) and the errors of f_{RR} and P_{RR}. Moreover, the depolarization effect introduced by the thermal velocity component of the electron beam in the EBIT was estimated [188, 189] and found to be negligibly small compared to the experimental errors. Therefore, no corrections are made.

Table 4.2: Initial, intermediate (excited) and final states are represented in standard atomic configuration notations. Each configuration in the table are in j–j coupling notation, where the round brackets stand for the angular momentum of coupled subshells and subscripts after the square brackets denote the total angular momentum of the given state. The radiative decay rates A_r^{df} (in s^{-1}) are calculated within electric dipole approximation using FAC code. In the last column, values in round bracket refer to the power of 10.

Label	Initial state	Excited state	Final states	A_r^{df}
He2	$[1s^2]_0$	$[(1s2s)_0 2p_{1/2}]_{1/2}$	$[1s^2 2s]_{1/2}$	8.18(14)
Li1	$[1s^2 2s]_{1/2}$	$[1s2s^2 2p_{1/2}]_1$	$[1s^2 2s^2]_0$	3.62(14)
			$[1s^2 2p_{1/2}^2]_0$	1.31(13)
			$[(1s^2 2p_{1/2})_{1/2} 2p_{3/2}]_1$	3.83(12)
			$[(1s^2 2p_{1/2})_{1/2} 2p_{3/2}]_2$	9.99(12)
Be2	$[1s^2 2s^2]_0$	$[(1s2s^2 2p_{1/2})_1 2p_{3/2}]_{3/2}$	$[1s^2 2s^2 2p_{1/2}]_{1/2}$	1.24(15)
			$[1s^2 2s^2 2p_{3/2}]_{3/2}$	2.95(14)
			$[1s^2 2p_{1/2}^2 2p_{3/2}]_{3/2}$	3.87(12)
			$[(1s^2 2p_{1/2})_{1/2} (2p_{3/2}^2)_2]_{3/2}$	3.29(12)
			$[(1s^2 2p_{1/2})_{1/2} (2p_{3/2}^2)_2]_{5/2}$	9.73(12)
			$[(1s^2 2p_{1/2})_{1/2} (2p_{3/2}^2)_0]_{1/2}$	3.37(12)
Be3	$[1s^2 2s^2]_0$	$[1s2s^2 (2p_{3/2}^2)_2]_{5/2}$	$[1s^2 2s^2 2p_{3/2}]_{3/2}$	5.40(14)
			$[1s^2 2p_{1/2}^2 2p_{3/2}]_{3/2}$	3.39(11)
			$[(1s^2 2p_{1/2})_{1/2} (2p_{3/2}^2)_2]_{3/2}$	8.71(12)
			$[(1s^2 2p_{1/2})_{1/2} (2p_{3/2}^2)_2]_{5/2}$	1.19(13)
			$[1s^2 (2p_{3/2}^3)_{3/2}]_{3/2}$	1.20(12)
B1	$[1s^2 2s^2 2p_{1/2}]_{1/2}$	$[1s2s^2 2p_{1/2}^2 2p_{3/2}]_1$	$[1s^2 2s^2 (2p_{1/2}^2)_0]_0$	1.21(15)
			$[1s^2 2s^2 2p_{1/2} 2p_{3/2}]_1$	1.20(14)
			$[1s^2 2s^2 2p_{1/2} 2p_{3/2}]_2$	5.30(14)
			$[1s^2 2s^2 (2p_{3/2}^2)_2]_2$	4.49(12)
			$[1s^2 2p_{1/2}^2 (2p_{3/2}^2)_2]_2$	8.43(12)
			$[1s^2 2p_{1/2}^2 (2p_{3/2}^2)_0]_0$	2.14(12)

4.3 Results and Discussion

To compare experimental results, the theoretical values of the degree of linear polarization of DR x rays are computed with the FAC code. As described previously in the theory section 2.2.2, the degree of linear polarization of x rays emitted in DR process depends on the alignment parameter $\mathcal{A}_2$ and the intrinsic anisotropy parameter α_2^{df}. The magnetic sublevel cross sections σ_{M_d} were calculated with the distorted–wave approximation, in order to evaluate the alignment parameter $\mathcal{A}_2$. Besides fully accounting for the Breit interaction in our calculations, we likewise limit our calculation of alignment parameter $\mathcal{A}_2$ to pure Coulomb terms. The calculated values of alignment parameter $\mathcal{A}_2$ is given in Table 4.3. The DR resonance (intermediate excited state) can decay to the final state by several possible close–lying radiative channels (see Fig. 2.4). The dominant $E1$ radiative channels and their decay rates are computed in order to get the "effective" intrinsic anisotropy parameter $\bar{\alpha}_2^{df}$. The radiative decay rates A_r^{df} are given in Table 4.2 as well as the "effective" intrinsic anisotropy parameter $\bar{\alpha}_2^{df}$ in Tab. 4.3. It should be noted that the radiative decay through higher-order multipole channels are found to be a few orders of magnitude less than the dominant $E1$ channels, therefore, their contributions are neglected in the present calculations.

Using the calculated values of $\mathcal{A}_2$ and $\bar{\alpha}_2^{df}$, according to Eq. 2.30, we give the final value of degree of linear polarization of x rays emitted in DR process. The comparison experimental and theoretical polarizations of DR x-ray lines are presented in Table 4.3. The experimental values agree very well with the theoretical values within statistical confidence limits.

The measured degree of linear polarization ranges from -0.84 to 0.46. We have observed that the x rays following the Be2, Be3, and B1 resonances have positive degrees of linear polarization, indicating that they are polarized within the reaction plane. The negative degree of polarization in the case of the Li1 resonance indicates that its x rays are polarized perpendicular to the reaction plane, see Fig. 4.5.

A positive degree of polarization can be expected since the angular momentum of the incoming electron in the target frame is perpendicular to the electron collision axis. This momentum is transferred into the total angular momentum J_d of the intermediate state predominantly populating magnetic sublevels with the least projection M_d. These are the sublevels with $M_d = 0$ for integer J_d and $M_d = \pm\ 1/2$ for half-integer J_d. In such cases, according to Eqs. (2.18) and (2.19), the alignment parameter $\mathcal{A}_2$ is negative. Hence, the degree of linear polarization is positive for the x-ray transitions with $\bar{\alpha}_2^{df} > 0$ following the Be2, Be3 and B1 resonances. On the other hand, in case

of Li1 resonance, the population of the magnetic sublevel with $M_d = 0$ is forbidden in the non-relativistic limit (see Ref. [136]). Therefore, the magnetic sublevels with $M_d = \pm 1$ are predominantly populated. This leads to the positive alignment $\mathcal{A}_2^d$ according to Eqs. (2.18). Consequently, the degree of linear polarization of x rays following Li1 resonance is negative.

It was previously discussed that the Breit interaction between the incident and the target electrons may strongly affect the anisotropy and the polarization of the emitted DR x rays [136, 139, 199]. A large contribution is expected for high-Z, since the Breit interaction occurs as a relativistic correction to the Coulomb repulsion. We found a rather strong contribution of the Breit interaction to the degree of linear polarization of DR x rays in krypton, which is significantly lighter than previously studied elements [93, 141, 195].

We found that the Breit interaction changes the value of polarization in the case of the Li1 and B1 resonances, while no change was noticed in the case of the Be2 and Be3 resonances. In brief, the latter case of Be2 and Be3 resonance can be explained by the fact that the electron–electron interaction operator V is scalar. Since it is a scalar, according to Eqs. (2.7), (2.15) and (2.16), V cannot affect the magnetic sublevel population of the excited ion if only one partial wave of the free electron is allowed in the resonant capture process. On the other hand, two partial waves are allowed in the resonant capture process forming Li1 and B1 resonances. In such cases, both the alignment parameters and the polarization of the characteristic radiation is governed by the interference between the different allowed partial waves of a free electron. This interference depends on the free–bound transition matrix elements. Hence, it also depends on the details of the electron–electron interaction [200, 201]. The influence of the Breit interaction on resonant capture process is discussed more in details in the following Chapter 5.3.3.

The Breit interaction decreases the alignment parameter $\mathcal{A}_2$ of B1 resonance by 1 % and of Li1 resonance by 9 %. The latter means that in the case of the Li1 resonance the population of the $M_d=0$ sublevels is increased due to the Breit interaction by a factor of 30, which is remarkable for a middle-Z element like krypton. This noticeable change in the population of the magnetic sublevels leads to a 13 % decrease in the degree of linear polarization of x rays produced by Li1 resonance. Although, this represents a small contribution of the Breit interaction as compared to the previously measured contributions in heavy elements [93, 195], this experiment is nonetheless precise enough to validate full-order theoretical calculations including the Breit interaction, and to rule out by 2σ calculations that treat the electron–electron interaction purely by the Coulomb repulsion. This precision is certainly a consequence of our experimental technique to

Table 4.3: The measured degree of polarization of x-ray transitions following five DR resonances is listed. These DR resonances with the centroid energies E_e are labeled by a number and identified by the intermediate excited states. The factors f_{RR} denote the amount of the RR background admixed to the DR x rays. Experimental uncertainties are given as 1σ. The alignment parameters $\mathcal{A}_2$, the intrinsic anisotropy parameters $\bar{\alpha}_2^{df}$ and the degrees of x-ray polarization P_{DR}(theory) are calculated with FAC. The theoretical results are given for the case of the Coulomb-only electron–electron interaction (C) and for the case of the full inter-electronic interaction with the Breit term included (C+B).

Label	Excited state	E_e (eV)	f_{RR}	P_{DR}(exp)	$\bar{\alpha}_2^{df}$	$\mathcal{A}_2$		P_{DR}(theory)	
						C	C+B	C	C+B
He2	$[(1s2s)_0 2p_{1/2}]_{1/2}$	8899.5	0.22 ± 0.01	0.02 ± 0.05	0.00	0.00	0.00	0.00	0.00
Li1	$[1s2s^2 2p_{1/2}]_1$	8954.0	0.18 ± 0.01	-0.84 ± 0.05	0.68	0.70	0.64	-0.95	-0.84
Be2	$[(1s2s^2 2p_{1/2})_1 2p_{3/2}]_{3/2}$	9197.8	0.04 ± 0.002	0.45 ± 0.04	0.32	-1.00	-1.00	0.42	0.42
Be3	$[1s2s^2 (2p_{3/2}^2)_2]_{5/2}$	9239.2	0.06 ± 0.003	0.46 ± 0.04	0.36	-1.07	-1.07	0.48	0.48
B1	$[1s2s^2 2p_{1/2}^2 2p_{3/2}]_1$	9296.8	0.10 ± 0.005	0.33 ± 0.06	0.46	-0.69	-0.68	0.41	0.40

measure the polarization of DR x rays with the help of novel Compton polarimeter.

4.4 Summary

In this work, we have studied theoretically and experimentally the polarization properties of dielectronic recombination lines in K-shell x-ray spectra of highly charge krypton ions. The degree of linear polarization of KLL DR x rays was measured with the Compton polarimetry technique. The experimental results are in excellent agreement with the theoretical calculations of FAC code. The contribution of the Breit interaction was precisely examined for mid-Z krypton. The Breit interaction contribution to electron–electron interaction was demonstrated to change the degree of linear polarization for the resonance state of Li-like krypton. The obtained data also benchmark the flexible atomic code for the x-ray polarization calculations for the mid-Z element. This experimental technique opens a window to look into the angular distribution and polarization properties of x rays emitted in atomic collisions, which are important for diagnostics of hot astrophysical and laboratory plasmas, such as those of International Thermonuclear Experimental Reactor ($ITER$).

Chapter 5

X-ray emission asymmetries in resonant recombination transitions

The polarization of dielectronic recombination transitions was measured at the electron beam ion trap with the help of a novel Compton polarimeter, discussed in the Chapter 4. The degree of linear polarization of x rays due to five DR resonance as well as due to RR of electrons into the $n = 2$ shell of highly charged krypton was measured in the experiment. This experiment had few limitations. Namely, the optimization for higher photon count rates led to a poor electron beam energy resolution, thereby, restricting the measurement only to "well-resolved" resonances. Even due to that the higher-order recombination resonances were not seen in the experiment. Furthermore, for each resonance, the data accumulation time for polarization was quite long. The need of laboratory data was clearly expressed in Sec. 1.3, which demands a fast and effective technique allowing the systematic investigation of polarization of dominant resonant recombination channels. This is necessary to develop reliable models for plasma polarization diagnostics. We know that the polarization and anisotropy, both properties of the emitted radiation are equivalent, within the electric dipole approximation [136] since they both are caused by a nonstatistical population of the magnetic sublevels in collisionally excited states. Therefore, the polarization properties of x rays produced in resonant recombination processes can be probed by measuring the angular distribution of these x rays.

In this chapter, we present the first systematic measurement of the x-ray angular distribution in the inter-shell dielectronic recombination (DR), trielectronic recombination (TR) and quadroelectronic recombination (QR) into highly charged iron and krypton
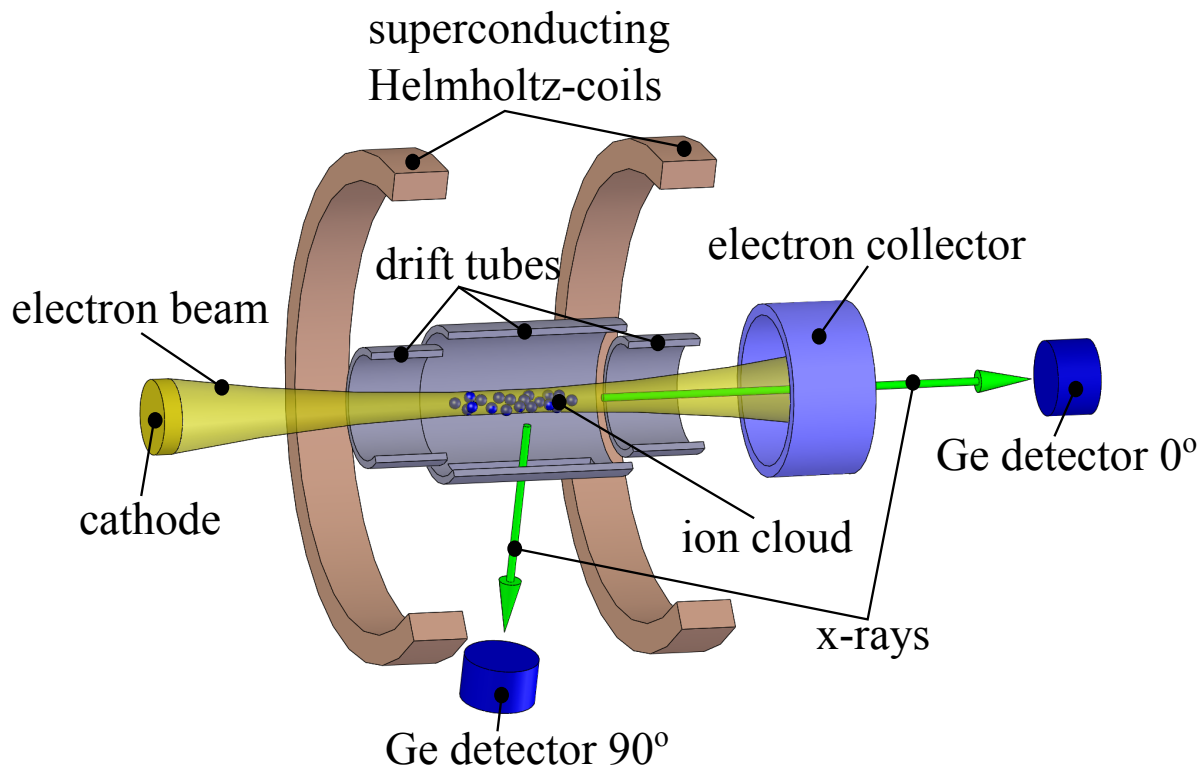
Figure 5.1: The experimental setup: the highly charged iron and krypton ions were produced and trapped within the intense monoenergetic and unidirectional electron beam. The energy of the electrons was tuned into the recombination resonances and the emitted x rays were observed by two identical germanium detectors placed at $0°$ and $90°$ with respect to electron beam propagation axis.

ions. An excellent electron energy resolution was achieved compared to the previous experiment. This allowed us to resolve a large number of DR, TR, and QR resonances. The x rays emitted in the decay of intermediate excited states were simultaneously observed by two germanium detectors aligned along and perpendicular to the electron beam propagation direction. The intensities of K-shell x-ray transitions from both detectors were recorded as a function of the electron beam energy. The degree of linear polarization was extracted from the measured x-ray emission asymmetries. Moreover, the polarization properties of hitherto neglected weaker processes such as TR and QR were measured for the first time.

The first section 5.1 describes the experimental technique, data analysis method and results of the experimental investigation involved highly charged iron ions. The second section 5.2 describes the same for the experiment with highly charged krypton ions. Finally, in section 5.3, the results of both experiments are discussed in details.

5.1 X-ray emission asymmetries: Resonant recombination of Fe$^{18+...24+}$

5.1.1 Experiment

The experiment was performed at the FLASH-EBIT [181] with trapped ions in the He-like through O-like iron ions produced by successive electron impact ionization. The experimental arrangement is shown in Fig. 5.1. The high magnetic field of 6 T at the trap center compresses the monoenergetic electron beam to a radius of ≈ 24.4 μm. Ions are trapped radially by its negative space charge, and axially by electrostatic potentials applied to the drift tubes. In the present experiment, iron was continuously being injected into the trap as a molecular compound (Fe(CO)$_5$ – iron pentacarbonyl), via the differential pumping system. The pressure at the injection and the trap was 1.1×10^{-7} mbar and 1.5×10^{-10} mbar, respectively. Overall, FLASH-EBIT was operated under ultrahigh vacuum conditions ($P \leq 5 \times 10^{-10}$ mbar) during the experiment.

For steady-state conditions [191], electron-ion collision energy was swept over the range of DR, TR, and QR resonance exciting K-shell electrons for iron ions. The electron beam energy was continuously scanned from 4.5 keV to 5.2 keV with the rate of 1.16 eV/s in a triangular shape wave function. The experimental parameters were optimized for two criteria as following:

(a) A deeper trap with a higher density of ions in highly charged state ions (He-, Li-like ions): For this purpose, the deeper axial trap was used with 100 mA of the electron beam current. The ion trap was dumped repeatedly for a second in every 20 seconds, therefore, greater density of higher charge states can be achieved by storing ions for a longer time. Considering the higher beam current with deeper trap setting, we bring about electron-ion collision energy resolution of 11 keV FWHM at 5 keV.

(b) For observation of the weak and blended higher-order resonances, high collision energy resolution is required. Therefore, in this case, we improved energy resolution by evaporative cooling technique [202] in combination with a moderate electron beam current (70 mA here) sufficient for an efficient ionization and recombination yield. This was comprehended by lowering the axial potential well applied to the drift tubes. Additionally, the ion dump frequency was increased (every 5 sec) to reduce accumulation of higher charge state ions as well as unwanted heavy ionic species like tungsten and barium from the electron gun. The intensity of x rays was recorded as a function of the time after the ion dump. The Fig. 5.3 shows that the higher charge states take more time to breed compared to lower charge states. With this method, the finest collision

Table 5.1: Operational parameters of the FLASH-EBIT in the present experiment. (a) and (b) corresponds to two different measurements.

Parameter	Value
Electron beam current	(a) 100 mA (b) 70 mA
Magnetic field	6 T
Trap offset potential	(a) 110 V (b) 20 V
Scan energy	4.2keV - 5.2 keV
Sweep rate	1.16 eV/s
Beam radius	$\approx 24.4\ \mu$m
Trap length	50 mm
Dump cycle	(a) 20 s (b) 5 s
Pressure of gas injector	(a) 1.2×10^{-6} mbar
	(b) 1.1×10^{-7} mbar

energy resolution of 6 keV FWHM at 5 keV was achieved. We note that the resolution in this energy range was higher than any previously reported and allowed to distinguish a well-resolved TR and QR along with DR resonances. A list of operational parameters of the FLASH-EBIT is summarized in Table 5.1.

To observe the angular distribution, the radiative decay of intermediate excited states have been simultaneously observed by two identical germanium detectors aligned parallel (0°) and perpendicular (90°) to the electron beam propagation axis, see Fig. 5.1. Both detectors have an intrinsic x-ray energy resolution of approximately 550 eV FWHM at 13 keV. The x-ray detection at EBIT is typically done perpendicular to the electron beam propagation axis. For this experiment, a beryllium window was installed at the electron beam collector chamber to observe x rays along the electron beam propagation axis. However, at this observation point, the solid angle and the x-ray flux are significantly reduced compared to detector perpendicular to the electron beam propagation axis. The solid angle was 0.0087 sr for detector at 90°, whereas the solid angle for x-ray detection along the electron beam was 0.00073 sr. Hence, the detector at 0° covered 11.9 times smaller solid angle compared to the detector at 90°.

A typical two-dimensional histogram of the electron-ion recombination processes observed in the *KLL* region is shown in Fig. 5.2. The x-ray energy was calibrated using radioisotopes, whereas the electron beam energy was calibrated using theoretical resonance energies. The visible bright spots are *KLL* resonances in He-like to O-like iron ions. Each resonance is identified by the initial charge state of iron in which resonant recombination occurred. The radiative recombination (RR) into the $n = 2$ shell is visible in the background of Fig. 5.2. It has a diagonal shape since it is the sum of the electron energy and the binding energy of the *L*-shell. The lower background is due to radiative
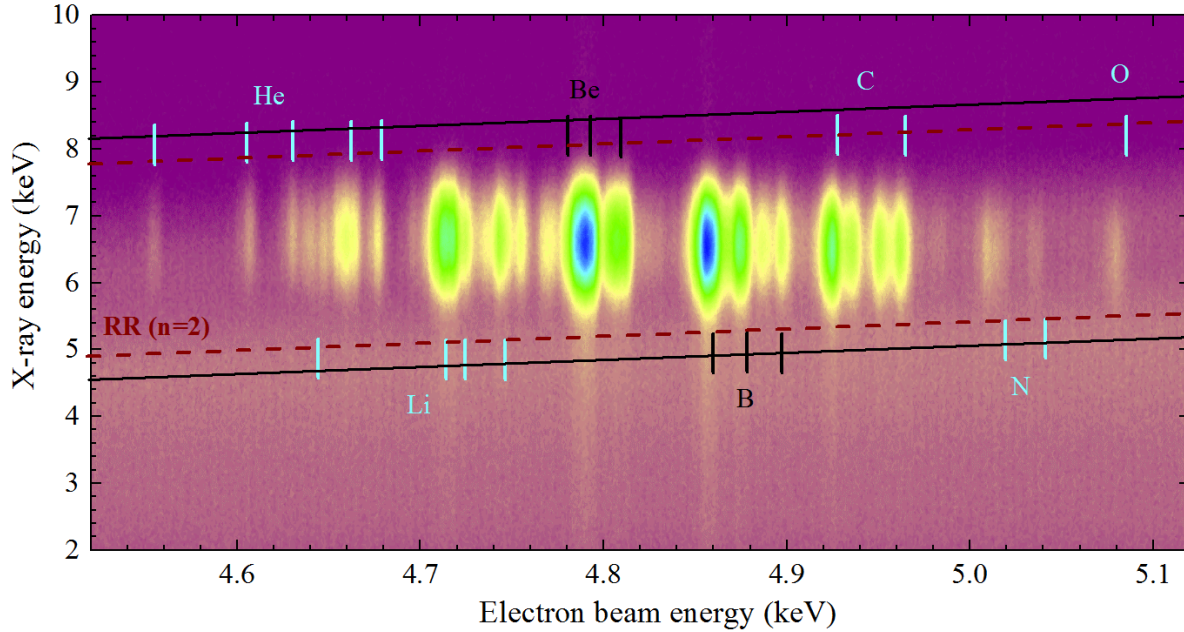
Figure 5.2: Scatter plot of x-ray intensity as functions of x-ray and electron beam energy. The solid lines delimit the region of interest for the horizontal projection. The dashed lines delimit the constant background of RR. Each bright spot is *KLL* DR resonance identified by the charge state of the initial ion. The x-ray intensity shown here is from the detector at 90°.
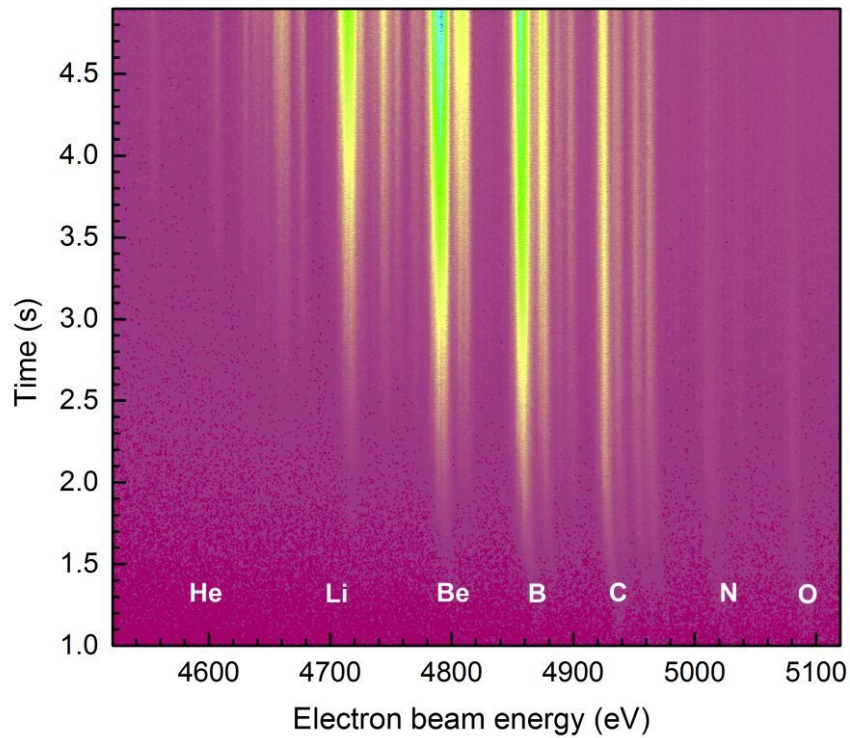
Figure 5.3: Evolution of the iron *KLL* recombination resonances in dependence of the dump cycle time.

recombination into other heavy elements present in the trap, like barium or tungsten. The observed x rays from the detector at 90° is shown in Fig. 5.2, a similar histogram was obtained for the detector at 0°.

5.1.2 Data analysis

The x-ray intensity as a function of electron beam energy was obtained by setting a cut in the data (illustrated by black solid lines in Fig. 5.2), which selects the events in the region of interest, shown in the middle panel of Fig. 5.4. Several x-ray resonance transitions were observed in this region of interest (See Fig. 5.4). The x-ray resonant transitions were identified by extensive and detailed calculations using the FAC code [158]. Full–order configuration interaction and mixing between the states are taken into account in order to identify TR and QR resonances. The corresponding theoretical resonant strength is also calculated to quantify the relative weight that each excited state contributes to the x-ray line. Several DR, TR and QR transitions were well resolved.

The electron beam energy is described by the sum of all accelerating potentials, including the scanning voltage, together with the space charge potential of the electron beam. The energy dependent part of the space charge potential was calculated at maximum and minimum acceleration potentials and can be considered to be constant along the energy scan [191]. Thus, the electron beam energy scale is calibrated using theoretical resonance energy. The electron beam energy scale of measurement (a) in Fig. 5.4 was calibrated using x-ray lines 1 and 8, corresponding to energies of 4554.4 eV and 4697.8 eV, respectively. Similarly, for measurement (b), the x-ray lines 20 (4858.9 eV) and 31 (4952.2 eV) were employed.

The observed spectra were corrected for the detector's solid angles and the background arising from radiative recombination. The background dominated by RR was fitted with a linear function and subtracted from the DR intensity. The detector's solid angle factor can be corrected using theoretically known isotropic DR transition. For the measurement (a), we selected the DR resonance $[1s2s^2]_{1/2}$ (line 1) formed by initial He-like ions to obtain the solid angle correction factor. It was found to be $\Omega_{0°}/\Omega_{90°} = 0.09 \pm 0.02$. Whereas in measurement (B), the observed isotropic transitions have very low statistics. Hence, we corrected detector solid angle using the TR resonance $[(1s2s^2 2p_{1/2})_0 2p_{3/2}^3]_{3/2}$ (line 31) formed by initial C-like ions. This resonance has the theoretical resonance strength ratio of $S(0°)/S(90°) = 1.55$. We selected this transition for its relative high resonance strength and null influence of the Breit interaction on its angular distribution [131]. For this case, the measured solid angle correction
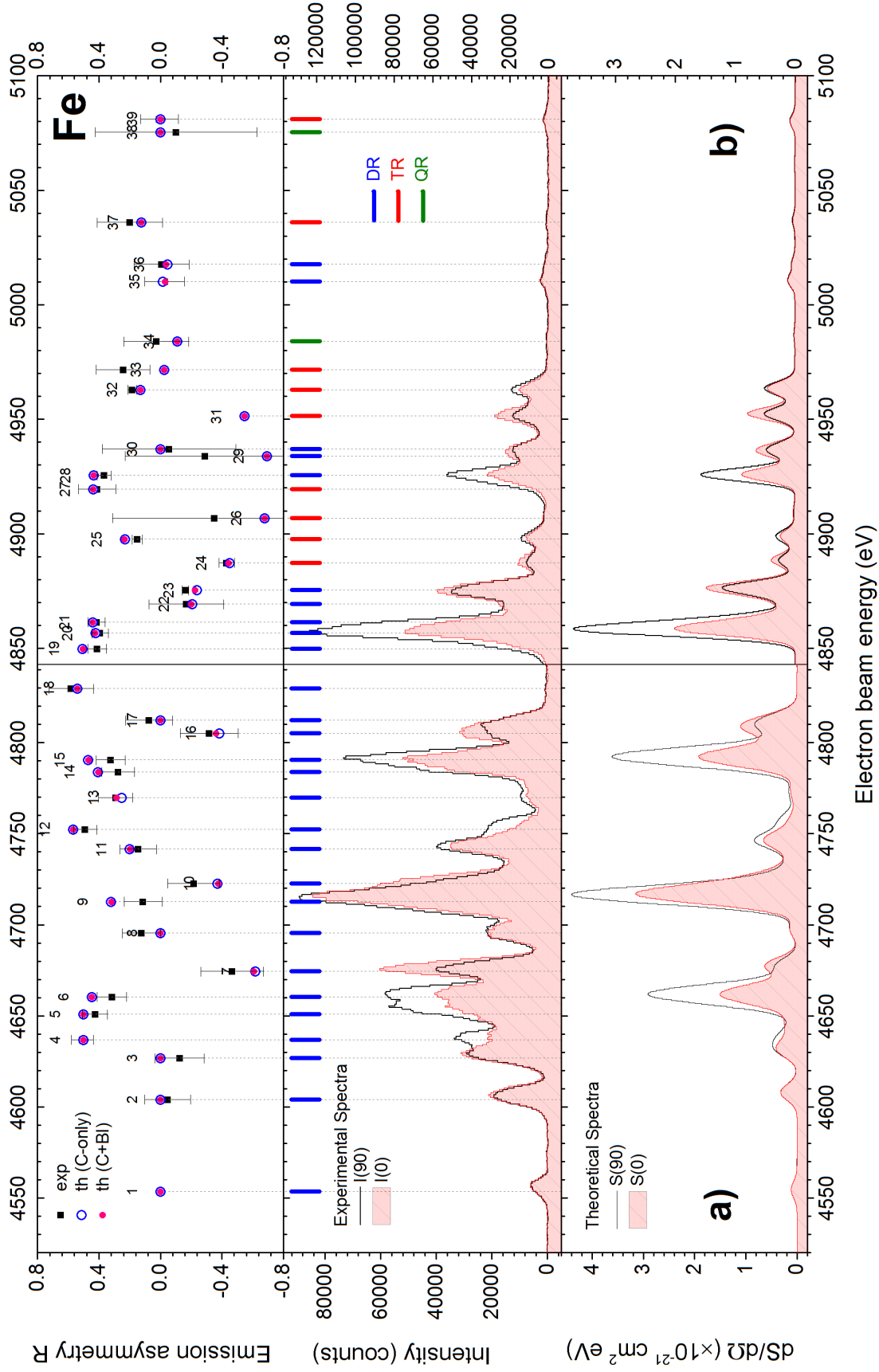
Figure 5.4: **Top panel** shows the extracted emission asymmetries $\mathcal{R}$ (black squares) for the individual resonances and the corresponding predictions with (magenta circles) and without Breit interaction (open blue circles). **Middle panel** shows the x-ray intensity registered by the two germanium detector plotted as a function of electron beam energy. Each line is identified by one or more excited state formed by a given charge state and process in Table 5.2. Vertical markers – Blue: DR, Red: TR and Green: QR. **Bottom panel** shows differential resonance strength ($dS/d\Omega$) as a function of electron beam energy. The black solid lines and the filled light red areas correspond respectively to the x rays observed along and perpendicular the electron beam in both middles and bottom panels. The labels (a) and (b) correspond to the two different measurement schemes.

factor was found to be $\Omega_{0°}/\Omega_{90°} = 0.08 \pm 0.003$. In both cases, the used normalization resonances were well separated from the neighboring transitions.

Each resonance in the spectrum can be described by a Gaussian centered around the resonant energy E_{res}. The amplitude of each resonance is obtained by fitting them with Gaussian functions. This can be done because the energy spread of the electron follows a normal distribution [99, 194] and the natural width of the excited state is much lower than energy spread. Since the fine-structure splitting scales with Z^4, resonances in lower-Z elements are less isolated. Thus, the selected energy region in the iron spectra contain high density of the excited states. For this reason, we make the following criteria, to avoid possible interference effects between two excited states in the fitting procedure. (1) We consider only excited states in the fitting procedure where the resonance energy difference between them is more than half the collision energy resolution – for measurement (a) 5 eV and (b) 3 eV. Otherwise, blended lines were fitted with a single Gaussian function. (2) The excited states with relative resonance strengths less than $\approx 5\%$ were not taken into the fit.

Applying these criteria, the amplitudes and centroids corresponding to each resonance were fitted to the spectrum observed by the detector placed perpendicular to the electron beam propagation direction. Referring to the higher solid angle covered by this detector, the spectrum at 90° had significantly higher statistics. In the first step of the fitting procedure, the widths of all resonances were fixed to the measured electron energy resolution and their corresponding energy distributions were taken to be Gaussians. In the second step, the similar procedure was performed for the spectrum observed along the electron beam propagation direction. Here, the line centroids were fixed to the ones received in the previous step, then extracted intensities were corrected for detector's solid angle factor. It should be noted that very large level of statistics allowed to reliably extract the centroids and the intensities of even blended strong resonance lines.

5.1.3 Results

The number of DR, TR, and QR resonances are prominent in the spectra. The line centroids extracted from the fitting procedure are in an excellent agreement with the resonance energies obtained with the FAC code. From Fig. 5.4, it is apparent that the intensities of most of the observed resonant transitions differ when it is observed along and perpendicular to the electron beam axis. This indicates that the x-ray emission from resonant transitions is anisotropic. We quantify the emission asymmetries by taking the

ratios:

$$\mathcal{R} \equiv \frac{I(90°) - I(0°)}{I(90°)}. \tag{5.1}$$

Following the data analysis method, the emission asymmetries $\mathcal{R}$ is extracted for each fitted recombination transition. The experimental values of $\mathcal{R}$ are summarized in the Table 5.2 as well as in the top panels of Fig. 5.4. The uncertainties in the emission asymmetries are taken as a quadrature sum of the errors arose from the fitting procedure and errors due to solid angle corrections.

Comparison with the theory:

As described in the theoretical section 2.2, the x-ray emission asymmetries and polarization result from the nonstatistical population of magnetic sublevels in the intermediate excited states. The angular distribution of x rays following aligned excited state of the ion is given by Eq. (2.24). Since all the radiative transitions observed at 90° and 0° with respect to the electron beam propagation axis and they are of electric dipole ($E1$) character, the angular distribution coefficients can be given as:

$$W(90°) = 1 - \frac{1}{2}\bar{\alpha}_2^{df}\mathcal{A}_2, \tag{5.2}$$

and

$$W(0°) = 1 + \bar{\alpha}_2^{df}\mathcal{A}_2. \tag{5.3}$$

where $\mathcal{A}_2$ is the alignment parameter and $\bar{\alpha}_2$ is the "effective" intrinsic anisotropy parameter, see Eq. (2.30).

Using Eqs. (5.2) and (5.3) into Eq. (5.1), the product $\alpha_2^{df}\mathcal{A}_2$ (sometime it is referred as the anisotropy parameter β [46, 94, 139, 203]) is given by:

$$\alpha_2^{df}\mathcal{A}_2 = -\frac{2\mathcal{R}}{3 - \mathcal{R}}. \tag{5.4}$$

The same product of parameters $\mathcal{A}_2\bar{\alpha}_2^{df}$ also defines the x-ray polarization. Within the leading $E1$ approximation the degree of linear polarization of x rays, emitted at the angle θ with respect to the incoming electron propagation direction can be expressed as:

$$P(\theta) \equiv \frac{I_\| - I_\perp}{I_\| + I_\perp} = \frac{3\mathcal{A}_2\bar{\alpha}_2^{df}\sin^2\theta}{\mathcal{A}_2\bar{\alpha}_2^{df}(1 - 3\cos^2\theta) - 2} = \frac{\mathcal{R}\sin^2\theta}{1 + \mathcal{R}\cos^2\theta}, \tag{5.5}$$

where $I_\|$ and $I_\perp$ are the intensities of the x rays polarized along and perpendicular to the plane defined by the collision and x-ray emission axes. This equation indicates that the

linear polarization of characteristic radiation measured in the direction perpendicular to the collision axis coincides — within the electric dipole approximation — with the emission asymmetry: $P(90°) = \mathcal{R}$. Therefore, our angular resolved measurements can provide the degree of linear polarization of the decay x rays.

The experimental emission asymmetries $\mathcal{R}$, i. e., degree of linear polarization is compared with the theoretical calculations of FAC code [158] and RATIP code [160]. The comparison with FAC results is outlined in Table 5.2 as well as in the top panel of Fig. 5.4. The theoretical calculation takes resonance strengths and unresolved radiative decay transitions into account. In the case of the unresolved intermediate excited state (blended resonance), the "weighted" emission asymmetry $\mathcal{R}$ is given to compare with experimental value. It is calculated according to the following formula:

$$\mathcal{R} = \frac{\sum_i S_i^{DR} \mathcal{R}_i}{\sum_i S_i^{DR}}. \tag{5.6}$$

where S^{DR} is the resonance strengths calculated according to Eq. 2.12. The emission asymmetry of line no. 7, 9, and the other in the Table 5.2 are calculated according to this equation.

Synthetic spectra:

Synthetic spectra are calculated with the help of FAC code in order to account all unresolved and weak transitions. For this purpose, all possible DR, TR and QR resonances and their resonance energies and strengths are computed with FAC code for *KLL*–configuration complex (see Sec. 2.3). Moreover, the parameters $\mathcal{A}_2$ and $\bar{\alpha}_2 s^{df}$ are also calculated in order to get the angular correction factors (or degree of linear polarization). The calculated parameters are presented in Appendix A.

The differential resonance strength for each resonance is obtained by multiplying the ionic abundance and the angular correction factors at respective angle 90° and 0°. The normalized ion abundance of each charge state $\mathbf{n}_{CS}$ is obtained by taking the ratio between the observed intensity of "well–separated" resonance formed by particular initial ionic state I_{CS} to the theoretical strength of that resonance S_{CS}. For example, in case of He-like initial ions, the normalized ionic abundance can be expressed by:

$$\mathbf{n}_{He} = \frac{\left[\frac{I_{He}(90°)}{S_{He}(90°)}\right]}{\sum \left[\frac{I_{CS}(90°)}{S_{CS}(90°)}\right]}, \tag{5.7}$$

where CS refers to charge states from He-like to O-like iron ions. Finally, the charge

state normalized differential resonance strengths are obtained for each resonance.

This charge state normalized differential resonance strength $dS/d\Omega$ as line amplitude and the resonance energies E_{res} as line centroids are convoluted with the experimental electron beam energy width to form theoretical Gaussian spectra. The bottom panel of figure 5.4 shows the differential resonance strength $dS/d\Omega$ obtained at both $90°$ and $0°$ as a function of electron beam energy. The qualitative agreement is obtained between the experimental and simulated spectra of FAC code.

Table 5.2: Measured emission asymmetry $\mathcal{R}$ between perpendicular and parallel observation of x rays emitted in the resonant recombination process. The label in the first column identifies the resonances in Fig. 5.4 made of a single excited state or an ensemble of unresolved excited states. The capital letter P stands for the resonant process in a given charge state CS of the initial ions from **He-like to O-like Fe**. The excited states configurations are given in standard atomic notations. The measured resonance energies E_{res} from the fits (except calibrated lines) are presented. Theoretical emission asymmetry $\mathcal{R}$ with only the Coulomb repulsion (C) are compared with a full treatment of the electron–electron interaction (C+BI).

Label	CS	P	Excited State $|d\rangle$	E_{res} (exp)	$\mathcal{R}$ (th)		$\mathcal{R}$ (exp)	
					C	C+BI	value	error
1	He	DR	$[1s2s^2]_{1/2}$	cal.	0.000	0.000	norm.	-
2	He	DR	$[(1s2s)_0 2p_{1/2}]_{1/2}$	4604.16	0.000	0.000	-0.047	0.150
3	He	DR	$[(1s2s)_1 2p_{3/2}]_{1/2}$	4626.78	0.000	0.000	-0.125	0.159
4	He	DR	$[(1s2p_{1/2})_1 2p_{3/2}]_{5/2}$	4636.94	0.500	0.500	0.508	0.072
5	He	DR	$[(1s2p_{1/2})_1 2p_{3/2}]_{3/2}$	4650.91	0.500	0.500	0.425	0.081
6	He	DR	$[1s(2p_{3/2}^2)_2]_{5/2}$	4660.44	0.445	0.446	0.315	0.095
7	He	DR	$[1s(2p_{3/2}^2)_2]_{3/2}$	4674.46	-0.617	-0.608	-0.467	0.204
	Li	DR	$[(1s2s2p_{1/2})_{3/2}2p_{3/2}]_3$					
8	He	DR	$[1s(2p_{3/2}^2)_0]_{1/2}$	cal.	0.000	0.000	0.123	0.124
9	Li	DR	$[((1s2s)_1 2p_{1/2})_{1/2}2p_{3/2}]_1$	4712.69	0.320	0.319	0.114	0.123
	Li	DR	$[((1s2s)_1 2p_{1/2})_{3/2}2p_{3/2}]_2$					
10	Li	DR	$[(1s2s)_1 (2p_{3/2}^2)_2]_1$	4722.76	-0.372	-0.377	-0.216	0.169
	Li	DR	$[(1s2s)_1 (2p_{3/2}^2)_2]_2$					
11	Li	DR	$[((1s2s)_0 2p_{1/2})_{1/2}2p_{3/2}]_2$	4741.58	0.198	0.197	0.144	0.119
	Li	DR	$[(1s2s)_1 (2p_{3/2}^2)_0]_1$					
12	Li	DR	$[(1s2s)_0 (2p_{3/2}^2)_2]_2$	4752.35	0.565	0.568	0.490	0.075
	Be	DR	$[1s2s^2 2p_{1/2}^2]_{1/2}$					
13	Li	DR	$[(1s2s)_1 (2p_{3/2}^2)_2]_1$	4769.89	0.251	0.284	0.291	0.112
	Be	DR	$[(1s2s^2 2p_{1/2})_1 2p_{3/2}]_{5/2}$					
14	Li	DR	$[1s2p_{1/2}^2 2p_{3/2}]_1$	4783.96	0.405	0.402	0.275	0.106
	Li	DR	$[(1s2p_{1/2})_0 (2p_{3/2}^2)_2]_2$					
15	Be	DR	$[(1s2s^2 2p_{1/2})_1 2p_{3/2}]_{1/2}$	4790.54	0.468	0.466	0.324	0.094
	Be	DR	$[(1s2s^2 2p_{1/2})_1 2p_{3/2}]_{3/2}$					
	Be	DR	$[1s2s^2 (2p_{3/2}^2)_2]_{5/2}$					
16	Be	DR	$[1s2s^2 (2p_{3/2}^2)_2]_{3/2}$	4805.16	-0.384	-0.364	-0.317	0.189
	Be	DR	$[1s2s^2 (2p_{3/2}^2)_0]_{1/2}$					

17	Be	DR	$[1s2s^2(2p_{3/2}^2)_0]_{1/2}$	4812.28	0.000	0.000	0.075	0.152
18	Be	DR	$[(1s2s)_1 2p_{1/2}^2 2p_{3/2}]_{3/2}$	4829.72	0.539	0.539	0.581	0.144
19	B	DR	$[1s2s^2 2p_{1/2}^2 2p_{3/2}]_1$	4849.86	0.505	0.503	0.412	0.062
20	B	DR	$[(1s2s^2 2p_{1/2})_0(2p_{3/2}^2)_2]_2$	cal.	0.421	0.423	0.392	0.053
21	B	DR	$[(1s2s^2 2p_{1/2})_1(2p_{3/2}^2)_2]_3$	4861.44	0.438	0.438	0.416	0.057
22	B	DR	$[(1s2s^2 2p_{1/2})_1(2p_{3/2}^2)_2]_1$	4869.28	-0.207	-0.201	-0.168	0.242
23	B	DR	$[(1s2s^2 2p_{1/2})_0(2p_{3/2}^2)_0]_0$	4875.45	-0.238	-0.227	-0.163	0.021
	B	DR	$[(1s2s^2 2p_{1/2})_1(2p_{3/2}^2)_2]_2$					
	B	DR	$[(1s2s^2 2p_{1/2})_1(2p_{3/2}^2)_0]_1$					
24	B	TR	$[1s2s^2 2p_{3/2}^3]_2$	4887.31	-0.451	-0.446	-0.431	0.050
25	B	TR	$[1s2s^2 2p_{3/2}^3]_1$	4897.63	0.230	0.231	0.151	0.035
26	Be	TR	$[(1s2s)_0 2p_{3/2}^3]_{3/2}$	4906.87	-0.680	-0.680	-0.350	0.663
27	Be	TR	$[1s2s^2(2p_{3/2}^2)_2]_{5/2}$	4919.52	0.435	0.435	0.412	0.123
28	C	DR	$[1s2s^2 2p_{1/2}^2(2p_{3/2}^2)_2]_{5/2}$	4925.57	0.432	0.432	0.366	0.045
29	C	DR	$[1s2s^2 2p_{1/2}^2(2p_{3/2}^2)_2]_{3/2}$	4933.96	-0.696	-0.696	-0.290	0.520
30	C	DR	$[1s2s^2 2p_{1/2}^2(2p_{3/2}^2)_0]_{1/2}$	4937.10	0.000	0.000	-0.057	0.435
31	C	TR	$[(1s2s^2 2p_{1/2}^1)_0 2p_{3/2}^3]_{3/2}$	cal.	-0.548	-0.548	norm.	-
32	C	TR	$[(1s2s^2 2p_{1/2})_1 2p_{3/2}^3]_{1/2,3/2}$	4962.92	0.129	0.129	0.184	0.026
33	B	TR	$[(1s2s^1 2p_{1/2}^2)_1(2p_{3/2}^2)_0]_1$	4971.73	-0.026	-0.026	0.242	0.174
34	B	QR	$[((1s2s)_0 2p_{1/2})_{1/2} 2p_{3/2}^3]_2$	4984.02	-0.110	-0.110	0.026	0.211
35	N	DR	$[1s2s^2 2p_{1/2}^2 2p_{3/2}^3]_2$	5010.22	-0.017	-0.032	-0.028	0.130
36	N	DR	$[1s2s^2 2p_{1/2}^2 2p_{3/2}^3]_1$	5017.66	-0.046	-0.038	-0.007	0.179
37	N	TR	$[(1s2s^2 2p_{1/2})_1 2p_{3/2}^4]_1$	5036.03	0.123	0.124	0.199	0.213
38	C	QR	$[1s2s 2p_{1/2} 2p_{3/2}^4]_{1/2}$	5075.40	0.000	0.000	-0.103	0.526
39	O	TR	$[1s2s^2 2p_{1/2}^2 2p_{3/2}^4]_{1/2}$	5081.11	0.000	0.000	0.006	0.123

The emission asymmetry of individual resonances, as well as the differential x-ray intensity spectra, are in excellent agreement with the theoretical calculations. Such comprehensive comparison confirms the accuracy of FAC predictions. With few exceptions, the agreement is excellent, even for inter-shell TR and QR *KLL* resonances, known since a few years only [74, 75, 159]. The obtained results will be discussed and summarized later in Sec. 5.3.

Table 5.3: Operational parameters of the FLASH-EBIT. (a) and (b) corresponds to two different measurements.

Parameter	Value
Electron beam current	70 mA
Magnetic field	6 T
Trap offset potential	(a) 130 V (b) 100 V
Scan energy	$8.7 - 9.8$ keV
Sweep rate	1.8 eV/s
Beam radius	≈ 24.34 μm
Trap length	50 mm
Dump cycle	107 s
Pressure of gas injector	3×10^{-7} mbar

5.2 X-ray emission asymmetries: Resonant recombination of $Kr^{28+...34+}$

In addition to the experiment with highly charged iron ions, we performed a similar experiment with highly charged krypton ions. This study helps to gain insight in the atomic number Z-dependency of the degree of linear polarization. The polarization of a few *KLL* DR resonances of highly charged Kr ions was already investigated in our previous experiment using the Compton polarimetry technique. Here, we make the complete measurement of the x-ray emission asymmetries in the *KLL* DR, TR, and QR transitions of highly charge Kr ions.

5.2.1 Experiment

In the present experiment, krypton gas with a natural isotopic abundance was injected into the trap. The pressure at the injection and trap was 3×10^{-7} mbar and 1.2×10^{-9} mbar, respectively. The electron beam energy was continuously scanned over the K-shell recombination resonances, namely from 8.7 keV to 9.8 keV. The trapped ions are dumped periodically every 107 seconds. The electron beam current was set to the moderate value of 70 mA in order to limit the energy spread of the electron-ion collision energy.

As in the previous case of iron, here, the trap settings were optimized for two criteria: (a) a deeper trap with a higher concentration of high charge states ions (e. g. He- and Li-like ions), with the resolution of 19 eV (FWMH). (b) a shallow trap with a lower concentration of high charge states and a better resolution of 12 eV. The operating parameters of the FLASH-EBIT for the present experiment is given in Table 5.3.

A typical 2D plot of x-ray energy as a function of scanned electron beam energy
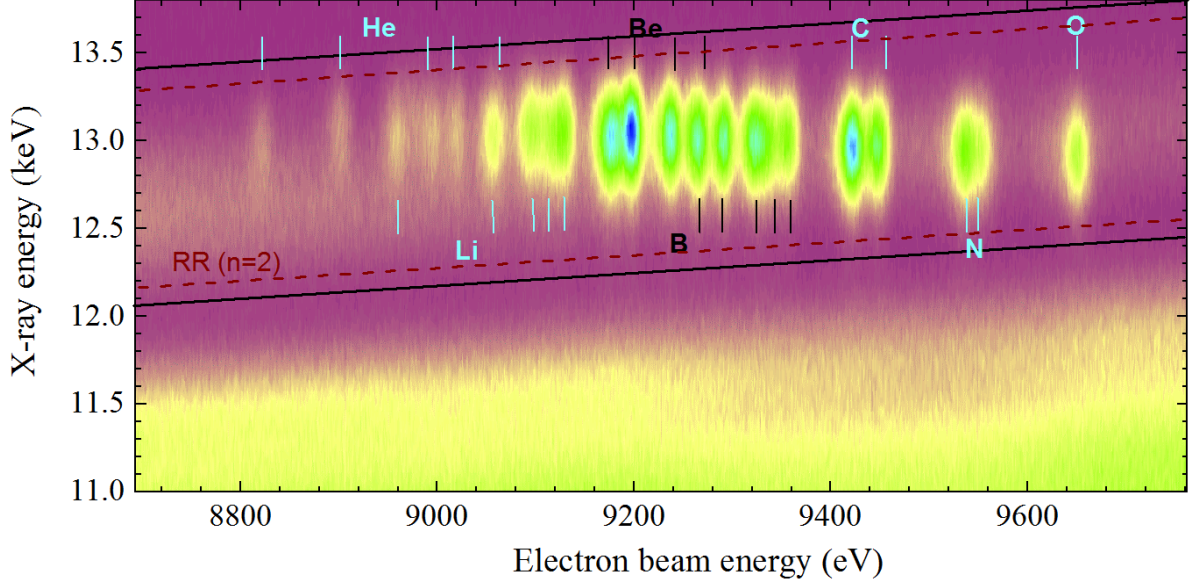
Figure 5.5: Scatter plot of x-ray intensity as functions of x-ray and electron beam energy. The solid lines delimit the region of interest for the horizontal projection. The dashed lines delimit the constant background of RR. Each bright spot corresponds to *KLL* DR resonance identified by an initial charge state of the ion. The x-ray intensity shown here is from the detector at 90°.

over *K*-shell Kr resonances is shown in Fig. 5.5. Here, the x-ray energy was calibrated using the radiation from the radioisotopes, whereas the electron beam energy was calibrated using theoretical resonance energies. The visible bright spots in Fig. 5.5 are *KLL* resonances produced by initial He-like to O-like krypton ions.

5.2.2 Data analysis

The total number of x rays detected within the outlined window in Fig. 5.5 is shown in the middle panel of the Fig. 5.6. The data analysis method used for the present experiment is rather similar to the previous section 5.1.2, except two points:

[1] The energy scale of measurement (a) in Fig. 5.6 was calibrated using two lines 3 and 24, corresponding to energies of 8899 eV and 9427 eV, respectively. Similarly, the energy scale of measurement (b) was calibrated with line no. 17 (9238 eV) and 24.

[2] The detector's solid angle for both measurements (a) and (b) is corrected with the same isotropic line. Here, we select the line 33, which corresponds to the excited state $[1s2s^2 2p_{1/2}^2 2p_{3/2}^4]_{1/2}$ formed by initial O-like ions. It is the most intense line among the isotropic lines. The solid angle factor is found to be $\Omega_{0°}/\Omega_{90°} = 0.1068 \pm 0.0007$. This factor is different from the one measured in the first experiment due to modifications in the setup.
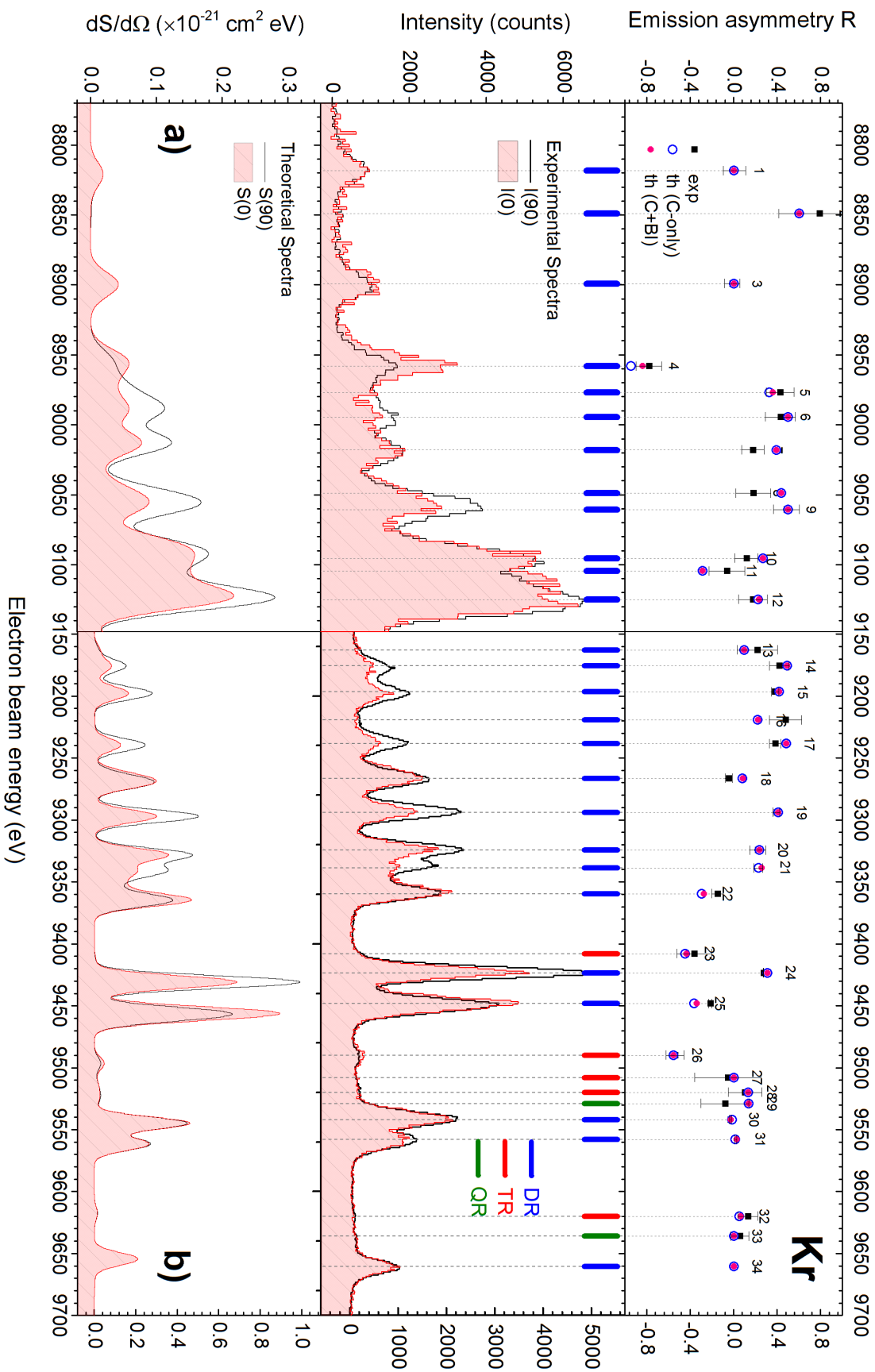
Figure 5.6: **Top panel** shows the extracted emission asymmetries $\mathcal{R}$ (black squares) for the individual resonances and the corresponding predictions with (magenta circles) and without Breit interaction (open blue circles). **Middle panel** shows the x-ray intensity registered by the two germanium detector plotted as a function of electron beam energy. Each line is identified by one or more excited state formed by a given charge state and process in Table 5.4. Vertical markers – Blue: DR, Red: TR and Green: QR. **Bottom panel** shows differential resonance strength ($dS/d\Omega$) as a function of electron beam energy. The black solid lines and the filled light red areas correspond respectively to the x rays observed side-on and head-on to the electron beam in both middles and bottom panels. The label (a) and (b) corresponds to two different measurements.

5.2.3 Results

The experimental resonance energies and the emission asymmetries $\mathcal{R}$ are extracted for each observed resonance following the fitting procedure. The experimental values of E_{res} and $\mathcal{R}$ are summarized in the Table 5.2 as well as in the top panels of Fig. 5.4. The uncertainties in the emission asymmetries are taken as quadrature sums of the errors arises from the fitting procedure and errors due to solid angle correction to the intensity observed along the electron beam propagation axis. The synthetic (or simulated) spectra are also obtained following the procedure described in the previous section 5.1.3. The bottom panel of Fig. 5.6 shows the synthetic spectra. We found qualitative agreement between the experimental spectra and the simulated spectra produced with the help of FAC code.

In addition to the previous experiment with iron, here, we took a series of independent spectra with acquired time of four days were recorded during the time of measurement that spanned over three months. This helped us to study possible time drifts of voltages during the experiment. The obtained values of the emission asymmetry ratio for few lines are shown in Fig. 5.7. The error bar in each measurement contains the combined error of the statistical error obtained from fitting the perpendicular and parallel spectra. It corresponds to one standard deviation. No clear dependence on the time of acquisition was observed.
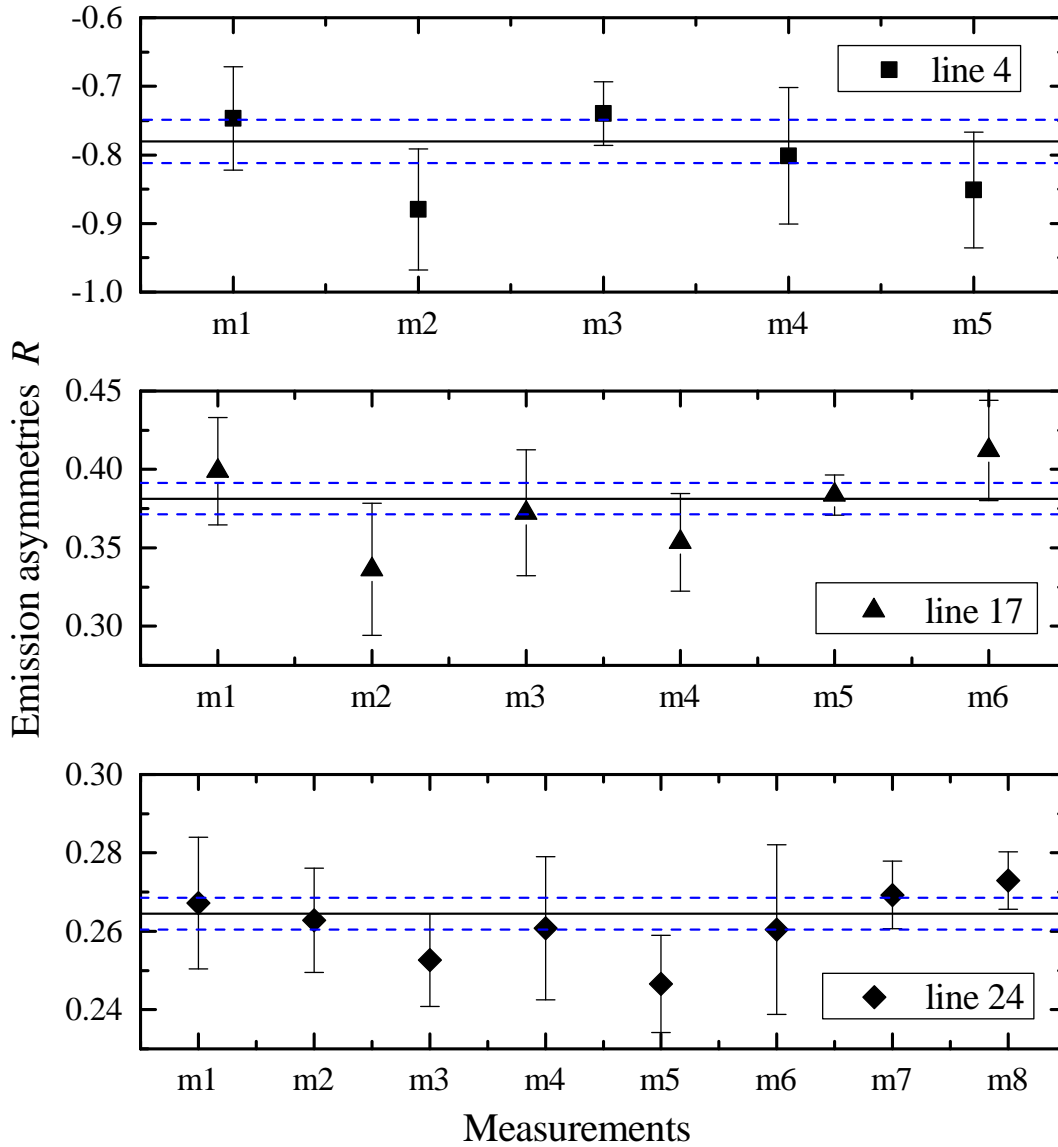
Figure 5.7: Values of extracted $\mathcal{R}$ corresponds to lines 4, 17 and 24 as a function of several independent measurements. The black solid line corresponds to the weighted average and the blue dashed line stands for the weighted average plus or minus σ.

Table 5.4: Measured emission asymmetry $\mathcal{R}$ between perpendicular and parallel observation of x rays emitted in the resonant recombination process. The label in the first column identifies the resonances in Fig. 5.6 made of a single excited state or an ensemble of unresolved excited states. The capital letter P stands for the resonant process in a given charge state CS of the initial ions from **He-like to O-like krypton**. The excited states configurations are given in standard atomic notations. The measured resonance energies E_{res} from the fits (except calibrated lines) are presented. Theoretical emission asymmetry $\mathcal{R}$ with only the Coulomb repulsion (C) are compared with a full treatment of the electron–electron interaction (C+BI).

Label	CS	P	Excited State $|d\rangle$	$E_{\rm res}$ (exp)	$\mathcal{R}$ (th)		$\mathcal{R}$ (exp)	
					C	C+BI	value	error
1	He	DR	$[(1s(2s^2)_0]_{1/2}$	8818.32	0.000	0.000	0.008	0.103
2	He	DR	$[(1s2s)_1 2p_{1/2}]_{3/2}$	8849.00	0.600	0.600	0.791	0.376
3	He	DR	$[(1s2s)_0 2p_{1/2}]_{1/2}$	cal.	0.000	0.000	-0.013	0.071
4	Li	DR	$[1s2s^2 2p_{1/2}]_1$	8958.26	-0.946	-0.842	-0.780	0.116
5	He	DR	$[(1s2s)_1 2p_{3/2}]_{1/2}$	8976.90	0.325	0.359	0.427	0.129
	He	DR	$[(1s2s)_0 2p_{3/2}]_{3/2}$					
6	He	DR	$[(1s2p_{1/2})_1 2p_{3/2}]_{5/2}$	8994.55	0.500	0.500	0.431	0.139
7	He	DR	$[(1s2p_{1/2})_0 2p_{3/2}]_{3/2}$	9018.11	0.391	0.391	0.176	0.104
	Li	DR	$[1s2s^2 2p_{1/2}]_2$					
8	Li	DR	$[((1s2s)_1 2p_{1/2})_{3/2} 2p_{3/2}]_3$	9049.00	0.438	0.438	0.183	0.160
9	He	DR	$[1s(2p^2_{3/2})_2]_{5/2}$	9060.69	0.500	0.500	0.485	0.120
10	Li	DR	$[((1s2s)_1 2p_{1/2})_{3/2} 2p_{3/2}]_2$	9095.44	0.269	0.269	0.118	0.105
11	Li	DR	$[((1s2s)_1 2p_{1/2})_{3/2} 2p_{3/2}]_1$	9104.70	-0.289	-0.289	-0.062	0.166
12	Li	DR	$[((1s2s)_0 2p_{1/2})_{1/2} 2p_{3/2}]_2$	9124.94	0.222	0.230	0.176	0.132
	Li	DR	$[(1s2s)_1 (2p_{3/2})^2_2]_3$					
13	Li	DR	$[1s2s^2 2p_{3/2}]_2$	9162.80	0.095	0.095	0.219	0.184
14	Be	DR	$[(1s2s^2 2p_{1/2})_1 2p_{3/2}]_{5/2}$	9175.55	0.492	0.492	0.420	0.090
15	Be	DR	$[(1s2s^2 2p_{1/2})_1 2p_{3/2}]_{3/2}$	9196.67	0.416	0.416	0.380	0.035
16	Li	DR	$[(1s2p_1/2)_0 (2p^2_{3/2})_2]_2$	9219.30	0.220	0.221	0.479	0.148
17	Be	DR	$[1s2s^2 (2p^2_{3/2})_2]_{5/2}$	cal.	0.481	0.481	0.381	0.053
18	Be	DR	$[1s2s^2 (2p^2_{3/2})_2]_{3/2}$	9266.56	0.079	0.081	-0.045	0.034
	B	DR	$[1s2s^2 (2p_{1/2})^2 2p_{3/2}]_2$					
	Be	DR	$[1s2s^2 (2p^2_{3/2})_0]_{1/2}$					
19	B	DR	$[1s2s^2 (2p_{1/2})^2 2p_{3/2}]_1$	9294.00	0.409	0.409	0.394	0.032
20	B	DR	$[(1s2s^2 2p_{1/2})_1 (2p^2_{3/2})_2]_2$	9324.40	0.234	0.236	0.222	0.074
21	B	DR	$[(1s2s^2 2p_{1/2})_1 (2p^2_{3/2})_2]_3$	9338.90	0.228	0.256	0.227	0.042

	B	DR	$[(1s2s^22p_{1/2})_1(2p^2_{3/2})_2]_1$					
22	B	DR	$[(1s2s^22p_{1/2})_0(2p^2_{3/2})_2]_2$	9359.62	-0.298	-0.274	-0.149	0.055
	B	DR	$[(1s2s^22p_{1/2})_1(2p^2_{3/2})_0]_1$					
23	B	TR	$[1s2s^22p^3_{3/2}]_2$	9408.00	-0.447	-0.438	-0.363	0.159
24	C	DR	$[1s2s^22p^2_{1/2}(2p^2_{3/2})_2]_{5/2}$	cal.	0.308	0.308	0.276	0.002
25	C	DR	$[1s2s^22p^2_{1/2}(2p^2_{3/2})_2]_{3/2}$	9448.28	-0.366	-0.344	-0.216	0.016
	C	DR	$[1s2s^22p^2_{1/2}(2p^2_{3/2})_0]_{1/2}$					
26	C	TR	$[(1s2s^22p_{1/2})_0 2p^3_{3/2}]_{3/2}$	9490.00	-0.555	-0.555	-0.540	0.082
27	C	TR	$[(1s2s^22p_{1/2})_1 2p^3_{3/2}]_{1/2}$	9508.00	0.000	0.000	-0.054	0.306
28	C	TR	$[(1s2s^22p_{1/2})_1 2p^3_{3/2}]_{3/2}$	9520.00	0.133	0.133	0.104	0.155
29	Be	QR	$[(1s2p_{1/2})_1 2p^3_{3/2}]_{3/2}$	9529.00	0.135	0.135	-0.080	0.220
30	N	DR	$[1s2s^2(2p_{1/2})^2 2p^3_{3/2}]_2$	9541.92	-0.018	-0.029	-0.029	0.009
31	N	DR	$[1s2s^2(2p_{1/2})^2 2p^3_{3/2}]_1$	9558.00	0.012	0.025	0.021	0.009
32	N	TR	$[(1s2s^22p_{1/2})_1 2p^4_{3/2}]_1$	9620.04	0.051	0.062	0.132	0.091
33	B	QR	$[1s2s^1 2p^4_{3/2}]_0$	9636.04	0.000	0.000	0.058	0.084
34	O	DR	$[1s2s^22p^2_{1/2} 2p^4_{3/2}]_{1/2}$	9660.56	0.000	0.000	norm.	-

The emission asymmetry $\mathcal{R}$ of individual resonances as well as the full experimental spectra are compared with the calculations of FAC code. With a few exceptions, we found an excellent agreement between them and benchmark FAC predictions. Few predictions of FAC code, such as, resonance energies are compared with the multiconfiguration Dirac-Fock (MCDF) calculations, and degrees of polarization are compared with RATIP computer code. We found good agreement between these different computer codes.

5.3 Discussion

5.3.1 Emission asymmetry and magnetic sublevel population

From all lines listed in the Tables 5.2 and 5.4, we observe that most of them have $\mathcal{R} > 0$, i. e., the photons are emitted predominately perpendicular to the electron beam axis. For the cases of initial He-, Be-, and C-like ions, the ground state having $J_i = 0$ restricts the population of magnetic sublevels to $M_d = \pm 1/2$. Therefore, the orientation of J_d is perpendicular to the electron trajectory, leading to a negative value of $\mathcal{A}_2$ and thus, to a perpendicular photon emission for $|J_d - J_f| = 1$.

For initial Li-like and B-like ions with the ground state of $J_i = 1/2$, the photon emission being mostly perpendicular to the electron beam axis indicates that transverse magnetic sublevels are predominantly populated. For resonant states with $J_d > 1$ the respective magnetic sublevels are restricted to $|M_d| \leq 1$, therefore even if $\sigma_{\pm 1} >> \sigma_0$ the alignment will be mostly perpendicular to the electron beam axis. Some observed lines have $\mathcal{R} < 0$, it is due to a negative value of $\bar{\alpha}_2^{df}$ for transitions where $J_d = J_f$, e. g., lines of Kr: 22, 25, 26, 29 and 30. Therefore, the general rule is that transverse magnetic sublevels with $|M_d| \leq 1$ and $M_d = \pm 1/2$ are mostly populated. This can be expected since the orbital angular momentum of the electron, which is perpendicular to the trajectory, is transferred perpendicular during the collision. Thus leading to an orientation of J_d that is mostly perpendicular to the electron beam axis, see case (a) of the Fig. 5.8.

However, resonant states with $J_d = 1$ can be aligned longitudinally if $\sigma_{\pm 1} > \sigma_0$. The observed *line 4* (of Kr) corresponding to the term $^3P_1$ is such an example, where the angular distribution indicates that sublevels with $M_d = \pm 1$ are predominately populated. According to Ref. [136, 199], this is a consequence of the population of sublevel $M_d = 0$ being forbidden in a non-relativistic limit due to angular selection rules associated with the term symbol $^3P_1$. Thus, $M_d = 0$ is forbidden and photon emission is predominately oriented along the electron beam axis, see case (b) of Fig. 5.8.

The case (c) of Fig. 5.8 describes the isotropic angular distribution of emitted photons when the magnetic sublevels are statistically populated.

5.3.2 Influence of other physical processes

In this section, we discuss the influence of other physical processes such as initial alignment, metastable states and radiative cascade on the observed emission asymmetries.

Highly charged states are produced by collisions of ions with directional electrons
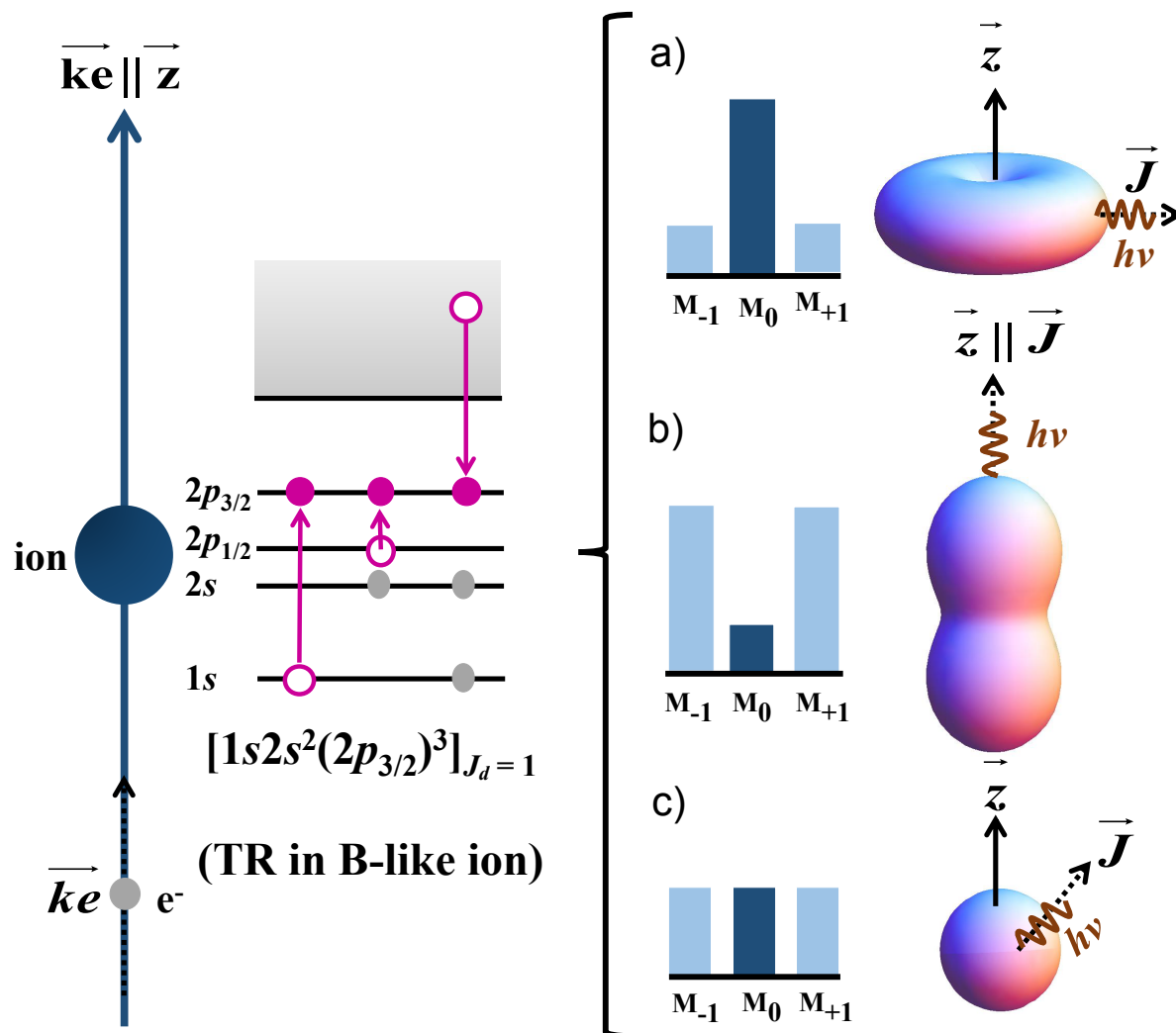
Figure 5.8: Relative magnetic sublevels M_d population of a resonant state with $J_d = 1$ after resonant capture process. The quantization axis z is defined by the direction of the wave-vector $\vec{ke}$ of the incoming electron toward the ion in the initial state (in blue). The scenario (a) stands for the magnetic sublevel $M_d = 0$ being mostly populated, the photons are predominantly emitted perpendicular to the quantization axis. (b) corresponds to the reverse case of (a). In the case of (c), the magnetic sublevels are statistically populated and the photon angular distribution is isotropic. For each scenario, one possible orientation of the total angular momentum J_d and photon angular distribution is shown dipole $|J_d - J_f| = 1$ transitions.

which result in ionized ions with aligned states in the EBIT. These ions are produced by electron impact ionization. They are assumed to be in the ground states since the electron density is very low ($< 3 \times 10^{12}$ cm^{-3}) so that the interaction time between the electrons and ions is longer than the lifetime of any metastable state of the ion [166, 204]. Therefore, even if ions are produced in excited states, they immediately decay to the ground state. However, there may exist few metastable states, such as $[1s^2(2s2p_{1/2})_0]_0$ or $[1s^22s^2(2p_{3/2}^2)_0]_0$ in Be-like and C-like ions with relatively longer lifetimes, that can be considered as alternative ground states. Moreover, for initial He-like to C-like ions, ground states contain $J_i = 0$ and $J_i = 1/2$, which cannot be aligned according to the definition of the alignment parameter. Whereas for N-like initial ions, ground states can be aligned with $J_i = 3/2$ resulted after impact ionization and deexcitation. Such ions with initial aligned state can transfer this initial alignment to the intermediate excited state during the resonant capture process. In principle, both the initial alignment of the ion and metastable excited states can influence the degree of linear polarization. However, in the present experiment, we cannot distinguish these small individual effects on the emission asymmetry, thereby, we neglect them.

The formed intermediate excited state after resonant capture process can decay either by single electronic transition or by several possible cascade channels to the ground state. The radiative cascade effects has previously shown to modify DR cross sections [205, 206] and the angular distribution of the emitted photons [207]. Considering the radiative cascade, the most likely channel first to occur is an inter-shell transition emitting keV x rays, followed by possible intra-shell transitions with few eV photon emission. In such cases, the latter channels are not observed by typical x-ray detectors. However, in principle, the inverse channel, i. e., intra-shell transition followed by inter-shell transition can affect the x-ray anisotropy and polarization. Here, the intermediate aligned excited state may decay with the intra-shell transition (unobserved photon) and create another aligned state with non-statistical magnetic sublevel populations. Such aligned state stabilizes by emitting an inter-shell transition x-ray with a different degree of polarization. However, this inverse decay channel is less likely to occur compared to the direct channel by at least a factor of 10^3 and can thus be neglected. In case of DR occurring in initial H-like Kr ions, recently studied in Ref. [111], both the singly $|s\rangle$ and doubly $|d\rangle$ excited states decay by the inter-shell transitions. In such cases, the alignment of the single excited state has also to be taken into account to describe angular distribution of the emitted photons. As discussed in Ref. [83], the effect of cascades can be described by

the deorientation parameter U_λ:

$$U_\lambda(J_d, J_s) = (-1)^{J_d+J_s+\lambda+L}\sqrt{(2J_d+1)(2J_s+1)}\begin{Bmatrix} J_d & J_d & \lambda \\ J_s & J_s & L \end{Bmatrix}, \qquad (5.8)$$

and the angular distribution of x rays emitted from singly excited states to the final states can be expressed as:

$$W(\theta) = \frac{d\Omega}{4\pi}\sum_{\lambda=\text{even}} \mathcal{A}_\lambda(J_d)U_\lambda(J_d, J_s)\alpha_\lambda(J_s, J_f)P_\lambda(\cos\theta), \qquad (5.9)$$

where, J_d, J_s, and J_f are the total angular momentum of the doubly excited, singly excited and final state, respectively. The effect of radiative cascades is included in our calculations, we observed a negligible change in the degree of linear polarization.

The presence of external magnetic and electric fields is shown to modify the DR cross section and magnetic sublevel population [208]. Since in the present experiment the direction of the external magnetic field is the same as that of the electron beam, the magnetic sublevel populations should not be redistributed [93]. Furthermore, the electron radial velocity component arising from cyclotron motion of the electrons shown to change the degree of linear polarization. We have estimated this radial velocity component according to Herman's optical theory of electron beam and found to reduce the measured emission asymmetries only within statistical error bars. The finite angle of acceptance of each detector is very small (3° and 1°), thus, it can be neglected. The degree of linear polarization of x rays following TR and QR resonances will be discussed in the next Chapter 6.

5.3.3 State selective influence of the Breit interaction

In the previous experiment, we measured the degree of linear polarization of x rays following 5 DR resonances and studied the Breit interaction effect on two of them. Here, we have measured total 73 KLL DR, TR and QR resonances in krypton and iron, that allows us to make a systematic study of Breit interaction effect for low-Z and medium-Z ions. We restrict our discussion to a selective set of lines that are well-separated from each other, thus, we avoid possible mixing of $\mathcal{A}_2$ between two excited states having energy differences less than the line width.

The list of selected lines of krypton measurements sorted by J_d is given in Table 5.5 together with theoretical values of $\mathcal{A}_2$ and $\bar{\alpha}_2^{df}$. Theoretical values of $\mathcal{A}_2$ are calculated, according to Eq. (2.17), with and without inclusion of the Breit interaction in the FAC

Table 5.5: Each excited state is identified by the label in the first column and sorted according to the total angular momentum J_d. The allowed partial waves of the free electron that contribute to the process of autoionization of the excited state are displayed in the third column. The "effective" anisotropy parameter $\bar{\alpha}_2^{df}$ is given in the fifth column. Theoretical values of $\mathcal{A}_2$ are displayed for the case of including the Breit interaction (C+BI) and only Coulomb interaction (C).

Label	J_d	Partial waves	Final state	$A_r^{df}(s^{-1})$	$\bar{\alpha}_2^{df}$	$\mathcal{A}_2$(C)	$\mathcal{A}_2$(C+BI)
4	1	$\epsilon p_{1/2},\ \epsilon p_{3/2}$	$[1s^2 2s^2]_0$	3.591(14)	0.682	0.704	0.64
			$[1s^2(2p_{1/2}^2)_0]_0$	1.235(13)			
			$[1s^2(2p_{1/2}2p_{3/2})_1]_1$	3.452(12)			
			$[1s^2(2p_{1/2}2p_{3/2})_2]_2$	8.865(12)			
19	1	$\epsilon s_{1/2},\ \epsilon d_{3/2}$	$[1s^2 2s^2 2p_{1/2}^2]_0$	1.138(15)	0.453	-0.694	-0.681
			$[1s^2 2s^2(2p_{1/2}2p_{3/2})_1]_1$	1.142(14)			
			$[1s^2 2s^2(2p_{1/2}2p_{3/2})_2]_2$	5.145(14)			
			$[1s^2 2s^2(2p_{3/2}^2)_2]_2$	2.771(12)			
15	3/2	$\epsilon d_{3/2}$	$[1s^2 2s^2 2p_{1/2}]_{1/2}$	1.163(15)	0.318	-1.000	-1.000
			$[1s^2 2s^2 2p_{1/2}]_{3/2}$	2.861(14)			
			$[1s^2 2p_{3/2}^3]_{3/2}$	3.599(12)			
			$[1s^2 2p_{1/2}(2p_{3/2}^2)_2]_{3/2}$	2.978(12)			
			$[1s^2 2p_{1/2}(2p_{3/2}^2)_2]_{5/2}$	8.662(12)			
26	3/2	$\epsilon d_{3/2}$	$[1s^2 2s^2 2p_{1/2}(2p_{3/2}^2)_2]_{3/2}$	1.080(15)	-0.314	-1.000	-1.000
			$[1s^2 2s^2 2p_{1/2}(2p_{3/2}^2)_2]_{5/2}$	2.563(14)			
			$[1s^2 2s^2 2p_{3/2}^3]_{3/2}$	1.317(14)			
10	2	$\epsilon d_{3/2},\ \epsilon d_{5/2}$	$[1s^2(2s2p_{1/2})_1]_1$	1.192(15)	0.27	-0.604	-0.604
			$[1s^2(2s2p_{3/2})_2]_2$	1.646(14)			
			$[1s^2(2s2p_{3/2})_1]_1$	9.222(13)			
20	2	$\epsilon d_{3/2},\ \epsilon d_{5/2}$	$[1s^2 2s^2(2p_{1/2}2p_{3/2})_1]_1$	5.114(14)	0.179	-0.929	-0.939
			$[1s^2 2s^2(2p_{1/2}2p_{3/2})_2]_2$	7.714(13)			
			$[1s^2 2s^2(2p_{3/2}^2)_2]_2$	1.272(14)			
6	5/2	$\epsilon d_{5/2}$	$[1s^2 2p_{3/2}]_{3/2}$	4.076(14)	0.374	-1.069	-1.069
9	5/2	$\epsilon d_{5/2}$	$[1s^2 2p_{3/2}]_{3/2}$	5.372(14)	0.374	-1.069	-1.069
14	5/2	$\epsilon d_{5/2}$	$[1s^2 2p_{3/2}^3]_{3/2}$	3.737(14)	0.354	-1.069	-1.069
			$[1s^2 2p_{1/2}(2p_{3/2}^2)_2]_{5/2}$	3.012(12)			
17	5/2	$\epsilon d_{5/2}$	$[1s^2 2p_{3/2}^3]_{3/2}$	5.128(14)	0.357	-1.069	-1.069
			$[1s^2 2p_{1/2}(2p_{3/2}^2)_2]_{5/2}$	1.122(13)			
24	5/2	$\epsilon d_{5/2}$	$[1s^2 2s^2 2p_{1/2}^2 2p_{3/2}]_{3/2}$	4.667(14)	0.21	-1.069	-1.069
			$[1s^2 2s^2 2p_{1/2}(2p_{3/2}^2)_2]_{3/2}$	3.190(14)			
			$[1s^2 2s^2 2p_{1/2}(2p_{3/2}^2)_2]_{5/2}$	2.023(14)			

code.

Table 5.5 outlines the allowed partial waves of a free electron which contribute in the formation of respective resonances. The allowed partial waves are restricted by the triangular rule contained in the Wigner 6-j symbols of Eq. (2.16) and parity selection rules. For example, if the total angular momentum of the ground state is $J_i = 0$, then the allowed j of the partial wave ϵl_j must be $j = J_d$. The orbital momentum l of these partial waves is defined by parity selection rules. Thus, the angular momentum of ground state $J_i = 0$ allows only a single partial wave in the formation of resonance state with J_d. This is exactly the case for the resonance formed by He-, Be-, or C-like initial ions with $J_i = 0$. For examples:

$$\text{Line6}: \ \text{e}^-(\epsilon d_{5/2}) + [1s^2]_0 \rightarrow [(1s2p_{1/2})_1 2p_{3/2}]_{5/2},$$

$$\text{Line15}: \ \text{e}^-(\epsilon d_{3/2}) + [1s^2 2s^2]_0 \rightarrow [(1s2s^2 2p_{1/2})_1 2p_{3/2}]_{3/2}.$$

Here, the population density $P_{J_i J_d}^{(L)}$ (or σ_{M_d}) does not depend on reduce matrix element $\langle \Psi_{J_d} \| V \| \Psi_{J_i}, \phi_{lj} \rangle$ for the resonant capture of a free electron, see Eq. (2.16). Thus, the alignment parameter $\mathcal{A}_2$ of these resonances reduces to the constant factor, which can be determined by the angular momenta of the states involved in the resonant capture process. Moreover, the alignment parameter become independent of atomic number Z in the nonrelativistic limit, since the reduced matrix elements in $P_{J_i J_d}^{(2)}/P_{J_i J_d}^{(0)}$ cancel with the respective one in the denominator. This implies, in general, that the Breit interaction cannot affect the angular distribution or degree of linear polarization of x rays produced by resonances formed with a single partial wave. Line no. 15, 26, 6, 9, 14, 17 and 24 shown in the Table 5.5 are the prime examples of such resonances.

On the other hand, if the total angular momentum of the ground state is $J_i > 0$, then the number of partial waves are not restricted to just one. The initial (ground) states of Li-, B-, and N-like ions can have total angular momentum $J_i > 0$. For such ions, two or more partial waves plays a role in the formation of intermediate resonance state. Examples:

$$\text{Line4}: \ \text{e}^-(\epsilon p_{1/2}, \epsilon p_{3/2}) + [1s^2 2s]_{1/2} \rightarrow [1s2s^2 2p_{1/2}]_1,$$

$$\text{Line19}: \ \text{e}^-(\epsilon s_{1/2}, \epsilon d_{3/2}) + [1s^2 2s^2 2p_{1/2}]_{1/2} \rightarrow [1s2s^2 2p_{1/2}^2 2p_{3/2}]_1.$$

Here, the population density $P_{J_i J_d}^{(L)}$ and the alignment parameter $\mathcal{A}_2$ can be affected by

the interference between the possible allowed partial waves of the free electron involved in the formation of resonant state. This interference depends on the reduced matrix element $\langle \Psi_{J_d} \| V \| \Psi_{J_i}, \phi_{lj} \rangle$ of resonant capture process, hence, on the electron–electron interaction operator (purely Coulomb or Breit interaction) that mediates it. Moreover, the reduced matrix elements in Eq. (2.16) does not cancel with the respective one in the denominator of the Eq. (2.16). Therefore, the alignment parameter can show the strong Z- dependency.

As can be observed in Table 5.5, line no. 4, 10, 19 and 20 have two partial waves contributing to the formation of respective resonances with an integer J_d. For these lines, the Breit interaction changes the value of the alignment parameter $\mathcal{A}_2$, respectively, 11%, 2% and 1% for line 4, 19 and 20. The change in alignment parameter of line 10 by the Breit interaction is less than the precision quoted in the Table 5.5. For a heavier element like uranium ($Z = 92$), the contributions of the Breit interaction to $\mathcal{A}_2$ considerably increases, and changes $\mathcal{A}_2$ by 173%, 2%, 25% and 16% for lines 4, 10, 19 and 20, respectively. Among these four lines, it can be observed that line 4 has the strongest influence of the Breit interaction over $\mathcal{A}_2$, thereby, over the angular distribution and the degree of linear polarization of x rays. With this exception of line 4, the influence of Breit interaction on the degree of linear polarization of K-shell x rays can be regarded as a negligible correction and was not observed in the present experiments.

The resonances formed by initial N-like ions are not considered here in the discussion due to the possibility of the initial states being aligned. However, in the cases of line no. 30, 31, 32 in the Tab. 5.4, it must be noted that the Breit interaction can modify the degree of polarization. One of the examples is shown the bottom right panel of the Fig. 5.9.

The state–selective influence of the Breit interaction over the degree of polarization becomes even more pronounced with higher atomic numbers [131, 139, 200]. The few examples are given here in order to see the influence of Breit interaction on the degree of polarization. The calculated degree of linear polarization with and without Breit interaction of few resonances is shown in Fig. 5.9. However, the influence of the Breit interaction for these resonances is smaller at iron and krypton, but Breit interaction influence becomes stronger at higher-Z.

A pronounced influence of Breit interaction was predicted for a resonance $[1s2s^2 2p_{1/2}]_1$ [136] and was experimentally demonstrated for the heavy elements [93, 195]. Here in case of significant lighter element krypton ($Z = 36$), we found better agreement between the experimental and theoretical value of the degree of polarization of line 4, when the Breit interaction is included, see Fig. 5.11. Moreover, this result of Line 4 also coincides with
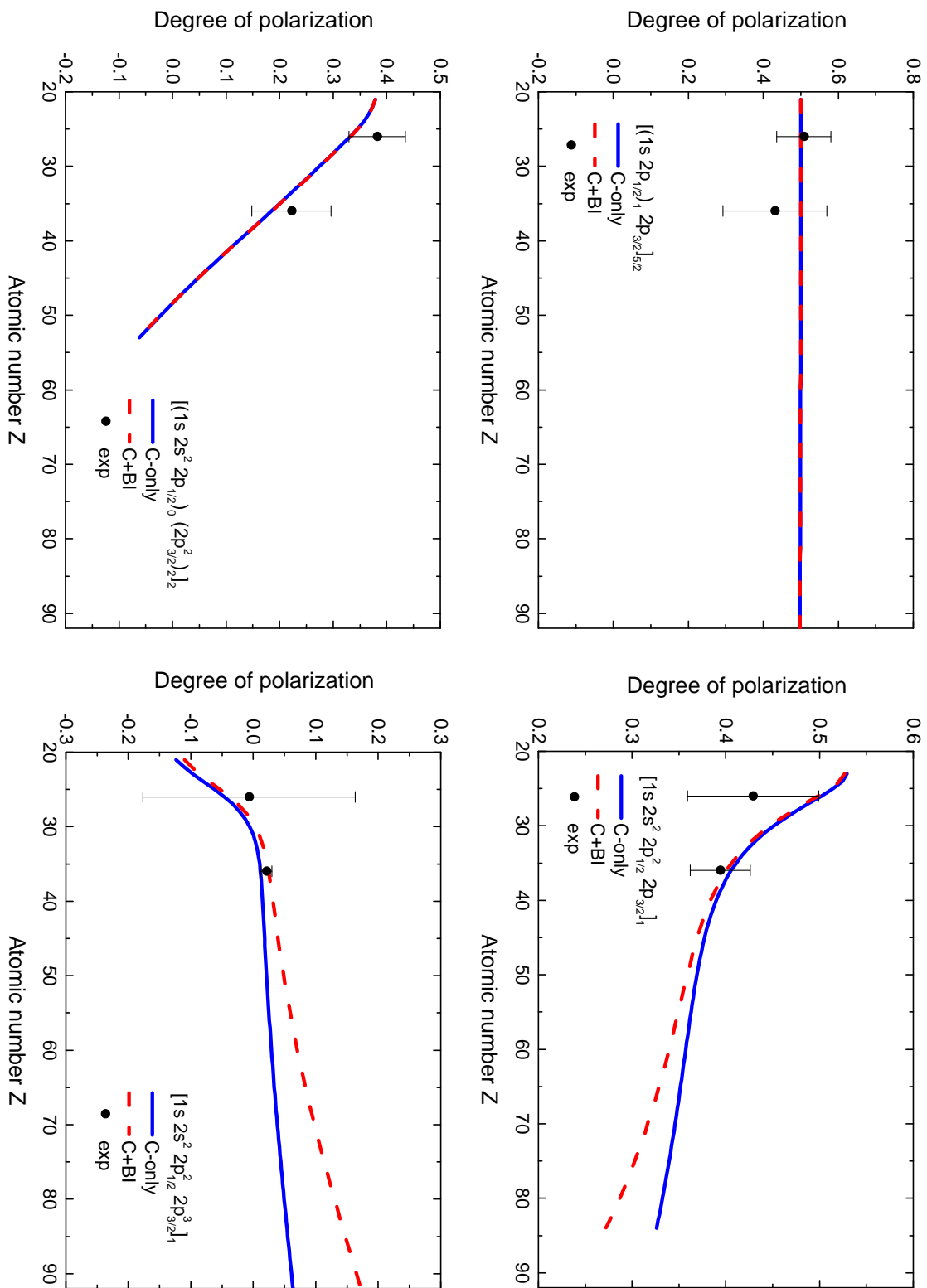
Figure 5.9: The degree of linear polarization of x rays following the intermediate excited state in DR of He-, B-, N-like Fe and Kr. The experimental results are shown by filled circles. The theoretical degree of linear polarization is plotted as a function of atomic number Z, calculated with Coulomb only (C-only) and with Breit interaction (C+BI).
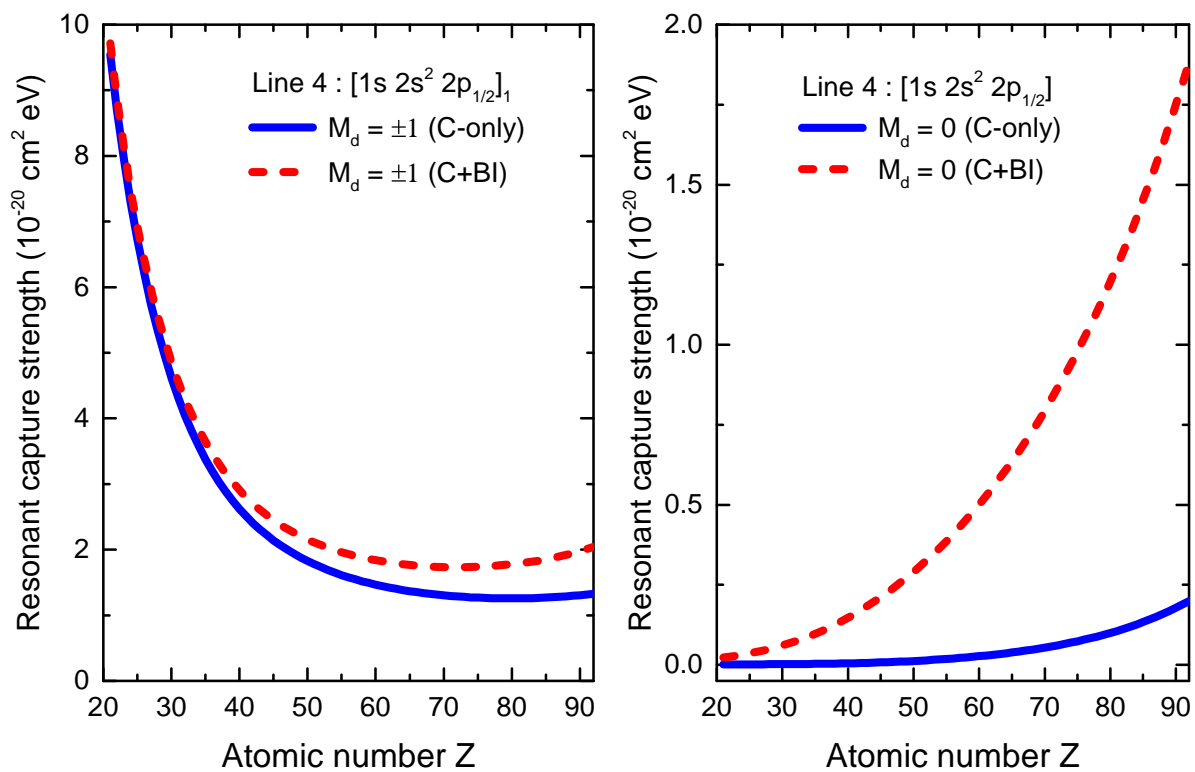
Figure 5.10: Calculated resonant capture strength for magnetic sublevel ($M_d = 0, \pm 1$) of a DR resonance $[1s2s^2 2p_{1/2}]_1$.

the results of Li1 line of the previous experiment based on the Compton polarimetry technique. Both experiments validate the theoretical calculations including Breit interaction and ruled out the calculations based on purely Coulomb interaction.

The relation between the magnetic sublevel population of intermediate excited states and the degree of linear polarization is already explained in Sec. 5.3.1. In order to explain why the Breit interaction is dominant for this particular Line 4, the magnetic sublevel cross sections of a resonance $[1s2s^22p_{1/2}]_1$ are calculated. Figure 5.10 shows the resonant capture strengths for the magnetic sublevels $M_d = 0$ and $M_d = \pm 1$. When only the Coulomb interaction is considered, the resonant capture strengths for $M_d = \pm 1$ sublevel decreases with the higher-Z, whereas $M_d = 0$ sublevel population have an insignificant Z-dependence. This can be understood in the nonrelativistic limit, since the magnetic sublevels with $M_d = \pm 1$ are allowed to be populated in resonant capture process [136]. On the other hand, both $M_d = \pm 1$ and $M_d = 0$ are modified due to the Breit interaction. The population of $M_d = 0$ sublevels are only allowed under the Breit interaction, thereby, the value of resonant capture strength of $M_d = 0$ sublevels rapidly increases with the atomic number Z. The substantial modification due to the Breit interaction can be seen in both the absolute value of $M_d = 0$ and the Z–dependent tendency, see Fig. 5.10. Thus, we can say that the strong Z–dependent tendency of the degree of linear polarization of x rays produced by a DR resonance shown in Fig. 5.11 is due to the substantial modification to $M_d = 0$ sublevel population by the Breit interaction.

The theoretical calculations of anisotropy parameter $\beta = \mathcal{A}_2 \bar{\alpha}_2^{df}$ for the similar resonance was presented by Tong and his coworkers [203]. The generalized Breit interaction (GBI) in nonzero–frequency limit was included in their calculations and found that the generalized Breit interaction modifies the anisotropy parameter not only qualitatively but quantitatively as well over the Breit interaction. Their results are shown in Fig. 5.11. Note that, our present calculations with the Breit interaction does not include the frequency of virtual photons (cf. FAC manual). Thus, we cannot establish the similar calculations.

It should also be noted here that the small shifts in binding energies due to the Breit interaction do not affect magnetic sublevel populations because the experimental electron–ion collision energy spread is large compared to these shifts.

5.4 Summary

In summary, we note that the systematic study of the x-ray emission asymmetries of all dominant KLL resonant recombination transitions into highly charged iron and krypton
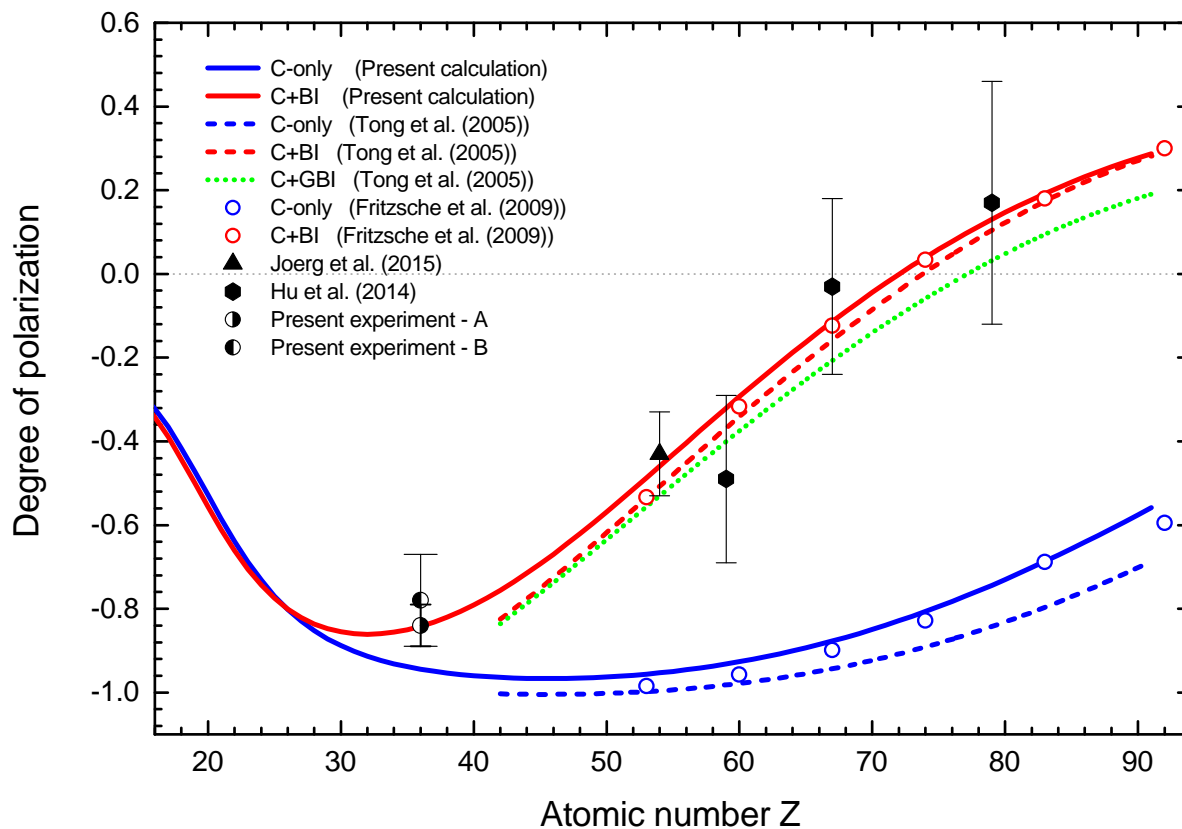
Figure 5.11: Degree of linear polarization of x rays following DR resonance $[1s2s^22p_{1/2}]_1$. The present FAC calculations of the degree of polarization with Coulomb only (C-only) and with Breit interaction (C+BI) is shown by red and blue solid lines, respectively. The theoretical calculations of Fritzsche *et. al.* [136] is shown by blue (C-only) and red (C+BI) open circles. Other calculations of Tong *et. al.* [203] is shown by blue dashed line (C-only), red dashed line (C+BI) and green dotted line (C+GBI). GBI refers to Generalized Breit interaction (see text). The experimental data of Pr (Z=59), Ho (Z=67) and Au (Z=79) are from [93] and the datum of Xe (Z=54) is from [195]. The present experiment–A refers to polarization measurement with the Compton polarimetry technique (previous Ch. 4), whereas the present experiment–B refers to the measurement presented in this chapter.

ions was performed for the first time. These asymmetries were measured for a number of DR, as well as hitherto neglected and generally considered to be weaker TR and QR transitions. The method developed for this measurement uses an EBIT and two conventional solid state x-ray detectors and it is simple enough to be used at nearly every EBIT. Thus, it allows covering a wide range of recombination resonances in highly charged ions of elements from a significant portion of the periodic table. With this technique, the contribution of the Breit interaction was precisely examined for mid-Z elements which confirms the results of the previous experiment. Only one resonance state formed by initial Li-like ions manifest a strong dependency of the degree of linear polarization on the Breit interaction. Alignment properties of other collision processes, such as radiative recombination, electron-impact excitation, and ionization, can also be accessed. Due to its high sensitivity it can also be applied for studies of weak radiative transitions, or, alternatively for high accuracy studies of the stronger transitions, in particular to those sensitive to relativistic interactions such as Breit interaction. The obtained data benchmark the established atomic code such as FAC. It may also find applications for the polarization diagnostics of hot astrophysical and fusion plasmas, such as those of *ITER*. We shall discuss this in the next Chapter 6. In particular, it will play an important role for interpreting the x-ray polarization measurements from the planned astrophysical x-ray polarimetry missions, e. g., *XIPE* [23] and *ASTROSAT* [25].

Chapter 6

Importance of resonant recombination in the plasma diagnostics

Resonant recombination of highly charged ions is known to be the dominant recombination mechanism and is decisive in determining the charge balance in hot, low-density plasmas, such as those found in the sun or in magnetic fusion devices. Many of such examples are given in the Chapter 1. In the first section of this chapter, we discuss the importance of higher-order resonant recombination processes in the plasma diagnostics and modeling. For this purpose, the total recombination rates were calculated including trielectronic (TR) and quadruelectronic (QR) recombination channels. Under the coronal approximation (as described later), newly calculated total recombination rates are added in the calculation of the charge state distribution for collisionally ionized iron plasmas. Furthermore, considering the future polarization diagnostics of hot anisotropic plasmas using polarization measurements, theoretical data of angular distribution and polarization of x rays following resonant recombination are implemented in the collisional-radiative model. The total degree of polarization is calculated for – dominant– $K\alpha$ x-ray line emitted due to resonant recombination into highly charged iron and krypton ions. The higher-order resonant recombination channels, as well as the relativistic effects, are systematically investigated. In the second section, we demonstrate the potential of resonant recombination polarization measurement for accurate diagnostics of the directionality of electron beam inside the hot anisotropic plasmas. The cyclotron motion within an electron beam propagating inside an electron beam ion trap

(EBIT) is investigated from the experimental data available from our measurements.

6.1 Higher-order (HO) resonant recombination: Plasma diagnostics

As mentioned in the previous sections 5.1 and 5.2, we have observed a large number of x-ray transitions involving dielectronic, trielectronic, and quadruelectronic recombination. The upper panel (a) of the Fig. 6.1 highlight the observed *KLL* TR and QR resonance in highly charged iron and krypton. Particularly, the experiments show the intensity of TR resonances is prominent as well as they emit highly anisotropic and polarized x rays.

The TR and QR resonances can only be evaluated properly if the triple- or quadruple-excited states are given as a linear combination of different configurations since the Coulomb or the Breit interaction is a two-body operator (see Eq. (2.7)). As a consequence, these TR and QR processes were assumed to be weaker in comparison with usual DR process. However, we found very strong TR resonances with comparable resonance strength to DR resonance of C-like Fe ions. For those ions, the configuration interaction (CI) and configuration mixing (CM) is particularly stronger and electron–electron correlation decides the strengths of these resonances. In order to check how much CI and CM could affect the intensity of these resonance lines, we first theoretically evaluated the spectrum of B-like initial ions with and without the inclusion of relativistic configuration interaction (R-CI), see middle panel (b) of the Fig. 6.1. To simulate the theoretical spectrum, the resonance energies and strengths of B-like Fe ions are convoluted with the experimental electron beam energy resolution. The experimental and theoretical spectra are compared and found to be in good agreement when the R-CI is included in the calculations. In contrast, when the R-CI is neglected in our calculations, the resonance energies and strengths are not in the agreement with the experiment. Moreover, it also shows that the TR resonances cannot be evaluated without the relativistic configuration interaction between the states. Similar results were obtained when the configuration mixing is neglected in our calculations, see bottom panel (c) of the Fig. 6.1. Therefore, the proper sets of configurations with R-CI and CM "On-mode" in the calculations are required to evaluate TR and QR resonances.

Recently, it was demonstrated that an extended set of configurations is necessary for the initial (ground) state for an improved evaluation of TR in Be-like ions [159]. For example, a triply excited state of Be-like ions such as $1s2s2p^3$ cannot have configuration mixing with the doubly excited state of type $1s2s^22p^2$ due to the opposite parity. This
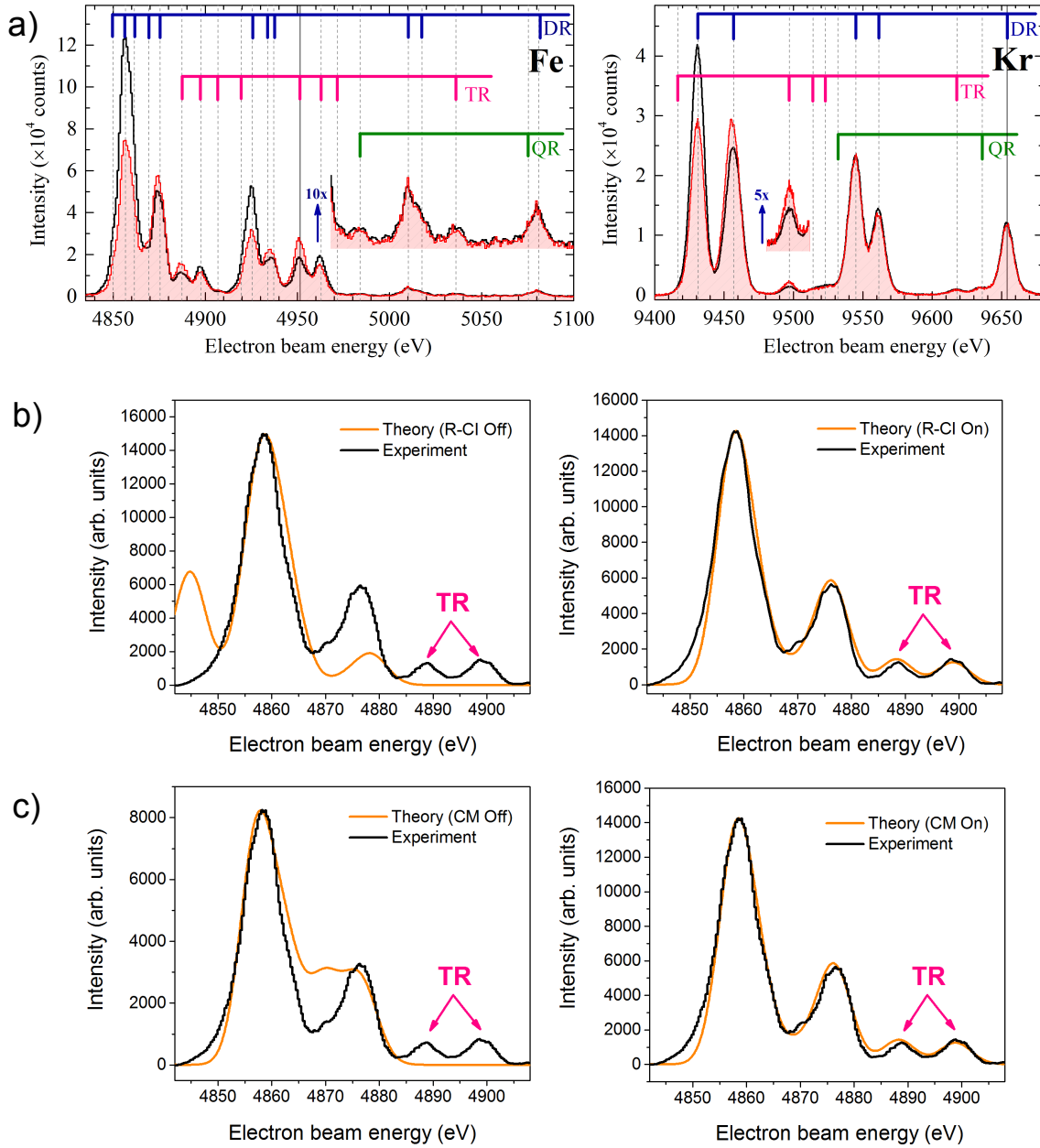
Figure 6.1: Top panel (a): X-ray asymmetries produced by resonant recombination into highly charged Fe and Kr ions are shown as a function of electron beam energy. Vertical lines identify each resonance formed by DR, TR, and QR processes. The middle panel (b) shows the part of the x-ray spectrum simulated with the theoretical data of Fe ions. The experimental spectrum is compared with the theoretical one calculated with relativistic configuration interaction (R-CI) (right) and without R-CI (left). A similar comparison is shown in the bottom panel (c) where the configuration mixing (CM) is neglected (left) and is included (right) in the calculation.
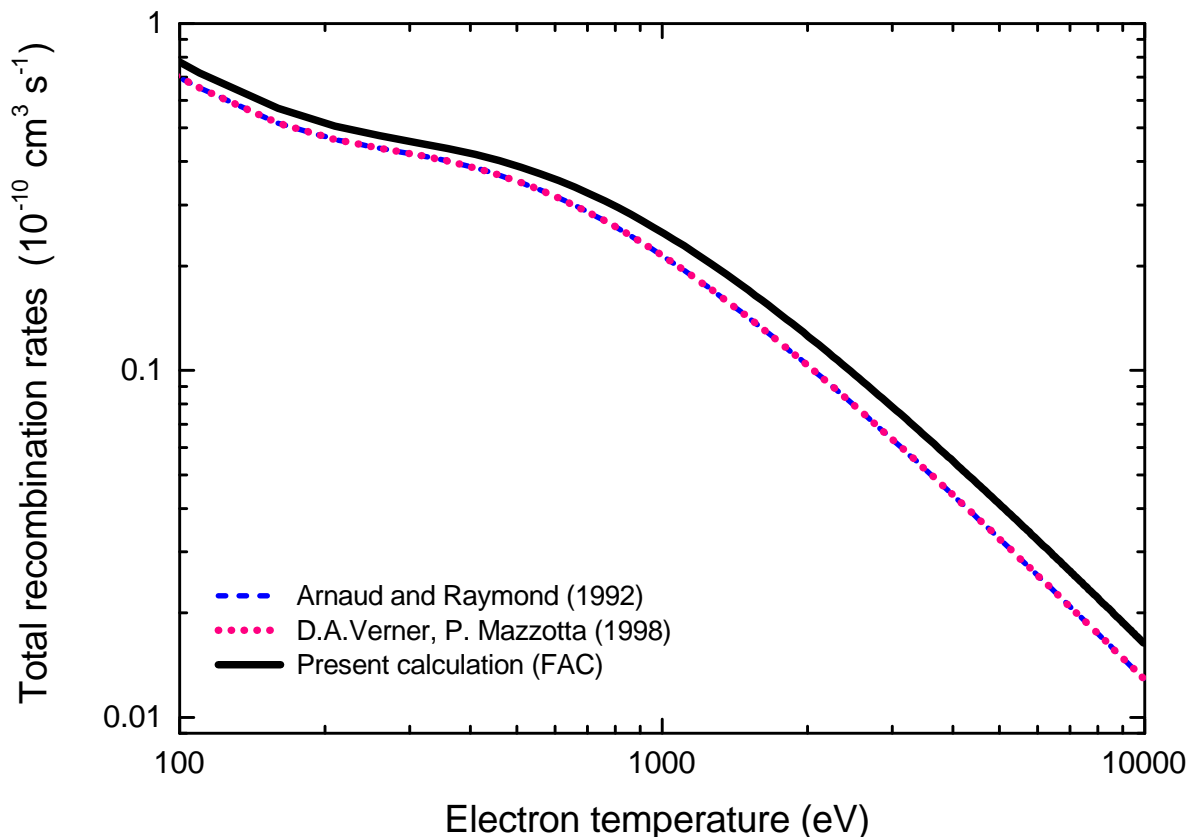
Figure 6.2: Total recombination rate coefficients of C-like ions of Fe are calculated as a function of electron temperature using the FAC code [158]. The solid black line refers to the present calculations. The dashed blue line and dotted magenta lines correspond to the results of Ref. [209] and of Ref. [210], respectively.

means that trielectronic state cannot mix due to parity violation. It may lead to the false conclusion that TR states cannot form by Be-like initial ions [74]. However, if the Be-like initial state $1s^22s^2$ is allowed to mix with excited states like $1s^22s2p$ and $1s^22p^2$, then a single Coulomb interaction or the Breit interaction gives rise to a sizable TR. In this work, we have included an extended set of configurations in the initial state of other charge states in order to identify otherwise-unexplained lines, such as line 33 (of Kr) and 26, 27 and 38 (of Fe). It shows that the high-resolution experiment like ours can benchmark such resonances which may claim to be forbidden in minimal configuration space.

6.1.1   Influence of HO on the ionization balance

The TR resonances with overwhelming density and the resonance strengths have appeared in our experiment with Fe and Kr ions. Similar results were previously obtained

in the experimental investigation of highly charged Si and Ar ions [75, 76]. As discussed in Sec. 1.3, the interpretation of observations from collisionally ionized plasmas, such as those formed in laboratory or in astrophysical objects, require deep knowledge of underlying charge state distribution of plasmas containing such ions. The sizable contribution of TR and QR resonances can in principle influence the charge state distribution and the cooling of collisionally ionized plasmas.

The simplest and most widely used model for collisionally ionized plasmas is the *coronal model* which was first applied to the solar corona. For this model, following conditions must be satisfied to be valid:

[1] The plasma is optically thin to its own radiation.

[2] The electron density is low so that the excited state populations are negligible compared to the ground state population.

[3] Electrons and ions are in thermal balance, and the steady-state equilibrium is reached both for bound atomic states and the ionization balance.

Under these assumptions, the equilibrium of collisionally ionized plasmas is determined by the balance of electron collisional ionization and high-temperature recombination rates. Therefore, the ionization balance under the coronal limit can be given by

$$\frac{N_{(q)}}{N_{(q-1)}} = \frac{\alpha_{(q-1)}^{ioniz}}{\alpha_{(q)}^{recomb}}, \tag{6.1}$$

where $N_{(q)}$ is the number of ions with charge state q, $\alpha_{(q-1)}^{ioniz}$ is the ionization rate coefficient and $\alpha_{(q)}^{recomb}$ is the recombination rate coefficient for X^{q+} ion.

According to the Eq. (6.1), the charge state distribution, in general, is determined by the rates of ionization $\alpha_{(q-1)}^{ioniz}$ and recombination $\alpha_{(q)}^{recomb}$. The significance of DR rates in the charge state distribution calculation is already established and experimentally verified by Foord *et al.* (2000) [113]. Since the TR and QR can also act as new recombination channels in the plasmas, it is necessary to include them into the charge state distribution calculations. This also means that omitting these additional recombination channels can lead to the prediction of mean ion charge state higher than it actually is.

In order to include TR and QR rates along with the RR and DR rates, the proper sets of electronic configurations with R-CI and CM are implemented in the calculation of the total recombination rate coefficients. Following the Refs. [151, 211], the radiative and resonant recombination rate coefficients are calculated for C-like iron ions according to the Eq. (2.2) and Eq. (2.13) using the FAC code. The investigation on C-like iron ions were chosen since they produce DR and TR resonances with almost comparable resonance strengths. The new total recombination rate coefficients of Fe^{20+} are shown
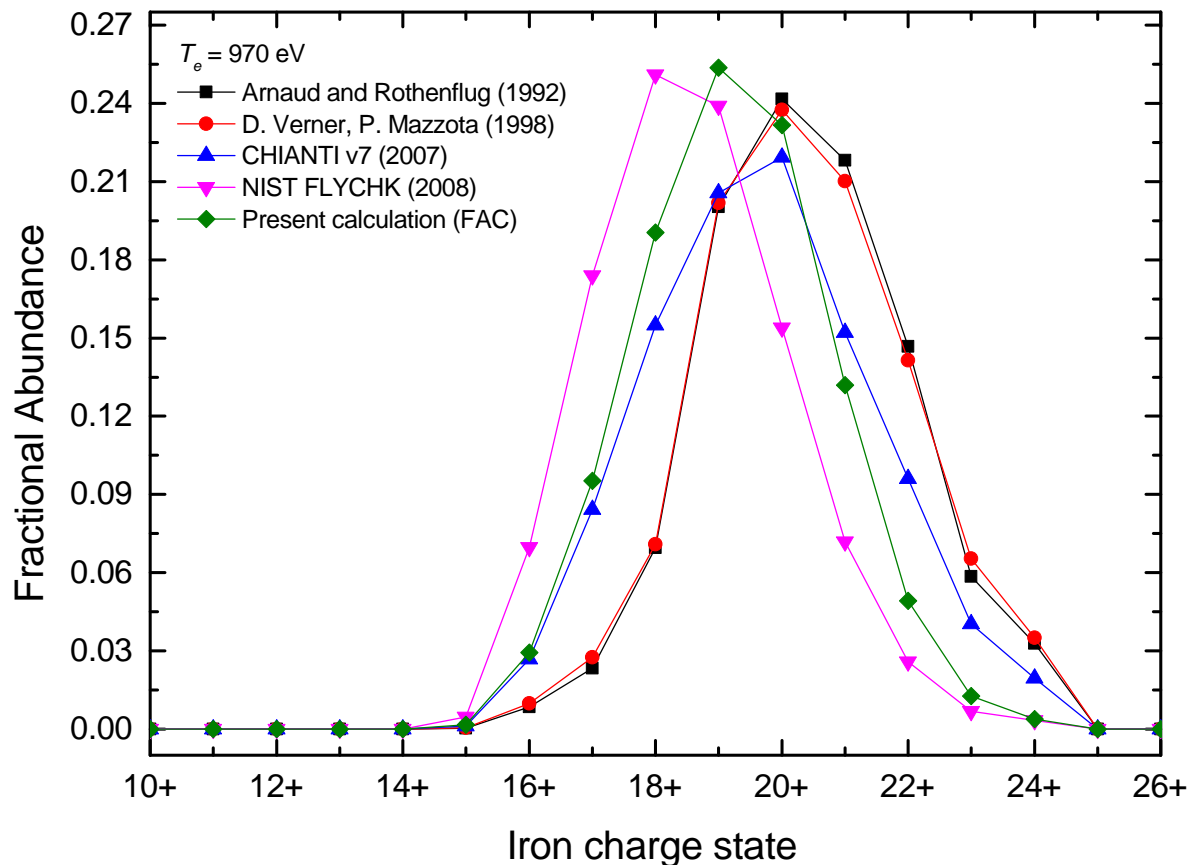
Figure 6.3: Fractional abundance of iron ions at electron temperature of $T_e \approx 970$ eV. The present calculation (green diamonds) is compared with the different ionization balance calculations: Arnaud and Rothenflug [209] (black squares), Verner and Mazzotta [210, 213] (red circles), CHIANTI code [214] (blue triangles) and FLYCHK code [215] (pink triangles).

in the Fig. 6.2 as a function of electron temperature (T_e) in the range of 100 to 10000 eV. Present calculations are then compared with the former calculations of Arnaud and Raymond (1992) [209, 212] and of Mazzotta (1998) [210]. The present calculations predict higher total recombination rates than the previous calculations. One of the reasons of this difference between the present and the former calculations could be the inclusion of TR and QR with the proper configuration mixing between the states.

The newly calculated total recombination rates were implemented into the calculation of charge state distribution of Fe ions, according to Eq. (6.1). The total ionization rates including direct ionization and the excitation autoionization rates are taken from D. A. Verner's online atomic database[1]. The fractional abundance of iron ions are then calculated at a fix electron temperature of $T_e \approx 970$ eV (or 10^7 K), shown in the Fig. 6.3.

---

[1]http://www.pa.uky.edu/~verner/atom.html
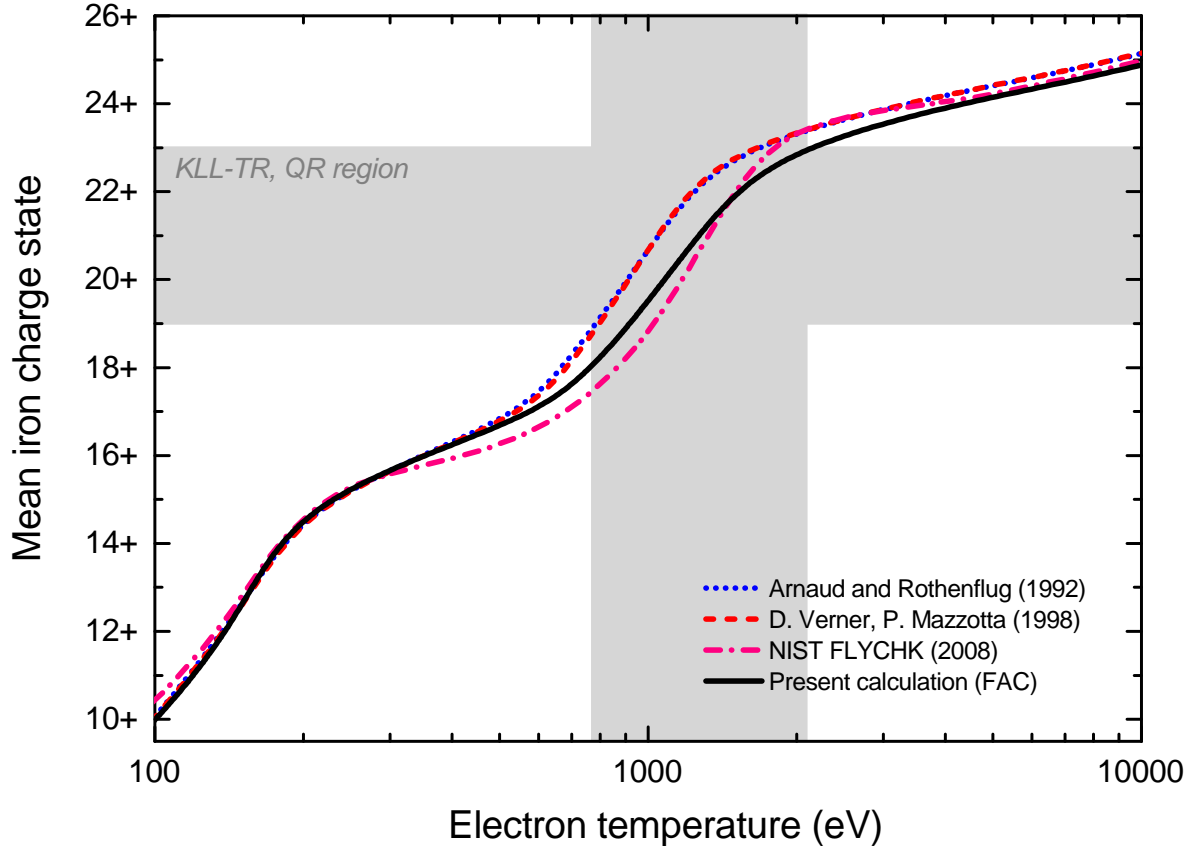
Figure 6.4: Mean charge state of iron ions as a function of electron temperature in the range of 100 to 10000 eV. The present calculation is compared with various ionization balance calculations, Refs. [65, 209, 210, 213, 215]

We see Fe^{19+} as maximally abundant ion at 970 eV temperature from our calculations, whereas the prediction of different databases of Arnaud and Rothenflug [209], and Verner and Mazzotta [210, 213] shows Fe^{20+} as most abundant ions at this temperature. This implies that the recombination rates predicted from the older databases are significantly lower than the present calculation. Even the most updated and widely used code in the astrophysical community CHIANTI [214] predicts the similar ion abundance. The strong inter-shell *KLL* TR resonances of C-like ions can be the one of the reasons behind this discrepancy since the inclusion of them reduces the number density of Fe^{20+} ions by recombining with the free electrons. Nonetheless, we cannot prove that the discrepancy is purely due to C-like TR resonances since we do not know the sets of configurations included in those calculations. Moreover, the FLYCHK code [215] of Nation Institute of Science and Technology (NIST) predicts even higher recombination rates, and conclude Fe^{18+} as a most abundant ion at a temperature of 970 eV in the collisionally ionized plasmas. The comparison between the different calculations is shown in Fig. 6.3.

In addition, not only TR and QR channels of C-like ions, but rather all inter-shell *KLL* TR QR resonances are included in the charge state distribution calculation in order to find the maximal abundant charge state of iron ions in the electron temperature range of 0.1–10 keV. Fig. 6.4 shows the predicted mean charge state of iron as a function of electron temperature. The predicted mean charge of iron significantly deviates from the other calculations in the region of temperature where iron ions are responsible in forming TR and QR resonances. This large divergence between the present and other calculations shows the importance of TR and QR resonances. It can be now interpreted that, neglecting sizable TR and QR resonances in the calculations can predict false mean charge state of the ion. However, it is not clear to us yet how much TR and QR resonances can contribute to the ionization balance of the plasmas, but we are inclined to believe that the importance of TR resonances is large and increases towards the ions with open-shell electronic configurations. Thus, the experiments measuring high-temperature recombination rates or the charge state distribution of iron ions are of interest in order to solve inconsistencies between these theoretical models.

6.1.2   Influence of HO on the polarization of $K\alpha$ x-ray line

The Compton polarimeter based on SiPIN diodes used in our experiment has limited energy resolution of ~ 3 keV FWHM at 13 keV [192]. Thus, it cannot separate the individual x-ray satellite lines of $K\alpha$ complex. The similar situation arises for the photoelectric polarimeter (micro-pattern gas detector) to be used in *XIPE* satellite mission [23] has energy resolution of ~ 1 keV FWHM at 5.4 keV [78]. Therefore, the polarization of $K\alpha$ x rays observed from these detectors include the contributions of all resonant recombination transitions as well as from continuum sources such as bremsstrahlung. Since the contribution of latter will depend on the energy resolution of the detector, here we calculate the cumulative effect of all resonant recombination transitions on the degree of linear polarization of $K\alpha$ x rays. For simplicity, we limited our analysis of x rays of the highest polarization which are emitted perpendicular to the collision axis, which would correspond to anisotropic electron distribution. In contrast, lower observed polarization values would be interpreted as the result of a less pronounced anisotropy or an observation at an acute angle to the beam axis.

For the calculation of total polarization of $K\alpha$ x rays, we assume optically thin plasmas (coronal limit), a good approximation for solar flares, (some) active galactic nuclei and tokamak plasmas. The charge state distribution $C^i(T_e)$ of both iron and krypton ions are calculated as a function of electron temperature by following the Ref. [151, 211].
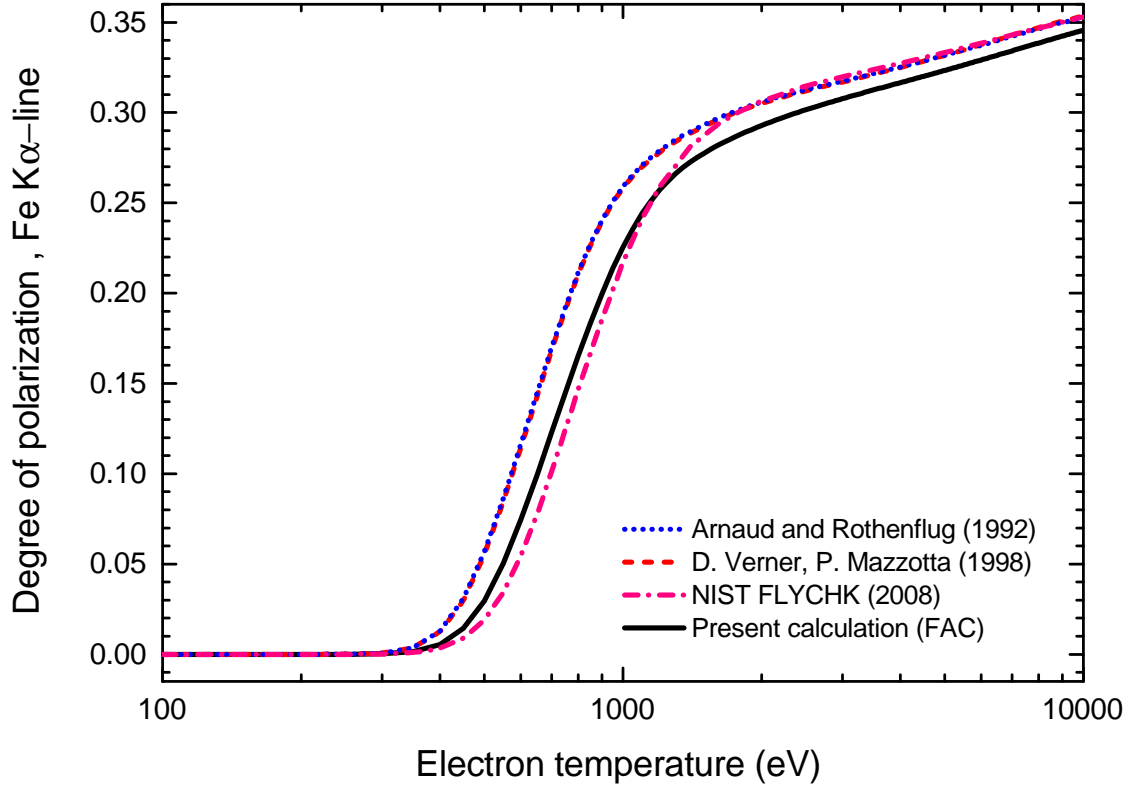
Figure 6.5: The total polarization of iron $K\alpha$ x-ray line as a function of electron temperature is calculated with the FAC code. The present calculation (black solid line) is compared with the calculations done with $C^i(T_e)$ available from Arnaud and Rothenflug [209] (blue dotted line), Verner and Mazzotta [210, 213] (red dashed line) and FLYCHK code [215] (magenta dot-dashed line).

The charge state distribution $C^i(T_e)$ together with the calculated resonance strength S_n^i and emission asymmetry $\mathcal{R}_n^i$ of individual resonant recombination transitions is used to calculate the total degree of linear polarization of x rays emitted by all KLL resonances. It can be expressed as:

$$P(T_e) = \frac{\sum\limits_{i,n} C^i(T_e) S_n^i \mathcal{R}_n^i / (1 - \mathcal{R}_n^i/3)}{\sum\limits_{i,n} C^i(T_e) S_n^i / (1 - \mathcal{R}_n^i/3)} \ , \tag{6.2}$$

where n being the resonance number. The factor $1/(1 - \mathcal{R}_n^i/3)$, according to Eq. (5.2), accounts for the anisotropy of x rays when they are observed perpendicular to the beam axis.

Fig. 6.5 shows the cumulative degree of linear polarization of $K\alpha$ x rays emitted by iron ions as a function of the electron temperature. The degree of polarization is found to be positive and increases as the temperature increases. The maximum value of
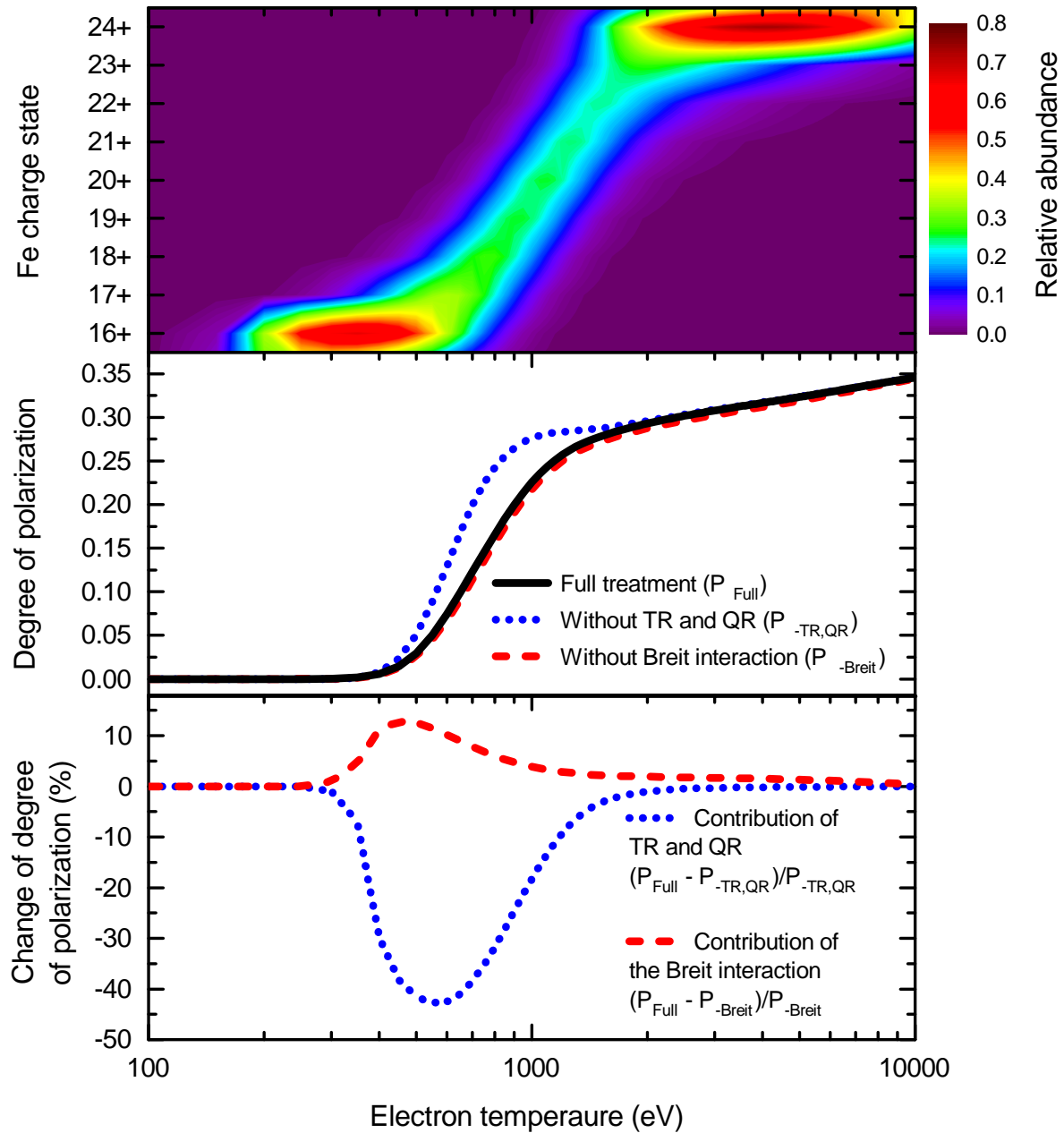
Figure 6.6: Top panel: Charge state distribution $C^i(T_e)$ in optically thin iron plasma as a function of temperature. Middle panel: Total polarization of iron $K\alpha$ x-ray line $P(T_e)$ calculated with the FAC code (black solid line). Hitherto neglected TR and QR resonances, as well as the Breit interaction, are taken into account. Bottom panel: The contributions of the TR and QR resonances (dotted blue line) and Breit interaction (red dashed line) to the degree of polarization are shown. They have a dominant effect at intermediate plasma temperatures, and strongly reduce the degree of polarization.

polarization is 35%. It corresponds to the x rays emitted by highly ionized states such as H-like or He-like ions. Similarly, using Eq. (6.2), the degree of polarization of $K\alpha$ x rays is calculated with $C^i(T_e)$ available from the various databases, see Fig. 6.5. They are compared with the present calculations and found a significant change in the degree of linear polarization in the temperature range from 500 to 2000 eV.

As can be understood from the Fig. 6.4, this discrepancy between the present and former calculations could be traced back once again to the inter-shell KLL TR and QR resonances of the highly charged iron. These TR and QR resonances are active in this range of electron temperatures where the discrepancy lies. Now the question is how much TR and QR resonance contributes to the total degree of linear polarization of Fe $K\alpha$ x rays. Hence, we again calculate the $P(T_e)$ as a function of electron temperature by neglecting TR and QR resonances from the calculations. Surprisingly, we found out that the hitherto neglected TR and QR have a dominant effect on the polarization in the range of temperatures found in many astrophysical sources. As shown for iron ions in the lower panels of Fig. 6.6, the contributions of TR and QR reduce the degree of polarization by approximately 50% at temperatures around $T_e = 600$ eV. At this temperature, the C-, N-, O-, F-, and Ne-like Fe ions are most abundant species in the plasmas. As can be viewed from Fig. 5.4, amongst these ions, the C- and N-like Fe ions exhibit strong KLL TR and QR transitions. Since the N-like ions populating TR transition (line 37) is nearly unpolarized, the C-like ions populating strong KLL TR transition (line 31) is responsible for this reduction in the degree of polarization of Fe $K\alpha$ x rays. To confirm that this observation was not accidental and specific only for iron ions, we made a similar study with krypton ions. Surprisingly, an analogous reduction in the degree of polarization of Kr $K\alpha$ x rays was observed for krypton ions at temperatures around $T_e = 2200$ eV commonly occurring in the tokamaks, see Fig. 6.7. Moreover, we also found out that the relativistic effect such as Breit interaction can affect the degree of linear polarization observed from the hot anisotropic iron plasmas. Fig. 6.6 shows the enhancement about 10% in the degree of linear polarization when the Breit interaction is considered in the calculations.

The present results show that, too simplified approach, i. e., neglecting higher-order resonances and relativistic effects in the calculations, can lead to the prediction of plasma polarization higher than it actually is. It also emphasizes our current lack of systematic understanding of atomic sources of polarization: as recently discovered TR and QR processes and the well-known relativistic effects have demonstrated to play a dominant role in the measurable x-ray polarization of a common type of astrophysical and laboratory plasmas.
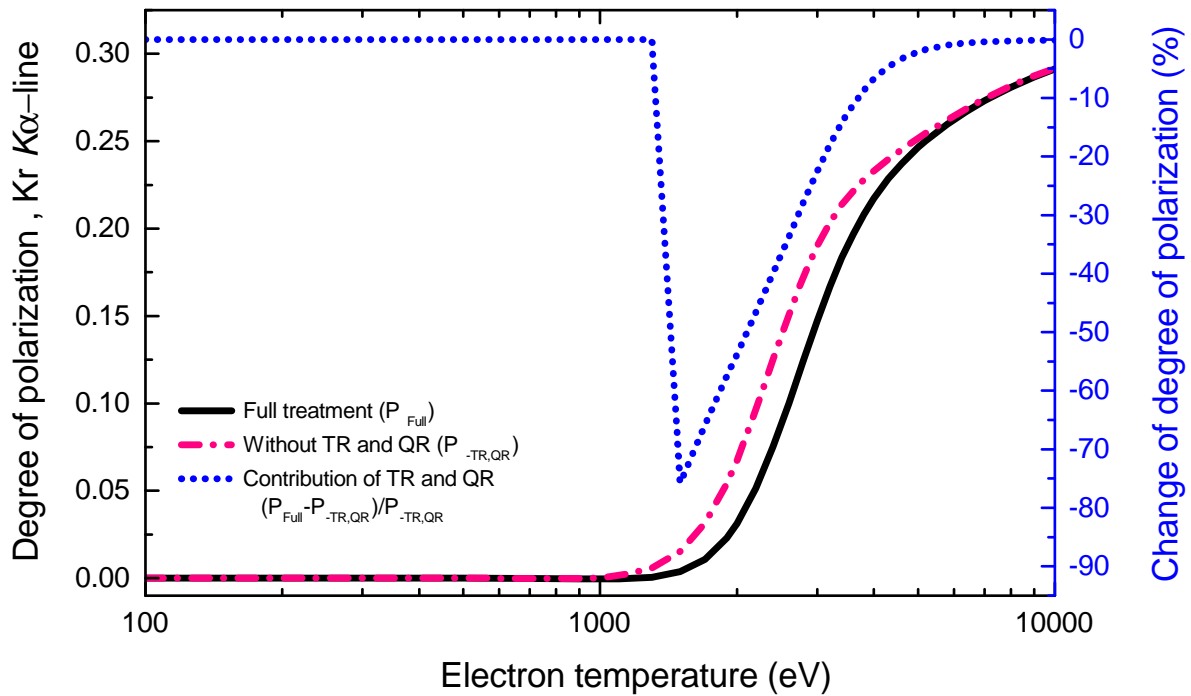
Figure 6.7: (Left Y-axis) The total polarization of krypton $K\alpha$ x-ray line (black solid line) calculated with FAC code. Magenta dash-dotted line corresponds to the calculation which neglect the TR and QR resonances. (Right Y-axis) The blue dotted line shows the reduction in the degree of linear polarization when TR and QR resonances are not considered in calculations.

6.2 Application of the plasma polarization diagnostics techniques at the EBIT

The ions excited by interactions with a directional beam of electrons may produce anisotropic and polarized line radiation. Due to this fact, the existence of directional electrons in the laboratory and astrophysical plasmas can be confirmed by measuring the polarization of the line radiation. This technique of plasma polarization spectroscopy [56] is already applied in several studies: tokamak [52], solar flares [30, 31, 143] and laser produced plasmas [53–55, 216]. Here, we diagnose the electron cyclotron motion within an electron beam propagating through a strong magnetic field of the EBIT by using the measurements of angular distribution and polarization of x rays.

The transversal energy component ($E_\perp$) and the pitch angle (γ) of an electron beam propagating inside the FLASH-EBIT is already discussed in the Sec. 3.2.3. Theoretical values of $E_\perp$ and γ were estimated by using optical theory of Herrmann and by using the principle of adiabatic magnetic flux invariance. Since we found a large difference in the estimated values from these two theories, the experimental determination of $E_\perp$ and γ is required in order to solve disparity between the models.

6.2.1 Experimental determination of the pitch angle and transversal energy of the electron beam

Theoretical treatment:

As mentioned earlier, electrons in an EBIT do not simply travel in the direction of beam propagation. Their path instead traces out a helix, as they spiral around the magnetic field lines aligned with the electron beam propagation axis. Thus, ions interaction with electrons, with velocity vectors that deviate from that of the beam propagation direction (as shown in Fig. 6.8).

An amount of change in emission asymmetry (or degree of polarization) depends on the pitch angle of the electron motion, which is the angle between the magnetic field lines $\vec{B}$ and electron velocity vector $\vec{\nu_e}$.

A simple expression can be derived to describe the change in the emission asymmetry $\mathcal{R}$ of the emitted radiation as a function of the pitch angle. As shown in Figure 6.8, the pitch angle γ introduce a new quantization axis of the electron-ion collision system. Therefore, the x-ray detector system sees either increase or decrease in the total intensity of the emitted photons. Following theoretical section, the new emission asymmetry $\mathcal{R}$
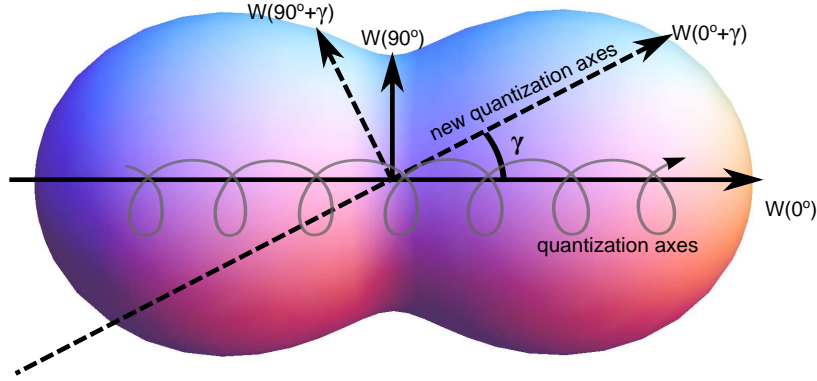
Figure 6.8: Emission asymmetry of the emitted photons with the introduction of the pitch angle γ, which is the angle between the magnetic field lines $\vec{B}$ and electron velocity vector $\vec{\nu_e}$.

of $E1$ x rays when the pitch angle γ is not zero ($\gamma \neq 0$) can be expressed as:

$$
\begin{aligned}
\mathcal{R} &= \frac{W(90\,^\circ + \gamma) - W(0\,^\circ + \gamma)}{W(90\,^\circ + \gamma)}, \\
&= \frac{[1 + \mathcal{A}_2\bar{\alpha}_2^{df} P_2(\cos(90^\circ + \gamma))] - [1 + \mathcal{A}_2\bar{\alpha}_2^{df} P_2(\cos(0^\circ + \gamma))]}{1 + \mathcal{A}_2\bar{\alpha}_2^{df} P_2(\cos(90^\circ + \gamma))}, \\
&= \frac{[1 + \mathcal{A}_2\bar{\alpha}_2^{df} P_2(\sin\gamma)] - [1 + \mathcal{A}_2\bar{\alpha}_2^{df} P_2(\cos\gamma)]}{1 + \mathcal{A}_2\bar{\alpha}_2^{df} P_2(\sin\gamma)}, \\
&= \frac{[1 + \mathcal{A}_2\bar{\alpha}_2^{df}(\frac{3}{2}\sin^2\gamma - \frac{1}{2})] - [1 + \mathcal{A}_2\bar{\alpha}_2^{df}(1 - \frac{3}{2}\sin^2\gamma)]}{1 + \mathcal{A}_2\bar{\alpha}_2^{df}(\frac{3}{2}\sin^2\gamma - \frac{1}{2})}, \\
&= \frac{3\mathcal{A}_2\bar{\alpha}_2^{df}(2\sin^2\gamma - 1)}{2 + \mathcal{A}_2\bar{\alpha}_2^{df}(3\sin^2\gamma - 1)}.
\end{aligned}
\tag{6.3}
$$

Relationship to the unidirectional case:

In ideal conditions, electron beam propagating inside an EBIT is perfectly unidirectional. In such cases, we assume that the pitch angle γ is zero ($\gamma = 0$). Therefore, the emission asymmetry $\mathcal{R}_0$ can be expressed as:

$$
\mathcal{R}_0 = \frac{W(90\,^\circ) - W(0\,^\circ)}{W(90\,^\circ)} = -\frac{3\mathcal{A}_2\bar{\alpha}_2^{df}}{2 - \mathcal{A}_2\bar{\alpha}_2^{df}}.
\tag{6.4}
$$

By combining the equations (6.4) and (6.3), the new intensity ratio $\mathcal{R}$ takes the form of

$$\mathcal{R} = \frac{\mathcal{R}_0(2\sin^2\gamma - 1)}{\mathcal{R}_0\sin^2\gamma - 1}. \tag{6.5}$$

By comparing the emission asymmetry $\mathcal{R}$ inferred from the experiment ($\gamma \neq 0$) to those predicted by theory $\mathcal{R}_0$ ($\gamma = 0$), we can determine the experimental value of the pitch angle and transversal energy component of the electron beam:

$$E_\perp = \frac{\mathcal{R}_0 - \mathcal{R}}{\mathcal{R}_0(2 - \mathcal{R})} \; E_e, \tag{6.6}$$

$$\gamma = \sin^{-1}\sqrt{\frac{\mathcal{R}_0 - \mathcal{R}}{\mathcal{R}_0(2 - \mathcal{R})}}. \tag{6.7}$$

where E_e is the electron beam energy and $\sin^2\gamma = E_\perp/E_e$ from the Fig. 3.2.3.

Experimental data and its analysis:

The emission asymmetries of x rays produced by resonant recombination into $Fe^{24+\ldots18+}$ and $Kr^{34+\ldots28+}$ ions were measured in our experiments, see chapter 5. The emission asymmetries indicate the alignment of the resonance state with respect to the quantization axis. An electron beam propagation direction acts as quantization axis in an EBIT. Following the theoretical description, we compare the experimental emission asymmetries $\mathcal{R}$ of "well-resolved" (not blended) transitions with the theoretical FAC calculated values $\mathcal{R}_0$. Therefore, according to the Eq. (6.6) and (6.7), we can determine the experimental values of pitch angle and transversal energy of the electron beam.

6.2.2 Results

The inferred values of $E_\perp$ and γ are given in the Tables 6.1 and 6.2, likewise they are shown graphically in Fig. 6.9.

The experimental uncertainties are determined as a quadrature sum of errors associated with Eqs. (6.6) and (6.7). They can be expressed as:

$$\Delta E_\perp = \frac{\mathcal{R}_0 - 2}{\mathcal{R}_0(\mathcal{R} - 2)^2} \; \Delta\mathcal{R} \; E_e, \tag{6.8}$$

$$\Delta\gamma = \frac{\mathcal{R}_0 - 2}{2(\mathcal{R} - 2)\sqrt{(\mathcal{R} - \mathcal{R}_0)(\mathcal{R}(\mathcal{R}_0 - 1) - \mathcal{R}_0)}} \; \Delta\mathcal{R}. \tag{6.9}$$
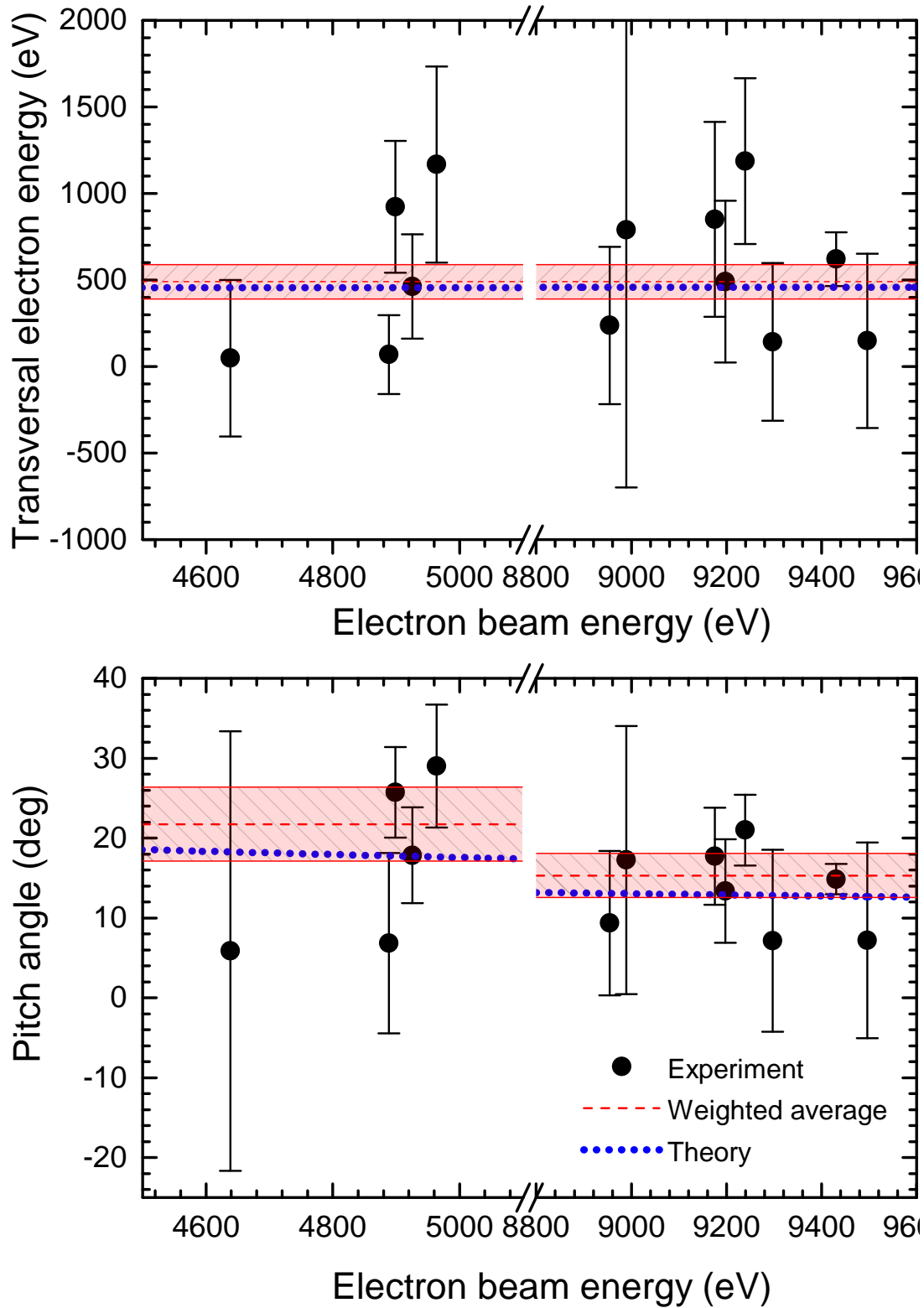
Figure 6.9: Experimental Transversal electron energy and pitch angle plotted against the electron beam energy. The red shaded area represents weighted average value and containing uncertainty. Blue dotted line represents the theoretical estimate that depends on experimental electron beam conditions: $B_c \approx 0$, $B = 6$ T, $r_c = 1.5$ mm and $T_c = 1400$ K.

Table 6.1: The value of $E_\perp$ inferred from the observed emission asymmetry $\mathcal{R}$ in the experiment. The label follows the element and the line numbers from Tables 5.2 and 5.4. The value of $\mathcal{R}_0$ calculated by using FAC code. Theoretical values of $E_\perp$ are estimated from the calculation of Herrmann radius r_H for following electron beam conditions, $B_c \approx 0$, $B = 6$ T, $r_c = 1.5$ mm and $T_c = 1400$ K. The weighted average μ and its error $\Delta\mu$ is given at the end of the table.

Label	E_e (eV)	$\mathcal{R}_0$	$\mathcal{R}$		$E_\perp$ (eV)	$E_\perp$ (eV)	
	th	th	exp	error	th	exp	error
Fe-4	4638.5	0.500	0.508	0.072	455.57	48.38	452.78
Fe-24	4888.3	-0.446	-0.431	0.050	455.77	69.13	227.65
Fe-25	4898.9	0.231	0.151	0.035	455.81	923.19	380.30
Fe-28	4925.7	0.432	0.366	0.045	455.80	462.57	301.28
Fe-32	4964.0	0.129	0.184	0.026	455.83	1167.98	566.38
Kr-4	8954.0	-0.842	-0.780	0.116	457.70	237.17	453.63
Kr-6	8989.6	0.500	0.431	0.136	457.72	790.67	1489.89
Kr-14	9175.3	0.492	0.420	0.050	457.77	849.83	563.26
Kr-15	9197.8	0.416	0.380	0.035	457.78	491.34	467.07
Kr-17	9239.2	0.481	0.381	0.043	457.79	1186.43	478.65
Kr-19	9296.8	0.404	0.394	0.032	457.81	143.29	455.66
Kr-24	9430.5	0.308	0.273	0.009	457.84	620.53	156.33
Kr-26	9496.2	-0.555	-0.533	0.074	457.86	148.61	504.21
						$\mu = 489.5$	$\Delta\mu = 94.4$

Table 6.2: Experimental values and theoretical estimates of the pitch angle γ.

Label	E_e (eV)	γ (degree)	γ (degree)	
	th	th	exp	error
Fe-4	4638.5	18.26	5.86	27.53
Fe-24	4888.3	17.78	6.83	11.30
Fe-25	4898.9	17.76	25.73	5.69
Fe-28	4925.7	17.71	17.85	6.01
Fe-32	4964.0	17.64	29.02	7.71
			$\mu = 21.74$	$\Delta\mu = 3.44$
Kr-4	8954.0	13.07	9.37	9.04
Kr-6	8989.6	13.04	17.25	16.76
Kr-14	9175.3	12.91	17.72	6.07
Kr-15	9197.8	12.89	13.36	6.47
Kr-17	9239.2	12.86	21.00	4.44
Kr-19	9296.8	12.82	7.13	11.40
Kr-24	9430.5	12.73	14.86	1.92
Kr-26	9496.2	12.68	7.19	12.26
			$\mu = 15.32$	$\Delta\mu = 1.58$

The emission asymmetry of a large number of transitions were measured as a function of the electron beam energy, thereby, we can determine values of pitch angle and transversal energy component from each transition. We give the weighted average value and the mean error of $E_\perp$ and γ by using following standard statistical formulas. Weighted average of the data points:

$$\mu = \frac{\sum \left(\frac{X_i}{\Delta X_i^2} \right)}{\sum \left(\frac{1}{\Delta X_i^2} \right)},$$

and the uncertainty:

$$\Delta \mu = \sqrt{\frac{1}{\sum \left(\frac{1}{\Delta X_i^2} \right)}}.$$

The theoretical values of $E_\perp$ and γ are estimated according to the Eqs. (3.7) and (3.8) with the following electron beam conditions: $B_c \approx 0$, $B = 6$ T, $r_c = 1.5$ mm and $T_c = 1400$ K. The theoretical estimated values are shown in the Fig. 6.9 as blue dotted line. The experimental $E_\perp$ values range from 50 to 1200 eV. These large inconsistencies arise from the poor Gaussian fit for the relatively weak transitions. The weighted average of $E_\perp$ is found to be 490.5 ± 94.4 eV. Similarly, we inferred the pitch angle γ of the electron beam, listed in Table 6.2. In case of iron we get the average value of $\gamma = 21.7° \pm 3.5°$, while in case of krypton we get the average value of $\gamma = 15.3° \pm 1.6°$. The experimentally inferred average values of $E_\perp$ and γ are in good agreement with the theoretical estimates of Herrmann's optical theory. Moreover, the electron beam radius at the trap was also deduced from the experimental value of $E_\perp$ according to Eq. 3.7. The experimental value of the electron beam radius was found to be 23.6 ± 4.2 μm which is also in agreement with Herrmann's optical theory.

6.2.3   Conclusion

The electron cyclotron motion within an electron beam propagating through a strong magnetic field was studied at the electron beam ion trap FLASH-EBIT at the Max Planck Institute for Nuclear Physics in Heidelberg. It was probed by measuring the angular distribution of the x rays produced by resonant electron recombination into highly charged iron and krypton ions. From the emission asymmetries of x rays, it was inferred that the electron cyclotron motion accounted for 490 ± 94 eV of total electron beam energy. The experimental values of $E_\perp$, γ, and r_H are in good agreement with the prediction of the optical theory of electron beam by Herrmann [187]. This is reassuring our measurements since the optical theory of Herrmann was used as one of the primitive

principles in the design of the electron beam ion trap [165]. The measured value does not agree with the estimates derived from the principle of adiabatic magnetic flux invariance. Since the fast moving electrons travel across the strong magnetic field gradient, from approximately few microteslas magnetic field at the gun to the 6 tesla at the trap, which invalidate the applicability of the principle of adiabatic magnetic flux invariance [189].

Chapter 7

Conclusions and Future work

The thesis deals with the experimental and theoretical study of the angular distribution and polarization of x rays emitted by highly charged iron and krypton ions in the process of resonant recombination. The aim of this work was to provide benchmark polarization measurements of x rays emitted by hot plasmas. The particular relevance of this work is for astrophysical plasmas in the framework of a *XIPE* space mission [23, 78] of ESA and for fusion plasmas in the framework of the *ITER* project [100, 145].

In the first experiment, the linear polarization of K-shell x rays emitted in dielectronic and radiative recombination of highly charged krypton ions was measured. The measurements were carried out at the electron beam ion trap (EBIT) using the Compton polarimetry technique. For this purpose, a simple and versatile Compton polarimeter for 10–30 keV x rays was developed using SiPIN diode detectors. Theoretical polarization calculations were performed using the Flexible Atomic Code (FAC), and they are in excellent agreement with the experimental results. Before this work, the contribution of the Breit interaction to the degree of linear polarization was assumed to be strong and relevant only for heavy elements. In the present experiment, for the first time, this contribution was precisely examined for the mid -Z element krypton. The Breit interaction contribution to electron–electron interaction was demonstrated to change the degree of linear polarization by 13% for a resonance state of Li-like krypton. The present work also demonstrates the application of the Compton polarimetry technique at the EBIT. It provides significant advantages over the Bragg polarimetry technique, previously used for DR polarization measurements at EBITs, by measuring both the degree and the angle of polarization and being applicable in a broad energy range.

In the second experiment, the polarization of K-shell x rays emitted in the resonant

recombination of highly charged iron and krypton was accessed by measuring the angular distribution of the emitted x rays. Here, the x-ray emission from highly charged ions excited by a unidirectional electron beam was observed with two x-ray detectors; one at 90° and another at 0° with respect to the electron beam axis. An excellent collision energy resolution was achieved by using an evaporative cooling technique. We note that this resolution was higher than in any previously reported measurement. It allowed resolving many DR, TR, and QR resonances. The x-ray emission asymmetry (or degree of polarization) was measured for 73 *KLL* resonances in iron and krypton. This is a significant progress compared to the direct polarization measurements (first experiment) where just 5 dielectronic recombination resonances could be accessed in a reasonable time. The experimental results are compared with the theoretical calculations of FAC and RATIP codes. With a few exceptions, the agreement is excellent, even for inter-shell TR and QR resonances. Furthermore, the contribution of the Breit interaction is systematically investigated for all resonances. We observed that the degree of linear polarization of x rays following only one resonance state in Li-like ions ($[1s2s^2 2p_{1/2}]_1$) manifests a strong sensitivity towards the Breit interaction.

The results of both experiments comprehensively benchmark relativistic distorted-wave calculations and confirm the accuracy of FAC and RATIP computer codes. A good agreement between theoretical predictions and experimental results of polarization of x rays due to K-shell DR, TR, and QR resonances is essential for developing reliable plasma polarization diagnostics. Such diagnostics may provide information about the momentum distribution of plasma electrons at specific energies [50, 52, 100, 138, 145].

Both experimental techniques are straightforward and sensitive. Moreover, they are applicable to all elements of astrophysical and fusion research interest. They allow covering a wide range of recombination resonances in highly charged ions of elements from a significant portion of the periodic table. Alignment resulting from many collisional processes, such as radiative recombination, as well as electron-impact excitation and ionization, can also be studied with the present techniques. Due to their high sensitivities, our techniques can also be used for studies of weak radiative transitions, or, alternatively, for high accuracy studies of stronger transitions, in particular of those sensitive to the effects of quantum electrodynamics.

The polarization of DR x rays is currently one of the most sensitive probes for the details of electron–electron interaction. For example, the degree of linear polarization of x rays produced by Li-like DR resonance is not only changed by the Breit interaction, but also by the generalized Breit interaction (GBI). The quantitative change in the degree of linear polarization due to the GBI at high-Z atomic ions was recently shown

by Tong and coworkers [203], see Fig. 5.11. The absolute change in the degree of linear polarization due to the virtual photon frequency dependence of the GBI is very small, ∼8% for Li-like Hg and Bi ions. In principle, it is possible to produce Li-like Hg and Bi ions at the Heidelberg EBIT, and it is possible to measure the GBI effect with our experimental techniques. To achieve this, a Compton polarimeter based on the annular segmented germanium detector is being built by our research group. This polarimeter should achieve the energy resolution of 2 keV and work in the x-ray energy range from 30 keV to 2 MeV. With this polarimeter, it will be possible to access GBI effects to the degree of linear polarization. We plan to make such measurements in the near future.

The application of polarimetry techniques at lower energies was so far limited by the energy resolution of the detectors. For instance, the SiPIN diodes used in the present polarimeter have x-ray energy resolution of 3 keV FWHM at 13 keV [192]. A better resolution polarimeter is required to measure the polarization of x-ray lines in densely-populated spectra. For this purpose, another polarimeter was built by our research group. It is based on the segmented silicon drift detectors. These detectors have the energy resolution of 140 eV at 6 keV and they are optimized for the energies from 6 to 30 keV. Both polarimeters can be applied for polarization diagnostics of hot laboratory plasmas such as those of tokamaks [51, 217], Z-pinches [49, 218, 219], electron cyclotron resonance (ECR) traps [220] and high-intensity lasers [55].

A further central point of this thesis has been the plasma diagnostics and modeling. A coronal model was developed in order to determine the recombination rate coefficients and ionization balance of optically thin iron plasma. Hitherto neglected inter-shell TR and QR channels of iron were included in the calculation for the first time. It was observed that the TR and QR processes strongly affect the recombination rate coefficients and ionization balance of the plasmas. The similar model has also been used to estimate the total polarization of $K\alpha$ x-ray line emitted by hot anisotropic iron and krypton plasmas. Once again the TR and QR was observed to play a dominant role in the x-ray polarization. Both findings pinpoint the urgent need of systematic inclusion of high-order effects in the corresponding plasma models, otherwise the interpretation of ionization balance and the polarization of x rays emitted by hot anisotropic plasmas can be misunderstood.

Recently, the importance of TR and QR was also recognized by Beiersdorfer [66] with regard to the reported discrepancy in the ionization balance measurement of tungsten in plasmas produced in the *ASDEX* Upgrade tokamak [64]. Since tungsten and iron data (cf. Fig. 6.3) are important in *ITER* tokamak and in astrophysically relevant plasmas, the experimental studies of ionization balance are highly desirable to resolve

such discrepancies. Such experiments can be made at the electron beam ion traps by creating a plasma with a certain energy distribution, e. g., Maxwellian distributions of given temperature [221–223]. We plan to produce such Maxwellian plasmas at the Heidelberg electron beam ion trap in order to measure the ionization balance of the collisionally ionized iron plasmas. At the same time, we plan to use the segmented silicon drift detector to measure the polarization of iron K-shell x-ray lines that are highly important in astrophysics.

The experimental data of polarization measurements were used to investigate the electron cyclotron motion within an electron beam propagating through a strong magnetic field of an electron beam ion trap. The transversal energy component and the pitch angle of the electron beam were extracted, and the results are in a good agreement with the optical theory of Herrmann [187]. It is important to determine the transverse energy of the electron beam since they have systematic effects on the polarization as well as the cross section measurements. This technique demonstrates the suitability of resonant recombination polarization measurements for directional diagnostics of electron beams inside the hot anisotropic plasmas. Such application of polarization measurements in plasma diagnostics was also recently demonstrated by our research group. A test measurement was conducted using the Compton polarimeter at superconducting ECR source in Laboratoire Kastler Brossel in Paris. In the preliminary data analysis, a high degree of polarization ($P \approx 70\%$) of x rays emitted by xenon plasma with 15 keV electron temperature was observed [224]. The results indicate the localization of hot electrons in a certain region of the magnetic field rather than being distributed across the whole ECR plasma volume.

To sum up, the present comprehensive experimental and theoretical studies opens numerous possibilities for diagnostics of anisotropies of hot laboratory and astrophysical plasmas.

Appendix A

KLL DR calculation of He-like to O-like iron ($Z{=}26$)

As described in section 2.2.2; the resonance energy E_{res}, resonance strength S^{DR}, alignment parameter $\mathcal{A}_2$, "effective" intrinsic anisotropy parameter $\bar{\alpha}_2^{df}$ and the degree of linear polarization of x rays P_L are calculated by the use of Flexible atomic code (FAC), given in the following tables. Theoretical calculations with only the Coulomb repulsion (C) are compared with a full treatment of the electron–electron interaction (C+BI).

EXPLANATION OF THE TABLES:

FAC level	The index of the energy levels in FAC.
Process	Order of the recombination process; DR: Dielectronic Recombination, TR: Trielectronic Recombination, QR: Quadruelectronic Recombination.
J_d	Total angular momentum of the intermediate excited state $|d\rangle$.
Configuration	The intermediate excited state configuration of the resonances are given in the *j-j* coupling notation, where subscript following the round brackets denotes angular momentum of the coupled subshells and another subscript following the square bracket denotes the total angular momentum of the state.
E_{res}	Resonance Energy in eV.
S^{DR}	Resonance Strength in units of $(\times10^{-21}\text{cm}^2 eV)$ calculated using equations (2.12).
$\bar{\alpha}_2^{df}$	The "effective" intrinsic anisotropy parameter weighted by the $E1$ radiative rates A_r^{df}, i. e., $\bar{\alpha}_2^{d} = \sum_f A_r^{df} \alpha_2^{df} / \sum_f A_r^{df}$.
$\mathcal{A}_2$	Alignment parameter is calculated using equation (2.27).
P_L	Degree of linear polarization (or emission asymmetry $\mathcal{R}$) calculated using equation (2.32).
C	Coloumb potential only.
C+BI	Coloumb+Breit interaction (fully relativistic calculation).

Table A.1: Calculated **He-like iron** KLL DR resonance energies E_{res} (in eV), resonance strength S^{DR} (in 10^{-21}cm^{2}eV) (C+BI = Coulomb+Breit, C = Coulomb only), intrinsic anisotropy parameter $\bar{\alpha}_2^{df}$, alignment parameter $\mathcal{A}_2$, and degree of linear polarization P_L. The intermediate state configuration of the resonances are given in the j-j coupling notation, where subscript following the round brackets denotes angular momentum of the coupled subshells and another subscript following the square bracket denotes the total angular momentum of the state.

FAC level	Process	J_d	Configuration	E_{res}	S^{DR}		$\bar{\alpha}_2^{df}$	$\mathcal{A}_2$		P_L	
					C	C+BI		C	C+BI	C	C+BI
4	DR	1/2	$[1s(2s^2)_0]_{1/2}$	4554.4	19.696	19.816	0.000	0.000	0.000	0.000	0.000
5	DR	1/2	$[(1s2s)_1 2p_{1/2}]_{1/2}$	4565.9	0.065	0.064	0.000	0.000	0.000	0.000	0.000
6	DR	3/2	$[(1s2s)_1 2p_{1/2}]_{3/2}$	4569.6	1.342	0.389	0.500	-1.000	-1.000	0.600	0.600
7	DR	5/2	$[(1s2s)_1 2p_{3/2}]_{5/2}$	4580.9	-	-	-	-	-	-	-
8	DR	1/2	$[(1s2s)_0 2p_{1/2}]_{1/2}$	4607.8	45.749	54.692	0.000	0.000	0.000	0.000	0.000
9	DR	3/2	$[(1s2s)_1 2p_{3/2}]_{3/2}$	4616.7	0.116	0.823	0.500	-1.000	-1.000	0.600	0.600
10	DR	1/2	$[1s(2p_{1/2}^2)_0]_{1/2}$	4624.2	0.235	0.083	0.000	0.000	0.000	0.000	0.000
11	DR	1/2	$[(1s2s)_1 2p_{3/2}]_{1/2}$	4631.2	64.064	61.188	0.000	0.000	0.000	0.000	0.000
12	DR	3/2	$[(1s2p_{1/2})_0 2p_{3/2}]_{3/2}$	4632.4	1.638	0.874	-0.396	-1.000	-1.000	-0.741	-0.741
13	DR	3/2	$[(1s2s)_0 2p_{3/2}]_{3/2}$	4634.5	0.943	0.943	0.500	-1.000	-1.000	0.600	0.600
14	DR	5/2	$[(1s2p_{1/2})_1 2p_{3/2}]_{5/2}$	4638.5	42.340	41.424	0.374	-1.069	-1.069	0.500	0.500
15	DR	3/2	$[(1s2p_{1/2})_1 2p_{3/2}]_{3/2}$	4658.3	210.249	207.058	0.400	-1.000	-1.000	0.500	0.500
16	DR	1/2	$[(1s2p_{1/2})_1 2p_{3/2}]_{1/2}$	4659.3	1.128	1.674	0.000	0.000	0.000	0.000	0.000
17	DR	5/2	$[1s(2p_{3/2}^2)_2]_{5/2}$	4663.9	279.999	281.691	0.374	-1.069	-1.069	0.500	0.500
18	DR	3/2	$[1s(2p_{3/2}^2)_2]_{3/2}$	4677.5	72.096	64.605	-0.387	-1.000	-1.000	-0.720	-0.720
19	DR	1/2	$[1s(2p_{3/2}^2)_0]_{1/2}$	4697.8	25.161	24.518	0.000	0.000	0.000	0.000	0.000

Table A.2: Same as Table A.1, but for **Li-like iron.**

FAC level	Process	J_d	Configuration	E_{res}	S^{DR} C	S^{DR} C+BI	$\bar{\alpha}_2^{df}$ C	$\bar{\alpha}_2^{df}$ C+BI	A_2 C	A_2 C+BI	P_L C	P_L C+BI
13	DR	0	$[1s2s^2 2p_{1/2}]_0$	4644.9	0.860	0.797	0.000	0.000	0.000	0.000	0.000	0.000
14	DR	1	$[1s2s^2 2p_{1/2}]_1$	4646.8	11.381	11.359	0.607	0.706	0.694	0.694	-0.819	-0.800
15	DR	2	$[1s2s^2 2p_{3/2}]_2$	4660.0	5.004	4.946	-0.156	-0.837	-0.839	-0.839	-0.210	-0.210
16	DR	1	$[(1s2s)_1 2p^2_{1/2}]_1$	4661.6	1.286	1.091	-0.001	-0.025	-0.012	-0.012	0.000	0.000
17	DR	2	$[((1s2s)_1 2p_{1/2})_{1/2} 2p_{3/2}]_2$	4669.1	0.829	0.572	-0.415	-0.604	-0.645	-0.652	-0.430	-0.469
18	DR	3	$[((1s2s)_1 2p_{1/2})_{3/2} 2p_{3/2}]_3$	4675.5	7.005	6.897	0.346	-0.990	-0.990	-0.990	0.438	0.438
19	DR	1	$[1s2s^2 2p_{3/2}]_1$	4678.2	3.396	2.718	0.684	0.650	0.678	0.678	-0.858	-0.906
20	DR	0	$[(1s2s)_0 2p^2_{1/2}]_0$	4708.6	0.894	1.012	0.000	0.000	0.000	0.000	0.000	0.000
21	DR	1	$[((1s2s)_1 2p_{1/2})_{1/2} 2p_{3/2}]_1$	4712.0	34.711	34.512	0.470	-0.645	-0.635	-0.635	0.395	0.390
22	DR	2	$[((1s2s)_1 2p_{1/2})_{3/2} 2p_{3/2}]_2$	4713.8	117.717	117.510	0.369	-0.599	-0.599	-0.599	0.298	0.298
23	DR	3	$[(1s2s)_1 (2p^2_{3/2})_2]_3$	4717.7	161.106	163.033	0.346	-0.990	-0.990	-0.990	0.438	0.438
24	DR	1	$[(1s2s)_1 (2p^2_{3/2})_2]_1$	4718.8	64.552	62.210	-0.258	-0.708	-0.706	-0.706	-0.302	-0.301
25	DR	2	$[(1s2s)_1 (2p^2_{3/2})_2]_2$	4726.0	47.113	45.549	-0.354	-0.762	-0.780	-0.780	-0.468	-0.481
26	DR	1	$[((1s2s)_0 2p_{1/2})_{1/2} 2p_{3/2}]_1$	4735.4	13.795	13.794	-0.106	-0.002	-0.007	-0.007	-0.001	-0.001
27	DR	0	$[((1s2s)_1 2p_{1/2})_{3/2} 2p_{3/2}]_0$	4737.3	0.463	0.369	0.000	0.000	0.000	0.000	0.000	0.000
28	DR	2	$[((1s2s)_0 2p_{1/2})_{1/2} 2p_{3/2}]_2$	4745.7	58.278	55.213	0.147	-1.168	-1.171	-1.171	0.236	0.237
29	DR	1	$[(1s2s)_1 (2p^2_{3/2})_0]_1$	4749.6	11.013	11.318	-0.021	-0.008	-0.010	-0.010	0.000	0.000
30	DR	2	$[1s2s^2 2p_{3/2}]_2$	4751.0	0.281	0.303	0.028	-0.837	-0.840	-0.840	0.035	0.035
31	DR	2	$[(1s2s)_0 (2p^2_{3/2})_2]_2$	4757.4	20.270	20.217	0.417	-1.187	-1.185	-1.185	0.594	0.594
32	DR	1	$[(1s2s)_1 (2p^2_{3/2})_2]_1$	4767.5	2.346	1.790	-0.351	-0.573	-0.566	-0.566	-0.336	-0.331
33	DR	0	$[(1s2s)_0 (2p^2_{3/2})_0]_0$	4775.6	7.873	7.841	0.000	0.000	0.000	0.000	0.000	0.000
34	DR	1	$[1s2s^2 2p_{3/2}]_1$	4780.2	0.207	0.198	0.594	0.683	0.697	0.697	-0.764	-0.784
35	TR	2	$[1s2p_{1/2}(2p^2_{3/2})_2]_2$	4781.8	0.361	0.377	0.348	-0.837	-0.840	-0.840	0.380	0.382
36	TR	3	$[1s2p_{1/2}(2p^2_{3/2})_2]_3$	-	-	-	-	-	-	-	-	-
37	TR	1	$[1s2p_{1/2}(2p^2_{3/2})_2]_1$	4792.1	0.111	0.108	-0.134	0.690	0.695	0.695	0.132	0.133
38	TR	2	$[1s2p_{1/2}(2p^2_{3/2})_2]_2$	4800.9	0.664	0.694	-0.417	-0.837	-0.840	-0.840	-0.635	-0.637
39	TR	0	$[1s2p_{1/2}(2p^2_{3/2})_0]_0$	4805.8	0.397	0.376	0.000	0.000	0.000	0.000	0.000	0.000
40	TR	1	$[1s2p_{1/2}(2p^2_{3/2})_0]_1$	4807.8	1.108	1.155	0.119	0.706	0.700	0.700	-0.131	-0.130
41	TR	2	$[1s2p^3_{3/2}]_2$	4815.6	1.307	1.348	-0.402	-0.837	-0.840	-0.840	-0.607	-0.609
42	TR	1	$[1s2p^3_{3/2}]_1$	4830.8	0.064	0.032	0.335	-0.002	0.557	0.557	0.001	-0.309

Table A.3: Same as Table A.1, but for **Be-like iron**.

FAC level	Process	J_d	Configuration	E_{res}	S^{DR} C	S^{DR} C+BI	$\bar{\alpha}_2^{df}$	$\mathcal{A}_2$ C	$\mathcal{A}_2$ C+BI	P_L C	P_L C+BI
25	DR	1/2	$[1s2s^22p_{1/2}^2]_{1/2}$	4755.8	1.030	0.932	0.000	0.000	0.000	0.000	0.000
26	DR	3/2	$[(1s2s^22p_{1/2})_02p_{3/2}]_{3/2}$	4764.7	0.063	0.032	-0.396	-1.000	-1.000	-0.740	-0.740
27	DR	5/2	$[(1s2s^22p_{1/2})_12p_{3/2}]_{5/2}$	4770.3	5.792	5.382	0.364	-1.069	-1.069	0.489	0.489
28	DR	5/2	$[(1s2s)_12p_{1/2}^22p_{3/2}]_{5/2}$	4780.9	-	0.000	-0.043	-1.069	-1.069	-0.071	-0.071
29	DR	1/2	$[(1s2s^22p_{1/2})_12p_{3/2}]_{1/2}$	4789.1	9.437	10.757	0.000	0.000	0.000	0.000	0.000
30	DR	3/2	$[(1s2s^22p_{1/2})_12p_{3/2}]_{3/2}$	4789.4	124.417	121.453	0.392	-1.000	-1.000	0.492	0.492
31	DR	5/2	$[1s2s^2(2p_{3/2}^2)]_{5/2}$	4794.4	147.485	145.722	0.355	-1.069	-1.069	0.478	0.478
32	DR	3/2	$[1s2s^2(2p_{3/2}^2)]_{3/2}$	4806.9	48.590	43.251	-0.382	-1.000	-1.000	-0.709	-0.709
33	DR	1/2	$[1s2s^2(2p_{3/2}^2)0]_{1/2}$	4812.5	40.995	40.852	0.000	0.000	0.000	0.000	0.000
34	TR	3/2	$[(1s2s)_12p_{1/2}^22p_{3/2}]_{3/2}$	4829.0	0.019	0.022	0.438	-1.000	-1.000	0.539	0.539
35	TR	5/2	$[(1s2s2p_{1/2})_{1/2}(2p_{3/2}^2)_2]_{5/2}$	4830.1	0.000	0.000	0.341	-1.069	-1.069	0.463	0.463
36	TR	1/2	$[(1s2s)_12p_{1/2}^22p_{3/2}]_{1/2}$	4831.2	0.028	0.025	0.000	0.000	0.000	0.000	0.000
38	TR	3/2	$[(1s2s2p_{1/2})_{3/2}(2p_{3/2}^2)_2]_{3/2}$	4837.1	0.090	0.093	-0.152	-1.000	-1.000	-0.247	-0.247
39	TR	1/2	$[(1s2s2p_{1/2})_{1/2}(2p_{3/2}^2)_0]_{1/2}$	4849.3	0.000	0.002	0.000	0.000	0.000	0.000	0.000
40	TR	5/2	$[(1s2s)_1(2p_{3/2}^3)_{3/2}]_{5/2}$	4850.3	0.000	0.000	-0.405	-1.069	-1.069	-0.829	-0.829
41	TR	3/2	$[(1s2s2p_{1/2})_{3/2}(2p_{3/2}^2)_0]_{3/2}$	4850.6	0.035	0.059	0.070	-1.000	-1.000	0.101	0.101
42	TR	3/2	$[(1s2s)_02p_{1/2}^22p_{3/2}]_{3/2}$	4867.5	0.553	0.555	-0.206	-1.000	-1.000	-0.345	-0.345
43	TR	5/2	$[(1s2s2p_{1/2})_{1/2}(2p_{3/2}^2)_2]_{5/2}$	4872.3	0.000	0.000	-0.343	-1.069	-1.069	-0.674	-0.674
44	TR	3/2	$[(1s2s2p_{1/2})_{3/2}(2p_{3/2}^2)_2]_{3/2}$	4876.1	0.194	0.192	-0.249	-1.000	-1.000	-0.426	-0.426
45	TR	3/2	$[(1s2s2p_{1/2})_{1/2}(2p_{3/2}^2)_2]_{3/2}$	4881.3	0.017	0.034	0.089	-1.000	-1.000	0.128	0.128
46	TR	1/2	$[(1s2s2p_{1/2})_{1/2}(2p_{3/2}^2)_0]_{1/2}$	4883.2	0.012	0.046	0.000	0.000	0.000	0.000	0.000
47	TR	5/2	$[(1s2s2p_{1/2})_{1/2}(2p_{3/2}^2)_2]_{5/2}$	4888.4	0.000	0.000	0.202	-1.069	-1.069	0.293	0.293
48	TR	3/2	$[(1s2s)_12p_{3/2}^3]_{3/2}$	4895.5	0.076	0.055	0.295	-1.000	-1.000	0.386	0.386
49	TR	1/2	$[(1s2s2p_{1/2})_{1/2}(2p_{3/2}^2)_0]_{1/2}$	4897.9	1.142	1.171	0.000	0.000	0.000	0.000	0.000
50	TR	3/2	$[(1s2s)_02p_{3/2}^3]_{3/2}$	4908.6	1.601	1.589	-0.370	-1.000	-1.000	-0.680	-0.680
51	TR	1/2	$[(1s2s)_12p_{3/2}^3]_{1/2}$	4912.4	0.681	0.646	0.000	0.000	0.000	0.000	0.000
52	DR	5/2	$[1s2s^2(2p_{3/2}^2)]_{5/2}$	4923.2	0.001	0.001	0.317	-1.069	-1.069	0.435	0.435
53	QR	3/2	$[(1s2p_{1/2})_02p_{3/2}^3]_{3/2}$	4933.4	0.000	0.000	-0.379	-1.000	-1.000	-0.701	-0.701
54	DR	1/2	$[1s2s^2(2p_{3/2}^2)0]_{1/2}$	4936.7	0.014	0.014	0.000	0.000	0.000	0.000	0.000
55	DR	3/2	$[1s2s^2(2p_{3/2}^2)]_{3/2}$	4951.0	0.002	0.002	-0.311	-1.000	-1.000	-0.553	-0.553
56	QR	5/2	$[(1s2p_{1/2})_12p_{3/2}^3]_{5/2}$	4955.4	0.006	0.006	-0.172	-1.069	-1.069	-0.303	-0.303
57	QR	3/2	$[(1s2p_{1/2})_12p_{3/2}^3]_{3/2}$	4963.1	0.005	0.005	0.090	-1.000	-1.000	0.129	0.129
58	QR	1/2	$[(1s2p_{1/2})_12p_{3/2}^3]_{1/2}$	4963.9	0.026	0.028	0.000	0.000	0.000	0.000	0.000
59	QR	1/2	$[(1s2p_{3/2}^4]_{1/2}$	4989.9	0.102	0.109	0.000	0.000	0.000	0.000	0.000

Table A.4: Same as Table A.1, but for **B-like iron**.

FAC level	Process	J_d	Configuration	E_{res}	S^{DR}		$\bar{\alpha}_2^{df}$	A_2		P_L	
					C	C+BI		C	C+BI	C	C+BI
35	DR	2	$[1s2s^22p_{1/2}^22p_{3/2}]_2$	4830.7	0.654	0.597	0.005	-0.871	-0.897	0.005	0.006
36	DR	1	$[1s2s^22p_{1/2}^22p_{3/2}]_1$	4856.9	48.390	47.362	0.589	-0.688	-0.684	0.505	0.503
37	DR	2	$[(1s2s^22p_{1/2})_0(2p_{3/2}^2)_2]_2$	4858.9	57.940	57.904	0.336	-0.972	-0.977	0.421	0.423
38	DR	3	$[(1s2s^22p_{1/2})_1(2p_{3/2}^2)_2]_3$	4862.6	25.959	26.110	0.346	-0.990	-0.990	0.438	0.438
39	DR	1	$[(1s2s^22p_{1/2})_1(2p_{3/2}^2)_2]_1$	4869.7	7.879	7.145	-0.199	-0.647	-0.630	-0.207	-0.201
40	DR	0	$[(1s2s^22p_{1/2})_0(2p_{3/2}^2)_0]_0$	4874.3	4.880	5.027	0.000	0.000	0.000	0.000	0.000
41	DR	2	$[(1s2s^22p_{1/2})_1(2p_{3/2}^2)_2]_2$	4875.7	26.652	24.640	-0.405	-0.623	-0.619	-0.434	-0.430
42	DR	1	$[(1s2s^22p_{1/2})_1(2p_{3/2}^2)_0]_1$	4877.4	16.891	16.957	0.075	-0.011	-0.013	0.001	0.001
43	DR	2	$[1s2s^22p_{3/2}^3]_2$	4888.3	11.674	10.874	-0.412	-0.634	-0.629	-0.451	-0.446
44	DR	1	$[1s2s^22p_{3/2}^3]_1$	4898.9	9.793	9.576	0.313	-0.532	-0.534	0.230	0.231
45	TR	3	$[1s2s_1 2p_{1/2}^2(2p_{3/2}^2)_{3/2}]_3$	4902.1	–	0.000	0.325	-0.990	-0.990	0.415	0.415
46	TR	2	$[(1s2s)_1 2p_{1/2}^2(2p_{3/2}^2)_{3/2}]_2$	4911.3	0.000	0.000	-0.410	-0.758	-0.758	-0.552	-0.552
47	TR	1	$[(1s2s)_1 2p_{1/2}^2(2p_{3/2}^2)_{3/2}]_1$	4915.2	0.003	0.001	0.068	-0.707	-0.707	0.070	0.070
48	TR	2	$[(1s2s)_1 2p_{1/2}^2(2p_{3/2}^2)_{3/2}]_2$	4946.9	0.044	0.045	-0.236	-0.871	-0.871	-0.344	-0.344
49	TR	1	$[(1s2s)_1 2p_{1/2}^2(2p_{3/2}^2)_{3/2}]_1$	4949.6	0.045	0.038	-0.317	-0.707	-0.709	-0.378	-0.379
50	QR	3	$[(1s2s)_1 2p_{1/2}^2(2p_{3/2}^2)_{3/2}]_3$	4952.4	–	0.000	-0.172	-0.990	-0.990	-0.278	-0.278
51	QR	2	$[1s2s2p_{1/2}^2(2p_{3/2}^2)_{3/2}]_2$	4954.7	0.023	0.021	0.141	-0.899	-0.899	0.178	0.178
52	QR	1	$[1s2s2p_{1/2}^2(2p_{3/2}^2)_{3/2}]_1$	4958.1	0.013	0.013	0.227	-0.707	-0.709	0.222	0.223
53	QR	0	$[1s2s2p_{1/2}^2(2p_{3/2}^2)_{3/2}]_0$	4959.6	0.077	0.098	0.000	0.000	0.000	0.000	0.000
54	TR	1	$[1s2s2p_{1/2}^2(2p_{3/2}^2)_{3/2}]_1$	4974.0	0.321	0.289	-0.024	-0.707	-0.709	-0.026	-0.026
55	TR	2	$[(1s2s)_0 2p_{1/2}^2(2p_{3/2}^2)_2]_2$	4976.6	0.003	0.003	0.098	-0.734	-0.734	0.104	0.104
56	TR	0	$[(1s2s)_0 2p_{1/2}^2(2p_{3/2}^2)_0]_0$	4985.6	0.235	0.247	0.000	0.000	0.000	0.000	0.000
57	QR	2	$[(1s2s)_0 2p_{1/2}^2(2p_{3/2}^2)_{3/2}]_2$	4986.7	0.341	0.351	-0.090	-0.784	-0.784	-0.110	-0.110
58	QR	1	$[(1s2s)_0 2p_{1/2}^2(2p_{3/2}^2)_{3/2}]_1$	4988.5	0.128	0.132	-0.200	-0.707	-0.709	-0.228	-0.229
59	QR	1	$[(1s2s2p_{1/2})_{3/2}(2p_{3/2}^2)_{3/2}]_1$	5002.0	0.126	0.116	-0.087	-0.707	-0.709	-0.095	-0.095
60	QR	0	$[(1s2s)_0 2p_{3/2}^4]_0$	5011.7	0.038	0.044	0.000	0.000	0.000	0.000	0.000
61	TR	2	$[1s2s^22p_{3/2}^3]_2$	5051.4	0.000	0.000	-0.210	-0.840	-0.854	-0.290	-0.295
62	TR	1	$[1s2s^22p_{3/2}^3]_1$	5059.3	0.004	0.005	0.177	-0.541	-0.529	0.136	0.134
63	QR	0	$[1s2p_{1/2}^22p_{3/2}^4]_0$	5068.3	0.005	0.006	0.000	0.000	0.000	0.000	0.000
64	QR	1	$[1s2p_{1/2}^22p_{3/2}^4]_1$	5078.8	0.015	0.016	0.174	-0.321	-0.322	0.082	0.082

Table A.5: Same as Table A.1, but for **C-like iron**.

FAC level	Process	J_d	Configuration	E_{res}	S^{DR}		$\bar{\alpha}_2^{df}$	$\mathcal{A}_2$		P_L	
					C	C+BI		C	C+BI	C	C+BI
35	DR	5/2	$[1s2s^22p_{1/2}^2(2p_{3/2}^2)_2]_{5/2}$	4925.7	37.705	38.002	0.315	-1.069	-1.069	0.432	0.432
36	DR	3/2	$[1s2s^22p_{1/2}^2(2p_{3/2}^2)_2]_{3/2}$	4935.5	10.253	9.324	-0.377	-1.000	-1.000	-0.696	-0.696
37	DR	1/2	$[1s2s^22p_{1/2}^2(2p_{3/2}^2)_0]_{1/2}$	4937.7	6.881	7.103	0.000	0.000	0.000	0.000	0.000
38	TR	3/2	$[(1s2s^22p_{1/2})_0(2p_{3/2}^3)_{3/2}]_{3/2}$	4952.2	18.453	17.148	-0.309	-1.000	-1.000	-0.548	-0.548
39	TR	5/2	$[(1s2s^22p_{1/2})_1(2p_{3/2}^3)_{3/2}]_{5/2}$	4956.7	0.273	0.311	-0.175	-1.069	-1.069	-0.310	-0.310
40	TR	1/2	$[(1s2s^22p_{1/2})_1(2p_{3/2}^3)_{3/2}]_{1/2}$	4962.2	5.291	5.244	0.000	0.000	0.000	0.000	0.000
41	TR	3/2	$[(1s2s^22p_{1/2})_1(2p_{3/2}^3)_{3/2}]_{3/2}$	4964.0	9.739	9.444	0.090	-1.000	-1.000	0.129	0.129
42	QR	1/2	$[1s2s^22p_{3/2}^4)]_{1/2}$	4980.3	0.044	0.040	0.000	0.000	0.000	0.000	0.000
43	TR	5/2	$[(1s2s)_12p_{1/2}^22p_{3/2}^3]_{5/2}$	5021.4	0.000	0.000	-0.187	-1.069	-1.069	-0.334	-0.334
44	TR	3/2	$[(1s2s)_12p_{1/2}^22p_{3/2}^3]_{3/2}$	5028.9	0.074	0.067	0.194	-1.000	-1.000	0.266	0.266
45	QR	1/2	$[((1s2s)_12p_{1/2})_12p_{3/2}^4]_{1/2}$	5035.4	0.025	0.019	0.000	0.000	0.000	0.000	0.000
46	TR	3/2	$[(1s2s)_02p_{1/2}^22p_{3/2}^3]_{3/2}$	5060.1	0.176	0.179	0.081	-1.000	-1.000	0.117	0.117
47	TR	1/2	$[(1s2s)_12p_{1/2}^22p_{3/2}^3]_{1/2}$	5063.5	0.091	0.090	0.000	0.000	0.000	0.000	0.000
48	QR	3/2	$[((1s2s)_12p_{1/2})_{3/2}2p_{3/2}^4]_{3/2}$	5079.0	0.094	0.104	-0.126	-1.000	-1.000	-0.202	-0.202
49	QR	1/2	$[((1s2s)_02p_{1/2})_12p_{3/2}^4]_{1/2}$	5086.0	0.009	0.012	0.000	0.000	0.000	0.000	0.000
50	QR	1/2	$[1s2s^22p_{3/2}^4)]_{1/2}$	5173.7	0.003	0.003	0.000	0.000	0.000	0.000	0.000

Table A.6: Same as Table A.1, but for N-like iron.

FAC level	Process	J_d	Configuration	E_{res}	S^{DR}		$\bar{\alpha}_2^{df}$		A_2		P_L	
					C	C+BI	C	C+BI	C	C+BI	C	C+BI
25	DR	2	$[1s2s^22p^2_{1/2}2p^3_{3/2}]_2$	5010.5	3.656	3.597	-0.209	-0.054	-0.100	-0.017	-0.032
26	DR	1	$[1s2s^22p^2_{1/2}2p^3_{3/2}]_1$	5018.0	1.749	1.721	0.176	0.172	0.143	-0.046	-0.038
27	TR	0	$[1s2s^22p^1_{1/2}2p^4_{3/2}]_0$	5026.7	0.051	0.046	0.000	0.000	0.000	0.000	0.000
28	TR	1	$[1s2s^22p^1_{1/2}2p^4_{3/2}]_1$	5036.7	1.163	1.268	0.173	-0.494	-0.496	0.123	0.124
29	TR	1	$[1s2s2p^2_{1/2}2p^4_{3/2}]_1$	5127.2	0.008	0.007	0.000	0.000	0.101	0.101	0.000	0.000
30	TR	0	$[1s2s2p^2_{1/2}2p^4_{3/2}]_0$	5156.2	0.012	0.013	0.000	0.000	0.000	0.000	0.000

Table A.7: Same as Table A.1, but for **O-like iron**.

FAC level	Process	J_d	Configuration	E_{res}	S^{DR}		$\bar{\alpha}_2^{df}$	$\mathcal{A}_2$		P_L	
					C	C+BI		C	C+BI	C	C+BI
13	DR	1/2	$[1s2s^22p_{1/2}^22p_{3/2}^4]_{1/2}$	5080.1	4.028	3.968	0.000	0.000	0.000	0.000	0.000

Appendix B

KLL DR calculation of He-like to O-like krypton ($Z{=}36$)

As described in section 2.2.2; the resonance energy E_{res}, resonance strength S^{DR}, alignment parameter $\mathcal{A}_2$, "effective" intrinsic anisotropy parameter $\bar{\alpha}_2^{df}$ and the degree of linear polarization of x rays P_L are calculated by the use of Flexible atomic code (FAC), given in the following tables. Theoretical calculations with only the Coulomb repulsion (C) are compared with a full treatment of the electron–electron interaction (C+BI).

EXPLANATION OF THE TABLE: same as appendix A

Table B.1: Same as Table A.1, but for He-like krypton.

FAC level	Process	J_d	Configuration	E_{res}	S^{DR}		$\bar{\alpha}_2^{df}$		A_2		P_L	
					C	C+BI	C	C+BI	C	C+BI	C	C+BI
4	DR	1/2	$[1s(2s^2)_0]_{1/2}$	8820.6	24.372	25.040	0.000	0.000	0.000	0.000	0.000	0.000
5	DR	1/2	$[(1s2s)_1 2p_{1/2}]_{1/2}$	8838.0	0.103	0.253	0.000	0.000	0.000	0.000	0.000	0.000
6	DR	3/2	$[(1s2s)_1 2p_{1/2}]_{3/2}$	8847.6	4.066	1.274	0.500	0.500	-1.000	-1.000	0.600	0.600
7	DR	1/2	$[(1s2s)_0 2p_{1/2}]_{1/2}$	8899.5	44.350	55.285	0.000	0.000	0.000	0.000	0.000	0.000
9	DR	1/2	$[1s(2p^2_{1/2})_0]_{1/2}$	8931.6	0.900	0.533	0.000	0.000	0.000	0.000	0.000	0.000
10	DR	3/2	$[(1s2s)_1 2p_{3/2}]_{3/2}$	8945.9	2.821	1.165	0.500	0.500	-1.000	-1.000	0.600	0.600
11	DR	1/2	$[(1s2s)_1 2p_{3/2}]_{1/2}$	8967.5	32.518	26.203	0.000	0.000	0.000	0.000	0.000	0.000
12	DR	3/2	$[(1s2p_{1/2})_0 2p_{3/2}]_{3/2}$	8976.6	38.462	39.031	0.500	0.500	-1.000	-1.000	0.600	0.600
13	DR	3/2	$[(1s2s)_0 2p_{3/2}]_{3/2}$	8977.7	2.055	0.738	-0.389	-0.389	-1.000	-1.000	-0.725	-0.725
14	DR	5/2	$[(1s2p_{1/2})_1 2p_{3/2}]_{5/2}$	8989.6	100.886	98.604	0.374	0.374	-1.069	-1.069	0.500	0.500
15	DR	1/2	$[(1s2p_{1/2})_1 2p_{3/2}]_{1/2}$	9006.9	0.819	1.621	0.000	0.000	0.000	0.000	0.000	0.000
16	DR	3/2	$[(1s2p_{1/2})_1 2p_{3/2}]_{3/2}$	9012.9	125.551	121.852	0.326	0.326	-1.000	-1.000	0.420	0.420
17	DR	5/2	$[1s(2p^2_{3/2})_2]_{5/2}$	9057.7	134.540	138.443	0.374	0.374	-1.069	-1.069	0.500	0.500
18	DR	3/2	$[1s(2p^2_{3/2})_2]_{3/2}$	9082.4	52.633	44.078	-0.399	-0.399	-1.000	-1.000	-0.747	-0.747
19	DR	1/2	$[1s(2p^2_{3/2})_0]_{1/2}$	9104.3	15.627	15.341	0.000	0.000	0.000	0.000	0.000	0.000

Table B.2: Same as Table A.1, but for Li-like krypton.

FAC level	Process	J_d	Configuration	E_{res}	S^{DR}		$\bar{\alpha}_2^{df}$	$\mathcal{A}_2$		P_L	
					C	C+BI		C	C+BI	C	C+BI
13	DR	0	$[1s2s^22p_{1/2}]_0$	8951.4	0.900	0.775	0.000	0.000	0.000	0.000	0.000
14	DR	1	$[1s2s^22p_{1/2}]_1$	8954.0	20.202	21.652	0.680	0.705	0.644	-0.946	-0.842
15	DR	1	$[(1s2s)_12p_{1/2}^2]_1$	8989.9	3.706	3.277	0.000	-0.008	0.000	0.000	0.000
16	DR	2	$[1s2s^22p_{3/2}]_2$	9013.8	7.095	6.986	-0.094	-0.837	-0.842	-0.123	-0.124
17	DR	2	$[((1s2s)_12p_{1/2})_{1/2}2p_{3/2}]_2$	9030.5	2.001	1.345	-0.414	-0.611	-0.683	-0.434	-0.494
18	DR	1	$[1s2s^22p_{3/2}]_1$	9037.4	5.541	4.479	0.689	0.662	0.668	-0.885	-0.896
19	DR	3	$[((1s2s)_12p_{1/2})_{3/2}2p_{3/2}]_3$	9048.2	32.165	31.344	0.346	-0.990	-0.990	0.438	0.438
20	DR	0	$[(1s2s)_02p_{1/2}^2]_0$	9052.6	1.758	1.852	0.000	0.000	0.000	0.000	0.000
21	DR	1	$[((1s2s)_12p_{1/2})_{1/2}2p_{3/2}]_1$	9082.3	13.615	13.929	0.392	-0.554	-0.510	0.295	0.273
22	DR	2	$[((1s2s)_12p_{1/2})_{3/2}2p_{3/2}]_2$	9091.5	72.477	71.975	0.327	-0.604	-0.603	0.269	0.270
23	DR	1	$[((1s2s)_12p_{1/2})_{3/2}2p_{3/2}]_1$	9104.8	45.362	43.284	-0.247	-0.710	-0.708	-0.289	-0.288
24	DR	0	$[((1s2s)_12p_{1/2})_{3/2}2p_{3/2}]_0$	9115.2	0.329	0.159	0.000	0.000	0.000	0.000	0.000
25	DR	1	$[((1s2s)_02p_{1/2})_{1/2}2p_{3/2}]_1$	9120.7	2.376	2.090	-0.084	-0.015	0.005	-0.001	0.001
26	DR	2	$[((1s2s)_02p_{1/2})_{1/2}2p_{3/2}]_2$	9122.6	49.940	48.597	-0.108	-1.111	-1.114	-0.193	-0.193
27	DR	3	$[(1s2s)_1(2p_{3/2}^2)_2]_3$	9124.9	96.290	98.794	0.346	-0.990	-0.990	0.438	0.438
28	DR	2	$[(1s2s)_1(2p_{3/2}^2)_2]_2$	9163.2	41.480	35.527	-0.302	-0.899	-0.899	-0.472	-0.472
29	DR	2	$[1s2s^22p_{3/2}]_2$	9163.9	0.866	0.930	0.078	-0.837	-0.842	0.095	0.095
30	DR	1	$[(1s2s)_1(2p_{3/2}^2)_0]_1$	9178.1	15.251	15.665	-0.018	-0.005	-0.006	0.000	0.000
31	DR	1	$[1s2s^22p_{3/2}]_1$	9193.4	0.266	0.233	0.466	0.659	0.704	-0.544	-0.589
32	DR	2	$[(1s2s)_0(2p_{3/2}^2)_2]_2$	9195.3	23.808	23.844	0.378	-1.175	-1.169	0.545	0.543
33	DR	1	$[(1s2s)_1(2p_{3/2}^2)_2]_1$	9199.3	6.179	4.829	-0.346	-0.682	-0.681	-0.401	-0.400
34	DR	0	$[(1s2s)_0(2p_{3/2}^2)_0]_0$	9220.7	5.502	5.644	0.000	0.000	0.000	0.000	0.000
35	TR	2	$[(1s2p_{1/2})_0(2p_{3/2}^2)_2]_2$	9221.5	0.172	0.184	0.189	-0.837	-0.842	0.220	0.221
37	TR	1	$[(1s2p_{1/2})_1(2p_{3/2}^2)_2]_1$	9244.9	0.005	0.005	-0.199	0.667	0.684	0.187	0.191
38	TR	2	$[(1s2p_{1/2})_1(2p_{3/2}^2)_2]_2$	9257.8	0.054	0.058	-0.380	-0.837	-0.842	-0.568	-0.572
39	TR	0	$[(1s2p_{1/2})_0(2p_{3/2}^2)_0]_0$	9266.4	0.164	0.142	0.000	0.000	0.000	0.000	0.000
40	TR	1	$[(1s2p_{1/2})_1(2p_{3/2}^2)_0]_1$	9270.1	0.350	0.394	0.222	0.702	0.659	-0.253	-0.236
41	TR	2	$[1s2p_{3/2}^3]_2$	9316.8	0.448	0.477	-0.416	-0.837	-0.842	-0.632	-0.637
42	TR	1	$[1s2p_{3/2}^3]_1$	9336.1	0.061	0.043	0.286	0.495	0.704	-0.228	-0.335

Table B.3: Same as Table A.1, but for Be-like krypton.

FAC level	Process	J_d	Configuration	E_{res}	S^{DR} C	S^{DR} C+BI	$\bar{\alpha}_2^{df}$ C	$\bar{\alpha}_2^{df}$ C+BI	$\mathcal{A}_2$ C	$\mathcal{A}_2$ C+BI	P_L C	P_L C+BI
25	DR	1/2	$[1s2s^22p^2_{1/2}]_{1/2}$	9114.5	8.353	7.944	0.000	0.000	0.000	0.000	0.000	0.000
26	DR	3/2	$[1s2s^22p_{1/2})_02p_{3/2}]_{3/2}$	9163.8	0.525	0.182	-0.389	-0.389	-1.000	-1.000	-0.724	-0.724
27	DR	5/2	$[(1s2s^22p_{1/2})_12p_{3/2}]_{5/2}$	9175.3	55.195	51.836	0.367	0.367	-1.069	-1.069	0.492	0.492
28	DR	1/2	$[(1s2s^22p_{1/2})_12p_{3/2}]_{1/2}$	9191.2	2.691	4.004	0.000	0.000	0.000	0.000	0.000	0.000
29	DR	3/2	$[1s2s^22p_{1/2})_12p_{3/2}]_{3/2}$	9197.8	98.367	94.898	0.322	0.322	-1.000	-1.000	0.416	0.416
30	DR	5/2	$[(1s2s^22p_{1/2})_12p_{3/2}]_{5/2}$	9209.8	0.000	0.000	0.051	0.051	-1.069	-1.069	0.080	0.080
31	DR	5/2	$[1s2s^2(2p^2_{3/2})_2]_{5/2}$	9239.2	87.897	88.322	0.357	0.357	-1.069	-1.069	0.481	0.481
32	DR	3/2	$[1s2s^2(2p^2_{3/2})_2]_{3/2}$	9262.9	43.430	36.272	-0.395	-0.395	-1.000	-1.000	-0.737	-0.737
33	DR	3/2	$[(1s2s)_12p^2_{1/2}2p_{3/2}]_{3/2}$	9263.2	0.049	0.046	0.352	0.352	-1.000	-1.000	0.449	0.449
34	DR	1/2	$[1s2s^2(2p^2_{3/2})_0]_{1/2}$	9271.4	27.470	27.971	0.000	0.000	0.000	0.000	0.000	0.000
35	TR	1/2	$[(1s2s)_12p^2_{1/2}2p_{3/2}]_{1/2}$	9275.9	0.117	0.085	0.000	0.000	0.000	0.000	0.000	0.000
36	TR	5/2	$[(1s2s2p_{1/2})_{1/2}(2p_{3/2})_{3/2}]_{5/2}$	9284.8	0.000	0.000	0.264	0.264	-1.069	-1.069	0.371	0.371
37	TR	3/2	$[(1s2s)_02p^2_{1/2}2p_{3/2}]_{3/2}$	9295.2	0.725	0.809	-0.094	-0.094	-1.000	-1.000	-0.147	-0.147
39	TR	3/2	$[(1s2s2p_{1/2})_{1/2}(2p_{3/2})_2]_{3/2}$	9322.7	0.278	0.341	-0.215	-0.215	-1.000	-1.000	-0.361	-0.361
40	TR	1/2	$[(1s2s2p_{1/2})_{1/2}(2p_{3/2})_1]_{1/2}$	9329.9	0.001	0.002	0.000	0.000	0.000	0.000	0.000	0.000
41	TR	5/2	$[(1s2s2p_{1/2})_{3/2}(2p_{3/2})_2]_{5/2}$	9334.2	0.000	0.000	-0.361	-0.361	-1.069	-1.069	-0.717	-0.717
42	TR	3/2	$[(1s2s2p_{1/2})_{3/2}(2p_{3/2})_0]_{3/2}$	9345.9	0.358	0.297	0.034	0.034	-1.000	-1.000	0.050	0.050
43	TR	3/2	$[(1s2s2p_{1/2})_{3/2}(2p_{3/2})_2]_{3/2}$	9361.4	0.077	0.069	-0.290	-0.290	-1.000	-1.000	-0.508	-0.508
44	TR	1/2	$[(1s2s2p_{1/2})_{3/2}(2p_{3/2})_2]_{1/2}$	9366.8	0.018	0.001	0.000	0.000	0.000	0.000	0.000	0.000
45	TR	3/2	$[(1s2s2p_{1/2})_{1/2}(2p_{3/2})_2]_{3/2}$	9368.3	0.004	0.000	0.038	0.038	-1.000	-1.000	0.057	0.057
46	TR	5/2	$[(1s2s2p_{1/2})_{1/2}(2p_{3/2})_2]_{5/2}$	9368.6	0.000	0.000	-0.143	-0.143	-1.069	-1.069	-0.249	-0.249
47	TR	1/2	$[(1s2s2p_{1/2})_{1/2}(2p_{3/2})_0]_{1/2}$	9393.3	0.513	0.578	0.000	0.000	0.000	0.000	0.000	0.000
48	TR	5/2	$[(1s2s)_1(2p^3_{3/2})_{3/2}]_{5/2}$	9397.0	0.000	0.000	-0.149	-0.149	-1.069	-1.069	-0.259	-0.259
49	TR	3/2	$[(1s2s)_1(2p^3_{3/2})_{3/2}]_{3/2}$	9422.0	0.084	0.060	0.265	0.265	-1.000	-1.000	0.351	0.351
50	DR	5/2	$[1s2s^2(2p^3_{3/2})_2]_{5/2}$	9436.0	0.001	0.001	0.217	0.217	-1.069	-1.069	0.312	0.312
51	TR	1/2	$[(1s2s)_12p^3_{3/2}]_{1/2}$	9448.1	0.205	0.167	0.000	0.000	0.000	0.000	0.000	0.000
52	TR	3/2	$[(1s2s)_02p^3_{3/2}]_{3/2}$	9449.2	0.633	0.654	-0.372	-0.372	-1.000	-1.000	-0.685	-0.685
53	DR	3/2	$[1s2s^2(2p^3_{3/2})_2]_{3/2}$	9461.2	0.000	0.000	-0.296	-0.296	-1.000	-1.000	-0.521	-0.521
54	DR	1/2	$[1s2s^2(2p^3_{3/2})_0]_{1/2}$	9471.0	0.032	0.036	0.000	0.000	0.000	0.000	0.000	0.000
55	QR	3/2	$[(1s2p_{1/2})_02p^3_{3/2}]_{3/2}$	9503.0	0.000	0.000	-0.312	-0.312	-1.000	-1.000	-0.555	-0.555
56	QR	5/2	$[(1s2p_{1/2})_12p^3_{3/2}]_{5/2}$	9516.7	0.001	0.001	-0.139	-0.139	-1.069	-1.069	-0.241	-0.241
57	QR	1/2	$[(1s2p_{1/2})_12p^3_{3/2}]_{1/2}$	9524.1	0.004	0.005	0.000	0.000	0.000	0.000	0.000	0.000
58	QR	3/2	$[(1s2p_{1/2})_12p^3_{3/2}]_{3/2}$	9531.9	0.002	0.002	0.094	0.094	-1.000	-1.000	0.135	0.135
59	QR	1/2	$[(1s2p^4_{3/2}]_{1/2}$	9601.4	0.017	0.019	0.000	0.000	0.000	0.000	0.000	0.000

Table B.4: Same as Table A.1, but for B-like krypton.

FAC level	Process	J_d	Configuration	E_{res}	S^{DR}		$\bar{\alpha}_2^{df}$	$\mathcal{A}_2$		P_L	
					C	C+BI		C	C+BI	C	C+BI
35	DR	2	$[1s2s^22p_{1/2}^22p_{3/2}]_2$	9269.5	21.275	19.857	0.062	-0.865	-0.895	0.079	0.081
36	DR	1	$[1s2s^22p_{1/2}^22p_{3/2}]_1$	9296.8	46.166	44.911	0.455	-0.694	-0.685	0.409	0.404
37	DR	2	$[(1s2s^22p_{1/2})_0(2p_{3/2}^2)_2]_2$	9327.8	43.276	43.814	0.182	-0.930	-0.939	0.234	0.236
38	DR	3	$[(1s2s^22p_{1/2})_1(2p_{3/2}^2)_2]_3$	9340.8	28.117	28.897	0.346	-0.990	-0.990	0.438	0.438
39	DR	1	$[(1s2s^22p_{1/2})_1(2p_{3/2}^2)_2]_1$	9351.5	12.656	10.632	-0.207	-0.712	-0.712	-0.239	-0.239
40	DR	0	$[(1s2s^22p_{1/2})_0(2p_{3/2}^2)_0]_0$	9362.6	4.568	4.821	0.000	0.000	0.000	0.000	0.000
41	DR	2	$[(1s2s^22p_{1/2})_1(2p_{3/2}^2)_2]_2$	9363.6	27.054	23.055	-0.373	-0.734	-0.727	-0.476	-0.471
42	DR	1	$[(1s2s^22p_{1/2})_1(2p_{3/2}^2)_0]_1$	9366.6	15.656	16.023	0.220	-0.026	-0.027	0.009	0.009
43	TR	3	$[(1s2s)_12p_{1/2}^2(2p_{3/2}^2)_2]_3$	9405.7	0.000	0.000	0.255	-0.990	-0.990	0.337	0.337
44	TR	2	$[1s2s^22p_{3/2}^3]_2$	9414.1	0.715	0.659	-0.413	-0.628	-0.617	-0.447	-0.438
45	TR	1	$[1s2s^22p_{3/2}^3]_1$	9431.7	1.213	1.161	0.275	-0.570	-0.572	0.218	0.219
46	TR	2	$[(1s2s)_12p_{1/2}^2(2p_{3/2}^2)_2]_2$	9436.5	0.001	0.001	-0.339	-0.992	-0.995	-0.607	-0.609
47	TR	1	$[(1s2s)_12p_{1/2}^2(2p_{3/2}^2)_0]_1$	9445.7	0.019	0.008	0.065	-0.707	-0.711	0.067	0.067
48	TR	1	$[(1s2s)_12p_{1/2}^2(2p_{3/2}^2)_2]_1$	9476.6	0.012	0.005	-0.282	-0.707	-0.711	-0.332	-0.334
49	TR	2	$[(1s2s)_02p_{1/2}^2(2p_{3/2}^2)_2]_2$	9479.1	0.003	0.003	-0.132	-0.974	-0.973	-0.206	-0.206
50	TR	2	$[(1s2s2p_{1/2})_{1/2}(2p_{3/2}^3)_{3/2}]_2$	9498.1	0.009	0.008	-0.049	-1.030	-1.032	-0.079	-0.078
51	TR	0	$[(1s2s)_02p_{1/2}^2(2p_{3/2}^2)_0]_0$	9505.8	0.136	0.176	0.000	0.000	0.000	0.000	0.000
52	QR	3	$[(1s2s2p_{1/2})_{3/2}(2p_{3/2}^3)_{3/2}]_3$	9507.3	0.000	0.000	-0.151	-0.990	-0.990	-0.242	-0.242
53	QR	1	$[(1s2s2p_{1/2})_{1/2}(2p_{3/2}^3)_{3/2}]_1$	9515.6	0.020	0.013	0.227	-0.707	-0.711	0.223	0.224
54	QR	2	$[(1s2s2p_{1/2})_{3/2}(2p_{3/2}^3)_{3/2}]_2$	9535.5	0.016	0.014	0.142	-0.752	-0.752	0.152	0.152
55	QR	1	$[(1s2s2p_{1/2})_{1/2}(2p_{3/2}^3)_{3/2}]_1$	9545.7	0.164	0.148	-0.021	-0.707	-0.711	-0.022	-0.023
56	QR	0	$[(1s2s2p_{1/2})_{3/2}(2p_{3/2}^3)_{3/2}]_0$	9548.8	0.101	0.102	0.000	0.000	0.000	0.000	0.000
57	QR	1	$[(1s2s2p_{1/2})_{1/2}(2p_{3/2}^3)_{3/2}]_1$	9562.1	0.076	0.074	-0.169	-0.707	-0.711	-0.191	-0.192
58	QR	2	$[(1s2s2p_{1/2})_{1/2}(2p_{3/2}^3)_{3/2}]_2$	9564.1	0.202	0.218	-0.105	-0.785	-0.785	-0.129	-0.129
59	QR	1	$[((1s2s)_12p_{3/2}^4]_1$	9607.3	0.020	0.021	-0.066	-0.707	-0.711	-0.072	-0.072
60	QR	0	$[((1s2s)_02p_{3/2}^4]_0$	9636.7	0.003	0.004	0.000	0.000	0.000	0.000	0.000
61	TR	2	$[1s2s^22p_{3/2}^3]_2$	9657.8	0.000	0.000	-0.211	-0.843	-0.870	-0.293	-0.303
62	TR	1	$[1s2s^22p_{3/2}^3]_1$	9675.2	0.000	0.000	0.176	-0.671	-0.657	0.169	0.164
63	QR	0	$[1s2p_{1/2}^22p_{3/2}^4]_0$	9725.2	0.002	0.002	0.000	0.000	0.000	0.000	0.000
64	QR	1	$[1s2p_{1/2}^22p_{3/2}^4]_1$	9732.3	0.005	0.006	0.178	-0.084	-0.082	0.022	0.022

Table B.5: Same as Table A.1, but for C-like krypton.

FAC level	Process	J_d	Configuration	E_{res}	S^{DR}		$\bar{\alpha}_2^{df}$		$\mathcal{A}_2$		P_L	
					C	C+BI	C	C+BI	C	C+BI	C	C+BI
35	DR	5/2	$[1s2s^22p_{1/2}^2(2p_{3/2}^2)2]5/2$	9430.5	44.516	46.002	0.214	-1.069	-1.069	0.308	0.308
36	DR	3/2	$[1s2s^22p_{1/2}^2(2p_{3/2}^2)2]3/2$	9454.9	32.850	28.089	-0.293	-1.000	-1.000	-0.515	-0.515
37	DR	1/2	$[1s2s^22p_{1/2}^2(2p_{3/2}^2)0]1/2$	9459.3	13.332	13.962	0.000	0.000	0.000	0.000	0.000
38	TR	3/2	$[1s2s^22p_{1/2})0(2p_{3/2}^3)3/2]3/2$	9496.2	2.114	1.897	-0.312	-1.000	-1.000	-0.555	-0.555
39	TR	5/2	$[1s2s^22p_{1/2})1(2p_{3/2}^3)3/2]5/2$	9509.5	0.134	0.163	-0.140	-1.069	-1.069	-0.243	-0.243
40	TR	1/2	$[(1s2s^22p_{1/2})1(2p_{3/2}^3)3/2]1/2$	9515.2	0.889	0.872	0.000	0.000	0.000	0.000	0.000
41	TR	3/2	$[(1s2s^22p_{1/2})1(2p_{3/2}^3)3/2]3/2$	9524.2	1.356	1.290	0.093	-1.000	-1.000	0.133	0.133
42	QR	1/2	$[1s2s^22p_{3/2}^4]1/2$	9583.2	0.003	0.003	0.000	0.000	0.000	0.000	0.000
43	TR	5/2	$[1s2s)_1 2p_{1/2}^2 2p_{3/2}^3]5/2$	9608.5	0.000	0.000	-0.188	-1.069	-1.069	-0.335	-0.335
44	TR	3/2	$[(1s2s)_1 2p_{1/2}^2 2p_{3/2}^3]3/2$	9630.4	0.036	0.032	0.172	-1.000	-1.000	0.237	0.237
45	QR	1/2	$[((1s2s)_1 2p_{1/2})1/2 2p_{3/2}^3]1/2$	9652.6	0.040	0.028	0.000	0.000	0.000	0.000	0.000
46	TR	3/2	$[(1s2s)_0 2p_{1/2}^2 2p_{3/2}^3]3/2$	9672.7	0.176	0.190	-0.008	-1.000	-1.000	-0.013	-0.013
47	TR	1/2	$[(1s2s)_1 2p_{1/2}^2 2p_{3/2}^3]1/2$	9691.8	0.014	0.012	0.000	0.000	0.000	0.000	0.000
48	QR	3/2	$[((1s2s)_1 2p_{1/2})3/2 2p_{3/2}^4]3/2$	9715.8	0.029	0.035	0.006	-1.000	-1.000	0.009	0.009
49	QR	1/2	$[((1s2s)_0 2p_{1/2})1/2 2p_{3/2}^4]1/2$	9742.1	0.002	0.003	0.000	0.000	0.000	0.000	0.000
50	QR	1/2	$[1s2s^22p_{3/2}^4]1/2$	9871.0	0.002	0.003	0.000	0.000	0.000	0.000	0.000

Table B.6: Same as Table A.1, but for N-like krypton.

FAC level	Process	J_d	Configuration	E_{res}	S^{DR}		$\bar{\alpha}_2^{df}$	$\mathcal{A}_2$		P_L	
					C	C+BI		C	C+BI	C	C+BI
25	DR	2	$[1s2s^22p^2_{1/2}2p^3_{3/2}]_2$	9544.5	18.861	19.057	-0.210	-0.056	-0.091	-0.018	-0.029
26	DR	1	$[1s2s^22p^2_{1/2}2p^3_{3/2}]_1$	9561.4	11.975	11.249	0.175	-0.044	-0.095	0.012	0.025
27	TR	0	$[1s2s^22p_{1/2}2p^4_{3/2}]_0$	9610.3	0.002	0.001	0.000	0.000	0.000	0.000	0.000
28	TR	1	$[1s2s^22p_{1/2}2p^4_{3/2}]_1$	9617.2	0.641	0.660	0.174	-0.200	-0.244	0.051	0.062
29	TR	1	$[1s2s2p^2_{1/2}2p^4_{3/2}]_1$	9756.3	0.018	0.015	0.000	0.101	0.101	0.000	0.000
30	TR	0	$[1s2s2p^2_{1/2}2p^4_{3/2}]_0$	9801.0	0.030	0.033	0.000	0.000	0.000	0.000	0.000

Table B.7: Same as Table A.1, but for O-like krypton.

FAC level	Process	J_d	Configuration	E_{res}	S^{DR}		$\bar{\alpha}_2^{df}$		$\mathcal{A}_2$		P_L	
					C	C+BI	C	C+BI	C	C+BI	C	C+BI
13	DR	1/2	$[1s2s^22p_{1/2}^22p_{3/2}^4]_{1/2}$	9654.2	9.459	9.221	0.000	0.000	0.000	0.000	0.000	0.000

Appendix C

RR (n=2) calculation of He-like to N-like krypton (Z=36)

Table C.1: The total cross section σ_{RR} and linear polarization P_L of radiative recombination (RR) into n=2 states of He-like to N-like krypton ions. $\sigma_\perp$ is the RR cross sections at 90° for x rays polarized in the direction perpendicular to the electron direction, and $\sigma_\parallel$ is the RR cross sections at 90° for x rays polarized in the direction parallel to the electron direction.

$\lvert i \rangle$	subshell	E_e (eV)	$\hbar\omega_{\mathrm{RR}}$ (eV)	σ_{RR} ($10^{-20}\mathrm{cm^2}$)	$\sigma_\perp/\sigma_\parallel$	P_L
He-like	$2s_{1/2}$	8700	12997	1.79E-03	4.53E-04	0.999
$[1s^2]_0$		8800	13097	1.77E-03	4.59E-04	0.999
		8900	13197	1.74E-03	4.57E-04	0.999
		9000	13297	1.71E-03	4.61E-04	0.999
		9100	13397	1.69E-03	4.65E-04	0.999
		9200	13497	1.67E-03	4.65E-04	0.999
		9300	13597	1.64E-03	4.69E-04	0.999
		9400	13697	1.62E-03	4.73E-04	0.999
		9500	13797	1.60E-03	4.75E-04	0.999
		9600	13897	1.57E-03	4.85E-04	0.999
		9700	13997	1.55E-03	4.78E-04	0.999
	$2p_{1/2}$	8700	12963	5.97E-04	2.58E-01	0.590
		8800	13063	5.84E-04	2.59E-01	0.589

		8900	13163	5.71E-04	2.61E-01	0.587
		9000	13263	5.59E-04	2.62E-01	0.585
		9100	13363	5.47E-04	2.64E-01	0.583
		9200	13463	5.36E-04	2.65E-01	0.581
		9300	13563	5.24E-04	2.66E-01	0.579
		9400	13663	5.14E-04	2.68E-01	0.578
		9500	13763	5.03E-04	2.69E-01	0.576
		9600	13863	4.93E-04	2.71E-01	0.574
		9700	13963	4.83E-04	2.72E-01	0.572
	$2p_{3/2}$	8700	12890	5.32E-04	2.57E-01	0.591
		8800	12990	5.20E-04	2.58E-01	0.589
		8900	13090	5.09E-04	2.60E-01	0.587
		9000	13190	4.98E-04	2.62E-01	0.585
		9100	13290	4.87E-04	2.63E-01	0.583
		9200	13390	4.76E-04	2.65E-01	0.581
		9300	13490	4.66E-04	2.66E-01	0.579
		9400	13590	4.56E-04	2.68E-01	0.577
		9500	13690	4.47E-04	2.70E-01	0.575
		9600	13790	4.37E-04	2.71E-01	0.573
		9700	13890	4.28E-04	2.73E-01	0.571
Li-like	$2s_{1/2}$	8700	12827	1.74E-03	4.47E-04	0.999
$[1s^22s_{1/2}]_{1/2}$		8800	12927	1.71E-03	4.53E-04	0.999
		8900	13027	1.69E-03	4.51E-04	0.999
		9000	13127	1.66E-03	4.55E-04	0.999
		9100	13227	1.64E-03	4.48E-04	0.999
		9200	13327	1.61E-03	4.62E-04	0.999
		9300	13427	1.59E-03	4.63E-04	0.999
		9400	13527	1.57E-03	4.60E-04	0.999
		9500	13627	1.55E-03	4.66E-04	0.999
		9600	13727	1.53E-03	4.71E-04	0.999
		9700	13827	1.50E-03	4.71E-04	0.999
	$2p_{1/2}$	8700	12779	5.99E-04	2.55E-01	0.594
		8800	12879	5.86E-04	2.57E-01	0.592
		8900	12979	5.73E-04	2.58E-01	0.590

		9000	13079	5.61E-04	2.59E-01	0.588
		9100	13179	5.49E-04	2.61E-01	0.586
		9200	13279	5.37E-04	2.62E-01	0.585
		9300	13379	5.26E-04	2.64E-01	0.583
		9400	13479	5.15E-04	2.65E-01	0.581
		9500	13579	5.04E-04	2.66E-01	0.579
		9600	13679	4.94E-04	2.68E-01	0.578
		9700	13779	4.84E-04	2.69E-01	0.576
	$2p_{3/2}$	8700	12708	5.33E-04	2.54E-01	0.595
		8800	12808	5.21E-04	2.55E-01	0.593
		8900	12908	5.10E-04	2.57E-01	0.591
		9000	13008	4.99E-04	2.59E-01	0.589
		9100	13108	4.88E-04	2.60E-01	0.587
		9200	13208	4.77E-04	2.62E-01	0.585
		9300	13308	4.67E-04	2.63E-01	0.583
		9400	13408	4.57E-04	2.65E-01	0.581
		9500	13508	4.47E-04	2.66E-01	0.579
		9600	13608	4.38E-04	2.68E-01	0.577
		9700	13708	4.29E-04	2.69E-01	0.576
Be-like $[1s^2 2s^2_{1/2}]_0$	$2p_{1/2}$	8700	12442	5.79E-04	2.52E-01	0.597
		8800	12542	5.66E-04	2.53E-01	0.596
		8900	12642	5.54E-04	2.55E-01	0.594
		9000	12742	5.42E-04	2.56E-01	0.592
		9100	12842	5.30E-04	2.58E-01	0.590
		9200	12942	5.19E-04	2.59E-01	0.589
		9300	13042	5.08E-04	2.60E-01	0.587
		9400	13142	4.98E-04	2.62E-01	0.585
		9500	13242	4.87E-04	2.63E-01	0.583
		9600	13342	4.77E-04	2.65E-01	0.581
		9700	13442	4.67E-04	2.66E-01	0.580
	$2p_{3/2}$	8700	12375	5.15E-04	2.50E-01	0.599
		8800	12475	5.04E-04	2.52E-01	0.597
		8900	12575	4.92E-04	2.54E-01	0.595
		9000	12675	4.81E-04	2.55E-01	0.593

		9100	12775	4.71E-04	2.57E-01	0.591
		9200	12875	4.61E-04	2.58E-01	0.589
		9300	12975	4.51E-04	2.60E-01	0.588
		9400	13075	4.41E-04	2.62E-01	0.585
		9500	13175	4.32E-04	2.63E-01	0.583
		9600	13275	4.23E-04	2.65E-01	0.582
		9700	13375	4.14E-04	2.66E-01	0.580
B-like	$2p_{1/2}$	8700	12271	5.66E-04	2.50E-01	0.600
$[1s^2 2s_{1/2}^2 2p_{1/2}]_{1/2}$		8800	12371	5.54E-04	2.52E-01	0.598
		8900	12471	5.42E-04	2.53E-01	0.596
		9000	12571	5.30E-04	2.55E-01	0.594
		9100	12671	5.19E-04	2.56E-01	0.592
		9200	12771	5.08E-04	2.57E-01	0.591
		9300	12871	4.97E-04	2.59E-01	0.589
		9400	12971	4.86E-04	2.60E-01	0.587
		9500	13071	4.76E-04	2.62E-01	0.585
		9600	13171	4.66E-04	2.63E-01	0.583
		9700	13271	4.57E-04	2.65E-01	0.582
	$2p_{3/2}$	8700	12207	5.03E-04	2.49E-01	0.602
		8800	12307	4.92E-04	2.50E-01	0.600
		8900	12407	4.81E-04	2.52E-01	0.598
		9000	12507	4.70E-04	2.53E-01	0.596
		9100	12607	4.60E-04	2.55E-01	0.594
		9200	12707	4.50E-04	2.57E-01	0.592
		9300	12807	4.40E-04	2.58E-01	0.590
		9400	12907	4.31E-04	2.60E-01	0.588
		9500	13007	4.22E-04	2.61E-01	0.586
		9600	13107	4.13E-04	2.63E-01	0.584
		9700	13207	4.04E-04	2.64E-01	0.582
C-like	$2p_{3/2}$	8700	12044	4.94E-04	2.47E-01	0.604
$[1s^2 2s_{1/2}^2 2p_{1/2}^2]_0$		8800	12144	4.83E-04	2.48E-01	0.602
		8900	12244	4.72E-04	2.50E-01	0.600
		9000	12344	4.61E-04	2.52E-01	0.598
		9100	12444	4.51E-04	2.53E-01	0.596
		9200	12544	4.41E-04	2.55E-01	0.594

		9300	12644	4.32E-04	2.56E-01	0.592
		9400	12744	4.22E-04	2.58E-01	0.590
		9500	12844	4.13E-04	2.60E-01	0.588
		9600	12944	4.05E-04	2.61E-01	0.586
		9700	13044	3.96E-04	2.63E-01	0.584
N-like	$2p_{3/2}$	8700	11885	4.85E-04	2.45E-01	0.607
$[1s^2 2s^2_{1/2} 2p^2_{1/2} 2p_{3/2}]_{3/2}$		8800	11985	4.74E-04	2.46E-01	0.605
		8900	12085	4.63E-04	2.48E-01	0.603
		9000	12185	4.53E-04	2.50E-01	0.601
		9100	12285	4.43E-04	2.51E-01	0.598
		9200	12385	4.33E-04	2.53E-01	0.596
		9300	12485	4.24E-04	2.55E-01	0.594
		9400	12585	4.15E-04	2.56E-01	0.592
		9500	12685	4.06E-04	2.58E-01	0.590
		9600	12785	3.97E-04	2.59E-01	0.588
		9700	12885	3.89E-04	2.61E-01	0.586

Bibliography

[1] C. Day, Physics Today **61**, 12 (2008).

[2] N. Werner, A. Finoguenov, J. S. Kaastra, A. Simionescu, J. P. Dietrich, J. Vink, and H. Böhringer, Astronomy & Astrophysics **482**, 5 (2008).

[3] H. Friedman, S. W. Lichtman, and E. T. Byram, Phys. Rev. **83**, 1025 (1951).

[4] R. Giacconi, H. Gursky, F. R. Paolini, and B. B. Rossi, Phys. Rev. Lett. **9**, 439 (1962).

[5] F. K. Baganoff, M. W. Bautz, W. N. Brandt, G. Chartas, E. D. Feigelson, G. P. Garmire, Y. Maeda, M. Morris, G. R. Ricker, L. K. Townsley, and F. Walter, Nature **413**, 45 (2001).

[6] M. L. Schattenburg and C. R. Canizares, The Astrophysical Journal **301**, 759 (1986).

[7] M. C. Weisskopf, E. H. Silver, H. L. Kestenbaum, K. S. Long, and R. Novick, Astrophys. J. **220**, L117 (1978).

[8] P. Mészáros, R. Novick, A. Szentgyörgyi, G. A. Chanan, and M. C. Weisskopf, The Astrophysical Journal **324**, 1056 (1988).

[9] J. R. P. Angel, The Astrophysical Journal **158**, 219 (1969).

[10] I. N. Gnedin and R. A. Sunyaev, Astronomy and Astrophysics **36**, 379 (1974).

[11] Y. N. Gnedin, G. G. Pavlov, and Y. A. Shibanov, Soviet Astronomy Letters **4**, 117 (1978).

[12] M. J. Rees, Mon. Not. R. Astron. Soc. **171**, 457 (1975).

[13] P. A. Connors, R. F. Stark, and T. Piran, Astrophys. J. **235**, 224 (1980).

[14] K. C. Phillips and P. Mészáros, The Astrophysical Journal **310**, 284 (1986).

[15] M. C. Weisskopf, G. G. Cohen, H. L. Kestenbaum, K. S. Long, R. Novick, and R. S. Wolff, Astrophys. J. **208**, L125 (1976).

[16] R. F. Elsner, B. D. Ramsey, S. L. O'dell, M. Sulkanen, A. F. Tennant, M. C. Weisskopf, S. Gunji, T. Minamitani, R. A. Austin, J. Kolodziejczak, D. Swartz, G. Garmire, P. Meszaros, and G. G. Pavlov, **190**, 790 (1997).

[17] H. L. Marshall, S. S. Murray, J. H. Chappell, H. W. Schnopper, E. H. Silver, and M. C. Weisskopf, **4843**, 360 (2003).

[18] W. Coburn and S. E. Boggs, Nature **423**, 415 (2003).

[19] D. Götz, S. Covino, A. Fernández-Soto, P. Laurent, and v. Bošnjak, Mon. Not. R. Astron. Soc. **431**, 3550 (2013).

[20] D. Götz, P. Laurent, S. Antier, S. Covino, P. D'Avanzo, V. D'Elia, and A. Melandri, Mon. Not. R. Astron. Soc. **444**, 2776 (2014).

[21] P. Laurent, J. Rodriguez, J. Wilms, M. Cadolle Bel, K. Pottschmidt, and V. Grinberg, Science **332**, 438 (2011).

[22] H. Krawczynski, A. G. III, Q. Guo, M. Baring, P. Ghosh, M. Beilicke, and K. Lee, Astropart. Phys. **34**, 550 (2011).

[23] P. Soffitta, X. Barcons, R. Bellazzini, J. Braga, E. Costa, G. Fraser, S. Gburek, J. Huovelin, G. Matt, M. Pearce, *et al.*, Exp. Astron. **36**, 523 (2013).

[24] European Space Agency web link, "THREE CANDIDATES FOR ESA'S NEXT MEDIUM-CLASS SCIENCE MISSION," (2015).

[25] T. Chattopadhyay, S. Vadawale, A. Rao, S. Sreekumar, and D. Bhattacharya, Exp. Astron. **37**, 555 (2014).

[26] S. Tashenov, T. Bäck, R. Barday, B. Cederwall, J. Enders, A. Khaplanov, Y. Fritzsche, K.-U. Schässburger, A. Surzhykov, V. A. Yerokhin, *et al.*, Phys. Rev. A **87**, 022707 (2013).

[27] J. H. Scofield, Phys. Rev. A **40**, 3054 (1989).

[28] M. Pajek and R. Schuch, Phys. Rev. A **46**, 6962 (1992).

[29] R. Novick, Space Science Reviews **18**, 389 (1975).

[30] E. Haug, Solar Phys. **25**, 425 (1972).

[31] E. Haug, Solar Phys. **61**, 129 (1979).

[32] A. G. Emslie, H. L. Bradsher, and M. L. McConnell, Astrophys. J. **674**, 570 (2008).

[33] M. L. McConnell, J. M. Ryan, D. M. Smith, R. P. Lin, and A. G. Emslie, Solar Physics **210**, 125 (2002).

[34] S. Nayakshin, Mon. Not. R. Astron. Soc. **376**, L25 (2007).

[35] M. Dovčiak, V. Karas, and G. Matt, Mon. Not. R. Astron. Soc. **355**, 1005 (2004).

[36] M. Dovčiak, R. W. Goosmann, V. Karas, and G. Matt, J. Phys. Conf. Ser. **131**, 012004 (2008).

[37] S. Y. Sazonov, E. M. Churazov, and R. A. Sunyaev, Mon. Not. R. Astron. Soc. **333**, 191 (2002).

[38] I. V. Zhuravleva, E. M. Churazov, S. Y. Sazonov, R. A. Sunyaev, W. Forman, and K. Dolag, Mon. Not. R. Astron. Soc. **403**, 129 (2010).

[39] I. Zhuravleva, E. Churazov, R. Sunyaev, S. Sazonov, S. W. Allen, N. Werner, A. Simionescu, S. Konami, and T. Ohashi, Monthly Notices of the Royal Astronomical Society **435**, 3111 (2013).

[40] M. C. Weisskopf, R. F. Elsner, D. Hanna, V. M. Kaspi, S. L. O'Dell, G. G. Pavlov, and B. D. Ramsey, ArXiv Astrophysics e-prints (2006).

[41] T. Kallman, Adv. Space Res. **34**, 2673 (2004).

[42] H. K. Tseng and R. H. Pratt, Phys. Rev. A **7**, 1502 (1973).

[43] S. Tashenov, T. Bäck, R. Barday, B. Cederwall, J. Enders, A. Khaplanov, Y. Poltoratska, K.-U. Schässburger, and A. Surzhykov, Phys. Rev. Lett. **107**, 173201 (2011).

[44] J. Eichler and A. Ichihara, Phys. Rev. A **65**, 052716 (2002).

[45] S. Tashenov, T. Stöhlker, D. Banaś, K. Beckert, P. Beller, H. F. Beyer, F. Bosch, S. Fritzsche, A. Gumberidze, S. Hagmann, *et al.*, Phys. Rev. Lett. **97**, 223202 (2006).

[46] A. Surzhykov, S. Fritzsche, A. Gumberidze, and T. Stöhlker, Phys. Rev. Lett. **88**, 153001 (2002).

[47] J. R. Henderson, , P. Beiersdorfer, C. L. Bennett, S. Chantrenne, D. A. Knapp, R. E. Marrs, M. B. Schneider, K. L. Wong, G. A. Doschek, J. F. Seely, *et al.*, Phys. Rev. Lett. **65**, 705 (1990).

[48] A. Iwamae, T. Sato, Y. Horimoto, K. Inoue, T. Fujimoto, M. Uchida, and T. Maekawa, Plasma Phys. Contr. F. **47**, L41 (2005).

[49] E. Baronova, G. Sholin, and L. Jakubowski, J. Exp. Theor. Phys. **69**, 921 (1999).

[50] E. O. Baronova, G. V. Sholin, and L. Jakubowski, Plasma Phys. Contr. F. **45**, 1071 (2003).

[51] S. Texter, S. Knowlton, M. Porkolab, and Y. Takase, Nuclear Fusion **26**, 1279 (1986).

[52] T. Fujimoto, H. Sahara, T. Kawachi, T. Kallstenius, M. Goto, H. Kawase, T. Furukubo, T. Maekawa, and Y. Terumichi, Phys. Rev. E **54**, R2240 (1996).

[53] J. C. Kieffer, J. P. Matte, H. Pépin, M. Chaker, Y. Beaudoin, T. W. Johnston, C. Y. Chien, S. Coe, G. Mourou, and J. Dubau, Phys. Rev. Lett. **68**, 480 (1992).

[54] J. C. Kieffer, J. P. Matte, M. Chaker, Y. Beaudoin, C. Y. Chien, S. Coe, G. Mourou, J. Dubau, and M. K. Inal, Phys. Rev. E **48**, 4648 (1993).

[55] Y. Inubushi, T. Kai, T. Nakamura, S. Fujioka, H. Nishimura, and K. Mima, Phys. Rev. E **75**, 026401 (2007).

[56] T. Fujimoto and S. A. Kazantsev, Plasma Phys. Contr. F. **39**, 1267 (1997).

[57] D. E. Osterbrock, *Astrophysics of gaseous nebulae and active galactic nuclei* (1989).

[58] S. Chakravorty, A. K. Kembhavi, M. Elvis, G. Ferland, and N. R. Badnell, Monthly Notices of the Royal Astronomical Society: Letters **384**, L24 (2008).

[59] P. Beiersdorfer, Annual Review of Astronomy and Astrophysics **41**, 343 (2003).

[60] T. R. Kallman and P. Palmeri, Reviews of Modern Physics **79**, 79 (2007).

[61] A. Müller, *Advances In Atomic, Molecular, and Optical Physics*, **55**, 293 (2008).

[62] R. K. Smith and N. S. Brickhouse, *Advances In Atomic, Molecular, and Optical Physics*, edited by P. R. B. Ennio Arimondo and C. C. Lin, Vol. 63 (Academic Press, 2014) pp. 271–321.

[63] H. Netzer, The Astrophysical Journal **604**, 551 (2004).

[64] T. Pütterich, R. Neu, R. Dux, A. D. Whiteford, M. G. O'Mullane, and t. A. U. Team, Plasma Physics and Controlled Fusion **50**, 085016 (2008).

[65] H. K. Chung, C. Bowen, C. J. Fontes, S. B. Hansen, and Y. Ralchenko, High Energy Density Physics **9**, 645 (2013).

[66] P. Beiersdorfer, J. Phys. B: At., Mol. Opt. Phys. **48**, 144017 (2015).

[67] M. Hahn and D. W. Savin, The Astrophysical Journal **800**, 68 (2015).

[68] M. Hahn and D. W. Savin, arXiv:1506.07127 [astro-ph, physics:physics] (2015).

[69] M. Schnell, G. Gwinner, N. R. Badnell, M. E. Bannister, S. Böhm, J. Colgan, S. Kieslich, S. D. Loch, D. Mitnik, A. Müller, M. S. Pindzola, S. Schippers, D. Schwalm, W. Shi, A. Wolf, and S.-G. Zhou, Phys. Rev. Lett. **91**, 043001 (2003).

[70] M. Fogle, N. R. Badnell, P. Glans, S. D. Loch, S. Madzunkov, S. A. Abdel-Naby, M. S. Pindzola, and R. Schuch, Astronomy & Astrophysics **442**, 10 (2005).

[71] S. Schippers, Nuclear Instruments and Methods in Physics Research Section B: Beam Interactions with Materials and Atoms **350**, 61 (2015).

[72] I. Orban, S. D. Loch, S. Böhm, and R. Schuch, Astrophys. J. **721**, 1603 (2010).

[73] C. Beilmann, O. Postavaru, L. H. Arntzen, R. Ginzel, C. H. Keitel, V. Mäckel, P. H. Mokler, M. C. Simon, H. Tawara, I. I. Tupitsyn, *et al.*, Phys. Rev. A **80**, 050702 (2009).

[74] C. Beilmann, P. H. Mokler, S. Bernitt, C. H. Keitel, J. Ullrich, J. R. Crespo López-Urrutia, and Z. Harman, Phys. Rev. Lett. **107**, 143201 (2011).

[75] C. Beilmann, Z. Harman, P. H. Mokler, S. Bernitt, C. H. Keitel, J. Ullrich, and J. R. Crespo López-Urrutia, Phys. Rev. A **88**, 062706 (2013).

[76] T. M. Baumann, Z. Harman, J. Stark, C. Beilmann, G. Liang, P. H. Mokler, J. Ullrich, and J. R. Crespo López-Urrutia, Phys. Rev. A **90**, 052704 (2014).

[77] P. H. Mokler, C. Beilmann, Z. Harman, C. H. Keitel, S. Bernitt, J. Ullrich, and J. R. Crespo López-Urrutia, *New Trends in Atomic and Molecular Physics*, edited by M. Mohan, Springer Series on Atomic, Optical, and Plasma Physics No. 76 (Springer Berlin Heidelberg, 2013) pp. 57–66.

[78] E. Costa, P. Soffitta, R. Bellazzini, A. Brez, N. Lumb, and G. Spandre, Nature **411**, 662 (2001).

[79] S. Ali, S. Mahmood, I. Orban, S. Tashenov, Y. M. Li, Z. Wu, and R. Schuch, J. Phys. B: At., Mol. Opt. Phys. **44**, 225203 (2011).

[80] T. Fuchs, C. Biedermann, R. Radtke, E. Behar, and R. Doron, Phys. Rev. A **58**, 4518 (1998).

[81] C. Biedermann, A. Förster, G. F. mann, and R. Radtke, Phys. Scr. **1997**, 360 (1997).

[82] K. Blum, *Density Matrix Theory and Applications*, Springer Series on Atomic, Optical, and Plasma Physics, Vol. 64 (Springer Berlin Heidelberg, Berlin, Heidelberg, 2012).

[83] R. M. Steffen and K. Alder, *The Electromagnetic Interaction in Nuclear Spectroscopy*, edited by W. D. Hamilton (North- Holland, New York, 1975) p. 505.

[84] P. Beiersdorfer, D. A. Vogel, K. J. Reed, V. Decaux, J. H. Scofield, K. Widmann, G. Hölzer, E. Förster, O. Wehrhan, D. W. Savin, *et al.*, Phys. Rev. A **53**, 3974 (1996).

[85] E. Takács, E. S. Meyer, J. D. Gillaspy, J. R. Roberts, C. T. Chantler, L. T. Hudson, R. D. Deslattes, C. M. Brown, J. M. Laming, J. Dubau, and M. K. Inal, Phys. Rev. A **54**, 1342 (1996).

[86] P. Beiersdorfer, J. R. Crespo López-Urrutia, V. Decaux, K. Widmann, and P. Neill, Rev. Sci. Instrum. **68**, 1073 (1997).

[87] A. S. Shlyaptseva, R. C. Mancini, P. Neill, P. Beiersdorfer, J. R. Crespo López-Urrutia, and K. Widmann, Phys. Rev. A **57**, 888 (1998).

[88] A. S. Shlyaptseva, R. C. Mancini, P. Neill, and P. Beiersdorfer, J. Phys. B **32**, 1041 (1999).

[89] P. Beiersdorfer, G. Brown, S. Utter, P. Neill, K. J. Reed, A. J. Smith, and R. S. Thoe, Phys. Rev. A **60**, 4156 (1999).

[90] N. Nakamura, D. Kato, N. Miura, T. Nakahara, and S. Ohtani, Phys. Rev. A **63**, 024501 (2001).

[91] D. L. Robbins, A. Y. Faenov, T. A. Pikuz, H. Chen, P. Beiersdorfer, M. J. May, J. Dunn, K. J. Reed, and A. J. Smith, Phys. Rev. A **70**, 022715 (2004).

[92] D. L. Robbins, P. Beiersdorfer, A. Y. Faenov, T. A. Pikuz, D. B. Thorn, H. Chen, K. J. Reed, A. J. Smith, K. R. Boyce, G. V. Brown, *et al.*, Phys. Rev. A **74**, 022713 (2006).

[93] Z. Hu, Y. Li, X. Han, D. Kato, X. Tong, H. Watanabe, and N. Nakamura, Phys. Rev. A **90**, 062702 (2014).

[94] G. Weber, H. Bräuning, A. Surzhykov, C. Brandau, S. Fritzsche, S. Geyer, S. Hagmann, S. Hess, C. Kozhuharov, R. Märtin, *et al.*, Phys. Rev. Lett. **105**, 243002 (2010).

[95] A. Gumberidze, S. Fritzsche, S. Hagmann, C. Kozhuharov, X. Ma, M. Steck, A. Surzhykov, A. Warczak, and T. Stöhlker, Phys. Rev. A **84**, 042710 (2011).

[96] H. S. W. Massey and D. R. Bates, Rep. Prog. Phys. **9**, 62 (1942).

[97] A. Burgess, Astrophys. J. **139**, 776 (1964).

[98] P. Beiersdorfer, T. W. Phillips, K. L. Wong, R. E. Marrs, and D. A. Vogel, Phys. Rev. A **46**, 3812 (1992).

[99] D. A. Knapp, R. E. Marrs, M. B. Schneider, M. H. Chen, M. A. Levine, and P. Lee, Phys. Rev. A **47**, 2039 (1993).

[100] R. Radtke, C. Biedermann, T. Fuchs, G. Fußmann, and P. Beiersdorfer, Phys. Rev. E **61**, 1966 (2000).

[101] S. Mahmood, S. Ali, I. Orban, S. Tashenov, E. Lindroth, and R. Schuch, The Astrophysical Journal **754**, 86 (2012).

[102] D. A. Knapp, R. E. Marrs, M. A. Levine, C. L. Bennett, M. H. Chen, J. R. Henderson, M. B. Schneider, and J. H. Scofield, Phys. Rev. Lett. **62**, 2104 (1989).

[103] N. Nobuyuki, P. K. Anthony, W. Hirofumi, A. S. Hiroyuki, L. Yueming, K. Daiji, J. C. Fred, and O. Shunsuke, Phys. Rev. Lett. **100**, 073203 (2008).

[104] W. D. Chen, J. Xiao, Y. Shen, Y. Q. Fu, F. C. Meng, C. Y. Chen, B. H. Zhang, Y. J. Tang, R. Hutton, and Y. Zou, Phys. Plasmas **15**, 083301 (2008).

[105] K. Yao, Z. Geng, J. Xiao, Y. Yang, C. Chen, Y. Fu, D. Lu, R. Hutton, and Y. Zou, Phys. Rev. A **81**, 022714 (2010).

[106] W. Zhang, K. Yao, Y. Yang, C. Chen, R. Hutton, and Y. Zou, Phys. Rev. A **82**, 020702 (2010).

[107] A. P. Kavanagh, H. Watanabe, Y. M. Li, B. E. O, ÄôRourke, H. Tobiyama, N. Nakamura, S. McMahon, C. Yamada, S. Ohtani, and F. J. Currell, Phys. Rev. A **81**, 022712 (2010).

[108] S. Mahmood, S. Ali, I. Orban, S. Tashenov, E. Lindroth, and R. Schuch, Astrophys. J. **754**, 86 (2012).

[109] D.-H. Zhang, Y.-L. Shi, J. Jiang, C.-Z. Dong, and K. Fumihiro, Chinese Physics B **21**, 013402 (2012).

[110] K. Yao, Z. Geng, J. Xiao, Y. Yang, C. Chen, Y. Fu, D. Lu, R. Hutton, and Y. Zou, Phys. Rev. A **81**, 022714 (2010).

[111] Z. Hu, Y. Li, and N. Nakamura, Phys. Rev. A **87**, 052706 (2013).

[112] G. Xiong, J. Zhang, Z. Hu, N. Nakamura, Y. Li, X. Han, J. Yang, and B. Zhang, Phys. Rev. A **88**, 042704 (2013).

[113] M. E. Foord, S. H. Glenzer, R. S. Thoe, K. L. Wong, K. B. Fournier, B. G. Wilson, and P. T. Springer, Phys. Rev. Lett. **85**, 992 (2000).

[114] B. J. Wargelin, S. M. Kahn, and P. Beiersdorfer, Phys. Rev. A **63**, 022710 (2001).

[115] K. W. Hill, S. von Goeler, M. Bitter, L. Campbell, R. D. Cowan, B. Fraenkel, A. Greenberger, R. Horton, J. Hovey, and W. Roney, Phys. Rev. A **19**, 1770 (1979).

[116] M. Bitter, K. W. Hill, N. R. Sauthoff, P. C. Efthimion, E. Meservey, W. Roney, S. von Goeler, R. Horton, M. Goldman, and W. Stodiek, Phys. Rev. Lett. **43**, 129 (1979).

[117] F. Bely-Dubau, M. Bitter, J. Dubau, P. Faucher, A. H. Gabriel, K. W. Hill, S. Von Goeler, N. Sauthoff, and S. Volonté, Phys. Lett. A **93**, 189 (1983).

[118] V. Decaux, M. Bitter, H. Hsuan, S. von Goeler, K. W. Hill, R. A. Hulse, G. Taylor, H. Park, and C. P. Bhalla, Phys. Rev. A **43**, 228 (1991).

[119] M. Klapisch, A. B. Shalom, J. L. Schwob, B. S. Fraenkel, C. Breton, C. de Michelis, M. Finkenthal, and M. Mattioli, Phys. Lett. A **69**, 34 (1978).

[120] B. C. Stratton, H. W. Moos, and M. Finkenthal, The Astrophysical Journal Letters **279**, L31 (1984).

[121] D. W. Savin, S. M. Kahn, J. Linkemann, A. A. Saghiri, M. Schmitt, M. Grieser, R. Repnow, D. Schwalm, A. Wolf, T. Bartsch, A. Müller, S. Schippers, M. H. Chen, N. R. Badnell, T. W. Gorczyca, and O. Zatsarinny, The Astrophysical Journal **576**, 1098 (2002).

[122] L. N. Labzowsky and A. V. Nefiodov, Phys. Rev. A **49**, 236 (1994).

[123] A. J. González Martínez, J. R. Crespo López-Urrutia, J. Braun, G. Brenner, H. Bruhns, A. Lapierre, V. Mironov, R. Soria Orts, H. Tawara, M. Trinczek, et al., Phys. Rev. Lett. **94**, 203201 (2005).

[124] A. J. González Martínez, J. R. Crespo López-Urrutia, J. Braun, G. Brenner, H. Bruhns, A. Lapierre, V. Mironov, R. Soria Orts, H. Tawara, M. Trinczek, et al., Phys. Rev. A **73**, 052710 (2006).

[125] Z. Harman, I. I. Tupitsyn, A. N. Artemyev, U. D. Jentschura, C. H. Keitel, J. R. Crespo López-Urrutia, A. J. González Martínez, H. Tawara, and J. Ullrich, Phys. Rev. A **73**, 052711 (2006).

[126] T. Fuchs, C. Biedermann, R. Radtke, E. Behar, and R. Doron, Phys. Rev. A **58**, 4518 (1998).

[127] M. Chevallier, C. Cohen, N. Cue, D. Dauvergne, J. Dural, P. Gangnan, R. Kirsch, A. L'Hoir, D. Lelièvre, J.-F. Libin, P. H. Mokler, J.-C. Poizat, H.-T. Prinz, J.-M. Ramillon, J. Remillieux, P. Roussel-Chomaz, J.-P. Rozet, F. Sanuy, D. Schmaus, C. Stephan, M. Toulemonde, D. Vernhet, and A. Warczak, Phys. Rev. A **61**, 022724 (2000).

[128] R. Schuch, E. Lindroth, S. Madzunkov, M. Fogle, T. Mohamed, and P. Indelicato, Phys. Rev. Lett. **95**, 183003 (2005).

[129] C. Brandau, C. Kozhuharov, A. Müller, W. Shi, S. Schippers, T. Bartsch, S. Böhm, C. Böhme, A. Hoffknecht, H. Knopp, N. Grün, W. Scheid, T. Steih, F. Bosch, B. Franzke, P. H. Mokler, F. Nolden, M. Steck, T. Stöhlker, and Z. Stachura, Phys. Rev. Lett. **91**, 073202 (2003).

[130] C. Brandau, C. Kozhuharov, Z. Harman, A. Müller, S. Schippers, Y. S. Kozhedub, D. Bernhardt, S. Böhm, J. Jacobi, E. W. Schmidt, P. H. Mokler, F. Bosch, H.-J. Kluge, T. Stöhlker, K. Beckert, P. Beller, F. Nolden, M. Steck, A. Gumberidze, R. Reuschl, U. Spillmann, F. J. Currell, I. I. Tupitsyn, V. M. Shabaev, U. D. Jentschura, C. H. Keitel, A. Wolf, and Z. Stachura, Phys. Rev. Lett. **100**, 073201 (2008).

[131] M. Gail, N. Grün, and W. Scheid, J. Phys. B **31**, 4645 (1998).

[132] N. R. Badnell, J. Phys. B: At., Mol. Opt. Phys. **21**, 749 (1988).

[133] S. Mannervik, D. DeWitt, L. Engström, J. Lidberg, E. Lindroth, R. Schuch, and W. Zong, Phys. Rev. Lett. **81**, 313 (1998).

[134] N. Nakamura, A. P. Kavanagh, H. Watanabe, H. A. Sakaue, Y. Li, D. Kato, F. J. Currell, and S. Ohtani, Phys. Rev. Lett. **100**, 073203 (2008).

[135] D. Bernhardt, C. Brandau, Z. Harman, C. Kozhuharov, A. Müller, W. Scheid, S. Schippers, E. W. Schmidt, D. Yu, A. N. Artemyev, I. I. Tupitsyn, S. Böhm, F. Bosch, F. J. Currell, B. Franzke, A. Gumberidze, J. Jacobi, P. H. Mokler, F. Nolden, U. Spillman, Z. Stachura, M. Steck, and T. Stöhlker, Phys. Rev. A **83**, 020701 (2011).

[136] S. Fritzsche, A. Surzhykov, and T. Stöhlker, Phys. Rev. Lett. **103**, 113001 (2009).

[137] M. K. Inal and J. Dubau, J. Phys. B **20**, 4221 (1987).

[138] M. K. Inal and J. Dubau, J. Phys. B **22**, 3329 (1989).

[139] M. H. Chen and J. H. Scofield, Phys. Rev. A **52**, 2057 (1995).

[140] A. S. Shlyaptseva, R. C. Mancini, P. Neill, and P. Beiersdorfer, Rev. Sci. Instrum. **68**, 1095 (1997).

[141] Z. Hu, X. Han, Y. Li, D. Kato, X. Tong, and N. Nakamura, Phys. Rev. Lett. **108**, 073002 (2012).

[142] G. Breit, Phys. Rev. **34**, 553 (1929).

[143] E. Haug, Solar Phys. **71**, 77 (1981).

[144] M. Bitter, H. Hsuan, C. Bush, S. Cohen, C. J. Cummings, B. Grek, K. W. Hill, J. Schivell, M. Zarnstorff, P. Beiersdorfer, *et al.*, Phys. Rev. Lett. **71**, 1007 (1993).

[145] K. Widmann, P. Beiersdorfer, V. Decaux, S. R. Elliott, D. Knapp, A. Osterheld, M. Bitter, and A. Smith, Rev. Sci. Instrum. **66**, 761 (1995).

[146] J. Dubau and S. Volonte, Rep. Prog. Phys. **43**, 199 (1980).

[147] D. Porquet, J. Dubau, and N. Grosso, Space Sci. Rev. **157**, 103 (2010).

[148] T. Stöhlker, P. H. Mokler, F. Bosch, R. W. Dunford, F. Franzke, O. Klepper, C. Kozhuharov, T. Ludziejewski, F. Nolden, H. Reich, P. Rymuza, Z. Stachura, M. Steck, P. Swiat, and A. Warczak, Phys. Rev. Lett. **85**, 3109 (2000).

[149] H. A. Kramers, Philosophical Magazine Series 6 **46**, 836 (1923).

[150] H. A. Bethe and E. E. Salpeter, *Quantum Mechanics of One- and Two-Electron Atoms* (Springer-Verlag, Berlin, 1957).

[151] M. F. Gu, Astrophys. J. , 1085 (2003).

[152] M. J. Seaton, Monthly Notices of the Royal Astronomical Society **119**, 81 (1959).

[153] Y. Hahn, Reports on Progress in Physics **60**, 691 (1997).

[154] E. Kallne and J. Kallne, Phys. Scripta **1987**, 152 (1987).

[155] V. V. Balashov, A. N. Grum-Grzhimailo, and N. M. Kabachnik, *Polarization and Correlation Phenomena in Atomic Collision* (Kluwer Academics/ Plenum Publishers, 2000).

[156] A. Surzhykov, U. D. Jentschura, T. Stöhlker, and S. Fritzsche, Phys. Rev. A **73**, 032716 (2006).

[157] M. F. Gu, Astrophys. J. **582**, 1241 (2003).

[158] M. F. Gu, Can. J. Phys. **86**, 675 (2008).

[159] C. Beilmann, P. Amaro, H. Bekker, Z. Harman, J. R. Crespo López-Urrutia, and S. Tashenov, Phys. Scripta **2013**, 014052 (2013).

[160] S. Fritzsche, Comput. Phys. Commun. **183**, 1525 (2012).

[161] S. Dobradey, "Studies of K-LL resonances and simultaneous inner-shell vacuum ultraviolet transitions in highly charged iron using an electron beam ion trap," (2015), Master thesis, Heidelberg University.

[162] E. D. Donets, V. I. Ilushchenko, and V. A. Alpert, Proc. of the 1st ICIS - Saclay , 635 (1969).

[163] E. D. Donets, Nucl. Instrum. and Methods , 522 (1985).

[164] C. Litwin, M. Vella, and A. Sessler, Nuclear Instruments and Methods in Physics Research **198**, 189 (1982).

[165] M. A. Levine, R. E. Marrs, J. R. Henderson, D. A. Knapp, and M. B. Schneider, Phys. Scripta **1988**, 157 (1988).

[166] D. Knapp, R. Marrs, S. Elliott, E. Magee, and R. Zasadzinski, Nuclear Instruments and Methods in Physics Research Section A **334**, 305 (1993).

[167] R. E. Marrs, P. Beiersdorfer, S. R. Elliott, D. A. Knapp, and T. Stöhlker, Phys. Scr. **1995**, 183 (1995).

[168] J. D. Silver et al., Rev. Sci. Instrum. **65**, 1072 (1994).

[169] J. D. Gillaspy, Phys. Scr. **1997**, 99 (1997).

[170] F. Currell et al., J. Phys. Soc. Jpn. **65**, 3186 (1996).

[171] J. R. Crespo López-Urrutia, A. Dorn, R. Moshammer, and J. Ullrich, Phys. Scr. **1999**, 502 (1999).

[172] Y. Zou and R. Hutton, Phys. Scr. **2005**, 47 (2005).

[173] Y. Fu, K. Yao, B. Wei, D. Lu, R. Hutton, and Y. Zou, Journal of Instrumentation **5**, C08011 (2010).

[174] M. Froese, C. Champagne, J. Crespo Lpez-Urrutia, S. Epp, G. Gwinner, A. Lapierre, J. Pfister, G. Sikler, J. Ullrich, and J. Dilling, Hyperfine Interact. **173**, 85 (2006).

[175] S. W. Epp, J. R. Crespo López-Urrutia, M. C. Simon, T. Baumann, G. Brenner, R. Ginzel, N. Guerassimova, V. Mäckel, P. H. Mokler, B. L. Schmitt, *et al.*, J. Phys. B **43**, 194008 (2010).

[176] S. Böhm, A. Enulescu, T. Fritio, I. Orban, S. Tashenov, and R. Schuch, Journal of Physics: Conference Series **58**, 303 (2007).

[177] G. Zschornack, M. Kreller, V. P. Ovsyannikov, F. Grossman, U. Kentsch, M. Schmidt, F. Ullmann, and R. Heller, Rev. Sci. Instrum. **79**, 02A703 (2008).

[178] N. Nakamura, H. Kikuchi, H. A. Sakaue, and T. Watanabe, Rev. Sci. Instrum. **79**, 063104 (2008).

[179] L. F. Buchauer, "Construction of a compact electron beam ion trap," (2012), Bachelor thesis, Heidelberg University.

[180] C. Beilmann, "Resonance strength of multi-electron photo-recombination and ionization," (2013), Doctoral thesis, Heidelberg University.

[181] S. W. Epp, J. R. Crespo López-Urrutia, G. Brenner, V. Mäckel, P. H. Mokler, R. Treusch, M. Kuhlmann, M. V. Yurkov, J. Feldhaus, J. R. Schneider, *et al.*, Phys. Rev. Lett. **98**, 183001 (2007).

[182] S. Bernitt, G. V. Brown, J. K. Rudolph, R. Steinbrügge, A. Graf, M. Leutenegger, S. W. Epp, S. Eberle, K. Kubicek, V. Mackel, *et al.*, Nature **492**, 225 (2012).

[183] S. Bernitt, "Resonant excitation of astrophysical X-ray transitions in HCI with the free-electron laser LCLS," (2013), Doctoral thesis, Heidelberg University.

[184] M. W. Froese, "The TITAN Electron Beam Ion Trap: Assembly, Characterization, and First Tests," (2006), Master thesis, University of Manitoba.

[185] L. Brillouin, Phys. Rev. **67**, 260 (1945).

[186] A. Ashkin, J. Appl. Phys. **28**, 564 (1957).

[187] G. Herrmann, J. Appl. Phys. **29**, 127 (1958).

[188] M. F. Gu, D. W. Savin, and P. Beiersdorfer, J. Phys. B **32**, 5371 (1999).

[189] P. Beiersdorfer and M. Slater, Phys. Rev. E **64**, 066408 (2001).

[190] W. R. Leo, *Techniques for Nuclear and Particle Physics Experiments: A How-to Approach* (Springer, 1994).

[191] B. M. Penetrante, J. N. Bardsley, D. DeWitt, M. Clark, and D. Schneider, Phys. Rev. A **43**, 4861 (1991).

[192] S. Weber, C. Beilmann, C. Shah, and S. Tashenov, Rev. Sci. Instrum. **86**, 093110 (2015).

[193] A. Georgiev, W. Gast, and R. M. Lieder, Nuclear Science, IEEE Transactions on **41**, 1116 (1994).

[194] D. A. Knapp, R. E. Marrs, M. A. Levine, C. L. Bennett, M. H. Chen, J. R. Henderson, M. B. Schneider, and J. H. Scofield, Phys. Rev. Lett. **62**, 2104 (1989).

[195] H. Jörg, Z. Hu, H. Bekker, M. A. Blessenohl, D. Hollain, S. Fritzsche, A. Surzhykov, J. R. Crespo López-Urrutia, and S. Tashenov, Phys. Rev. A **91**, 042705 (2015).

[196] S. Agostinelli, J. Allison, K. Amako, J. Apostolakis, H. Araujo, P. Arce, M. Asai, D. Axen, S. Banerjee, G. Barrand, F. Behner, L. Bellagamba, J. Boudreau, L. Broglia, A. Brunengo, *et al.*, Nuclear Instruments and Methods in Physics Research Section A: Accelerators, Spectrometers, Detectors and Associated Equipment **506**, 250 (2003).

[197] J. Allison, K. Amako, J. Apostolakis, H. Araujo, P. Dubois, M. Asai, G. Barrand, R. Capra, S. Chauvie, R. Chytracek, G. A. P. Cirrone, G. Cooperman, G. Cosmo, G. Cuttone, G. Daquino, *et al.*, Nuclear Science, IEEE Transactions on **53**, 270 (2006).

[198] G. Depaola, Nuclear Instruments and Methods in Physics Research Section A: Accelerators, Spectrometers, Detectors and Associated Equipment **512**, 619 (2003).

[199] S. Fritzsche, N. M. Kabachnik, A. Surzhykov, and T. Stöhlker, Nucl. Instr. Meth. Phys. Res. A **267**, 257 (2009).

[200] S. Fritzsche, A. Surzhykov, and T. Stöhlker, Phys. Scripta **2011**, 014002 (2011).

[201] S. Fritzsche, A. Surzhykov, A. Gumberidze, and T. Stöhlker, New J. Phys. **14**, 083018 (2012).

[202] C. Beilmann, J. R. Crespo López-Urrutia, P. H. Mokler, and J. Ullrich, J. Instrum. **5**, C09002 (2010).

[203] X.-M. Tong, Z. Hu, Y. Li, X. Han, D. Kato, H. Watanabe, and N. Nakamura, J. Phys. B **48**, 144002 (2015).

[204] M. B. Schneider, D. A. Knapp, M. H. Chen, J. H. Scofield, P. Beiersdorfer, C. L. Bennett, J. R. Henderson, M. A. Levine, and R. E. Marrs, Phys. Rev. A **45**, R1291 (1992).

[205] S. Xi-Heng, W. Yan-Sen, C. Chong-Yang, and G. Ming-Feng, Chinese Physics **14**, 959 (2005).

[206] E. Behar, P. Mandelbaum, and J. L. Schwob, Phys. Rev. A **59**, 2787 (1999).

[207] O. Matula, S. Fritzsche, and A. Surzhykov, Phys. Scr. **T156**, 014051 (2013).

[208] F. Robicheaux and M. S. Pindzola, Phys. Rev. Lett. **79**, 2237 (1997).

[209] M. Arnaud and J. Raymond, The Astrophysical Journal **398**, 394 (1992).

[210] P. Mazzotta, G. Mazzitelli, S. Colafrancesco, and N. Vittorio, Astronomy and Astrophysics Supplement Series **133**, 7 (1998).

[211] M. F. Gu, Astrophys. J. **590**, 1131 (2003).

[212] M. Arnaud and R. Rothenflug, Astronomy and Astrophysics Supplement Series **60**, 425 (1985).

[213] D. A. Verner, Phys. Scr. **T83**, 174 (1999).

[214] E. Landi, G. Del Zanna, P. R. Young, K. P. Dere, and H. E. Mason, The Astrophysical Journal **744**, 99 (2012).

[215] H. K. Chung, M. H. Chen, W. L. Morgan, Y. Ralchenko, and R. W. Lee, High Energy Density Physics **1**, 3 (2005).

[216] H. Yoneda, N. Hasegawa, S. Kawana, and K. Ueda, Phys. Rev. E **56**, 988 (1997).

[217] J. Weinheimer, I. Ahmad, O. Herzog, H.-J. Kunze, G. Bertschinger, W. Biel, G. Borchert, and M. Bitter, Rev. Sci. Instrum. **72**, 2566 (2001).

[218] J. Shi, S. Xiao, J. Qian, X. Huang, and H. Cai, Nuclear Instruments and Methods in Physics Research Section A: Accelerators, Spectrometers, Detectors and Associated Equipment **624**, 137 (2010).

[219] F. Walden, H.-J. Kunze, A. Petoyan, A. Urnov, and J. Dubau, Phys. Rev. E **59**, 3562 (1999).

[220] D. G. S. Greene, J. L. Shohet, and P. A. Raimbault, Phys. Rev. Lett. **27**, 90 (1971).

[221] K. L. Wong, M. J. May, P. Beiersdorfer, K. B. Fournier, B. Wilson, G. V. Brown, P. Springer, P. A. Neill, and C. L. Harris, Phys. Rev. Lett. **90**, 235001 (2003).

[222] M. J. May, K. B. Fournier, P. Beiersdorfer, H. Chen, and K. L. Wong, Phys. Rev. E **68**, 036402 (2003).

[223] M. J. May, S. B. Hansen, J. Scofield, M. Schneider, K. Wong, and P. Beiersdorfer, Phys. Rev. E **84**, 046402 (2011).

[224] S. Tashenov, Priv. Comm. (2015).

List of publications

The following articles resulting from the work presented in this thesis:

Refereed articles

C. Shah, H. Jörg, S. Bernitt, S. Dobrodey, R. Steinbrügge, C. Beilmann, P. Amaro, Z. Hu, S. Weber, S. Fritzsche, A. Surzhykov, J. R. Crespo López-Urrutia and S. Tashenov, Polarization measurement of dielectronic recombination transitions in highly charged krypton ions, Phys. Rev. A **92**, 042702 (2015), Editor's Suggestion.

S. Weber, C. Beilmann, **C. Shah** and S. Tashenov, Compton polarimeter for 10 – 30 keV x rays, Rev. Sci. Instrum. **86**, 093110 (2015).

C. Shah, P. Amaro, R. Steinbrügge, C. Beilmann, S. Bernitt, S. Fritzsche, A. Surzhykov, J. R. Crespo López-Urrutia and S. Tashenov, Comprehensive study of resonant recombination in iron and krypton ions as a strong source of polarization of K_α x-rays from hot astrophysical and laboratory plasmas, Phys. Rev. Lett. Under review.

Conference Proceedings

C. Shah, P. Amaro, R. Steinbrügge, C. Beilmann, S. Bernitt, S. Fritzsche, A. Surzhykov, J. R. Crespo López-Urrutia and S. Tashenov, Complete measurements of anisotropic x-ray emission following recombination of highly charged ions", J. Phys.: Conf. Ser. **635**, 052093 (2015).

C. Shah, H. Jörg, Z. Hu, S. Bernitt, H. Bekker, M. A. Blessenohl, D. Hollain, S. Weber, S. Dobrodey, S. Fritzsche, A. Surzhykov, J. R. Crespo López-Urrutia and S. Tashenov, Linear polarization of x rays due to dielectronic recombination into highly charged ions", J. Phys.: Conf. Ser. **635**, 052091 (2015).

P. Amaro, **C. Shah**, S. Tashenov, C. Beilmann, S. Bernitt, J. R. Crespo López-Urrutia, S. Fritzsche, O. Kovtun, J. K. Rudolph, R. Steinbrügge and A. Surzhykov, Measurement of the angular distribution of Dielectronic Recombination into highly charged Krypton ions, J. Phys.: Conf. Ser. **488**, 062030 (2014).

Articles in preparation

P. Amaro, **C. Shah**, R. Steinbrügge, C. Beilmann, S. Bernitt, S. Fritzsche, A. Surzhykov, J. R. Crespo López-Urrutia and S. Tashenov, State selective influence of Breit interaction on photon angular distribution in dielectronic recombination.

C. Shah, P. Amaro, R. Steinbrügge, S. Bernitt, S. Fritzsche, A. Surzhykov, J. R. Crespo López-Urrutia and S. Tashenov, Measurement of the x-ray emission anisotropy in the resonant photorecombination of $Fe^{18+...24+}$.

C. Shah, P. Amaro, R. Steinbrügge, S. Bernitt, J. R. Crespo López-Urrutia and S. Tashenov, Diagnostics of the electron cyclotron motion in an electron beam ion trap.

Z. Hu, **C. Shah**, S. R. McConnell, A. Surzhykov and S. Tashenov, Dynamic effect on the alignment of L_{III} subshell vacancies in nuclear α decay.

Acknowledgments

At the end of my Ph.D., I would wish to convey my earnest gratitude to the people who contributed to this work, helped and supported me during my work.

Foremost of all, I would like to forward my special thanks to my supervisor Dr. Stanislav Tashenov for being extremely supportive and helpful right from the day one. I am really grateful to him for believing in my abilities and providing me an opportunity to pursue Ph.D. here in Heidelberg. I would like to sincerely thank him for answering all my questions, offering helpful comments, and showing faith and immense patience during past three years.

I wish to thank my co-supervisor at MPIK, Dr. José R. Crespo Lopéz-Urrutia. I owe a great deal to José, who guided me in the operation of Heidelberg electron beam ion traps and gave me the freedom to work with the machines in his laboratory. He always found time to help me and to have plenty of discussion on physics. It is a pleasure to talk about any topic with him. The experience and the experimental skills I learned from him and Stanislav are invaluable and utterly essential in carrying out this work.

I am very thankful to Dr. Stanislav Tashenov and Dr. Zoltán Harman for agreeing to referee my thesis and additionally Prof. Thomas Pfeifer and Prof. Werner Aeschbach-Hertig for agreeing to be in the examination committee. I would like to thank Stanislav, Zoltán, Sven and Pedro for correcting parts of my thesis. Thanks to Holger Jörg for his help in translating the thesis abstract into German. I am likewise thankful to my graduate schools, HGSFP and IMPRS-QD, for their assistance and funding.

I would like to thank my colleagues at Physics Institute: Pedro Amaro, Oleksiy Kovtun, Zhimin Hu, Vanessa Simon, Holger Jörg, Armen Hyrapetyan, Oliver Matula, Thorsten Jahrsetz, Sebastian Weber, Sean McConnell and Allison Pinto. It was a great joy to work in the friendly environment created by my colleagues. I would likewise wish to forward my thanks to colleagues at Max-Planck-Institute: Sven Bernitt, René Steinbrügge, Stepan Dobrodey, Christian Beilmann, Hendrik Bekker, Oscar Versolato,

Alexander Windberger, Thomas Baumann and Jan Rudolph. I have benefited greatly through discussion with Sven Bernitt, René Steinbrügge, Zhimin Hu and Pedro Amaro. This work could not have been possible without their continuous help and support.

The part of this work has been extensive theoretical calculations. I would like to thank exclusively Pedro Amaro for introducing me to the world of theoretical calculations. His constant guidance during my Ph.D. time helped me a lot in carrying out this work. I wish to thank Prof. Stephan Fritzsche and Dr. Andrey Surzhykov for a fantastic and fruitful collaboration. Their precise comments and suggestions were of a special importance for my work.

I would wish to show my gratitude to my previous supervisors and teachers in India especially, Prof. Shyam Lal, Dr. CVS Rao, Dr. Shankar Joisa, Prof. A. C. Sharma, Prof. C. F. Desai and Dr. B. P. Shah.

I would wish to thank all my friends in Heidelberg especially, Chintan Trivedi, Rajesh, Ishaan, Swati, Puneet, Sagar, Rahul, Bala, Deepti, Ankita and Sonal. I thank all of them for making me feel less far from family. I would also wish to thank my friends in India, Ketan, Arpit, Rajni, Mayur, Jay and Yesha for always being helpful and supportive.

I really cannot imagine myself here without the love and efforts from my family back in India. Thank you 'Mammi' and 'Pappa' for supporting me throughout my studies and always encouraging me to follow my dreams. Thanks to them for teaching me the merits of discipline and the rewards of my education. I wish to thank my elder sister 'Rinkal' who had played very important role in my studies. I am also really thankful to accept blessings from my grandma.

Chintan Shah

October 2015, Heidelberg